YEARBOOK
2023

INSTITUTE OF TECHNICAL PHYSICS AND MATERIALS SCIENCE
HUN-REN CENTRE FOR ENERGY RESEARCH
PART OF THE HUNGARIAN RESEARCH NETWORK

http://www.mfa.kfki.hu/

Published by the
Institute of Technical Physics and Materials Science
HUN-REN Centre for Energy Research
Part of the Hungarian Research Network

HUN-REN EK MFA Yearbook 2023

Director: Prof. Béla Pécz, corr. member of HAS

Address: Konkoly-Thege Miklós út 29-33, H-1121 Budapest, Hungary
Postal: P.O.Box 49, H-1525 Budapest, Hungary
Phone: +36-1-392 2224
E-mail: info@mfa.kfki.hu
URL: http://www.mfa.kfki.hu/
Editor: Krisztina Szakolczai, Ph.D.
Published by: HUN-REN EK MFA, Budapest, Hungary, 2024.

Content

GENERAL INFORMATION

Director's foreword

As the director of MFA, it is my pleasure to welcome the reader. I recommend browsing the present yearbook which continues the series of the former ones and contains results achieved in 2023.

2023 was the fourth whole year what we spent as the member of Eötvös Loránd Research Network (ELKH) I wanted to write, but this is wrong. The name of our research network was changed for HUN-REN, i.e. Hungarian Research Network, that caused us some extra administrative tasks during the year. The administration rules and the "equation" via the next year budget support is calculated was changed in the central administration, but being members of the Centre for Energy Research (CER) we always benefit of the synergy and of the complementary behaviour of the three member institutes of CER.

Although we observed and felt that the R&D costs in Hungary were substantially lowered down to 1.38% of GDP, thanks to our projects we gained before, we could work without any big obstacles. Furthermore 5 new OTKA projects were gained by colleagues.

Already in 2022 we faced a new challenge, what was the elevated price of gas heating increased by a magnitude of order. The appropriate heat pumps were immediately selected, the installation work started and was successfully finished in 2023. As a result, both buildings of MFA are heated (the technology building is even cooled) by those devices. MFA does not use anymore gas for heating.

MFA could continue to pay publication award for the young authors of the best publications.

The salaries are still very low, what we also pointed out in the self assessment which we had to write and submit to our central administration. An assessment of an international committee is expected next Spring and hopefully that will bring at least a modest salary increase for our staff…

In 2023 some of our colleagues achieved successful scientific qualification. Levente Tapasztó got the Doctor of Academy title, and we had also five successful PhD candidates, namely: Márton Szendrő, Nikolett Hegedűs, Mohamed Arfaouri, Klára Hajagos Nagy, György Benjámin Kalas, we are very proud of them and congratulate to the supervisors as well. Péter Beatrix and Zámbó Dániel successfully fulfilled a habilitation process and became senior research fellow.

Our Attila Szolnoki was awarded by the highest Physics Prize at the Hungarian Academy, Physics Section of Sciences for his work and results he achieved in statistical physics. I am also pleased to inform you that the Officer's Cross of the Hungarian Order of Merit was donated to our Péter Barna, who is our research professor emeritus. Parallel to that our Katalin Balázsi received the Hungarian Gold Cross of Merit. The Széchenyi Prize (the highest scientific prize in Hungary) was donated to Professor Katalin Kamarás who is our colleague via a part time contract, we enjoy the common work with her and congratulate warmly.

We are also proud of the scientific results achieved by our colleagues, I hope you will enjoy learning them in this book. Here I note that the former MFA Yearbooks are available electronically at http://www.mfa.kfki.hu/hu/yearbook.

Prof. Béla Pécz
Director

Organizational structure

Director: Prof. Béla Pécz

Scientific departments	
Thin Film Physics Department	Katalin BALÁZSI, Ph.D.
Complex Systems Department	Géza ÓDOR, D.Sc.
Photonics Department	Péter PETRIK, D.Sc.
Nanobiosensorics Department	Róbert HORVÁTH, Ph.D.
Microsystems Department	Péter FÜRJES, Ph.D.
Nanosensorics Laboratory	János VOLK, Ph.D.
Nanostructures Department and "Lendület" group - 2D Materials	Levente TAPASZTÓ, Ph.D.
"Lendület" group - Topological Nanostructures	Péter NEMES-INCZE, Ph.D.

Directly supervised functions	
Head of Scientific Advisory Council	Levente TAPASZTÓ, Ph.D.
Scientific secretary, projects and PR	Krisztina SZAKOLCZAI, Ph.D.
Quality control, patents, MTMT, REAL admin	Andrea BOLGÁR
Technical support	Károly BODNÁR
Financial administration	Zsuzsanna KELEMEN
Innovation manager, patents	Valéria OSVÁTH
Technology transfer (IPR)	Antal GASPARICS, Ph.D.

Key Figures of MFA

MFA budget 2003-2023 (million HUF)

You can follow the budget of MFA in the last 20 years in the chart below. Basic subsidy is growing slightly, but far from following inflation. The periodicity of large calls for tenders - eg. EU grants and domestic innovation grants from different ministrys- can be observed in the evolution of the institute's budget. These have major effect on our everyday life. Fortunatelly the last few years were successful in terms of grant applications. Three Thematic Excellence Programmes (TKP2021) projects have started in the beginning of 2022. Also the EU Key Digital Technology project, the ECSEL JU project, MSCA fellowships, and a Pathfinder project, together with ERA-NET grants provided international visibility and utilization of the results. These gave stability for major research lines in our laboratories for 3-4 years.

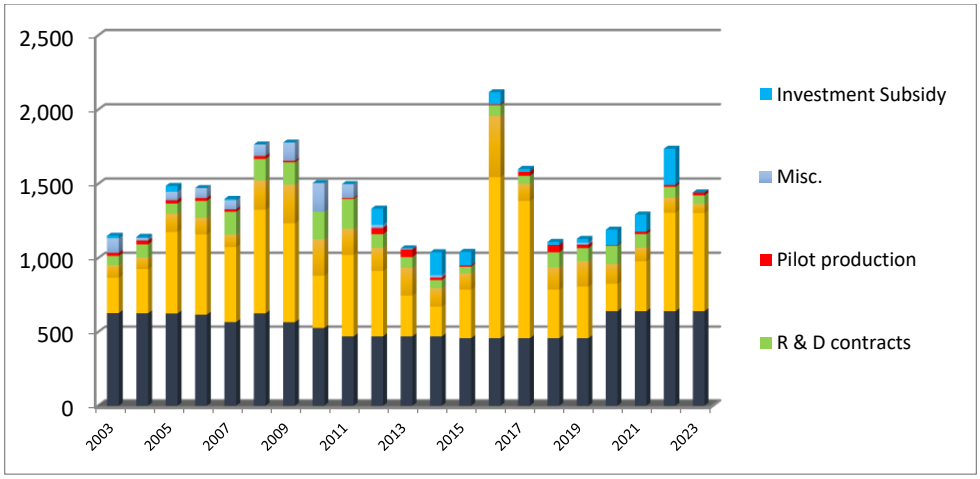

MFA and its predecessor's publications and citations per year since 1998

According to the Thomson-Reuters ISI "Web of Knowledge", and MTMT2 databases, the Institute has an average publication activity of ca. 110 scientific papers in IF journals a year (link). Recently MFA researchers tend to publish in journals with higher impact factors and the number of citations are constantly increasing.

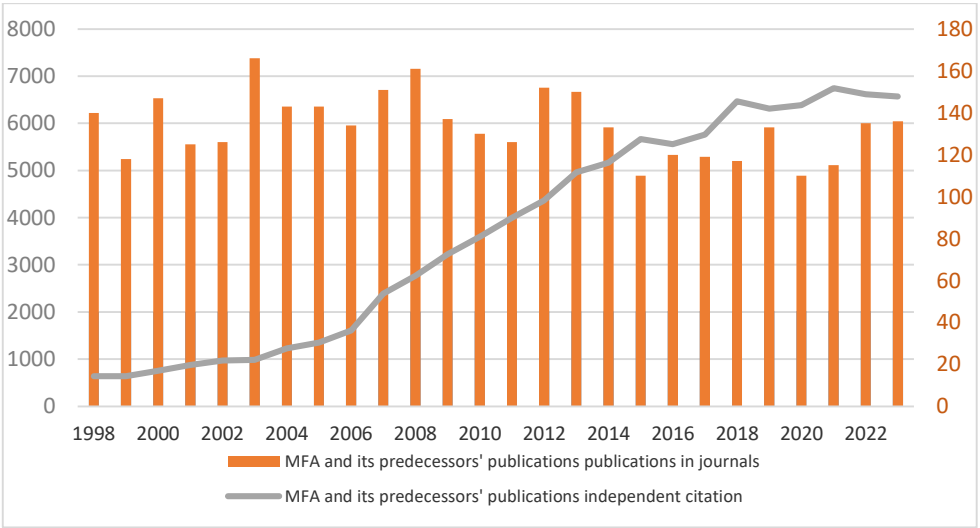

Prizes and Distinctions

	Katalin KAMARÁS	Széchenyi Prize
	Péter B BARNA	Officer's Cross of the Hungarian Order of Merit
	Katalin Balázsi	Hungarian Gold Cross of Merit
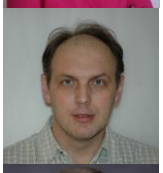	Attila SZOLNOKI	Physics Prize at the Hungarian Academy
	**Gábor PISZTER**	Róbert Bárány Prize of the the Hungarian Academy
	**Juhász Zoltán**	Pima Prize
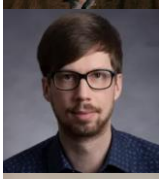	**Gábor PISZTER**	Tibor Jermy Prize of the Hungarian Museum of Natural Sciences
	**György SÁFRÁN**	MFA institute prize
	**András DEÁK**	MFA institute prize

Dániel ZÁMBÓ MFA postdoc researchers prize

Gábor PISZTER MFA postdoc researchers prize

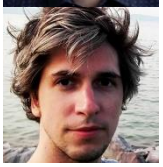

Márton SZENDRŐ MFA young researchers prize

Gábor Piszter receives the Tibor Jermy Prize at the Hungarian Museum of Natural Sciences

The 115 km race length of the 5th Ultrabalaton Trail running race was completed by our collegues. The team of 7 completed the extreme distance in 12 hours and 35 minutes in a relay, finishing in 113th place out of 204 teams with this time result. The team members: Barbara Beiler, Dóra Bereczki, Ferenc Braun, Péter Fürjes, Levente Illés, Zsombor Szomor and János Volk.

SCIENTIFIC REPORTS

1 - Nanostructures Laboratory

Head: Dr. Levente TAPASZTÓ, D.Sc., research advisor

Research Staff:

- Prof. László Péter BIRÓ, Member of the HAS
- Zsolt Endre HORVÁTH, D.Sc., Deputy Head of Laboratory
- Gergely DOBRIK, Ph.D.
- Krisztián KERTÉSZ, Ph.D.
- Antal Adolf KOÓS, Ph.D.
- Géza István MÁRK, Ph.D.
- Péter NEMES-INCZE, Ph.D.
- Zoltán OSVÁTH, Ph.D.
- András PÁLINKÁS, Ph.D.
- Gábor PISZTER, Ph.D.
- Péter SÜLE, Ph.D.
- Péter VANCSÓ, Ph.D.

M.Sc./Ph.D. students:

- Konrád KANDRAI, Ph.D. student
- Soma KESZEI
- Péter KUN, Ph.D. student
- Krisztián MÁRITY, Ph.D. student
- Márton SZENDRŐ, Ph.D. student
- György KÁLVIN, Ph.D. student

The research activity of the Nanostructures Laboratory is based on the two-decade-long expertise in the synthesis, characterization and engineering of various nanostructures using scanning probe microscopy as the main experimental technique. Since more than a decade, our research efforts are focused on the investigation of two-dimensional materials. Besides graphene, in the last couple of years, novel 2D materials, mainly form the family of transition metal chalcogenides (TMC) have been intensely studied. Recently, we have further extended our activity with the investigation of layered topological insulator crystals. We have also successfully continued our research on bioinspired photonic nanoarchitectures.

Identification of graphite with perfect rhombohedral stacking by electronic Raman scattering

OTKA KKP 138144, TKP2021-NKTA-05, OTKA K 146156, OTKA PD 146479, OTKA K 134258, OTKA K 132869, OTKA FK 142985, 2022-1.2.5-TÉT-IPARI-KR-2022-00006

A. Pálinkás, K. Márity, K. Kandrai, Z. Tajkov, M. Gmitra (CLTP SAS, SK), P. Vancsó, L. Tapasztó, and P. Nemes-Incze

There are two energetically favorable configurations for stacking graphene layers in graphite: the stable and most common hexagonal (or AB), and the naturally rare, metastable rhombohedral (or ABC) stackings (Fig. 1.1.a). While the hexagonal phase has well-known properties, the latter is now receiving significant interest. That is because rhombohedral graphite (RG) is one of the simplest systems that can host a multitude of emergent, strongly correlated electronic phenomena. In recent years, state-of-the-art measurements have demonstrated, for example, unconventional superconductivity in 3-layer, correlated insulators in 4-layer, and fractionalization of the Hall resistance in 5-layer RG. The strength of electronic interactions, which drive these phenomena, increases with the addition of more rhombohedrally stacked graphene layers. However, until now, there were no reliable methods to identify thicker, perfect (defect-free) rhombohedral graphite layers. We have shown that perfect RG with 3 to 12 layers has a unique fingerprint owing to the Electronic Raman Scattering (ERS) process, which can be harnessed to overcome the identification challenge.

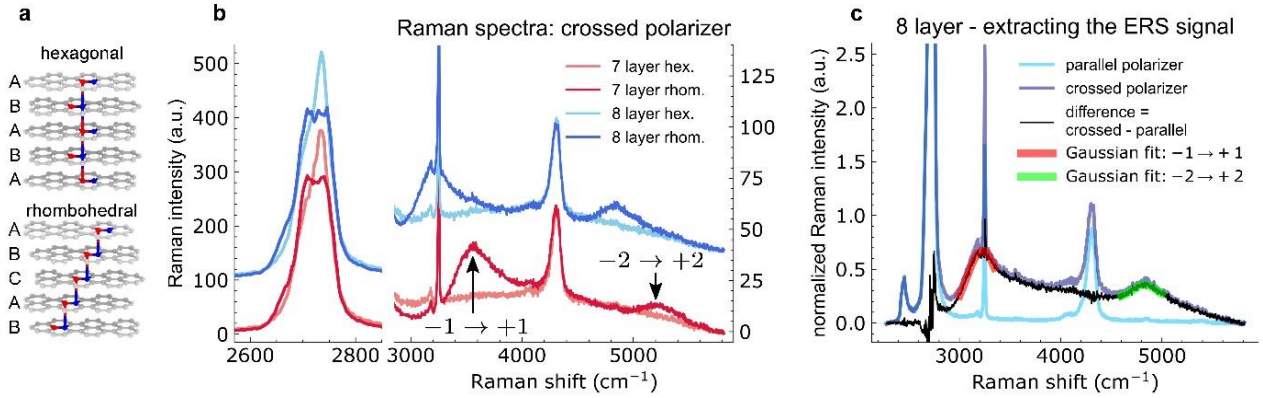

Figure 1.1 *a) Schematic representation of the hexagonal and rhombohedral stackings of graphite layers. b) Raman spectra of the 7 and 8 layer regions of hexagonal or rhombohedral stackings, measured using crossed polarization. Arrows mark the ERS signal. c) Extracting the ERS signal. This is achieved by subtracting the spectrum measured with parallel polarization from the one measured, using the crossed polarizer configuration.*

Fig. 1.1.b displays the phonon-originated 2D peak in the Raman spectrum alongside a broad ERS response for a 7- and 8-layer thick graphite sample, having perfectly stacked rhombohedral and hexagonal regions. Note, a polarizer is positioned in the path of the scattered light, oriented perpendicularly to the polarization of the incoming excitation laser. This "crossed polarizer" setup amplifies the visibility of the ERS signal, which otherwise is only ~1% of the 2D peak intensity, therefore cannot be detected in most measurements. Thanks to this "crossed polarizer" arrangement it becomes ~10% of the 2D peak intensity, as shown in Fig. 1.2.b. The polarization dependence of the scattered light also confirms that the broad peaks stem from ERS. If the polarizer in the path of the scattered light is in the parallel configuration, the broad peaks are absent, whereas they are clearly present in the crossed polarizer setup (Fig. 1.1.c). This comparison can also be used to separate the ERS peaks from phonon peaks of graphite. Subtracting the parallel polarized spectra, leaves us with the ERS signal. We fit the resulting ERS peaks by Gaussians to determine the Raman shift of the peaks. The result of this procedure is shown in Fig. 1.1.c.

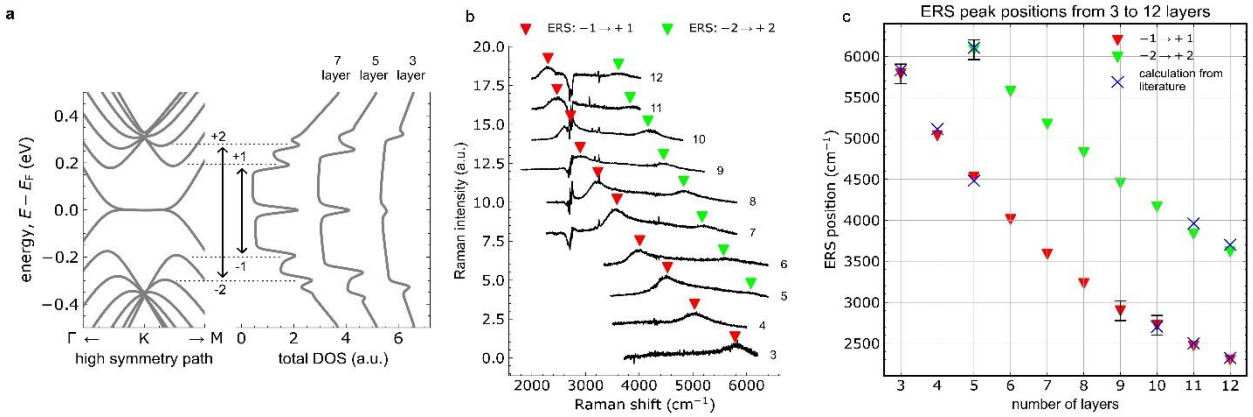

Figure 1.2. *(a) Left: Band structure around the K point of a 7-layer RG slab. Energy is with respect to the Fermi level (E_F). Right: density of states (DOS) at selected RG thicknesses. The transitions between the DOS peaks, which result in the ERS signal, are shown by arrows. (b) Difference of crossed/parallel spectra for perfect RG with graphene layer numbers between 3 and 12. Positions of the ERS peaks are shown by red and green triangles. (c) ERS peak positions for the first and second transitions are showing a clear trend on layer number. Blue crosses show the previously calculated ERS peak positions from the literature* [Ref. 1.1 and Ref.1.2].

This procedure is applied to defect-free RG samples with thicknesses varying from 3 to 12 graphene layers (Fig. 1.2.b). Each sample undergoes meticulous examination using atomic force microscopy (AFM) to ensure accurate layer count. A clear trend can be observed in Fig. 1.2.c: with increasing layer number the $-1 \rightarrow +1$ and $-2 \rightarrow +2$ peaks continuously shift to lower energy (lower Raman shift). The ERS measurements directly reveal the energy of the electron-hole excitations related to the DOS peak separations ($-1 \rightarrow +1$ and $-2 \rightarrow +2$) of the bulk band edges (Fig. 1.2.a).

The introduction of ERS as a fast and accessible optical characterization method to identify rhombohedral graphite without stacking faults, breaks down a major hurdle in exploring the properties of RG. ERS characterization of RG samples is expected to enable a consistent comparison of results from different samples and research groups, which is essential for the development of the field. These findings enable the identifications and the further examinations of perfect, thick RG, represent a great step forward over the state-of-the-art, and thus would play a role in exploring the myriad of strongly-correlated electronic phenomena.

Stabilizing giant moiré superlattices in twisted bilayer graphene

OTKA KKP 138144, TKP2021-NKTA-05, OTKA K 132869, OTKA FK 142985, 2022-1.2.5-TÉT-IPARI-KR-2022-00006

G. Dobrik, P. Kun, M. Szendrő, P. Vancsó, R. Csanádi, P. Nemes-Incze, and L. Tapasztó

Realizing moiré superlattices with small twist angles in bilayer graphene, corresponding to large moiré wavelengths (> 10 nm) is required for engineering a flat band, which in turn can give rise to various correlated electronic states at low temperatures. This has been demonstrated in the so-called magic angle graphene with a twist angle of about 1.1º, and moiré wavelength of about 13 nm. Moreover, theory predicts that four more magic angles are expected at lower twist angles, hence larger moiré wavelengths. However, the experimental realization of twisted bilayer graphene samples with twist angles smaller than 1º turned out highly challenging, due to the strong structural reconstruction emerging at such small twist angles.

Unfortunately, these reconstructions destroy the flat band, and hence no correlated electronic states are expected for reconstructed moiré superlattices. In fact, it has been shown that even at the first magic angle, structural reconstructions are already present, and they are increasing the dispersion of the flat band; however, their effect is not strong enough to fully destroy the flatness of the band. This is not the case for twist angles around 0.5 degrees, corresponding to the second predicted magic angle, hence the experimental realization and investigation of lower magic angles remained elusive. This is even more regrettable, as it has been predicted that the correlation effects become stronger at lower magic angles. Therefore, stabilizing moiré superlattices against structural reconstructions is highly desirable, as it can further increase the correlation effects at the first magic angle, and it can also enable the realization and study of the predicted lower magic angles in twisted bilayer graphene (TBG).

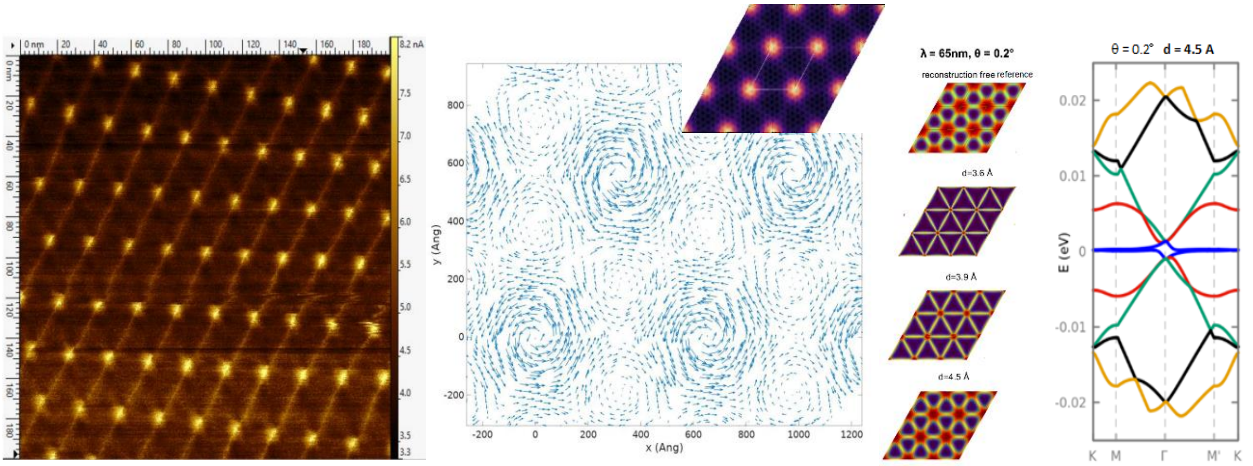

Figure 1.3. *a) Strongly reconstructed moiré superlattice in a twisted bilayer graphene (TBG) with a twist angle of 0.5º, measured by conductive AFM. b) Molecular dynamics simulations of structural reconstructions in TBG for a twist angle of 0.2º. c)Simulated lattice structures of TBG for different interlayer distances revealing the weakening of the structural reconstructions with increasing interlayer gap. The electronic structure of a 0.2º rotated TBG at an increased interlayer distance preserving the flat band*

After accidentally realizing an unreconstructed moiré superlattice with 65 nm wavelength, corresponding to a twist angle of 0.2 degrees, we have been systematically investigated by simulations, which effects could be responsible for stabilizing such small twist angle superlattices, against structural reconstructions. We have investigated various factors such as heterostrain, or substrate pinning, but found that only increasing the interlayer distance will enable avoiding the reconstructions and preserving the flat band at lower (magic) twist angles. Indeed, we were able to measure an increased interlayer distance in our

sample displaying reconstruction-free moiré superlattice corresponding to 0.2~ twist angle. Next, we have investigated by systematic simulations, what can cause an increased interlayer distance. We have investigated the effect of corrugation both induced by the SiO_2 support, as well as induced into the bottom graphene sheet (by cyclic thermal annealing); however, none of these factors could assure an increased interlayer separation. Intercalating atoms in between the two graphene layers would obviously increase the interlayer distance. However, there are two problems with this approach: (1) unless the intercalation is done by a fully continuous and ordered atomic intercalant layer, the interlayer separation would not be homogeneous, resulting in samples of poor quality, and (2) intercalating even a single atom (eg. Ar), will separate the layers further apart than needed, in order to avoid mechanical coupling, but preserve the electronic coupling between various stacking configurations. We observed experimentally an interlayer separation of about 0.7 A, by AFM measurements, yet still the (unreconstructed) moiré superlattice has been observed in topographic STM images, due to electronic effects, as well as a flat band has been observed in tunneling spectroscopy measurements.

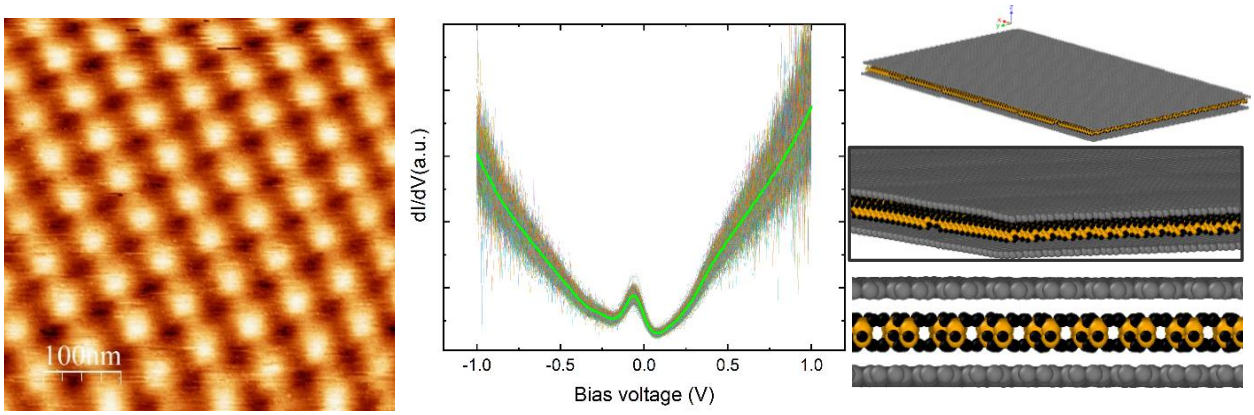

Figure 1.4 *a) STM image of a reconstruction-free TBG superlattice with a periodicity of 65 nm, corresponding to a twist angle of 0.2 degrees. b) Tunneling spectra revealing the presence of flat band in the form of a peak in the local density of states, near the Fermi level. c) Structural model from molecular dynamics simulations of a TBG with a spacer layer of self-organized alkane molecules intercalated between the graphene layers.*

What is a suitable spacer molecule that is capable to form a continuous self-organized molecular layer in between the two graphene layers? Recently we have shown that such continuous, self-organized layers can indeed spontaneously form on top of graphene under ambient exposure, consisting of simple alkanes. We have run the simulations to see if such a self-organized alkane layer would indeed be suitable to act a spacer layer, and decouple mechanically the two graphene layers. Our MD simulations show that this is indeed the case, since the interlayer separation is increased to about 0.8 A in good quantitative agreement with the measurements. The important question remaining is, how can the two layers be still electronically coupled at such large separations. Our detailed calculations revealed that the p_z graphene orbitals decay much slower in the van der Waals (vdW) gap when the alkane layer is present in the vdW gap, corresponding to an effective distance of about 0.4 A in vacuum, which indeed nicely reproduces the formation of the flat bands without structural reconstructions. The next step is to develop a sample preparation method when such TBLG samples with a self-organized alkane spacer layer can be fabricated with a good yield in order to enable the systematic study of lower magic angles and stronger correlations in twisted bilayer graphene samples

2D MoS_2 crystals can stabilize semiconducting Pt structures

OTKA KKP 138144, OTKA K 132869, TKP2021-NKTA-05, GrapheneCore3 Flagship

T. Ollár, P. Kun, P. Vancsó, A. Koós, P. Nemes-Incze, J.S. Pap, L. Tapasztó

Decreasing the size of the metal nanoparticles is a viable route to improve the noble metal utilization efficiency in catalysts. As the metal particle size is reduced, besides increasing the fraction of accessible surface atoms, an energy gap is also expected to open, below a critical size, due to quantum confinement effects. However, experimentally realizing and studying an energy gap in metal nanoparticles, turned out highly challenging. An energy gap has been observed in small Au nanocrystals, particularly, when their thickness has been reduced to one or two atomic layer. The observation of an energy gap in Pt nanostructures turned out even more challenging. Recent studies report the opening of an energy gap of about 0.2 eV in thiol capped, small (< 2.5 nm) Pt nanoparticles, based on NMR studies. However, the catalytic properties of nonmetallic Pt nanocrystals remained largely unexplored. We emphasize that here we focus on unoxidized, elemental Pt nanoparticles, as opposed to oxidized Pt structures that have been studied before, and are often also referred to as nonmetallic Pt.

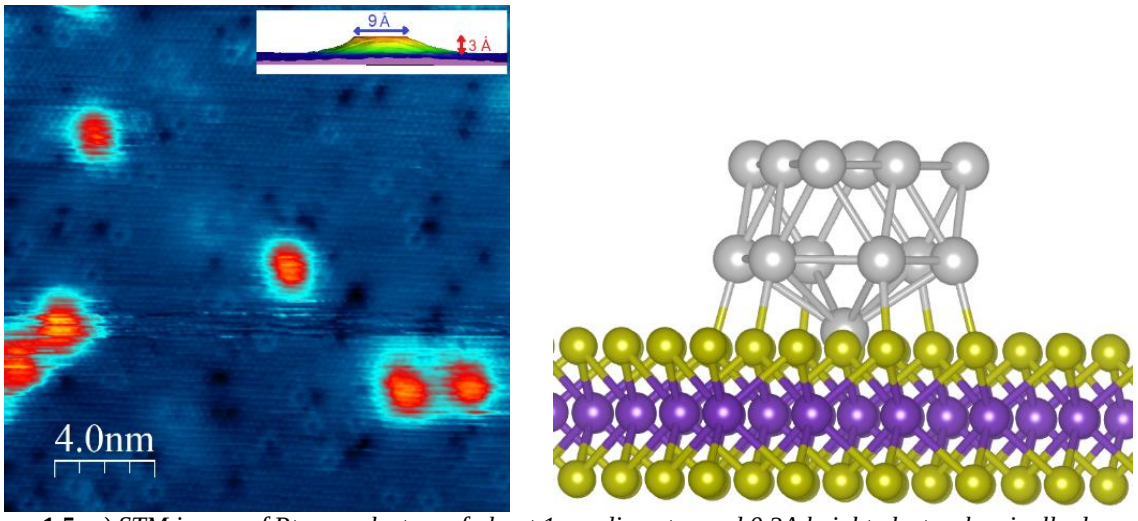

Figure 1.5. *a) STM image of Pt nanoclusters of about 1 nm diameter and 0.3A height electrochemically deposited on 2D MoS_2 crystals. The flattened geometry corresponding to two Pt atom thickness, indicates a strong metal-support interaction. The smaller bright and dark features in the STM image correspond to S atom vacancy defects of the 2D MoS_2 support that can act as anchors for stabilizing ultra-fine Pt clusters. b) Simulated (DFT) structure of a Pt_{13} cluster anchored to a S atom vacancy of the 2D MoS_2 crystal, reproducing the experimentally observed bilayer Pt structure.*

Metal-support interaction is a powerful tool for engineering the atomic and electronic structure of metal nanoparticles. While MoS_2 is regarded as a rather weakly interacting support, the chemical affinity between Pt and S holds the potential for a strong interaction.
However, unleashing the full strength of Pt-MoS_2 interactions for Pt nanocrystals is hindered by their large (> 10%) lattice mismatch with MoS_2. A better interface matching can be achieved for small (< 1 nm) Pt clusters, due to their higher plasticity. However, we show that under proper kinetic deposition conditions, a strongly enhanced adhesion can be realized between small (~1nm) Pt clusters and 2D MoS_2 crystals.

Gaining information on the electronic structure of Pt nanoparticles is of key importance for understanding and optimizing their catalytic performance. This, is of particular importance in our case, since both the flattened morphology (quantum size effects), and the enhanced metal-support interaction are expected to have a strong influence on the electronic structure. While tunneling spectroscopy measurements can directly probe the electronic structure of metal nanostructures, the available data on catalyst nanoparticles is very scarce. This is mainly due to charging effects, owing to the weak electronic coupling to the support. Due to the enhanced coupling emerging from the stronger Pt/MoS_2 interaction, we were able to resolve the fine details of the local density of states (LDOS) of small Pt clusters by tunneling spectroscopy, within the energy window (-1.8 eV to + 0.3 eV), opened by the band gap of the 2D MoS_2 support. The most striking feature, is a sizeable energy gap of about 0.3 eV, with fully suppressed Pt LDOS near the Fermi energy (0 V), evidencing the semiconducting nature of bilayer Pt clusters (Fig.1.6.a).

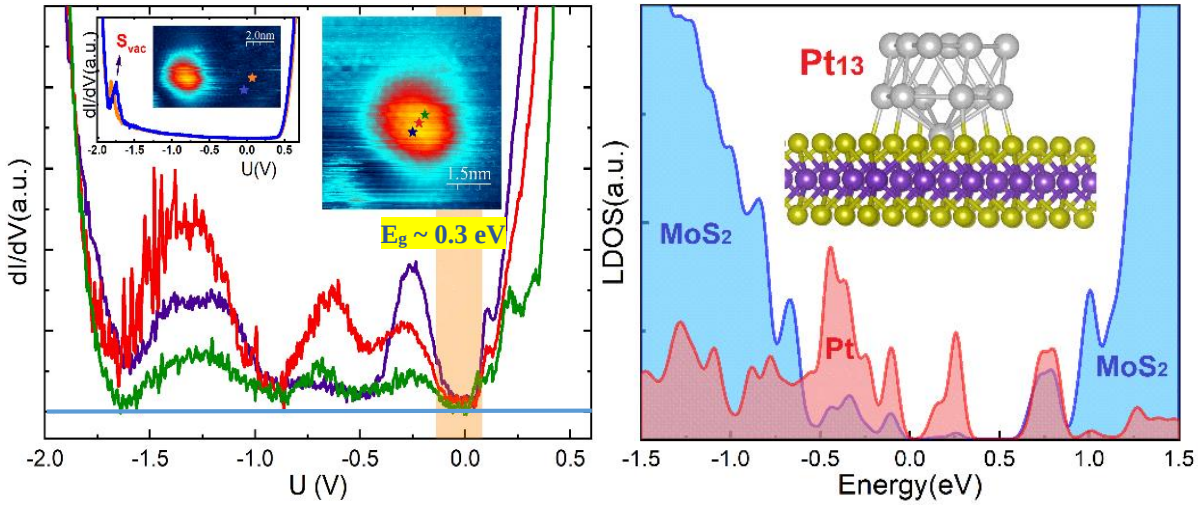

Figure 1.6. *a) Tunneling spectra recorded on a Pt cluster at the positions marked in the right inset, revealing a bandgap of ~300 meV. Left inset shows the tunneling spectra on MoS_2 away from Pt clusters, with a single peak characteristic to sulphur vacancies. b) Calculated (DFT) local density of states (LDOS) of a Pt_{13} cluster, anchored by an S_{vac} to the 2D MoS_2 support. Red and blue areas represent contributions from the Pt cluster and the MoS_2 support, respectively.*

To compare with the measured STM data, we have calculated the topographic STM images of the simulated bilayer Pt cluster structures, and found their heights to be about 3-4 Å, in good quantitative agreement with the experimentally measured cluster heights. To directly compare with our tunneling spectroscopy measurements, we have calculated by DFT the local density of states (LDOS) of such bilayer Pt clusters adsorbed on 2D MoS_2, comprising 10, 13 and 27 Pt atoms. We found that all the investigated bilayer Pt clusters are characterized by a sizeable energy gap at the Fermi level, in good agreement with the experimental findings. The calculated LDOS of the Pt_{13} clusters (Fig. 1.6.b) displays the best agreement with tunneling spectroscopy measurements (Fig. 1.6.a), which also matches the size of the measured clusters most closely.

Hybrid Bio-Nanocomposites by Integrating Nanoscale Au in Butterfly Scales Colored by Photonic Nanoarchitectures

K. Kertész, G. Piszter, A. Beck, A. Horváth, G. Nagy, Gy. Molnár, Gy. Z. Radnóczi, Zs. E. Horváth, L. Illés and L. P. Biró

Plasmonic metallic nanoparticles, like Au, can be used to tune the optical properties of photonic nanoarchitectures occurring in butterfly wing scales possessing structural color. The effect of the nanoscale Au depends on the location and the amount deposited in the chitin-based photonic nanoarchitecture. The following three types of Au introduction methods were compared regarding the structural and optical properties of the resulting hybrid bio-nanocomposites: (i) growth of Au nanoparticles inside the nanopores of butterfly wing scales by a light-induced in situ chemical reduction of $HAuCl_4$ in aqueous solution containing sodium citrate, as a new procedure we have developed, (ii) drop-drying onto the wing of the aqueous Au sol formed during procedure (i) in the bulk liquid phase, and (iii) physical vapor deposition of Au thin film onto the butterfly wing. We investigated all three methods at two different Au concentrations on the wings of laboratory-bred, blue-colored male *Polyommatus icarus* butterflies and characterized the optical properties of the resulting hybrid bio-nanocomposites.

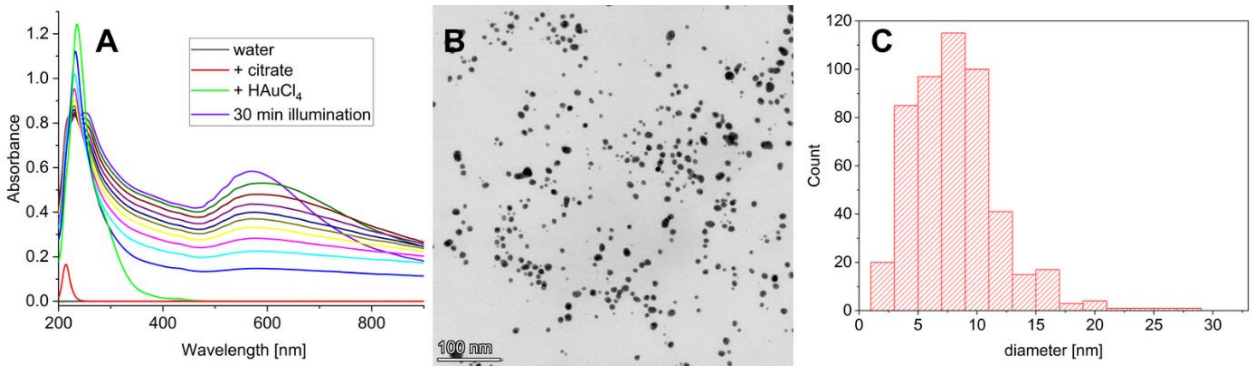

Figure 1.7 *a) Evolution of the absorbance spectra of the reaction medium on the addition of the reactants and during 30-min of illumination, b) TEM image, and c) size histogram of prepared Au nanoparticles.*

Starting with ultrapure water, sodium citrate and $HAuCl_4$ precursors in a cuvette with white light illumination first, gold seed nucleation occurs followed by growth, and this process can be observed with naked eye: the solution turns from pale yellow to light red. The formation of the nanoparticles was followed by spectral analysis of the solution's absorbance; the characteristic peak of the precursor decreases, and at the same time, the peak of the plasmonic resonance of the spherical nanoparticles appears at around 580-590 nm (Fig. 1.7.a). Using this protocol, we obtained spherical Au nanoparticles (Fig. 1.7.b) with size distribution shown in Fig. 1.7.c.

When Au nanoparticles are grown inside the nanopores of the wing scales (by placing as a piece of wing in the cuvette under illumination) or are deposited by drop-drying Au sol on the wing, the original optical properties of the biological photonic nanoarchitecture are tuned by the integration of the Au nanoparticles into the photonic nanoarchitecture. As shown by the spectra in Fig. 1.8.d and 1.8.e, the spectral properties are borrowed both form the pristine chitin photonic nanoarchitecture and the Au nanoparticles as modificatory components. Opposite to this, when the wing is coated by physical vapor deposition by 5 nm or 15 nm Au, no shift is seen in the spectral position of the reflectance maxima (Fig. 1.8.f) for any of the two gold thicknesses used.

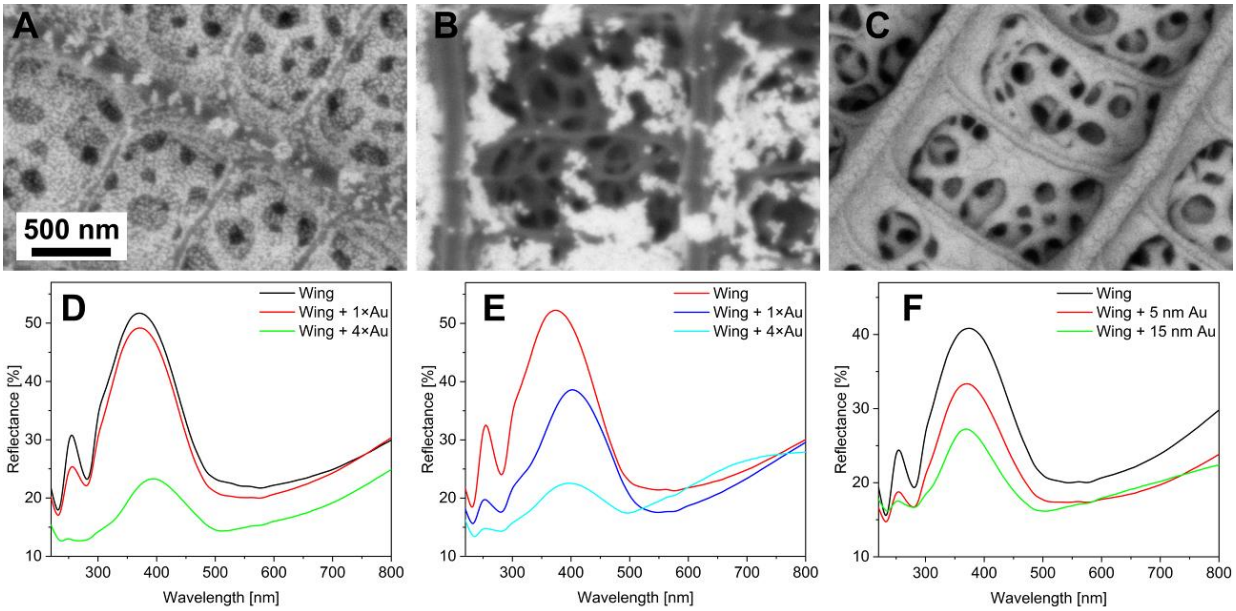

Figure 1.8. *Top view SEM images of the* Polyommatus icarus *wing scales decorated with Au nanoparticles using a) in situ growth, b) drop-drying and c) physical vapor deposition methods. Reflectance spectra of the ethanol pretreated wings before and after d) in situ growing using 1 and 4 doses of Au precursor, e) drop drying of sols prepared in d), and d) physical vapor deposition of 5 and 15 nm of Au.*

The reduction in the amplitude of the reflectance maximum is associated with the reduced transmittance of the Au layers; the effect is that of a filter placed into the light path between the illuminating source – wing, wing – detector system. In all cases, the magnitude of the observed effect scales with the amount of the Au used to alter the properties of the butterfly wing. When comparing the in situ growth with the drop-dying of Au sol, the former is more advantageous for the production of samples with uniform and deep penetration of the Au nanoparticles into the original biological photonic nanoarchitecture than the drop-drying method.

The increased amount of Au nanoparticles incorporated in the hybrid photonic nanoarchitecture increased the magnitude of the spectral shift, but at the same time reduced the amplitude of the reflectance maximum associated with the initial biological photonic nanoarchitecture. Therefore, one has to balance these two effects. Fortunately, nature has developed a very large “library” of precisely tuned photonic nanoarchitectures in butterfly wings, which can be produced in a cheap and environmentally friendly process. Thus, by selecting wings with suitable physical color, the desired spectral modifications can be easily achieved.

Photocatalytic dye degradation with biotemplated ZnO photonic nanoarchitectures based on *Morpho* butterfly wings

OTKA PD 143037, TKP2021-NKTA-05

G. Piszter, G. Nagy, K. Kertész, Zs. Baji, K. Kovács, Zs. Bálint, Zs. E. Horváth, J. S. Pap, and L. P. Biró

Photonic nanoarchitectures of butterfly wings can serve as biotemplates to prepare semiconductor thin films by atomic layer deposition. The resulting biotemplated nanoarchitecture preserves the structural and optical properties of the natural system, while it also has the features of the deposited functional material. When photocatalytic thin films are applied, such as ZnO or TiO_2, the coated wings can be used directly in heterogeneous photocatalysis to decompose pollutants dissolved in water upon visible light illumination.

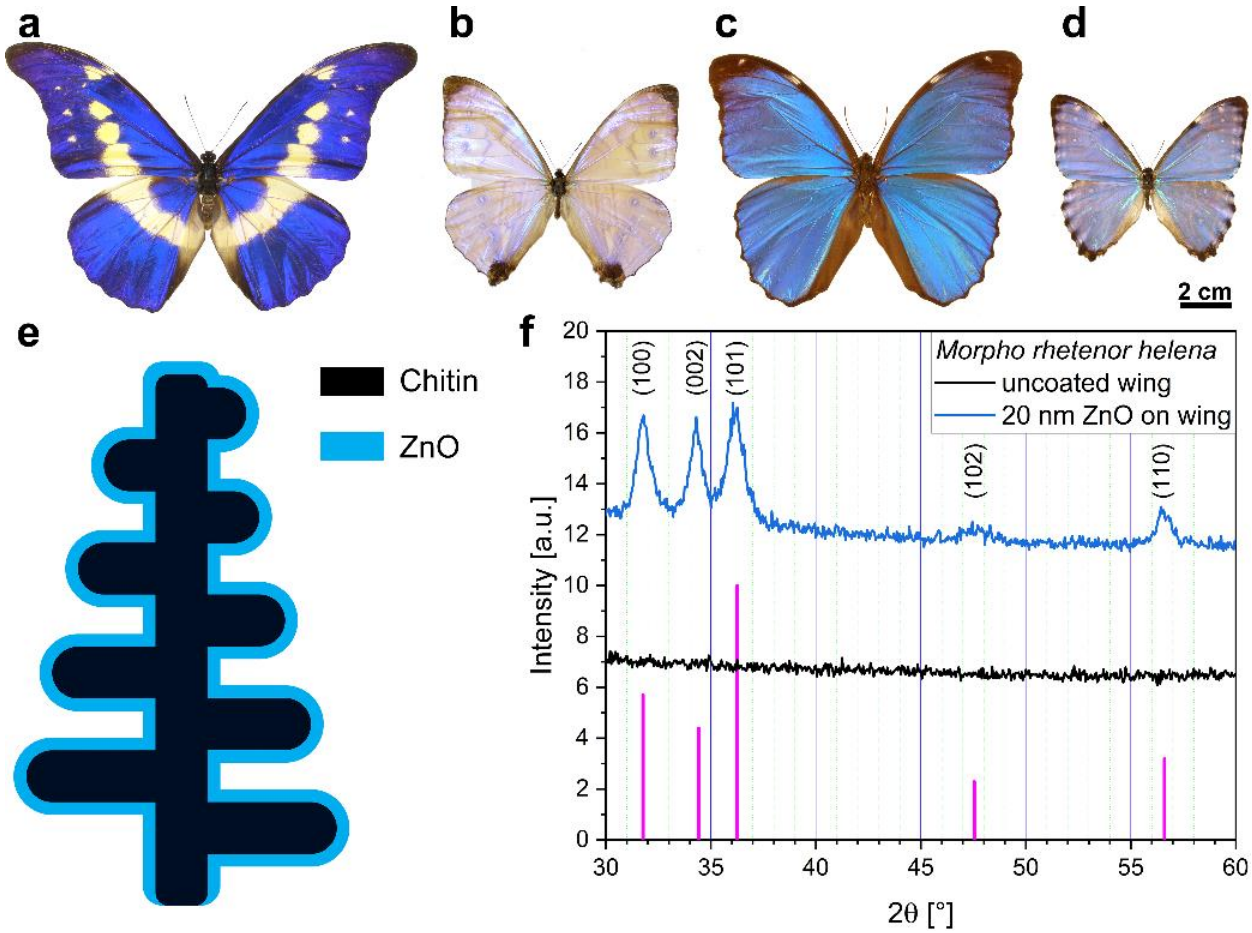

Figure 1.9. *Photographs of male* Morpho *specimens in dorsal view. a)* M. rhetenor helena, *b)* M. sulkowskyi, *c)* M. menelaus, *d)* M. portis *are shown. e) Schematics of a* Morpho*-type nanostructure cross-section with the as-deposited ZnO thin film. f) X-ray diffractogram shows a nanocrystalline, wurtzite-type structure of 20 nm ZnO deposited on the* Morpho *wing.*

In the present work, we utilized photonic nanoarchitectures of *Morpho* butterflies as biotemplates for ZnO thin films. According to our previous studies, the *Morpho*-based templates were the most effective photocatalysts. Therefore, we extended our investigations to four species representing this butterfly genus, with similar photonic nanoarchitectures in their wing scales, but with different structural colors (Fig. 1.9.a-d, from deep blue to greenish blue). To our best knowledge, it is for the first time that biotemplates with similar nanostructures, but with different optical properties are used within the same experimental setup to test the relation of the different optical properties with the photocatalytic performance.

ZnO is one of the semiconductors that can be grown on the surface of the biological photonic nanoarchitectures using low-temperature atomic layer deposition. This way, the micro- and nanoscale features of the chitinous cover scales are well preserved by the thin films without the need for a post-annealing process which would damage the biological material. X-ray diffraction measurements showed that the as-deposited ZnO had a nanocrystalline, wurtzite-type structure on the butterfly wings (Fig. 1.9.f).

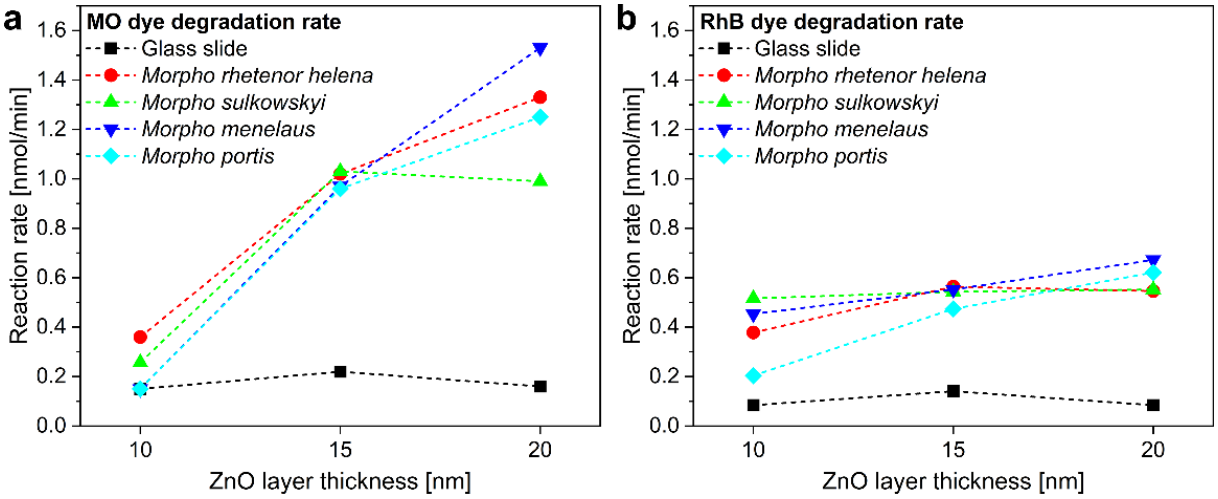

Figure 1.10. *Reaction rate versus ZnO layer thickness for glass slide substrates and* Morpho *butterfly wings when a) methyl orange or b) rhodamine B test dyes were decomposed upon visible light illumination.*

We examined how the decomposition rate of methyl orange (MO) and rhodamine B (RhB) dyes depends on the structural color of the biotemplates and the thickness of the applied ZnO coating upon visible light illumination. Using methyl orange, we measured a ten-fold increase in photodegradation rate when the 20 nm ZnO-coated wings were compared to similarly coated glass substrates (Fig. 1.10.a). Using rhodamine B, a saturating relationship was found between the degradation rate and the thickness of the deposited ZnO on butterfly wings (Fig. 1.10.b). We concluded that the enhancement of the catalytic efficiency can be attributed to the slow light effect due to a spectral overlap between the ZnO-coated *Morpho* butterfly wings' reflectance with the absorption band of dyes, thus the photocatalytic performance could be changed by the tuning of the structural color of the butterfly biotemplates.

Our findings may facilitate the application of biotemplated semiconductor photonic nanoarchitectures as a bioinspired testing platform of photocatalysts, where evolutionary adjustments in the structural color can tune the activity of the surface to achieve a selective catalytic degradation of different pollutants.

2 - Photonics Department

Head: Dr. Peter PETRIK, D.Sc., scientific advisor

Research Staff:

- Miklós FRIED, D.Sc., Head of Ellipsometry Laboratory
- András DEÁK, Ph.D., Head of Chemical Nanostructures Laboratory
- Antal GASPARICS, Ph.D.
- Norbert NAGY, Ph.D.
- Zoltán LÁBADI, Ph.D.
- Boglárka NYERGES
- Ferenc RIESZ, C.Sc.
- Dániel ZÁMBÓ, Ph.D.
- Alekszej ROMANENKO
- Miklós SERÉNYI, D.Sc., retired
- Gábor VÉRTESY, D.Sc. , Prof. emeritus
- György KÁDÁR, D.Sc., Prof. emeritus
- Tivadar LOHNER, D.Sc., Prof. emeritus
- János MAKAI, C.Sc., retired
- András HÁMORI, dr. univ., retired
- György JUHÁSZ, dr. univ., retired

Students:

- Deshabrato MUKHERJEE, Ph.D.
- Berhane NUGUSSE, Ph.D.
- Noor TAHA ISMAEL, Ph.D.
- Géza SZÁNTÓ
- Áron FOGARASY,
- Noémi JAKAB,
- Dávid KOVÁCS,
- Rita NÉMEDI,
- Máté STIFT

The Photonics Department develops unique methods and tools for non-destructive optical and magnetic measurement of surface nanostructures and materials (spectroscopy; magnetic material testing; biosensors; surface curvature measurement; surface testing; water contamination). One of the most important tasks of the Department is patenting and application of the methods in international projects with partners representing the industry and the high technology.

Key achievements of the Photonics Department in 2023(detailed summaries of the research results can be found in the following project descriptions):

- experimental and theoretical study of the self-assembly of gold nanoprisms and nanospheres in bulk phase
- Determination of the photophysical and photocatalytic properties of Cu2O/Au multicomponent systems
- Combined ion beam analytical and spectroscopic ellipsometric investigation of the transformation of ε-Ga2O3 during heat treatment
- progress in the Hungarian and international acceptance and industrial utilization of the solid-liquid adhesion work patent
- further development of the evaluation of the Makyoh topographic measurement by comparing the visual image of the back side and the projected image of the front side
- development of gallium oxide and gallium oxynitride sputtering process from a liquid source
- development of an in-situ test method for testing the electrochromic properties of combinatorial TiO2-SnO2 layers
- microscopic ellipsometer patent from a proof-of-concept application

- patent process for determining thin layer phase diagram in progress
- Dániel Zámbó's senior researcher qualification
- András Deák MFA research award
- Dániel Zámbó MFA postdoctoral award

Contact angle determination by the Capillary Bridge Probe and Sessile Drop method on PTFE surfaces

OTKA FK 128901

N. Nagy

The developed indirect Capillary Bridge Probe method combines the accuracy of the Wilhelmy method and the general usability of the sessile drop method without their limitations. The method is based on the use of a liquid bridge as a probe: the capillary bridge of the test liquid is stretched between the base of a cylinder and the investigated surface under equilibrium conditions. The advancing contact angle on the sample can be measured during the stepwise or slow (quasi-static) decrease of the bridge length. The receding contact angle is determined during the retraction of the cylinder (Fig. 2.1).

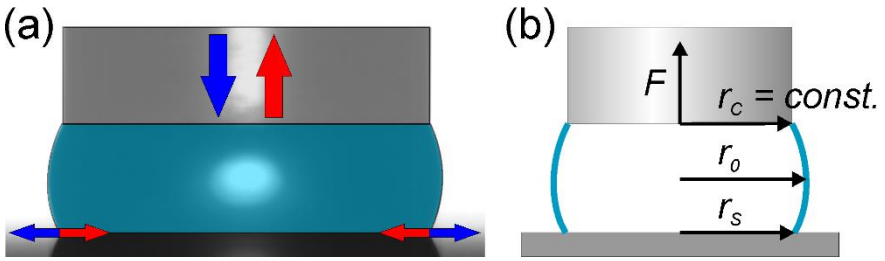

Figure 2.1. *a) Recorded image (colored) of a water capillary bridge on a PTFE surface. The blue and red arrows indicate the advancing and receding phase. b) Schematics of an r-ϑ type liquid bridge with all parameters necessary for the analytical evaluation: capillary force (F), neck/haunch radius (r_0), and surface radius (r_s). The radius of the upper contact line is constant ($r_c \equiv 1$ mm) due to the contact line pinning on the cylinder's rim.*

The contact angle is calculated from Delaunay's analytical solution, while the three necessary parameters are the measured capillary force (F_c), the radius of neck or haunch (r_0), and the radius of the contact line (r_s) on the investigated surface. The latter two parameters are obtained from the automated analysis of the captured image of the liquid bridge. The radius of the upper contact line (r_c) is constant since it pins on the rim of the cylinder.

Fig. 2.2.a shows the measured capillary force as a function of the bridge length recorded on a PTFE surface. The bridge volume was 1.7 µL. The graph shows hysteresis. After the snap-in, the capillary force increases with the decreasing bridge length. It changes its sign during the cycle: there is an F=0 µN transition in the approaching phase and in the retraction phase, after the turn. The negative (attractive) force has a minimum value in the retraction phase. After this point, the magnitude of the capillary force decreases until the pull-of. The insets show typical bridge shapes during the measurement cycle.

In Fig. 2.2.b, the lower drawings show the idea to find identical complete bridge shapes corresponding to the different classes. The determined contact angle as a function of the contact radius (r_s) are plotted in Fig. 2.3.a Plotting contact angles vs. contact radius is a useful representation because the change of the radius indicates that the angle actually corresponds to advancing or receding state of the contact line. The contact angles in Fig. 2.3.a were calculated based on the measured data of Fig. 2.2.a.The insets show characteristic evaluated profiles for different classes. It can be seen that the captured profiles are in remarkable agreement with the calculated ones. Contact angle hysteresis can be observed during the approach-retraction cycle.

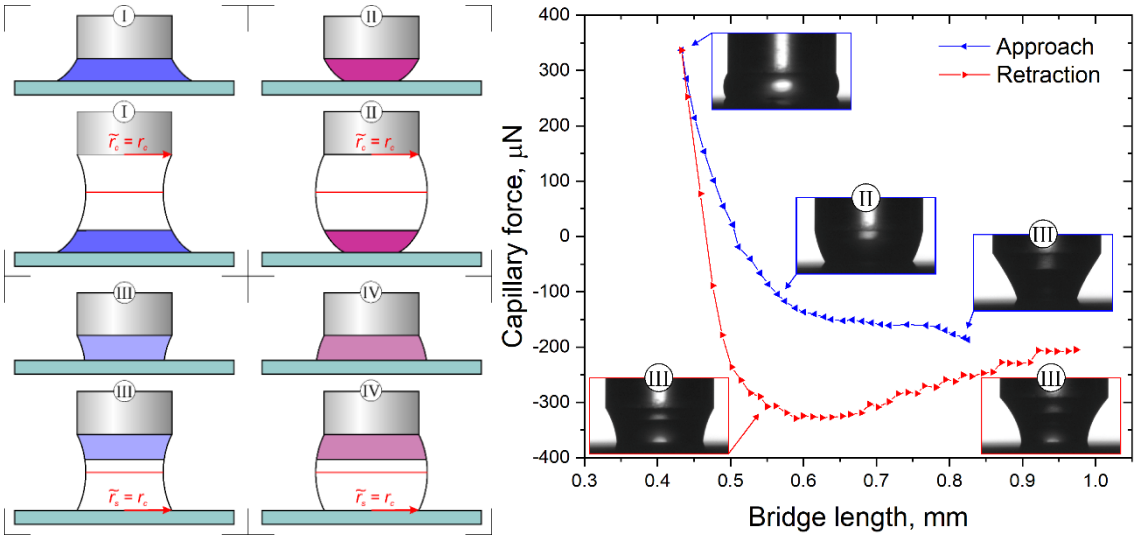

Figure 2.2. *a) Capillary force as a function of the bridge length measured on a PTFE surface. The insets show typical equilibrium states of water capillary bridges during the measurements. The Roman numbers refer to the class of the incomplete form b) Schematics of the classification of incomplete capillary bridges.*

.

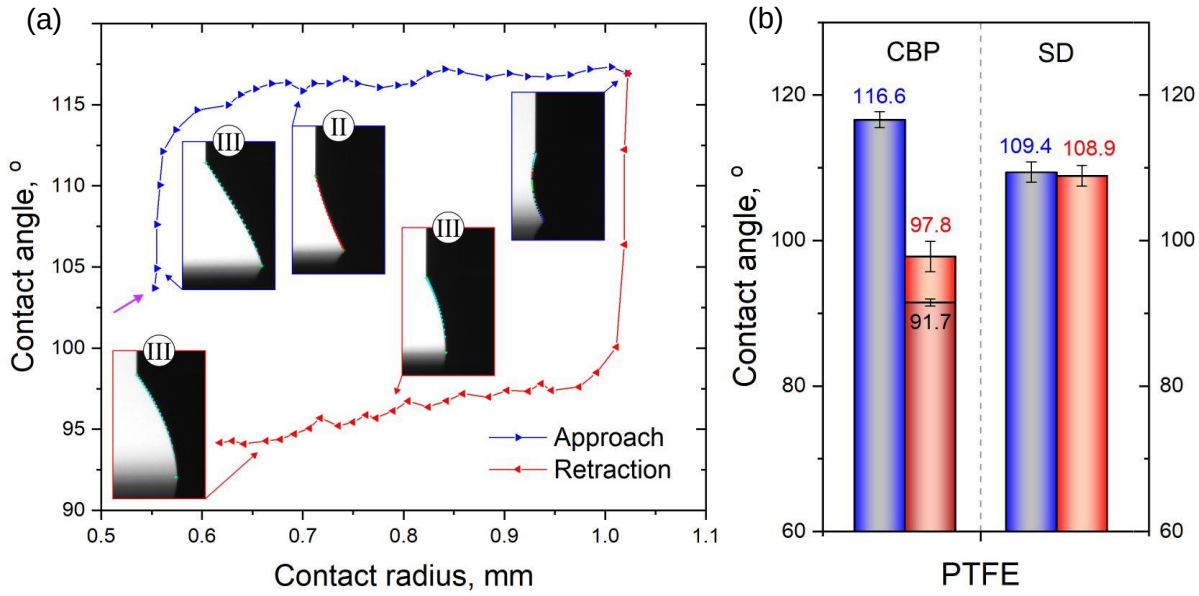

Figure 2.3. *a) Contact angle as a function of the contact radius determined on a PTFE surface. The insets show the evaluated profiles of the capillary bridges. b) Advancing and receding contact angles determined by the capillary bridge probe (CBP) and the sessile drop (SD) methods.*

Sessile drop measurements were carried out on the same PTFE surfaces for comparison. The advancing and receding contact angles were determined applying the drop build-up technique in the range of 6–20 µL at five different measuring position. The comparison chart is shown in Fig. 2.3.b. The results of the sessile drop method practically do not show any contact angle hysteresis, while the magnitude of the standard deviation refers to the presence of surface imperfections. However, according to the capillary bridge probe method the hysteresis is considerable (>18°). The shorter length of the contact line can explain the higher sensitivity of this method on surface imperfections. Furthermore, the AFM analysis revealed micrometer size granular regions between large smooth plateaus. These deeper imperfections are not wetted during the sessile drop measurements, but a Cassie-Wenzel wetting transition was occurred due to high capillary pressures during the capillary bridge probe measurements [Ref.2.1, Ref. 2.2].

Surface sodification and self-assembly of gold nanoprisms

OTKA FK FK128327

*D. Zámbó, D. Kovács, G. Südi, Z. Zolnai, A. Deák**

Nanosized gold nanoparticles are of interest in many research fields as they have a large optical extinction cross-section at specific wavelength due to the excitation of localized surface plasmons. At the wavelength (photon energy) of these sharp resonant peaks the optical spectrum is determined primarily by the shape and size of the particles, allowing the design of nanoparticles for a specific application in sensorics, photothermal or energy harvesting applications. For every application, however, the surface ligand layer of the particles is of crucial importance, as its presence is always necessary to ensure processability and functionality of the particles.

Our recent research focused on the latter aspect of this field, namely the formation of a composite ligand layer on the surface of gold nanoprisms [Ref. 2.3]. The importance of composite ligand layers lies in their ability to combine different molecular functionalities at the same time, e.g. particle stability and specific functional groups. In our study we relied on the subtle changes in the plasmon resonance peak of the nanoprisms upon exposing them to a combination of different thiolated molecules. When these molecules bind to the particles' surface, their impact is twofold. First, they will influence the resonant energy as it depends on the dielectric properties of the particles' optical near field. Second, the surface-bound molecules induce image dipoles at the surface, that leads to an enhanced scattering of the electrons. This additional plasmon decay channel leads to broadening of the plasmon peak and is referred to as chemical interface damping. Detailed analysis of the simultaneous change of the plasmon energy (energy shift) and damping change (peak broadening) can help to clarify the build-up and structure of mixed ligand layers. To access these values, however, the optical changes have to be monitored in-situ in the liquid environment and the level of individual particles, otherwise inhomogeneous peak broadening inherently present in an ensemble measurements does not allow to extract the necessary information.

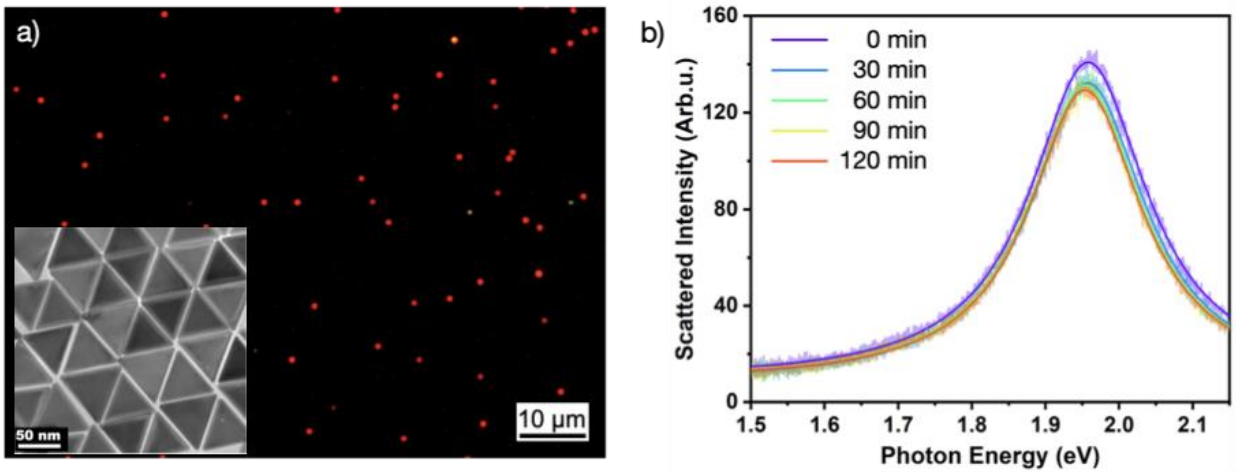

Figure 2.4. *Typical optical dark-field microscopy image of a nanoprism sample for single-particle spectroscopy a). The inset shows the TEM image of the particles.*
In b) the time-dependent scattering spectra of a single nanoprism is shown upon exposing it to 100 µM aqueous mPEG-SH solution. The spectra are evaluated with by fitting a intraband-transition corrected damped oscillator model (solid lines) to obtain resonance energy (ΔEres) and damping (ΔΓ) changes

For this purpose, we performed our measurements on individual gold nanoprisms in a liquid flow cell combined with a laboratory-developed microspectroscopy setup that allows to investigate the scattering spectra of individual nanoparticle with high confidence and accuracy (see. Fig. 2.4.). The thiol molecules used for the mixed ligand shell preparation were (MTAB), a positively charged thiol which is the thiolated analogue of the original capping ligand of the prisms, and a 5000 Da large neutral polymer (thiolated PEG - mPEG-SH).

Fig. 2.5. shows the changes of the resonance energy and plasmon damping as a function of time upon thiol addition. When the two thiols are introduced sequentially into the flow cell (Fig. 2.5.a and Fig. 2.5.b), the resonance energy change for the MTAB/PEG sequence (Fig. 2.5.a) indicates that PEG can bind to the surface even when MTAB is already present: there is an additional significant red-shift (ΔE_{res} decrease) upon introducing PEG after 30 minutes which cannot be observed for opposite order of addition. This also means that already surface bound neutral polymer (PEG) might block the adsorption of the second, charged thiol (MTAB). Interestingly, when the two molecule types are applied simultaneously (Fig. 2.5.c), both the damping and resonance energy changes are significantly larger. This means a ligand layer that is more dense than in the previous two cases. This can be interpreted as the formation of a composite ligand layer, where the MTAB molecules occupy the surface area between the PEG anchoring points, the latter being inherently further away from each other due to the steric repulsion between the polymer chains.

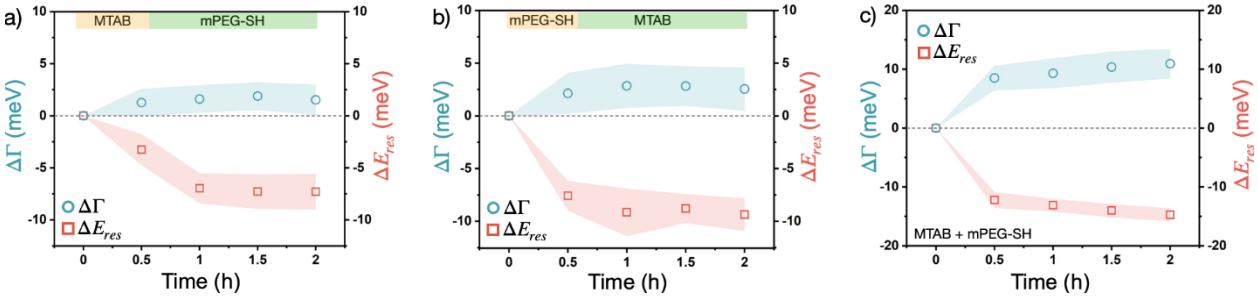

Figure 2.5. *Resonance energy (ΔE_{res}) and damping ($\Delta\Gamma$) changes for individual nanoparticle when exposed to two thiol molecules of different types. For a) and b) the two thiols are applied sequentially as indicated by the colour-bar in the top of the figures. For c) the mixture of the two molecules is applied. For all cases the concentration is 10 μM MTAB, 100 μM mPEG-SH.*

Besides the fundamental character of the results of this study, their practical implication are that when two molecules of different size are to be used for surface modification in order to dress the particles with different functionalities, the following should to be considered: sequential adsorption with the smaller sized thiol added first is to be used when accessibility of this surface modified particle surface region is of importance but the simultaneous addition of the molecules should be preferred when the goal is to achieve highest molecular loading.

Multicomponent heteronanoparticles for photocatalytic application

TKP2021-NKTA-05, OTKA FK 142148

*D. Kovács, A. Deák, Gy. Z. Radnóczi, Zs. E. Horváth, A. Sulyok, R. Schiller, D. Zámbó**

Multicomponent nanoparticles are in the spotlight of the nanoscience owing to the synergistic properties emerging between components at the nanoscale. Especially in semiconductor-metal heteronanosystems, the combination of the nanoparticle building blocks enables the utilization of novel photophysical processes. Exciting the charge carriers in the semiconductor component generates electrons and holes being relevant in photo-driven applications such as photocatalysis. Nevertheless, metal nanoparticles or domains being in direct contact with the semiconductor acts as an efficient electron reservoir due to the larger work function of most of the metals compared to that of the transition metal-chalcogenide semiconductors. This is not only advantageous in the separation of the photogenerated charge carriers, but also expands the lifetime of the electrons, thus, they can be utilized in a wider timescale in reduction reactions.

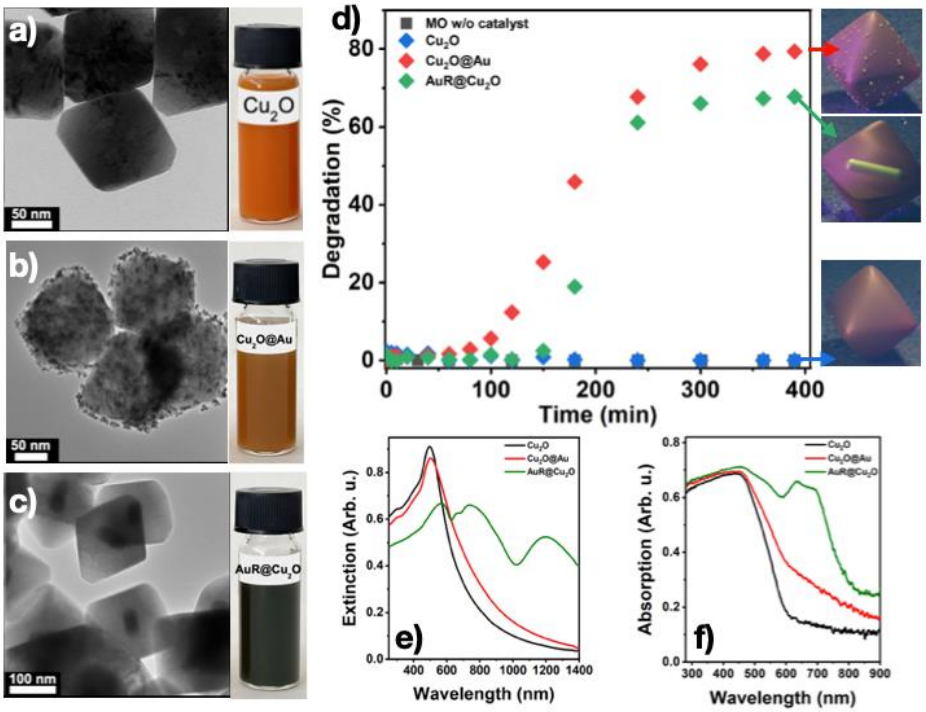

Figure 2.6. *TEM images and the corresponding photographs of the pristine Cu_2O (a), Cu_2O@Au (b) and AuR@Cu_2O (c) nanoparticles. Photocatalytic degradation of methyl orange by using the different heteronanoparticles as catalyst (d). Extinction (e) and absorption spectra of the heteroparticles' aqueous solutions at identical Cu_2O concentrations.* [Ref. 2.4]

Copper(I)-oxide is an abundant, ecofriendly, and easy-to-synthesize p-type semiconductor, which – in a form of a nanoparticle – shows tunable optical and electronic properties depending on its morphology. Although it had been demonstrated recently that Cu_2O nanoparticles are promising photocatalysts, its potential is significantly limited due to the intraparticle photophysical properties. Despite the high carrier density, the low mobility, short diffusion length of the minority carrier and the often-existing defects in the crystal structure restrict the utilization of the generated carriers upon illumination. Our aim was to circumvent this limitation *via* combining the Cu_2O with gold nanoparticles.

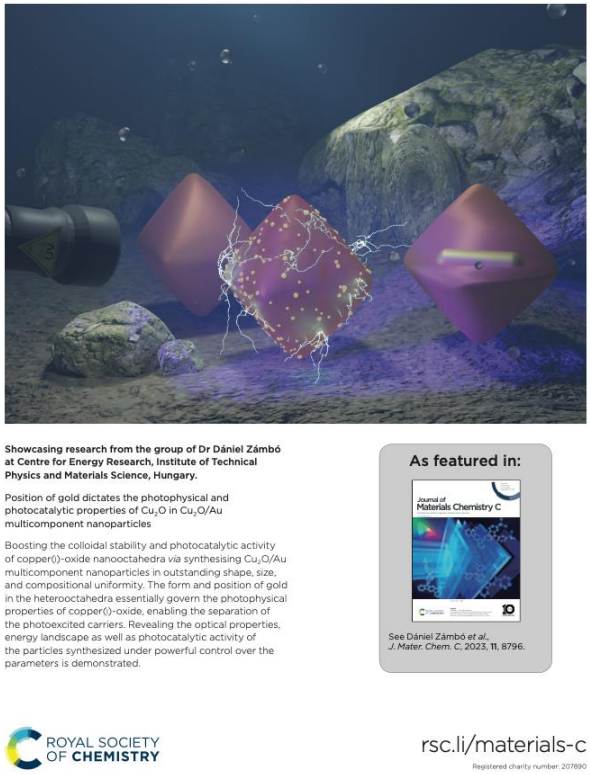

Figure 2.7 *Published cover artwork for our article in The Journal of Materials Chemistry [Ref. 2.5]*

While gold had already demonstrated the capability of enhancing the photocatalytic properties of Cu_2O, it was still unclear how the form and the location of the gold governs the underlying processes. Thus, we designed model systems, in which the morphology, concencentration and the composition of the Cu_2O and Au were kept identical while the form of the gold was varied. We compared the optical, photophysical and photocatalytic properties of pristine Cu_2O octahedra with that of Cu_2O/Au heteronanoparticles, where the gold was introduced in two different ways: gold nanorods were embedded into octahedral Cu_2O particles (AuR@Cu_2O) or small Au nanograins were deposited onto the surface of the octahedra (Cu_2O@Au). It was an important aspect of the work to demonstrate that the photophysical properteis of Cu_2O can be improved upon low-power UV illumination being off-resonant with the plasmon modes of the gold components, thus, we were able to investigate the processes from the semiconductor point of view instead of utilizing any plasmon-generated processes such as hot-electron injection or plasmon-assisted charge transfer.

We showed that the radative recombination of the photogenerated excitons are suppressed in the heteronanoparticles, however, this does not directly imply their better spatial separation. Therefore, the energy landscape of the particles was revealed by single-point Kelvin probe and a major difference in the Schottky-barriers was identified: in the AuR@Cu_2O particles, only the photogenerated electrons could reach the particles outer surface, while in its Cu_2O@Au counterpart, both generated carriers can be available for chemical reactions. This also manifested in the photocatalytic activity of the particles, namely the pristine Cu_2O was found to be inactive in the degradation of a model pollutant (methyl orange), however, the Cu_2O/Au systems showed enhanced activity [Ref. 2.4]. It is important to note that AuR@Cu_2O particles can suffer from significant photocorrosion, while Cu_2O@Au particles preserved their moprhology and showed even higher activity (80% of dye degradation). The work has been published in *The Journal of Materials Chemistry C* [Ref. 2.4] and we also provided a cover artwork for the issue (Fig. 2.7) [Ref. 2.5]. The work underlined the role of the position and form of the gold in the multicomponent Cu_2O/Au heteronanoparticles and paved to way towards the preparation of novel photocatalysts.

3-color ellipsometric mapping tool without moving components

VOC-DETECT M-era-Net project, OTKA NNE 131269

B. Nugusse[1,2], Gy. Juhász[1], Cs. Major[1], P. Petrik[1,4], S. Kálvin[1], Z. Gy. Horváth[3], M. Fried[1,2*]

[1]Institute of Technical Physics and Materials Science, Centre for Energy Research, [2]Institute of Microelectronics and Technology, Obuda University, [3]Institute for Solid State Physics & Optics, Wigner Research Centre for Physics, [4]Department of Electrical Engineering, University of Debrecen

Non-destructive techniques are important methods to use during all stages of the thin film processes. Spectroscopic Ellipsometry (SE) is one of such methods. SE is a non-destructive, noninvasive and non-intrusive optical technique. It is a technique that measures the change in polarization state of the measurement beam induced by reflection from or transmission though the sample. Ellipsometry measures the amplitude ratio (tan ψ) and phase difference (Δ) between the parallel (p) and normal (s) polarizations. During data analysis, information about the system under the study is obtained by fitting measured ellipsometric spectra to optical and structural models, as ellipsometry does not give a direct information of the sample in consideration.

Generally, the aim of this research is to make a prototype optical mapping tool for materials using only cheap parts such as a tablet, monitor, big screen TV (LCD or LED) and a pinhole camera [Ref. 2.6-2.8] with CMOS Sensor with Integrated 4-Directional Wire Grid Polarizer Array (Sony's IMX250MYR CMOS), shown in Fig.2.8. Our arrangement shows similarity to the solution of Bakker et al [Ref. 2.9], using a computer screen as a light source and a webcam as a detector in an imaging off-null ellipsometer. The new concept of the non-collimated beam ellipsometer prototype is set up as shown in Fig. 2.8.

A LED-LCD monitor (or a TV), see Fig. 2.8.a (C) serves the polarized RGB colored light (see the built-in polarizer sheet, number 4 in Fig. 2.8.b) and a polarization sensitive camera behind a pinhole (7&8) together. The LCD monitor (Dell UltraSharp™ U2412M, GB-LED) is used in a 45-degree rotated position, measured by a digital angle gauge with 0.1 deg precision. In straight-through position, we can detect the extinction of the polarization sensitive camera better than 10^{-2}. The polarization sensitive camera sensor (The Imaging Source Company's DYK 33UX250 USB 3.0 Polarsens camera), see in Fig. 2.8.a (A) and in Fig. 2.9, serves the polarization state data, from 0, 45, 90, 135-degree rotation positions (plus 3 RGB colors in each position). This arrangement is equal to a conventional static photometric rotating analyzer ellipsometer. The sample is illuminated by a non-collimated light through a fixed polarizer at an azimuth of 45 degrees to the plane of incidence. The reflected light passes through a virtual "rotating analyzer" and the intensity is captured by a two-dimensional position sensitive photodetector system at four different angular positions of the analyzer. Minimum 3 different analyzer positions are required. These four polarization states (intensity) data (at 0, 45, 90, 135-degree rotation positions) are enough (the fourth date is good to reduce the error) to determine the ellipsometric angles: ψ and Δ. Our camera serves the data for 3 colors, so we have 3x2 measured ψ and Δ. Schematic structure of a 2/3-inch Sony CMOS Pregius Polarsens sensor (IMX250MZR) is shown in Fig. 2.9.b and Fig. 2.9.c. The main advantage of the assembly is that *there are no moving parts in the system*!

We used a Woollam M-2000DI Rotating Compensator Spectroscopic Ellipsometer as a control measuring device. The M2000 SE system with the CompleteEASE software is used to serve the optical properties, layer thicknesses and other related parameters of the sample. In principle, as the angle of incidence varies along the surface, a point-by-point angle of incidence calibration (see Fig. 2.8.b) is needed using a well-known silicon-dioxide-silicon (SiO2/Si) sample. Each pixel gets a calibrated angle value. The procedure is similar to a conventional ellipsometric measurement. The refractive indices are known, only the angle of incidence and the thickness of the SiO2 layer are the unknown parameters, where they can be calculated from the measured ellipsometric parameters.

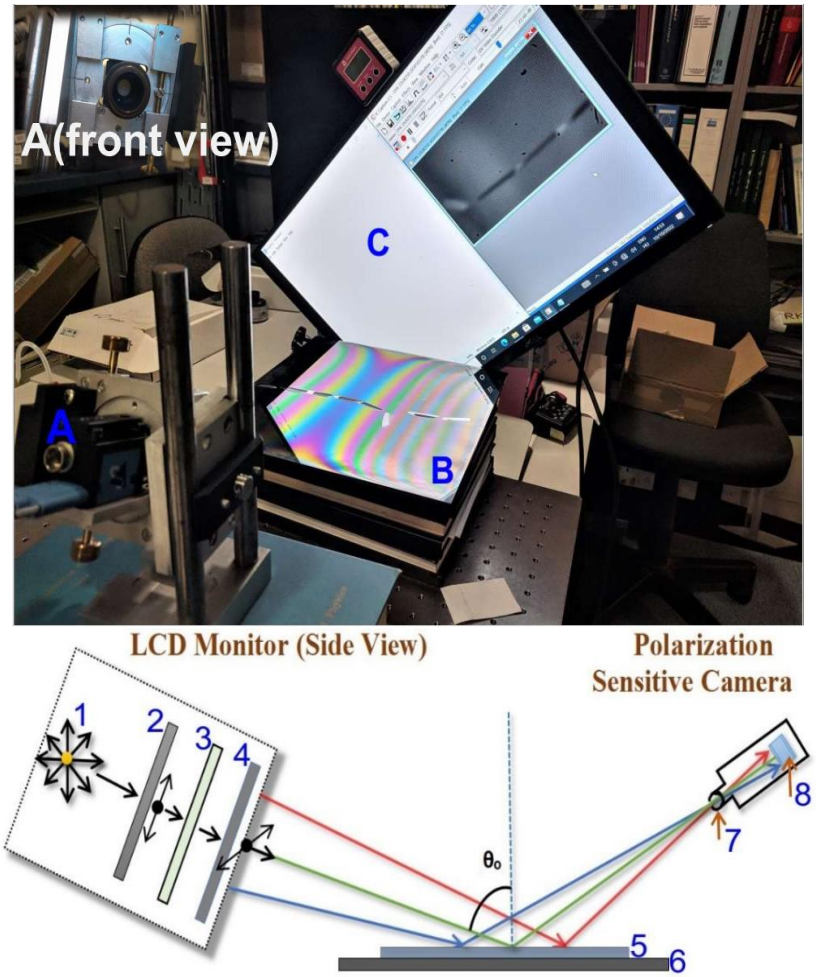

Figure 2.8. *(a) Experimental set-up: A) Polarization sensitive camera B) Sample + Sample holder C) LCD monitor rotated into 45° position – Upper-left: the pinhole in front of the camera (b) Schematics of the non-collimated beam ellipsometer: 1) Light source 2) Vertical polarizer 3) Liquid crystal cell 4) Horizontal polarizer - (C) 5) Sample - (B) 6) Sample holder 7) Pinhole (sub-mm size) 8) Camera sensor (A)*

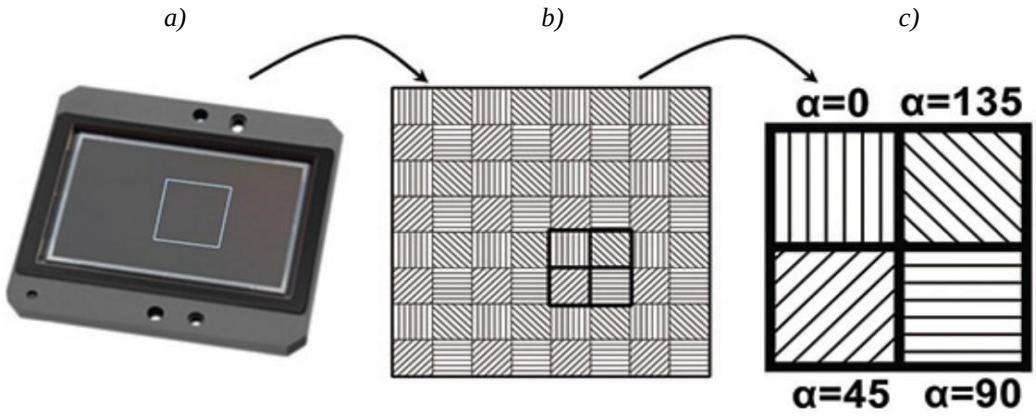

Figure 2.9. *Schematic structure of a 2/3 inch Sony CMOS Pregius Polarsens sensor (IMX250MZR) a). Camera sensor b). Polarizer array matched to detector pixels c). Unit cell (Super pixel)*

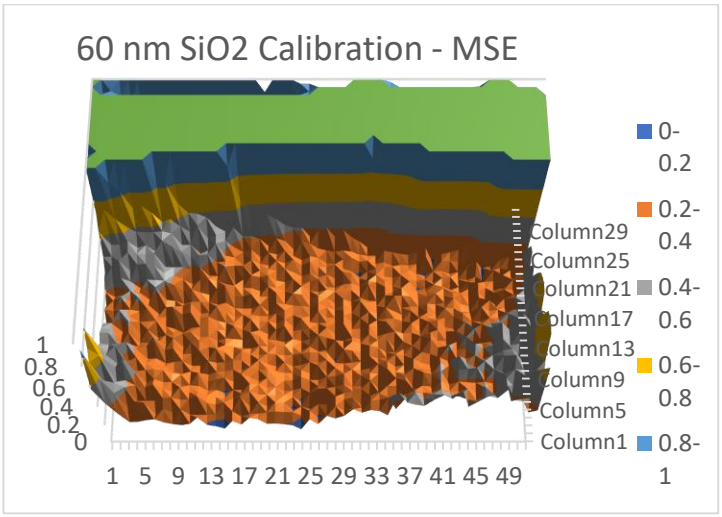

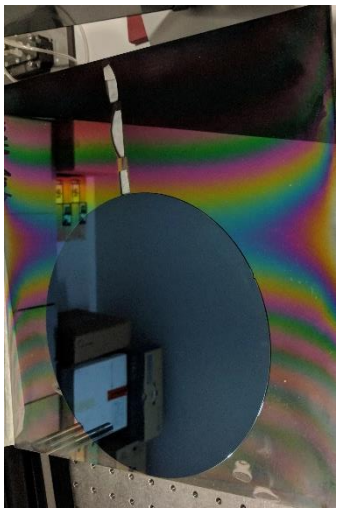

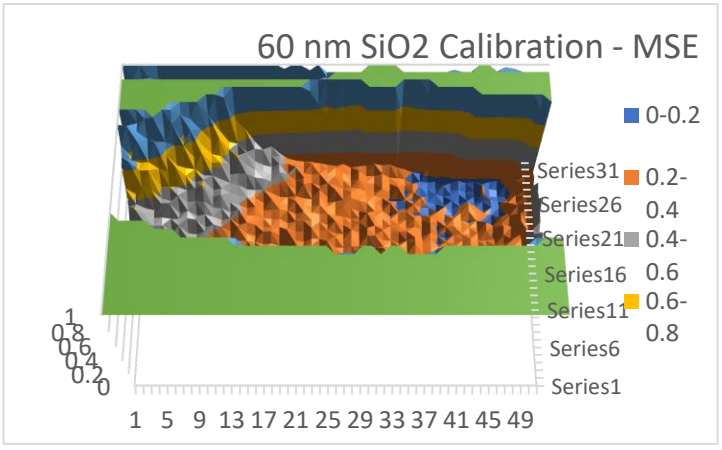

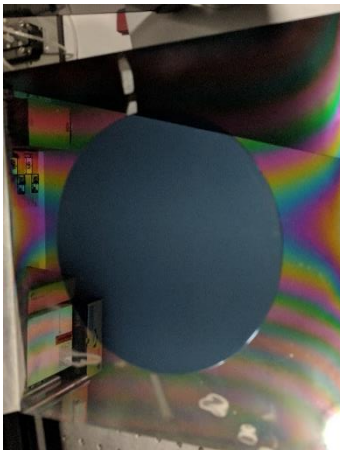

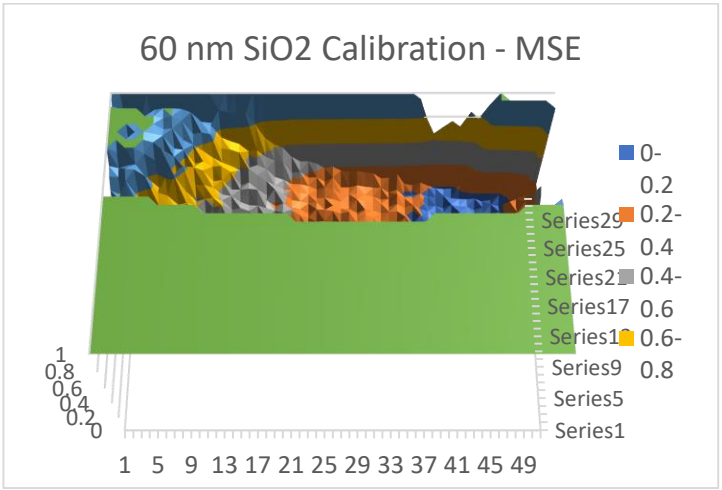

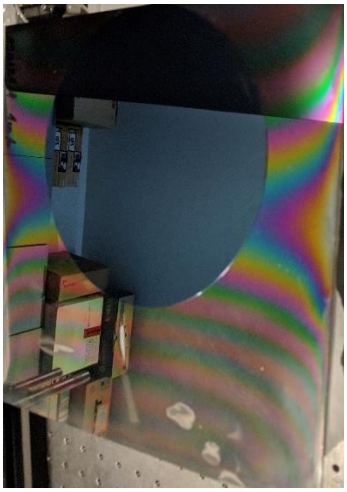

Figure 2.10. *The Mean Squared Error (MSE) maps of the 20 cm diameter SiO2 samples in the case of different positions. The higher MSE values show the areas, where no sample.*

A 20 cm diameter, nominally 60nm thick SiO2/Si sample was used to determine the angle of incidence point-by-point. We put the sample different positions (see the photos in Fig. 2.10) and one can see "good" areas from the Mean Squared Error (MSE) maps. The second step was choosing the points of lowest MSE values from the experimental results of these three different positions and developing corresponding single map calibration of the MSE and actual angle of incidence calibration for each coordinates. The results are shown in Fig. 2.11 below.

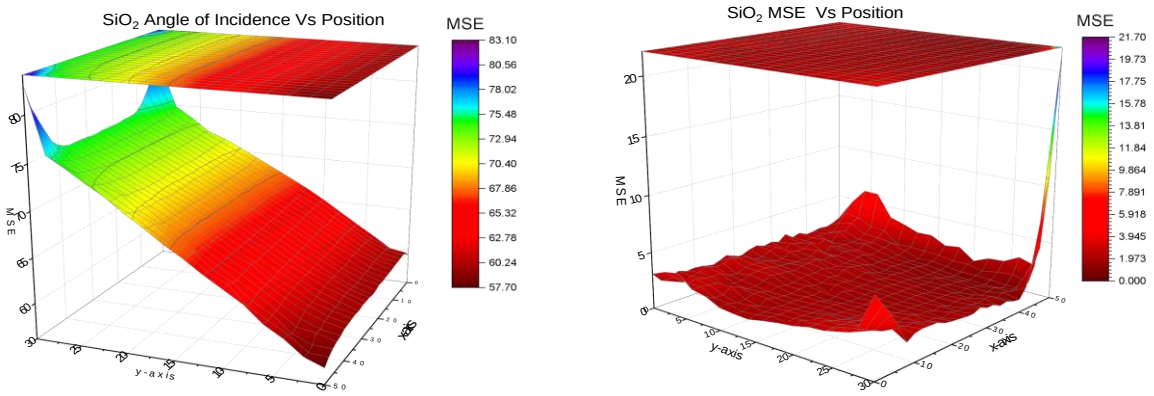

Figure 2.11. *MSE and corresponding angle of incidence calibration for each coordinates, respectively.*

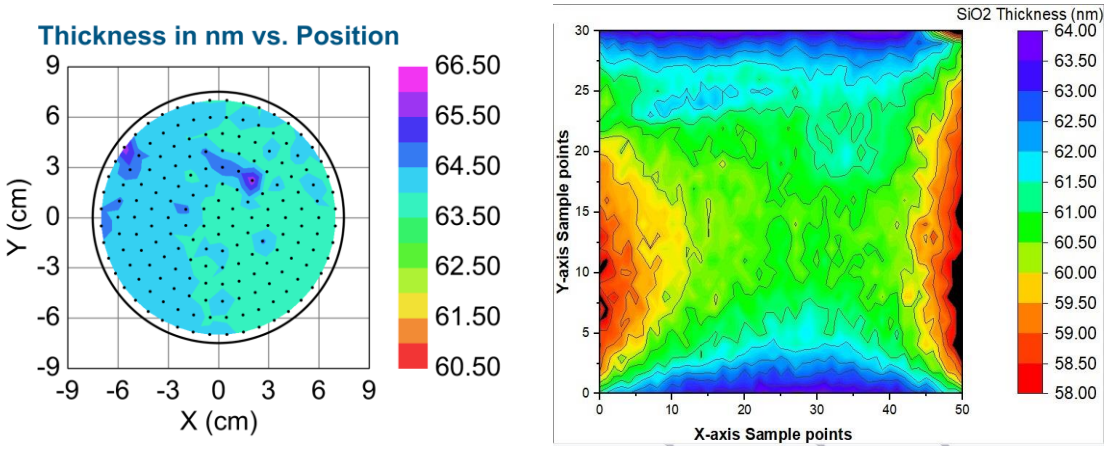

Figure 2.12. *Determined thickness maps from M2000 ellipsometer (left) and the corresponding measurements from the "Cheap" imaging tool assembly (right). The two scale are shifted by 2.5 nm.*

Our M2000 ellipsometer can map only 15 cm diameter area in one cycle, while the "Cheap" imaging tool assembly maps bigger area than the actual size of the measured Si-wafer, see Fig. 2.10. The more interesting part is only the central part of the map, a region that shows the thickness of the sample, about 60-61 nm, which is close to the other (to the left) map from the conventional M2000 ellipsometer. The two scales are shifted by 2.5 nm. Determined thickness differences between "Cheap" imaging tool and M2000 measurements are about 2 nm, see Fig. 2.12.

The pinhole camera couple the sample points directly to the pixels of the sensor matrix one-by-one. This detection system is almost without background. The measured area is determined by the size of the monitor and the sensor-pinhole, pinhole-sample and sample monitor distance-ratios. The lateral resolution is also determined by the distance ratios and the pinhole diameter. The pinhole diameter (presently 0.2 mm) is a compromise between the detected intensity (measuring time, presently 1-4 seconds) and the lateral resolution. One can see the illustration of the resolution (presently better than 5 mm) on Fig. 2.13, where a chessboard-like etched silicon dioxide-covered silicon wafer "delta-contrast" picture can be seen. The bright parts are the original (nominally 100 nm thick) oxide layer, the dark squares are the 4x4 mm sized

etched native oxide covered silicon surface. The MSE map shows where the sample is (low MSE, blue part) and one can see the squares in the thickness-map, too, see Fig. 2.13 center [Ref. 2.10].

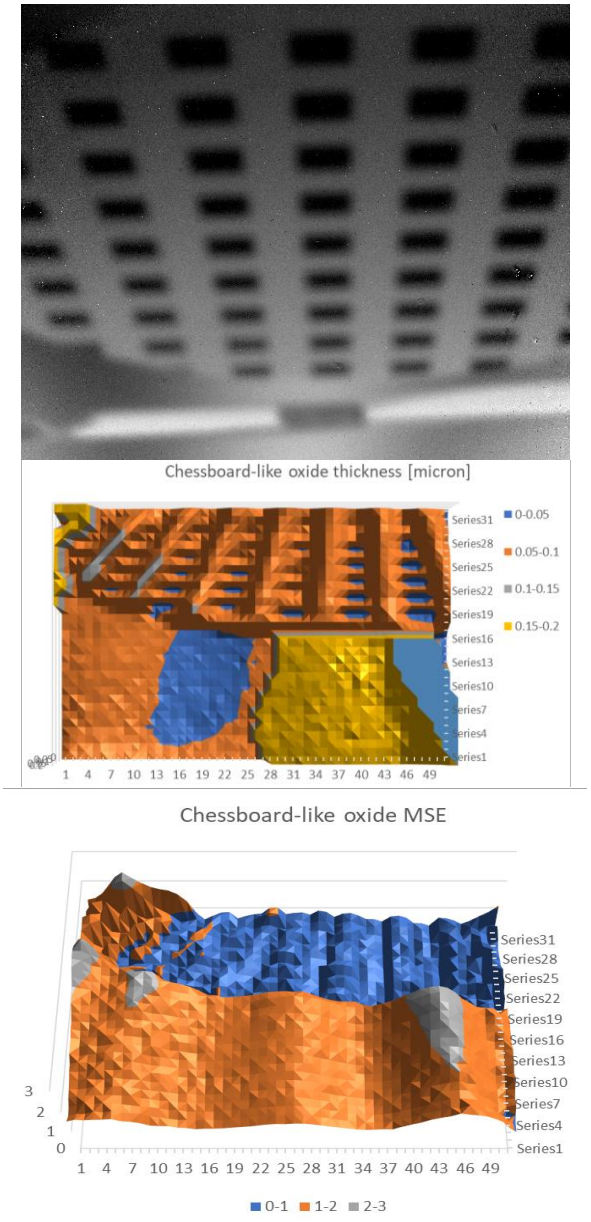

Figure 2.13. *Illustration of the resolution, which is better than 5 mm. This is a silicon dioxide-covered silicon wafer "delta-contrast" picture (top). The bright parts are the original (nominally 100 nm thick) oxide layer, which is shown in the thickness-map, too (center). The dark squares are the 4x4 mm sized etched native oxide covered silicon surface.*

Nanoscale Monitoring of Water Condensation in Electrochemical Migration-Induced PCB Failure

TKP2021-EGA-04, OTKA K 131515

A. Romanenko, A. Gharaibeh, B. Medgyes, P. Petrik

Electrochemical migration (ECM), triggered by humidity in conductor-dielectric-conductor systems, poses a reliability challenge in miniature electronic systems. This study focused on the inadequacy of existing methods to monitor nanoscale water buildup during ECM. The experiments utilized an FR-4 board with Sn electrodes, subjected to controlled cooling by a Peltier module. Dual-spot in-situ ellipsometry, electrical measurements, and optical imaging were employed (Fig 2.14). The ellipsometry setup, provided high sensitivity to nanoscale changes in the adsorbed water layer. The experiment involved shifting the light spot between the Sn film and the solder mask surface, ensuring comparability under the same environmental conditions. The initial adsorption phase, not visible by optical microscopy, was revealed, and the growth of droplets was tracked. Ellipsometry spectra were analyzed to separate the water layer thickness and volume fraction, providing nanoscale insights into water condensation.

The results showed differences in water condensation behavior between the solder mask and Sn surface, influencing the ECM process. This research highlights the unique capabilities of ellipsometry in characterizing nanoscale films during ECM. The study identifies the quasi-static limit as a critical factor influencing ellipsometry measurements during droplet formation. Differences in droplet size and density between the solder mask and Sn surface were observed, shedding light on the water condensation dynamics at a molecular level.

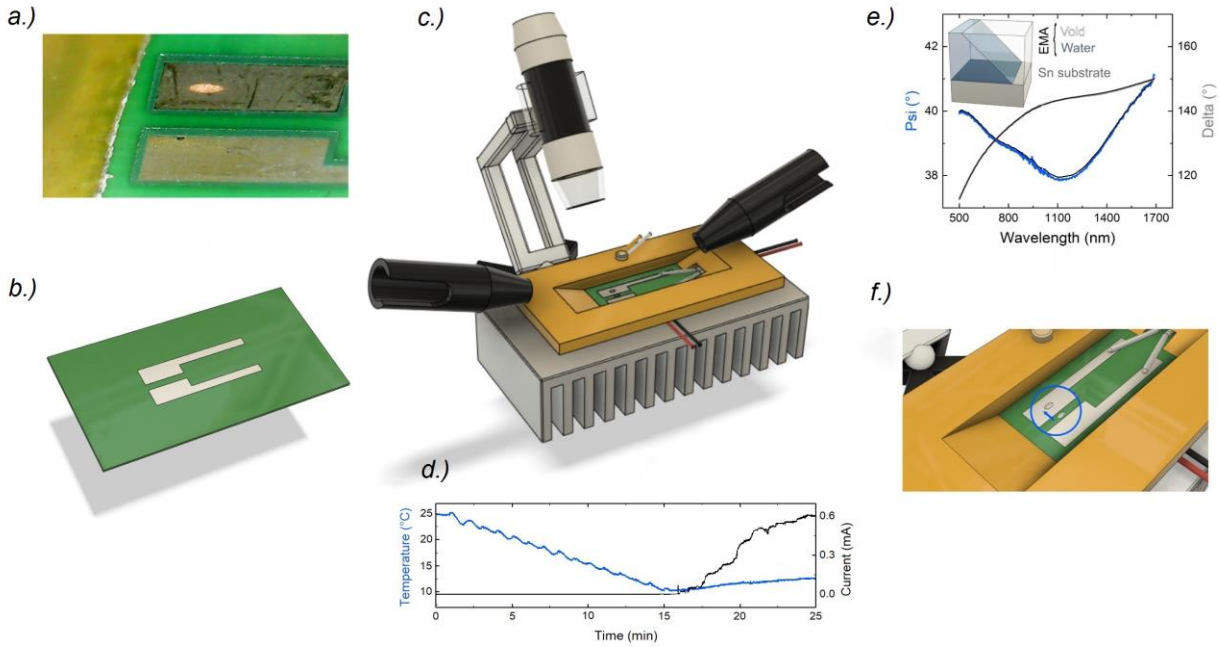

Figure 2.14. *a) Top-down image of the sample and the condensed water layer. b) Sematic image of the sample layout. c) The measurement setup. d) The shortcut current. e) Typical measured (solid lines) and fitted (dashed lines) ellipsometry spectra on the Sn film of the sample at 7minutes. f) Demonstration of the two-channel simultaneous in-situ measurement46 by moving the focused light spot back and forth between the Sn film and the FR-4 board.*

Investigation of Electrochromic, Combinatorial TiO_2-SnO_2 Mixed Layers

OTKA NN 131269 , OTKA K 128319, OTKA K 131515

N. T. Ismaeel, Z. Lábadi, P. Petrik, M. Fried

Electrochromic films have been used as smart windows for preservation of buildings from extra heating materials and also applied in energy-effective glassing, automobile sunroofs, smart windows and mirrors. Metal oxides are widely studied with respect to their electrochromic behavior and properties for the applications as display devices and smart windows. Transition metal oxides such as titanium, tungsten, nickel, vanadium and molybdenum oxides have been considered as promising electrochromic materials [Ref. 2.11]. The colored state of pure TiO_2 coatings is gray and this oxide was not used alone in electrochromic devices because its coloration is not very strong. Chronoamperometric experiments associated with transmittance spectra in $LiClO_4$-propylene carbonate solutions were carried out and compared with the optical properties of titanium oxide films with different stoichiometries. While TiO_2 was investigated as electrochromic material, SnO_2 or TiO_2-SnO_2 mixtures were studied only as photocatalytic material. During this work, reactive magnetron sputtering (in Ar-O_2 plasma) have been used to produce all combinations of TiO_2-SnO_2 mixed layers on silicon wafers. The object of this study was to investigate the properties of TiO_2-SnO_2 mixed layers as electrochromic materials, to compare the 'goodness' of the diverse Spectroscopic Ellipsometry optical models, and to find the optimal composition of mixed metal oxides deposited by reactive sputtering.

TiO_2-SnO_2 mixed layers were deposited in a reactive (Ar + O_2) gas mixture at ~10^{-3} mbar process pressure. 30 sccm/s Ar and 30 sccm/s O_2 volumetric flow rates have been applied inside the chamber. The substrates were 4-inch diameter IC-grade and 3-inch diameter highly conductive (0.001 Ωcm) Si-wafers. The linear walking speed was 5 cm/s (back and forth) at the geometry which can be seen in Fig. 2.15. 50-50 % composition can be expected in the middle of the specimen. The Si-wafers and control Si-stripes were placed on a 30 cm × 30 cm glass, see Fig. 2.15. The power of the plasma was in the range of 0.75–1.5 kW for the two targets autonomously. 300 walking cycles were applied. Fig. 2.15 presents that the sputtering targets have been placed at 35 cm from each other. According to the measurements, the two ‘material streams’ have been overlapped around the center of the substrate glass. The Metal/Oxygen atomic ratio of the layers was 1:2 at the applied oxygen partial pressure according to the SEM-EDS measurements.

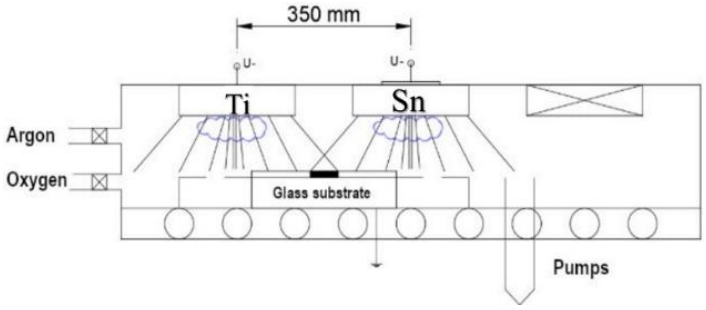

Figure 2.15. *Arrangements of the two targets in closer position (35 cm from each other).*

Optical mapping was performed by a Woollam M2000 SE equipment; the measurements were evaluated with the CompleteEASE software. To obtain the mapping parameters, oscillator functions and compact optical models have been used. The „goodness” of the optical model is depending on the value of the Mean Squared Error (MSE), so the lower MSE refers to the better fit because of the difference between curves. The silicon wafers and Si-stripes (Fig. 2.16.a) have been used for Scanning Electron Microscopy (SEM, Dual-beam SEM+FIB Thermo Scientific Scios2) with Energy Dispersive Spectroscopy (EDS) measurements.

a b

Figure 2.16. *a) Combinatorial TiO_2-SnO_2 layer on a 4-inch Si-wafer in the SEM-chamber b) Electrochemical fluid cell for in-situ, real-time SE measurements.*

In order to characterize the coloration process electrochemical Li injection was carried out on layers deposited onto the 3-inch diameter highly conductive (0.001 Ωcm) Si-wafers. The electrochemical measurements were performed in a liquid cell filled with 1 M lithium perchlorate (LiClO4) / propylene carbonate electrolyte, and a Pt wire counter electrode was placed into the electrolyte alongside with a reference electrode, see Fig. 2.16.b. Controlled potential was applied through the cell during a 4 min coloration. After the coloration process, the whole sample (in dry state) was mapped by Spectroscopic Ellipsometry. In order to evaluate the SE spectra we applied a multilayer optical model (Si-substrate/interface-layer/T-L(TiO_2)+T-L(SnO_2)-mixed layer/surface-roughness-layer), and compared two dispersion relations: a., the Bruggeman Effective Medium Approximation (EMA) calculation, and b., The Tauc-Lorentz (T-L) oscillator model. Details of the calculation can be found in [Ref. 2.12]. Both models give good results, however, the MSE (Mean Squared Error) is significantly lower for the 2-T-L model especially around the 50-50 % composition. After the coloration process, we could map the colorized layer using a simple one-layer Cauchy dispersion optical model. We see a maximum value (maximum light absorption) around 0.5 cm. Comparing this results with the composition curve, we can state that the optimal composition is 30-70 % for TiO2-SnO2.

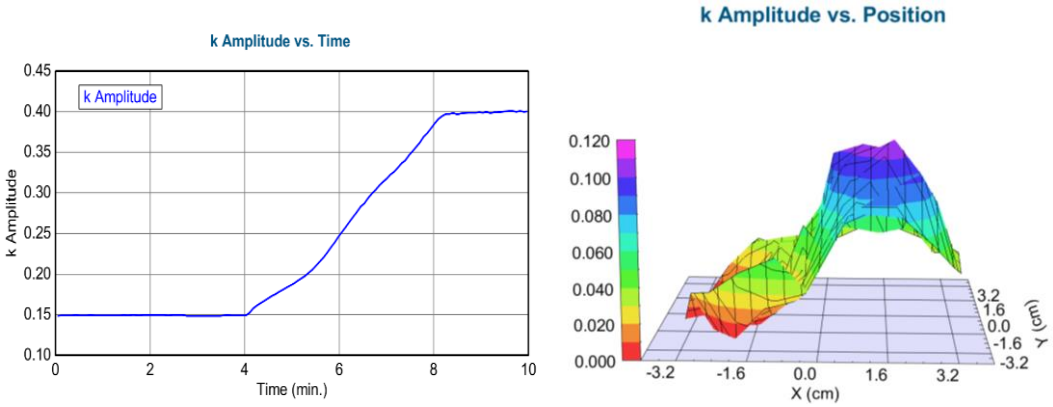

Figure 2.17. *Imaginary part of the refractive index (k Amplitude) as a function of time for highly-conductive-Si in liquid-cell during coloration (time-scan, simple Cauchy-model). Here we can mention that from (0-4) minute's there is low absorption but from (4-8) minute's there is a growing absorption. Map of the k parameter after coloration (simple Cauchy-model)*

Reactive Sputter Deposition of Ga_2O_3 Thin Films Using Liquid Ga Target

TKP2021-NKTA-05

M. Gajdics, M. Serényi, T. Kolonits, A. Sulyok, Zs. E. Horváth and B. Pécz

Ga_2O_3, as an ultrawide bandgap semiconductor has numerous potential applications in the field of optoelectronics, high-power electronics and gas sensing. Gallium oxide thin films can be grown by a variety of methods, among them, sputtering is a commonly used technique. In most cases, a ceramic Ga_2O_3 target is used for sputtering of Ga_2O_3. In our work, we demonstrate an alternative method, i.e. reactive sputtering of a liquid Ga target. Modeling of this reactive sputtering process was performed based on the Berg model [Ref. 2.13].

Liquid gallium was placed in a circular crucible fabricated from a 0.2 mm Ni plate. The diameter of the container was 75 mm and the height of its side wall was about 3 mm. This target was reactively sputtered in a radio frequency sputtering device. Different samples were prepared by varying the oxygen flow and the DC target potential. The composition of the samples was analyzed by energy dispersive spectroscopy and X-ray photoelectron spectroscopy, respectively. The optical parameters and the thickness of the films were determined by spectroscopic ellipsometry.

It was shown that using high enough oxygen flow rate (32 sccm – standard cubic centimeter per minute), it is possible to achieve higher oxygen atomic ratios than for a film sputtered non-reactively using a ceramic Ga_2O_3 target. Although, the DC target potential has only a minor effect on the average oxygen atomic ratio of the layers, using higher potentials can be detrimental to the surface quality of the films as little Ga-rich droplets can form on the surface. Ellipsometry measurements have shown that the extinction coefficient of the films prepared at higher oxygen flow rates becomes zero in the UV wavelength range (Fig. 2.18.a), thus they have the potential for solar-blind optoelectronic applications. It was also found that the refractive index (at 632.8 nm) of the layers tend to decrease as the oxygen atomic ratio increases (Fig 2.18.b).

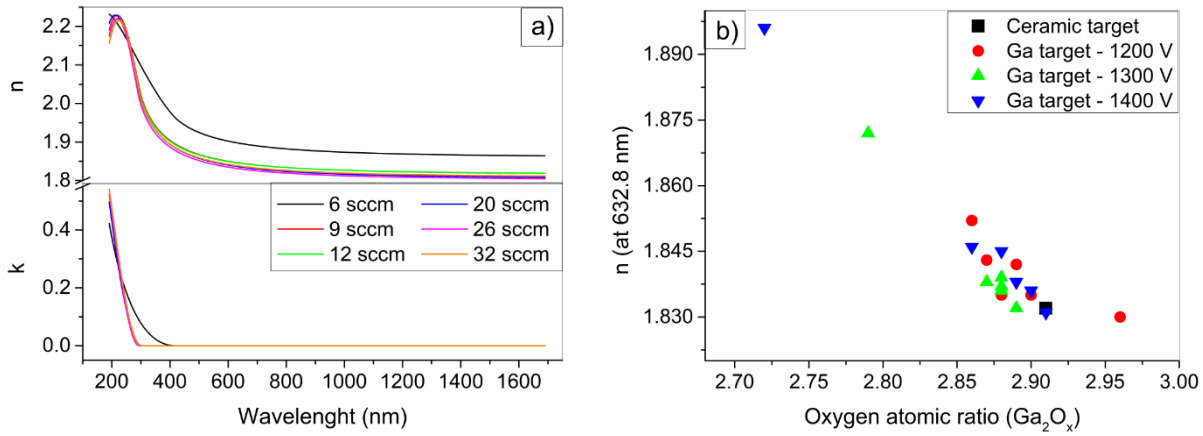

Figure 2.18. *a) The refractive indices (n) and extinction coefficients (k) as a function of the wavelength for the samples sputtered at a 1400 V DC target potential. b) The refractive indices (at 632.8 nm) of the gallium oxide films as a function of the oxygen atomic ratio.*

The thickness of the films was also determined by ellipsometry (see Fig. 2.19). Significantly higher deposition rates were found for the samples prepared using the liquid target compared to the ceramic one. For example, 9.4 nm/min growth rate was achieved at 20 sccm oxygen flow rate (0.113 Pa O_2 pressure) for the liquid target, while only 5.3 nm/min for the ceramic one (using 1400 V DC target potential in both cases). The upgraded Berg model was used to model the reactive sputtering process and the thickness data were fitted based on this model (Fig. 2.19., solid lines). As a result, different sputtering parameters such as the sputtering yields and the sticking coefficient were determined. The fitted parameters suggest that the preferential sputtering of Ga becomes more significant as the DC target potential increases.

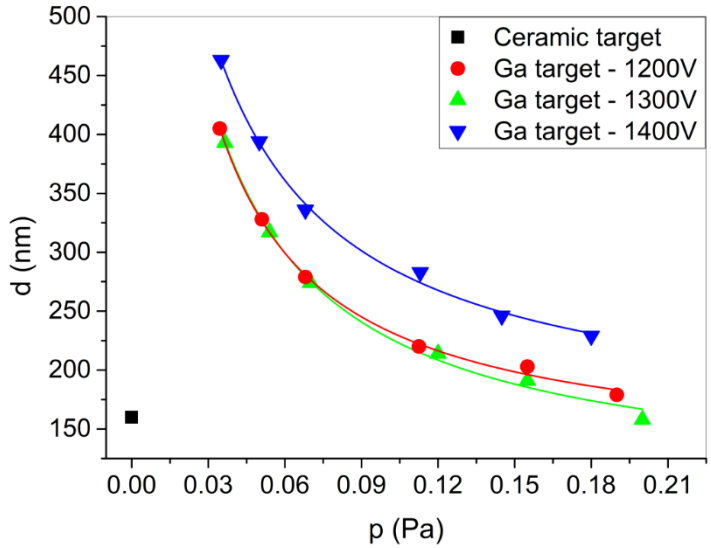

Figure 2.19. *The film thickness at different oxygen partial pressures and DC target potentials, as measured by ellipsometry, and the fit to the data points (solid lines) using the Berg model.*

Resonance-based Kretschmann-Raether ellipsometry utilizing plasmonic and periodic nanostructures at solid-liquid interfaces

TKP2021-EGA-04, EMPIR POLight 20FUN02, OTKA K 146181

D. Mukherjee, B. Kalas, S. Burger, Gy. Sáfrán, M. Serényi, M. Fried, P. Petrik

Because of their beneficial and adaptable characteristics, nanostructures have been the subject of extensive investigation for a long time. One of the many avenues of scientific and medical inquiry that nanostructures have opened up is plasmonic nanostructures. Research and technology in the subject of plasmonics, in general, rely on the collective oscillation of free electrons in metallic thin films or other metallic nanostructures in response to electromagnetic radiation [Ref. 2.14] Plasmonic nanostructures are those that have the ability to produce and regulate light at the nanoscale. These nanoscale devices' small size and form allow them to manipulate light waves in a variety of ways. The interaction of plasmons with light causes surface plasmon polariton (SPP) resonance to be seen at the interface of metal layers and dielectrics (such as air or liquids). This is the result of an intensely restricted surface wave that spreads over the interface and decays exponentially in the dielectric ambient and the metal layer. To subtly customize the ideal wavelength range for SPP, several metals are alloyed together to change the plasmonic material's chemical makeup [Ref. 2.15]. It works well for adjusting metallic nanostructures and thin films' optical response. Noble metals like Ag, Au, and Pt have been favored for SPP applications because of their abundance of free electrons, despite the well-known optical losses caused by interband optical transitions. Ag is the most readily available material in the Vis-NIR range and has the finest properties for plasmonic applications. Moreover, metal alloys and intermetallics are interesting possibilities for alternative plasmonic materials due to their high free electron densities [Ref. 2.16]

In SPR spectroscopy, a thin Au film is commonly used as the sensing layer. When surface plasmons are present, incoming light can couple with them to produce a dip in the reflectance spectrum. The precise wavelength (λ) value of this dip is determined in large part by the thickness (d) and optical properties of the Au layer, the angle of incidence (θ) of the light beam, the optical properties of the configuration, and - most importantly - the optical properties of the investigated ambient close to the Au surface. Developing original layer designs can also help to boost sensitivity. Using one or more 2D layers (such as graphene or molybdenum disulfide) on top of the Au film in addition to the naked Au layer might result in improved sensing performance.

The Kretschmann-Raether configuration [Ref. 2.17], which enables the study of the optical characteristics of materials, is based on the concepts of ellipsometry, in which light is reflected at an interface between a solid and a liquid. The use of nanostructures to in-situ surface-enhanced Kretschmann-Raether ellipsometry has proven successful. Using this kind of optofluidics technology, ellipsometric measurements may be performed by non-invasively transducing evanescent fields to surface plasmon polariton. Using a Woollam M-2000DI rotating compensator spectroscopic ellipsometer in the λ = 190-1700 nm wavelength range and adjustment using the Kretschmann-Raether (KR) geometry, the θ was allowed to be extended up to 75◦ for focus extension. For the KR ellipsometry (KRSE) configuration, an enhanced hemisphere has been utilized to provide an ideal signal-to-noise ratio in the critical spectral band below 300 nm.

Micro combinatory was used to deposit a combinatorial film at room temperature on a thin UV-grade FS substrate measuring 25 mm by 10 mm (length by width) and 150±25 μm. A layer with a gradient composition of AgxAl1−x, spanning from $0 < x < 1$, was generated by the deposition. On the 25 mm long substrate, a gradient track of 20 mm is bounded by 2.5 mm long lead-in portions of one target's flux. The setup moves a shutter with a 1 mm by 10 mm slot above the substrate in tiny increments, and the power of the two magnetrons is controlled in time with the slot movement. As the slot passes over the substrate, the

Ag fluence progressively drops from 100 to 0 and the Al fluence gradually increases from 0 to 100 resulting in the required composition gradient. The variable thickness, which may be used to modify the wavelength of maximum sensitivity, was made possible by the exact control of the slot movement (Fig. 2.20).

Principal advantages of the combinatorial deposition method are:

(i) When the deposited layer is created in a single process step, all sample preparation parameters and substrate properties are guaranteed to be the same, with the exception of the modulated parameter (the composition and/or thickness).

(ii) They are also easier to use and more efficient since the optical measurement and assessment may be automatically carried out by a lateral scan. The evaluation approach also supports an interpretation based on a single process. This method allows for the characterization of more substantial modulations and unanticipated fluctuations of the qualities, without assuming any lateral dependency.

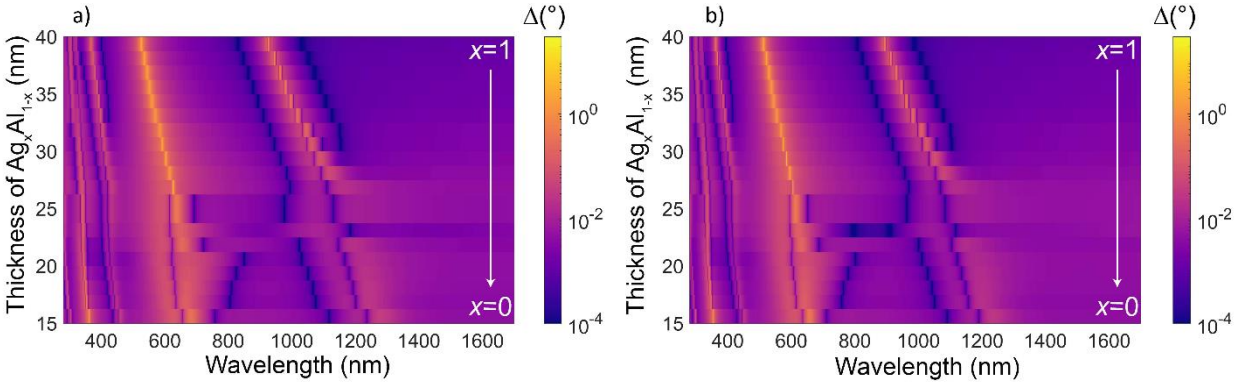

Figure 2.20. *Variation of the ellipsometric phase shift ($\Delta = arg(r_p/r_s)$) as a function of the thickness of the Ag_xAl_{1-x} layer and the wavelength for angles of incidence of 71° (a) and 73° (b).*

The generated sensor structure's compositions with x = 0 (pure Al) and x = 1 (pure Ag) had optimal thicknesses because the optical properties of these pure phases were believed to be more reliable than those of mixed phase references. This one-sample combinatorial device is now tuned only for linearly graded compositions and thicknesses, but it would be feasible to tweak the lateral thickness profile after finding the optical properties for all values. To examine the change in Δ for $\Delta n_{water} = 10^{-4}$, transfer matrix method (TMM) computations were performed. These statistics clearly show that the lower AOI value (71°), which is the closest to the comparable value of the total internal reflection angle, is where the highest sensitivity may be attained.

It was demonstrated that the phase information obtained from ellipsometry, in conjunction with variable resonant features, can be applied to periodic Au grating structures (Fig. 2.21) as well as combinatorial Ag_xAl_{1-x} structures made by sputtering on glass plates connected to a hemi-cylinder in the KR geometry. $\Delta = arg(r_s/r_p)$ is the phase measurement formula, where r_p and r_s are the polarized light reflection coefficients parallel and perpendicular to the plane of incidence, respectively.

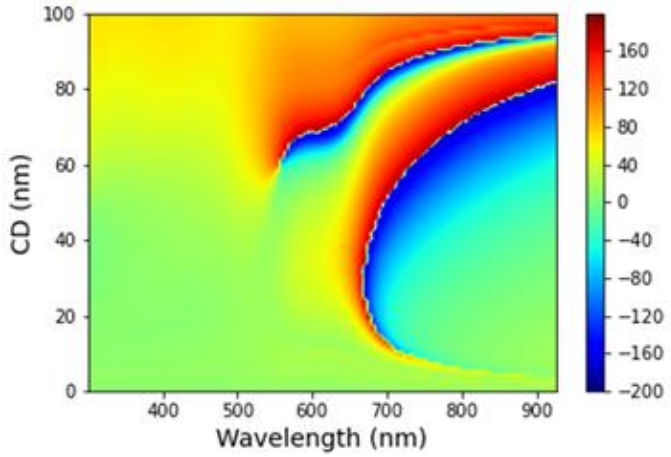

Figure 2.21. *Δ ellipsometric angle calculated for different critical dimension (CD) and wavelength values in the KR configuration for a gold layer on glass with a thickness and period of 200 nm and 100 nm, respectively.*

The ellipsometer resolution in space (focused spot) and time is generally 0.3 mm by 0.9 mm and 1 s, respectively. Sensitivities of 10^{-6} and 10 pg/mm^2 in refractive index and surface mass density units, respectively, may be reached at an ideal plasmonic setup. Au gratings were designed and modeled utilizing transfer matrix and finite element (JCMwave) methods in order to build phase retrieval and sample parameter reconstruction method. They are mostly significant for determining which grating settings in experimental studies show the greatest promise.

Makyoh imaging and topography

F. Riesz

Makyoh imaging, named after the Japanese ‘magic mirror’, denotes an optical imaging mechanism, where a plane (or, more generally, a spherical) wave is reflected from a flat, or slightly convex mirror having small height deviations, causing intensity variations in a far-field screen image because of the local ray deflections. The intensity distribution reflects somehow the mirror height map. The first application of this principle was probably the Oriental magic mirror; a modern application is Makyoh topography, used mostly for the visualisation of surface defects or texture of semiconductor wafers.

The main result of the past year is the proposal of a novel approach for the imaging of the ancient mirror: the *visual image* of the back relief pattern, rather than its height topography is compared to the reflected Makyoh image (Fig. 2.22) [Ref. 2.18]. The visual image depends on the environmental illumination conditions (light directionality and scattering degree) and surface reflection properties in a complex way, but it can be stated the both images are essentially emphasise edges (gradient changes) of the back relief, thus their correspondence can be established. Fig. 2.22 shows intensity profile calculations of the Makyoh and the visual back images for three characteristic back patterns: a narrow and a wide mound and a ridge for diffuse and directional (oblique) back illumination; back reflection is assumed mixed (diffuse with wide specular component). Convolution with a Gaussian was used for pattern transfer modeling to obtain the front surface profiles. For diffuse illumination, the correspondence of the two images is striking; the specular component can relate to the main reflection peak for the narrow mound.

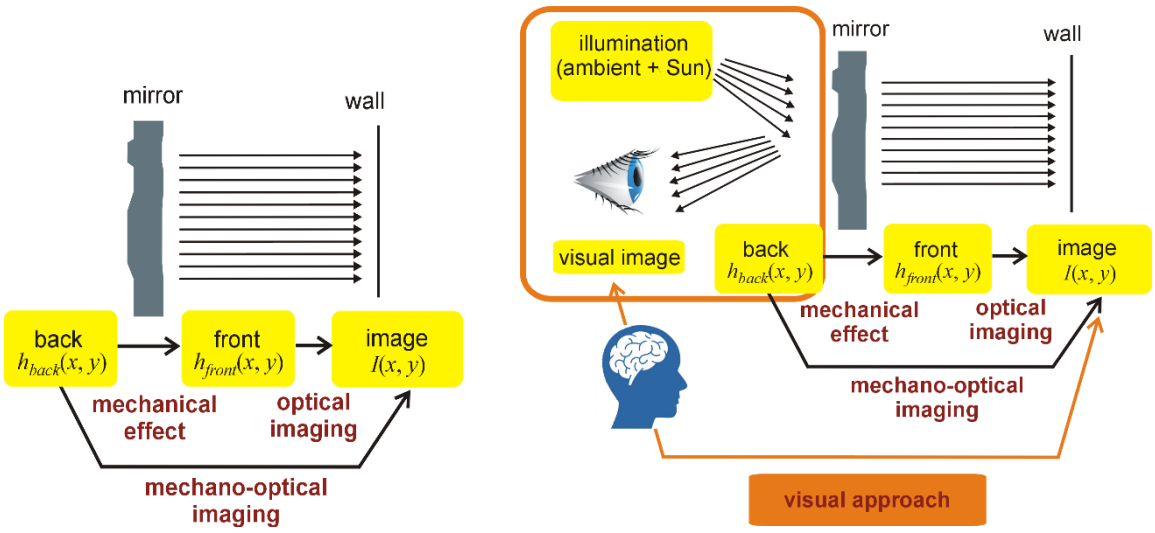

Figure 2.22. *Scheme of the traditional mechano-optical (left) and the proposed visual (right) approaches of Makyoh imaging.*

Related to this, the various approximations of the Makyoh imaging were analysed and compared. The most popular is the Laplacian approximation introduced by Berry. We hypothesised that a certain class of ancient mirrors (namely, Japanese mirrors) operate in the post-Laplacian regime, where stronger focusing of the concave ares occur, leading narrower and higher-intensity image regions (Fig. 2.24). This imaging is characteristic to globally flat or less curved mirrors. These results have relevance to the modern application of Makyoh as well, since the studied samples (mostly, semiconductor wafers) are usually also globally flat.

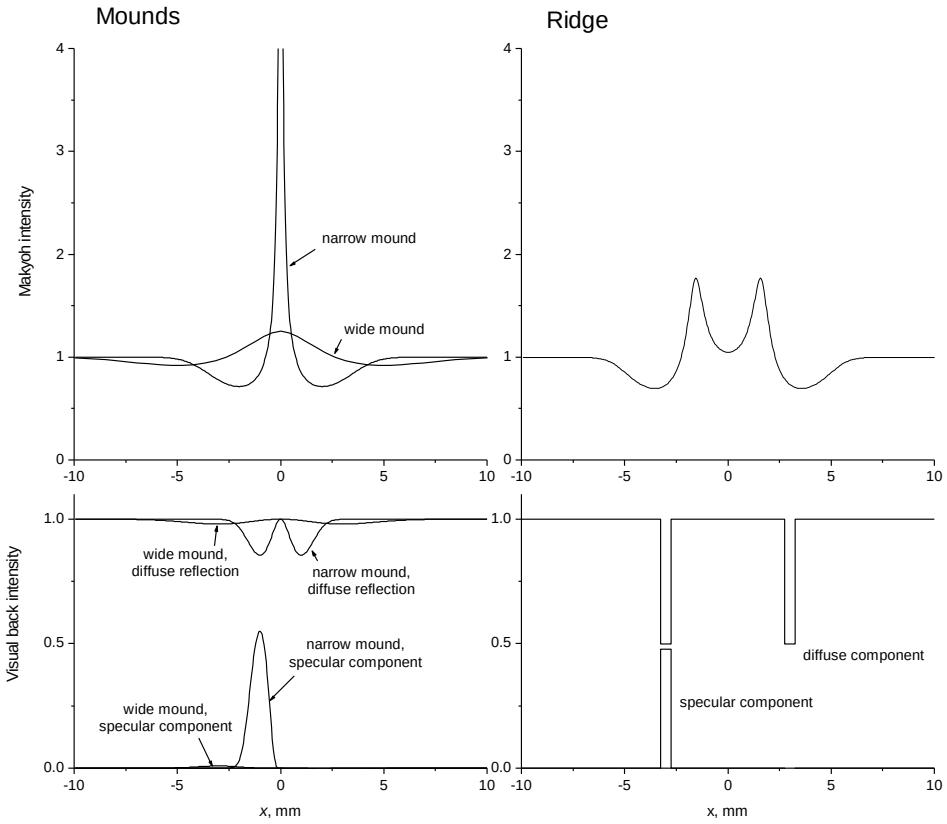

Figure 2.23. *Calculated intensity profiles of the Makyoh and the reflection visual back images for three characteristic back relief patterns.*

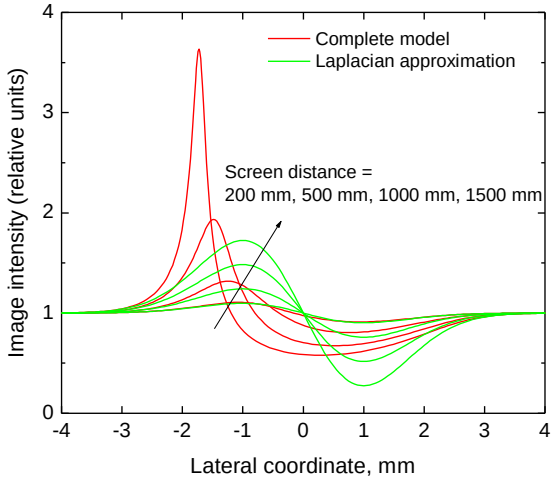

Figure 2.24. *Makyoh image intensity profiles produced by a one-dimensional abrupt back surface step (after convolution with a Gaussian with d = 1 mm, resulting 1-μm height in the front face) at various screen distances, calculated using the Laplacian aproximation and the complete model.*

3 - Thin Film Physics Department

Head: Dr. Katalin Balázsi, Ph.D., senior scientist

Research Staff

- Csaba BALÁZSI, D.Sc.
- Haroune R. BEN ZINE (until Dec. 2023)
- Ildikó CORA, Ph.D.
- Zsolt CZIGÁNY, D.Sc.
- Zsolt FOGARASSY, Ph.D.
- Mónika FURKÓ, Ph.D.
- Tamás KOLONITS
- Viktória KOVÁCSNÉ-KIS, Ph.D.
- Béla PÉCZ, D.Sc., deputy general director of HUN-REN Centre for Energy Research, MFA director
- György Zoltán RADNÓCZI, Ph.D.
- Adél RÁCZ, Ph.D.
- György SÁFRÁN, D.Sc.
- Attila SULYOK, Ph.D.
- Péter B. BARNA, D.Sc., Prof. emeritus
- Miklós MENYHÁRD, D.Sc., Prof. emeritus
- György RADNÓCZI, D.Sc., Prof. emeritus
- János LÁBÁR, D.Sc, Prof. emeritus

Ph.D. students

- Dániel OLASZ
- Erzsébet DÓDONY
- Klára HAJAGOS-NAGY
- Nikolett HEGEDÜS
- Maroua H. KAOU (Hungaricum stipendium)
- Wasan ALKAron (Hungaricum stipendium)

1.

2. Technical Staff

- Andrea JAKAB-FENYVESINÉ
- Andor KOVÁCS
- Balázs ERKI
- Valéria OSVÁTH
- Noémi SZÁSZ
- Viktor VARGA

The scientific results of the Thin Film Physics Department are related to thin film and ceramic fields. The main research topics are in line with modern trends of material science with the respect to a 50 years long history of the department. The development of the 2D semiconductor, multicomponent thin films and technical ceramics were the important base research fields supported by several international basic scientific projects and collaborations in 2023.

The uniqueness of the Department in national and international level as well was the structural investigation of various materials by transmission electron microscopy (TEM). The effect of the structure on the developed material´s properties was demonstrated by TEM. It was demonstrated that the optimal structure can be directed in a controlled way. All topics were supported by methodical developments based on electron diffractions.

In 2023, 59 scientific publications (10pc D1, 27pc Q1) appeared in refereed journals with a cumulative impact factor of 270. In addition, 22 papers were published with no impact factor conference proceedings. Members of the group presented an invited lectures, oral talks at national and international conferences. The group received ~ 3800 independent citations in the examined interval of the last two years. Research members of the group lectured some courses at universities and held few laboratory practices. All courses were for full semester (Eötvös Lóránd University - ELTE, and Budapest University of Technology and Economics - BME, and University of Pannonia- UP and Óbuda University - OE). In addition, 6 PhD students were supervised.

The researchers of the Department organized major national and international conferences in 2023:

- Annual conference of the Hungarian Microscopic Society 2023 (MMT) Siófok 2023 May 4-6 – Pécz Béla, Lábár János Radnóczi Gy. Zoltán
- 47th International Conference and Expo on Advanced Ceramics and Composites (ICACC2023) USA– Balázsi Csaba, Balázsi Katalin (symposium lead org.) Daytona Beach, USA 2023 January 27-February 3
- 48th International Conference and Expo on Advanced Ceramics and Composites (ICACC2024) USA – Balázsi Csaba, Balázsi Katalin (symposium lead org.)) Daytona Beach, USA 2024 January 23-February 2
- 14th International Conference on Ceramic Materials and Components for Energy and Environmental Systems (CMCEE14), HU - Balázsi Csaba, Balázsi Katalin (conference chairs) Budapest, 2024 August 18-22
- Annual conference of the Hungarian Microscopic Society 2024 (MMT) Siófok 2024 May – Pécz Béla, Lábár János Radnóczi Gy. Zoltán
- 2nd International Summit on Graphene & 2D Materials (ISG2DM2024) Germany Munich 2024 May 20 –Balázsi Katalin (conference chair)
- Social activity of the group is landmarked by nearly 20 memberships in different committees of the Hungarian Academy of Sciences and in boards of international societies (European and American Ceramic Society, International Ceramic Society, International Union for Vacuum Science).

TEM of innovatively used of PtSi contact material

2019 2.1.7-ERA-NET-2022-00032, QuantERA II SIQUOS

J. Lábár, B. Pécz, Y. Yao[1], D. F. Fernandes[1], T. Košutová[1], T. Kubart[1], Z. Zhang[1], F. Lefloch[2], F. Gustavo[2], A. Leblanc[2], S.-L. Zhang[1]

[1] Division of Solid-State Electronics, Department of Electrical Engineering, Uppsala University, Sweden,
[2] Université Grenoble Alpes, CEA, Grenoble, France

PtSi has long been used as contact material in microelectronics. It is usually formed by the self-aligned-silicide (SALICIDE) process. Novel application of PtSi in cryogenic temperatures as superconducting material of source and drain in silicon-based Josephson field-effect transistors (JoFETs) requires that the thickness of the PtSi layer is reduced considerably. Our SIQUOS project aims at manufacturing such JoFETs as part of Qubits. This reduction in thickness brought up new technological challenges that did not exist in conventional microelectronics.

Current SALICIDE process involves thermal oxidation at 600°C to protect the formed PtSi from being etched off during the subsequent chemical etching in aqua regia aiming to selectively remove unreacted Pt present on the surrounding oxide layers. However, sub-10 nm PtSi films tend to agglomerate and even break into discrete PtSi islands upon thermal treatments above 500°C. To mitigate this technical issue, an innovative ambient-temperature chemical oxidation step was introduced. The results below prove that this change in technology was successful. While 5 nm thick layers manufactured with the conventional technology broke into islands (Fig.3.1), the new process flow resulted in homogeneous PtSi layers (Fig. 3.2) of the same thickness. All technology steps except the new oxidation were identical, including subsequent etching in aqua regia.

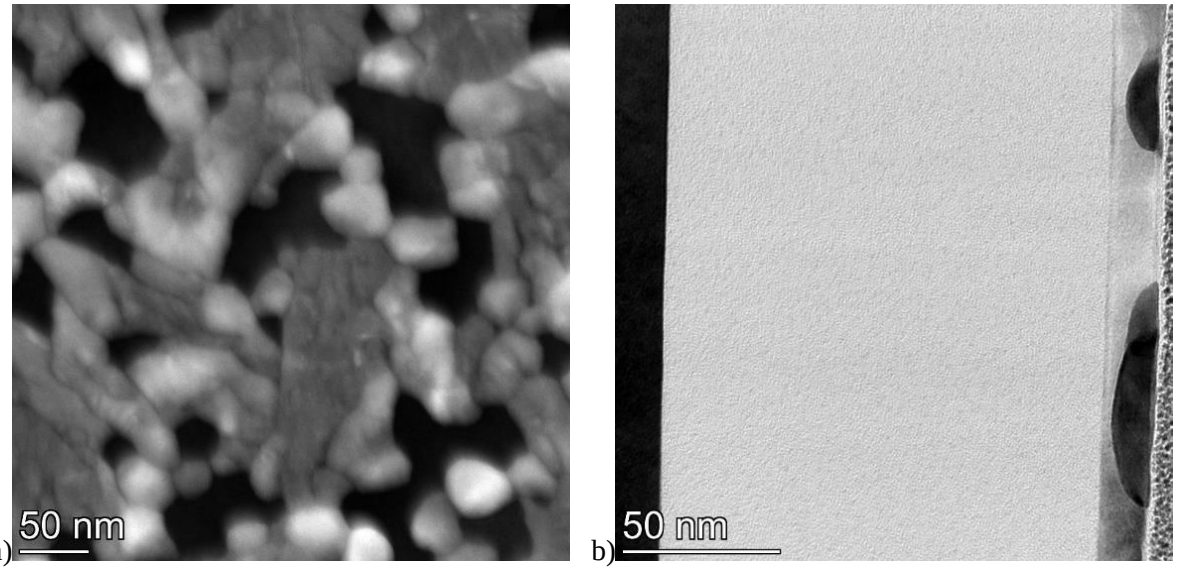

Figure 3.1. *a). Plan-view HAADF image of 5 nm thick PtSi layer. Thermal oxidation and subsequent etching in aqua regia. The layer is full of holes. b) Cross-section BF image of 5 nm thick PtSi layer. Thermal oxidation and subsequent etching in aqua regia. The layer broke into islands.*

In contrast to the conventional Pt-SALICIDE process involving thermal oxidation, the new process flow with chemical oxidation produces continuous, uniform protecting oxide on top of PtSi, which protects the ≤5nm thick PtSi from being etched away (when remaining Pt is removed). Superconductivity of the layers is measured and slight dependence on both layer thickness and annealing temperature is determined [Ref. 3.1].

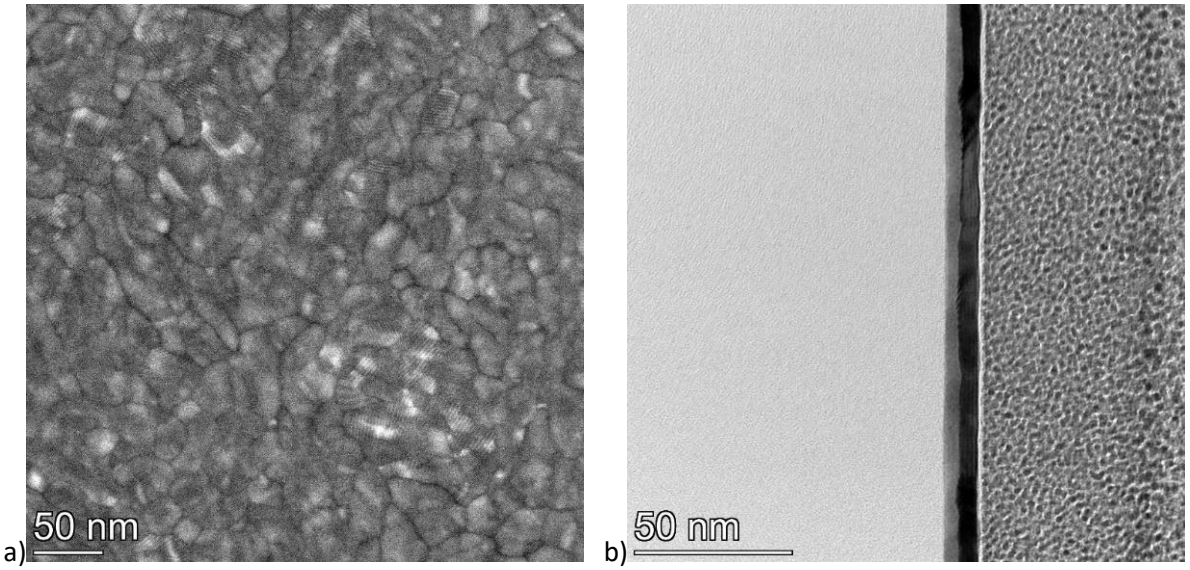

Figure 3.2. *a) Plan-view HAADF image of 5 nm thick PtSi layer. New, ambient temperature, chemical oxidation and subsequent etching in aqua regia. The layer is continuous, even pin holes cannot be observed in it. b) Cross-section BF image of 5 nm thick PtSi layer. New, ambient temperature, chemical oxidation and subsequent etching in aqua regia. The layer is continuous.*

Reactive Sputter Deposition of Ga2O3 Thin Films Using Liquid Ga Target

TKP2021-NKTA-05

M. Gajdics, M. Serényi, T. Kolonits, A. Sulyok, Zs. E. Horváth and B. Pécz

Ga_2O_3, as an ultrawide bandgap semiconductor has numerous potential applications in the field of optoelectronics, high-power electronics and gas sensing. Gallium oxide thin films can be grown by a variety of methods, among them, sputtering is a commonly used technique. In most cases, a ceramic Ga_2O_3 target is used for sputtering of Ga_2O_3. In our work, we demonstrate an alternative method, i.e. reactive sputtering of a liquid Ga target. Modeling of this reactive sputtering process was performed based on the Berg model [Ref. 3.2].

Liquid gallium was placed in a circular crucible fabricated from a 0.2 mm Ni plate. The diameter of the container was 75 mm and the height of its side wall was about 3 mm. This target was reactively sputtered in a radio frequency sputtering device. Different samples were prepared by varying the oxygen flow and the DC target potential. The composition of the samples was analyzed by energy dispersive spectroscopy and X-ray photoelectron spectroscopy, respectively. The optical parameters and the thickness of the films were determined by spectroscopic ellipsometry.

It was shown that using high enough oxygen flow rate (32 sccm – standard cubic centimeter per minute), it is possible to achieve higher oxygen atomic ratios than for a film sputtered non-reactively using a ceramic Ga_2O_3 target. Although, the DC target potential has only a minor effect on the average oxygen atomic ratio of the layers, using higher potentials can be detrimental to the surface quality of the films as little Ga-rich droplets can form on the surface. Ellipsometry measurements have shown that the extinction coefficient of the films prepared at higher oxygen flow rates becomes zero in the UV wavelength range (Fig. 3.3.a), thus they have the potential for solar-blind optoelectronic applications. It was also found that the refractive index (at 632.8 nm) of the layers tend to decrease as the oxygen atomic ratio increases (Fig 3.3.b).

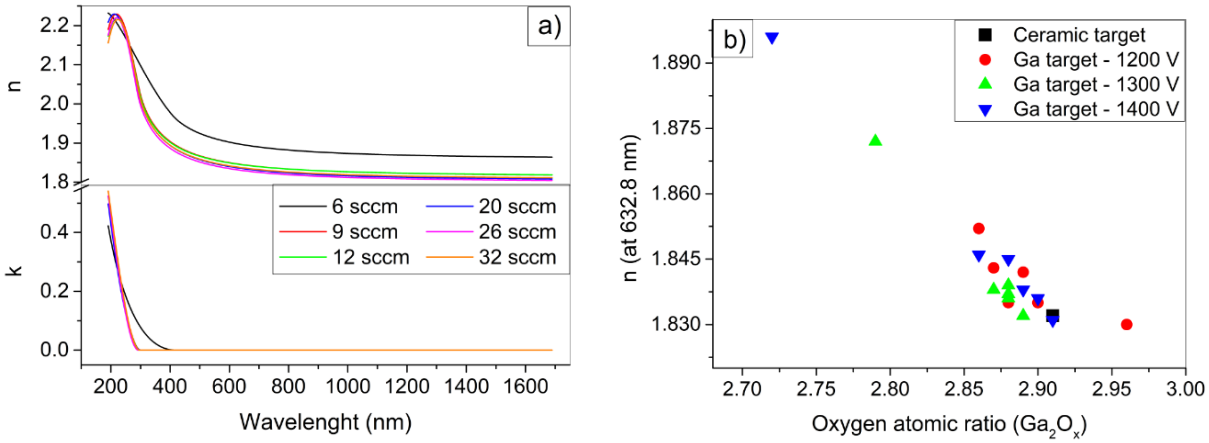

Figure 3.3. *The refractive indices (n) and extinction coefficients (k) as a function of the wavelength for the samples sputtered at a 1400 V DC target potential a). The refractive indices (at 632.8 nm) of the gallium oxide films as a function of the oxygen atomic ratio b).*

The thickness of the films was also determined by ellipsometry (see Fig. 3.4). Significantly higher deposition rates were found for the samples prepared using the liquid target compared to the ceramic one. For example, 9.4 nm/min growth rate was achieved at 20 sccm oxygen flow rate (0.113 Pa O2 pressure) for the liquid target, while only 5.3 nm/min for the ceramic one (using 1400 V DC target potential in both cases).

The upgraded Berg model was used to model the reactive sputtering process and the thickness data were fitted based on this model (Fig. 3.4, solid lines). As a result, different sputtering parameters such as the sputtering yields and the sticking coefficient were determined. The fitted parameters suggest that the preferential sputtering of Ga becomes more significant as the DC target potential increases.

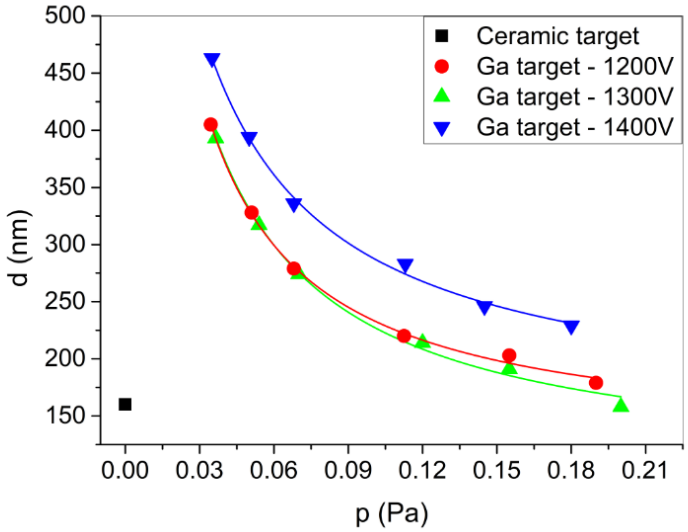

Figure 3.4. *The film thickness at different oxygen partial pressures and DC target potentials, as measured by ellipsometry, and the fit to the data points (solid lines) using the Berg model.*

Industrially deposited hard and damage resistant W-B-C coatings

VEKOP-2.3.3-15-2016-00002, VEKOP-2.3.2-16-2016-00011

Zs. Czigány, K. Balázsi, M. Krokker[1], P. Soucek[1], P. Vasina[1]

[1] Department of Physical Electronics, Masaryk University, Brno, Czech Republic

The study investigates the properties of deposited W-B-C coatings, examining the influence of chemical composition and deposition regimes on mechanical properties of sputter-deposited coatings composed of tungsten, boron and carbon [Ref. 3.3]. The research employs an industrial batch-coater equipped with a segmented target, examining the coatings under both laboratory-like and industrial preparation conditions through stationary and single-axis rotation depositions. The coatings are systematically studied across a range of chemical compositions, revealing predominantly amorphous structures (Fig. 3.5).

Intriguingly, specific compositions exhibit the formation of short-range ordered tungsten borides or nanocrystalline cubic tungsten carbide structures. Morphological differences are observed, with stationary coatings generally more compact and smoother, while rotation induces columnar growth. Surface roughness varies across compositions and regimes, with high-boron coatings exhibiting rugged surfaces. Despite inherent multilayer formation during industrial preparation with substrate rotation, the impact on structure and composition is found to be minimal. The W2BC composition, in particular, displays a fully amorphous structure and impressive mechanical properties despite the lack of internal stress. Mechanical properties, including hardness and effective elastic modulus, range from 10 GPa to 29 GPa and 130 GPa to 440 GPa, respectively. Higher boron content correlates with increased hardness and modulus. Residual stress analysis reveals that nanocrystalline coatings exhibit higher internal compressive stress. Damage resistance assessment based on elastic modulus reduction under indentation is generally used to ranks coatings. W2BC demonstrates superior damage resistance compared to nitrides (TiN, AlCrN). No severe cracking or chipping was caused by the load applied to the cube-corner indenter and the imprints exhibited a pile-up of material. The study extends comparisons with Mo-B-C coatings, highlighting similarities in mechanical properties despite structural differences. W-B-C emerges as a unique amorphous material with good damage resistance and mechanical performance, offering potential applications in protective coatings.

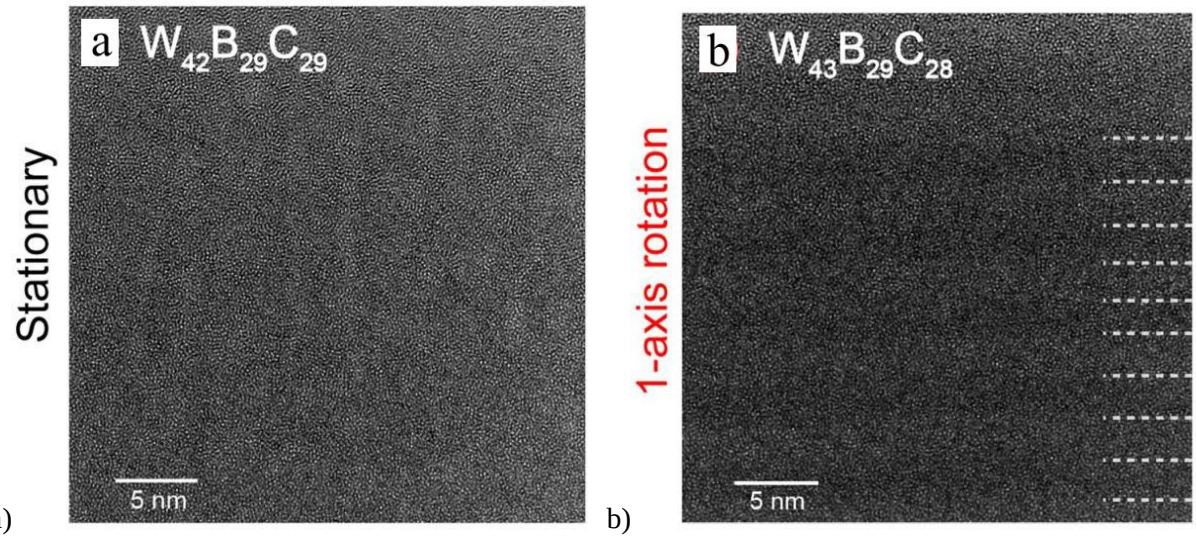

a) b)

Figure 3.5. *a) HRTEM images of WBC coatings deposited on stationary and b) rotating substrate. In figure b) the film shows a slight multilayer character due to substrate rotation.*

Effect of Nb incorporation in Mo2BC coatings on structural and mechanical properties - ab initio modelling and experiment

VEKOP-2.3.3-15-2016-00002, VEKOP-2.3.2-16-2016-00011

Zs. Czigány, K. Balázsi, J. Ženíšek [1], P. Soucek[1], P. Vasina[1]

[1] Department of Physical Electronics, Masaryk University, Brno, Czech Republic

This study [Ref. 3.4] investigates the structural and mechanical implications of niobium (Nb) incorporation into magnetron-sputtered Mo_2BC coatings, employing both theoretical ab initio modeling and experimental approaches. The aim was to explore the stability of the orthorhombic $(Mo_{1-x}Nb_x)_2BC$ phase as molybdenum is gradually replaced by niobium.

Theoretical calculations, based on substituting Mo atoms in the orthorhombic Mo_2BC cell, predicted the stability of the $(Mo_{1-x}Nb_x)_2BC$ solid solution up to 37.5% Nb substitution. At this point, the elastic and shear moduli were maximized, and the enthalpy of formation suggested increased stability compared to common coatings like AlTiN. However, experimental results unveiled the formation of an unexpected fcc NbC-like structure at high Nb contents, challenging the theoretical predictions. All coatings exhibited a columnar structure with nanometer-sized grains and amorphous regions, impacting the stability of the orthorhombic Mo_2BC-like phase compared to theoretical calculations. At the stability limit, coating hardness increased by 25%, and the elastic modulus rose by 60%, attributed to lattice strain generated by Nb substitution. The study concludes with an exploration of the mechanical properties of $(Mo_{1-x}Nb_x)_2BC$ solid solutions. Theoretical predictions showcased a non-linear relationship with Nb content, explained by microstrain within the nanolaminated structure and crosslinking of boron chains. Theoretical stability predictions aligned with experimental trends up to 37.5% Nb substitution, beyond which structural changes led to decreased stability.

SAED investigation provides insights into the challenges of distinguishing between cubic and orthorhombic structures, especially for small grain sizes. Diffraction analysis of Mo_2BC shed light on the similarities of the two structures. Strong reflections in the SAED pattern of Mo_2BC also can be indexed as an fcc phase which has a 111 preferred orientation. However if we want to interpret all the reflections of Mo_2BC, the structure of orthorhombic Mo_2BC seems a proper choice. Mo_2BC can be better indexed as orthorhombic Mo_2BC, however, its strong reflections coincide with allowed reflections of fcc structure, and weak reflections coincide with cubic reflections forbidden in fcc system (Fig. 3.6).

Therefore, the orthorhombic cell can be interpreted as a supercell generated from the fcc cell. The orthorhombic phase contains alternating planes containing stiff carbidic and boridic bonds with a high degree of ionicity and weaker metallic planes. Within the orthorhombic unit cell, the arrangement of heavy metal atoms (Mo, Nb) preserve a cubic (fcc) arrangement characteristic for cubic transition metal carbides. In summary, this research contributes to the detailed understanding of Nb incorporation in Mo_2BC coatings, emphasizing the need for a holistic approach encompassing theoretical modeling and experimental validation for informed coating design and development.

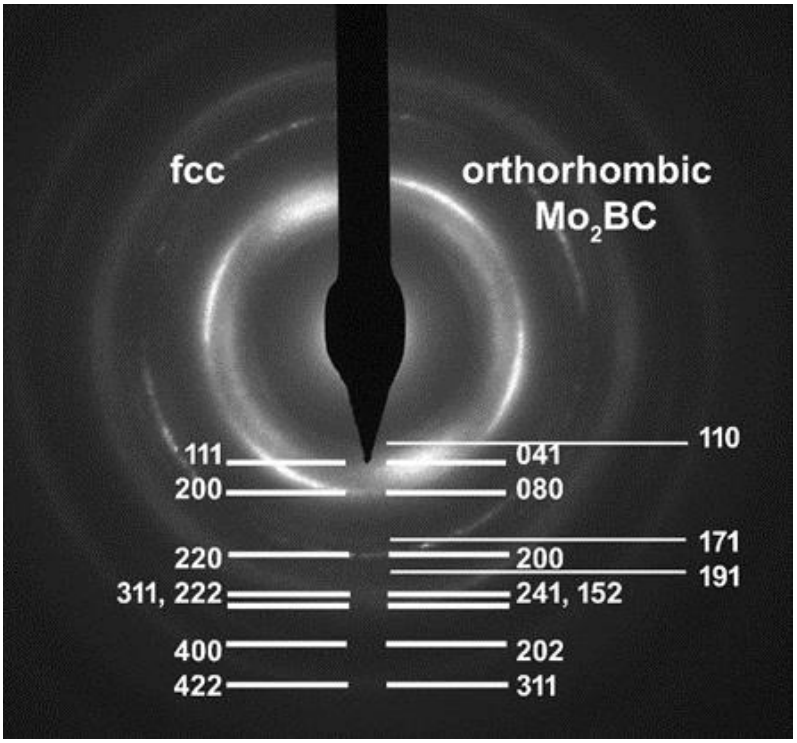

Figure 3.6. *Electron diffraction pattern of Mo2BC. Strong reflections can be indexed as an fcc phase which has a 111 preferred orientation. The strong reflections of orthorhombic structure coincide with allowed reflections of fcc, however weak reflections of orthorhombic structure coincide with cubic reflections forbidden in fcc system. Therefore, the orthorhombic cell can be interpreted as a supercell generated from the fcc cell.*

Composition dependent structure, morphology and mechanical properties of the Al1-xCux thin film system

Ministry of Culture and Innovation KDP-2021 C1792954, OTKA K 143216

D. Olasz, G. Sáfrán, N. Szász, T. Kolonits, N.Q.Chinh

We continued the nanoindentation measurements on the AlCu thin film system (Fig. 3.7) with a comprehensive TEM study to explore the correlations between mechanical, morphological and structural properties. FIB cross-sectional lamellae were prepared from 15 layers of ~ 1.7 μm thickness of different compositions formed by DC sputtering representing the full $Al_{1-x}Cu_x$ composition range ($0 \leq x \leq 1$), of which 12 have already been TEM examined [Ref. 3.5].

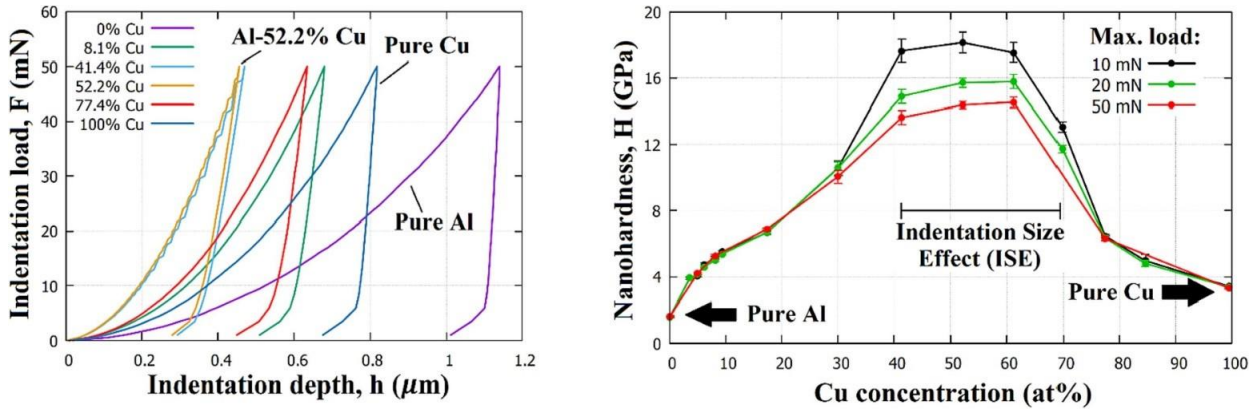

Figure 3.7. *a) Indentation curves and b) hardness of AlCu thin films as a function of Cu alloying concentration*

In Fig. 3.8, bright field TEM images show the morphological evolution of the layers at the indicated copper concentrations x ($Al_{1-x}Cu_x$) with increasing alloying concentration. A drastic reduction in grain size can be observed even with small amounts of Cu alloying. Using selected area electron diffraction (SAED) techniques, we have shown that in the range x = 3.6 - 17.4 % Cu, the θ-Al2Cu phase appears in addition to the α-Al phase, which is in agreement with the predictions of the equilibrium phase diagram [Ref. 3.6]. Both the grain size decrease and the appearance of the θ phase [Ref. 3.7], lead to a significant increase in the strength and hardness of the layer, which can be clearly observed in Fig. 3.7. The layer containing 52.2 at% Cu shows a γ-Al4Cu9 phase composition, which is no longer consistent with the equilibrium phase diagram - and this indicates the non-equilibrium nature of the sputtered thin film. The γ phase is a high strength phase of ~ 15 GPa [Ref. 3.7], which is in good agreement with our measured hardness of ~ 16 GPa.

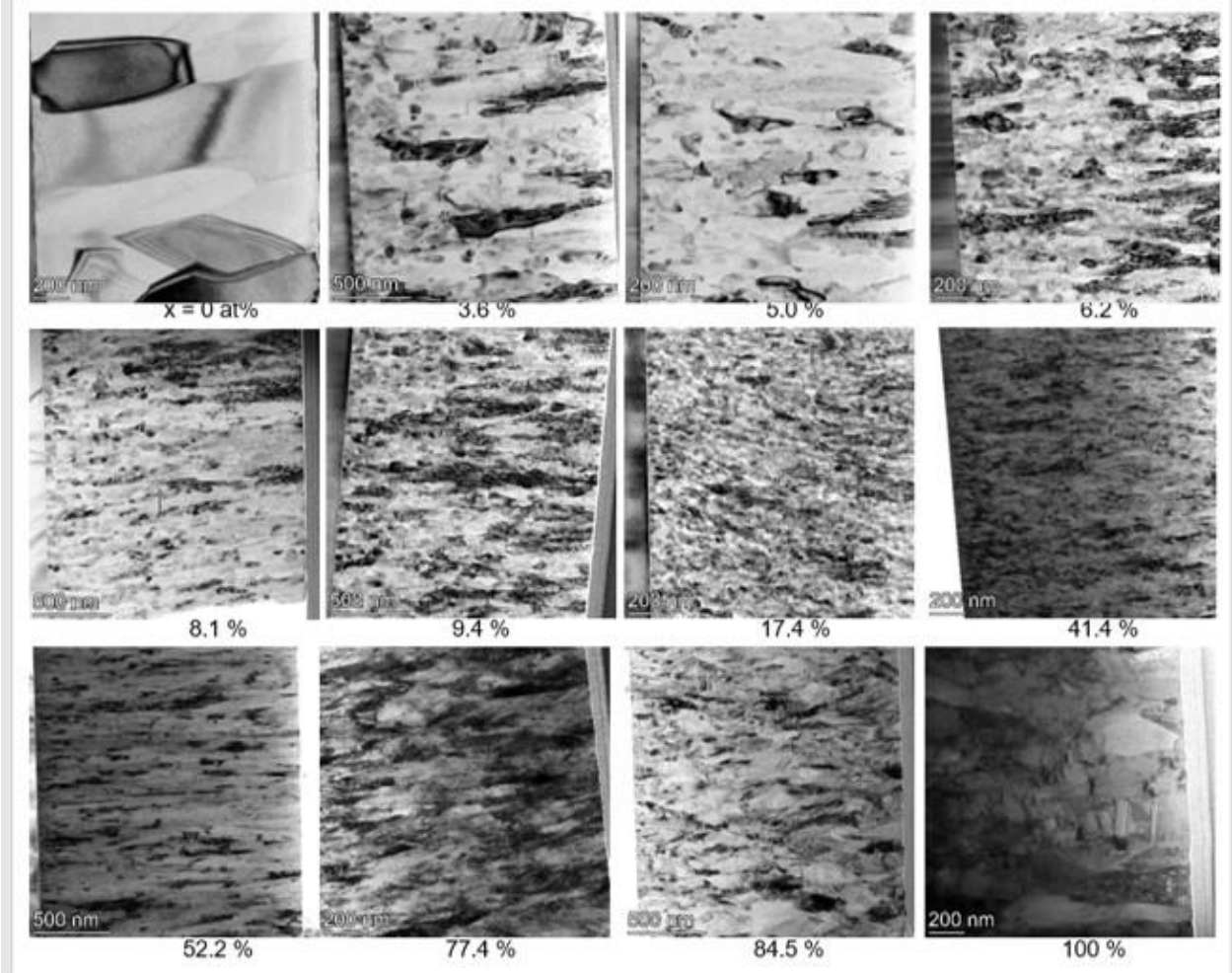

Figure 3.8. *BF TEM cross-section series showing the morphological evolution of AlCu layers as a function of Cu (x) alloying concentrations representing the full compositional range.*

Combinatorial characterisation of the complete Y-Ti-O thin layer system; issues of DC and HIPIMS sputtering processes

Ministry of Culture and Innovation KDP-2021 C1792954, OTKA K 143216

D. Olasz, M. Serényi, M. Gajdics, V.K. Kis, I. Cora, M. Németh, G. Sáfrán

The Y-Ti-O family of materials, which has several promising phases from a technological point of view, offers an excellent opportunity for a comprehensive microstructural characterisation by microcombinatorial fabrication and testing techniques. The results [Ref. 3.8] of the microstructural investigation of the reactive DC magnetron sputtered variable composition coatings are summarized in the phase map shown in Fig. 3.9, which covers the whole Y-Ti composition range up to 800 °C. A very important result is that the pyrochlore-structured Y2Ti2O7 phase could be produced under favourable conditions at a significantly lower temperature, as low as 700 °C, compared to other methods.

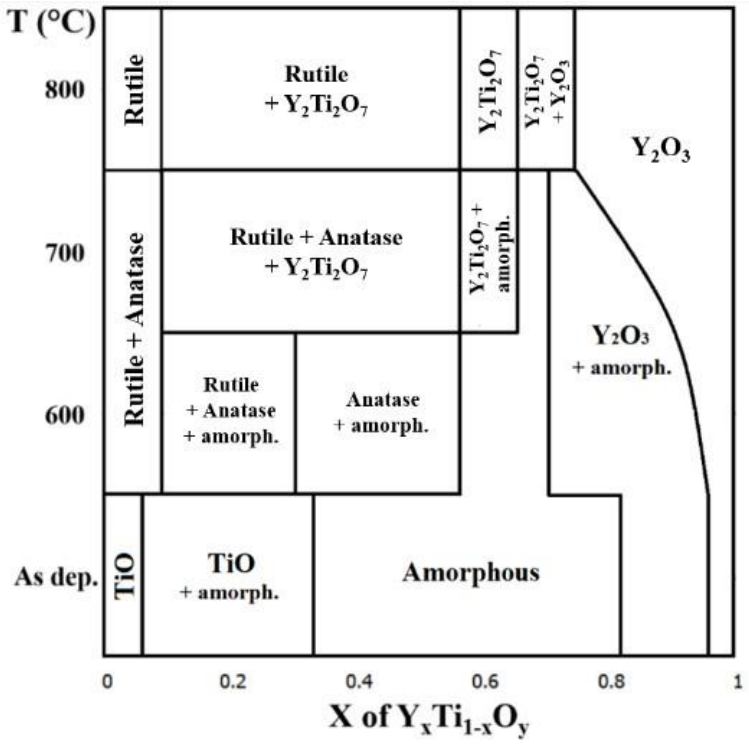

Figure 3.9. *Phase map of the YxTi1-xOy thin film system prepared by microcombinatorial DC magnetron sputtering over the entire 0≤x≤1 composition range up to 800 °C.*

High Power Impulse Magnetron Sputtering (HIPIMS) is a more stable and controllable growth technique than DC, which offers an excellent opportunity to produce the desired perovskite lattice ($YTiO_3$) phase with the right experimental parameters. When reactively sputtering two targets with very different sputtering properties -Y and Ti - together, finding the right settings is a very difficult task, which is not well discussed in the literature. The method used for combinatorial characterization via DC sputtering - varying the power - cannot be applied in reactive sputtering due to its non-linear behaviour (Fig. 3.10).

In the experiments carried out in the last year, we have determined the fundamental parameters: frequency and pulse length, optimal pulsation parameters of the reactive gas, optimal bias voltage of the

sample holder etc. The variation of the layer composition we made possible by using the "burst" mode: by varying the number of bursts (N) separately for each target, it is possible to vary the composition of the sputtered layer along the length of the combinatorial sample (Table 3.1).

N_Y	N_{Ti}	x; $Y_xTi_{1-x}O_y$ (SEM EDS)
10	10	0.49
10	3	0.60
3	10	0.24

Table 3.1. *Effect of the number of Y and Ti bursts (NY;NTi) on the composition of the layer.*

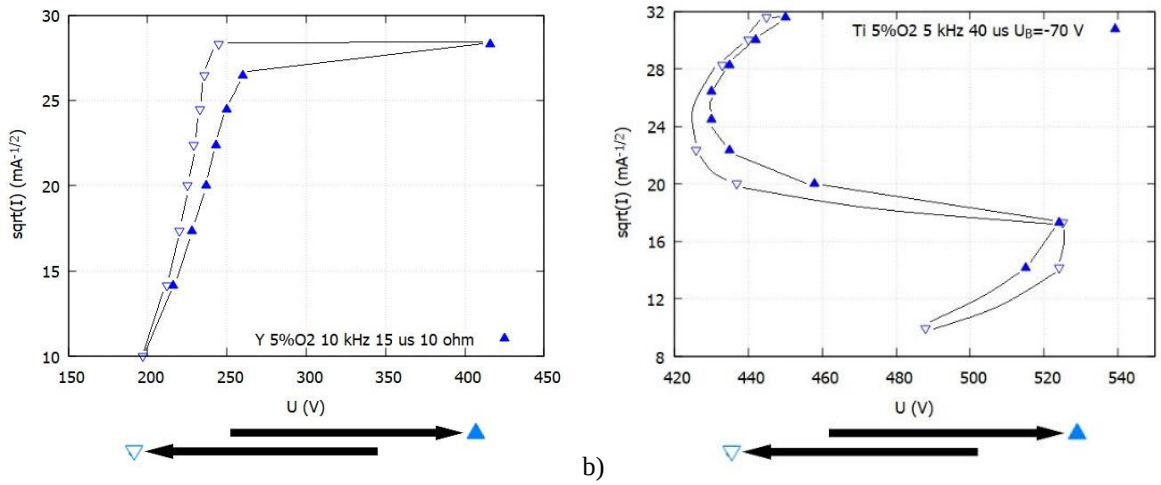

a) b)

Figure 3.10. *Features of U-I hysteresis during reactive sputtering in 5 % O_2 gas for (a) Y target (b) %Ti target.*

Fig 3.11.a shows the the chamber during HIPIMS sputtering of a Y-Ti-O layer in burst mode, and Fig. 3.11.b shows a combinatorial Y-Ti-O layer of varying composition deposited along a Si substrate. Understanding the further effects of the sputtering parameters, we plan to deposit combinatorial layers for TEM analysis onto TEM grids so that comprehensive structural analysis can be efficiently performed.

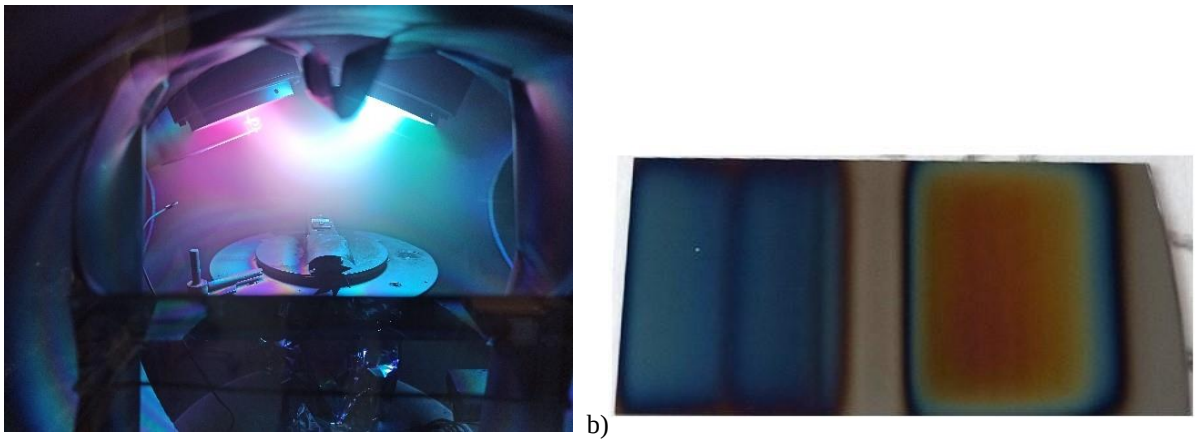

a) b)

Figure 3.11. *a) Y-Ti-O layer growth in burst-HIPIMS sputtering mode. b) combinatorial Y-Ti-O thin film*

Catalytic Methane Pyrolysis Combined with Microcombinatorial TEM Studies

OTKA K 143216, OTKA K 146032

A. Horváth, M. Németh, A. Beck, Zs. Horváth, D. Olasz, M. Serényi, Gy. Sáfrán

Methane pyrolysis ($CH_4 \rightleftharpoons C+2H_2$) yields extremely clean hydrogen gas and only solid carbon, without the production of any CO2, but the process is not industrialized yet. Application of proper catalysts can decrease the temperature requirement of the reaction and produce valuable nanostructured carbon beside hydrogen [Ref. 3.9]. Sample preparation was done by i) chemical deposition of Ni and Mo metal precursor ions over the MgO support or ii) microcombinatorial TEM method [Ref. 3.5] using DC magnetron sputtering over a TEM grid.

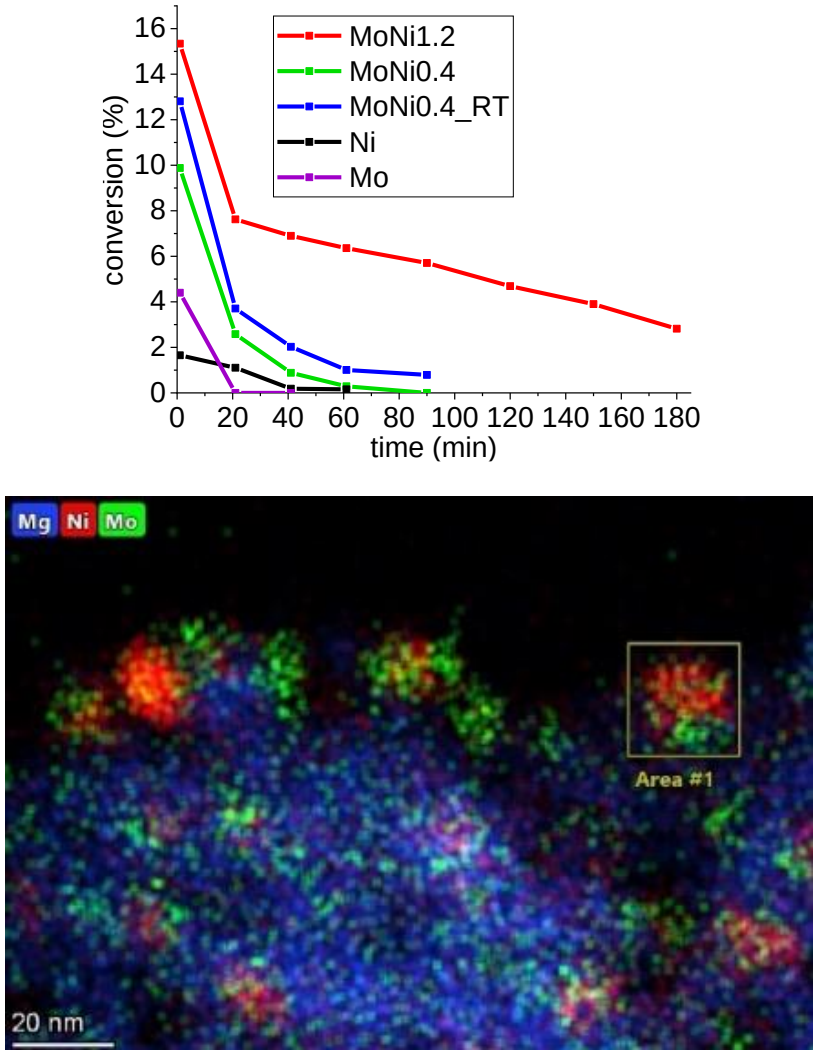

Figure 3.12. *CH_4 conversion during the pyrolysis tests at 800 °C on the MgO supported samples (top); elemental maps of the reduced MoNi1.2 sample (bottom).*

This latter method is able to produce thin layers of two components with linearly changing composition across a TEM grid, and these layers upon high temperature reduction transform into metallic particles or islands. NiMo/MgO catalyst samples (7 wt% Ni and 4% or 12% Mo loading designated by MoNi0.4 and MoNi1.2 atomic ratios, respectively) were reacted in 50% CH4/Ar stream using a horizontal reactor at 800 °C. The supported catalysts were investigated by XRD, TPR, XPS, HRTEM and STEM-EDS prior to and after the CH4 pyrolysis [Ref. 3.10]. The microcombinatorial Ni-Mo samples were investigated by XPS, TEM and STEM-EDS before and after a reduction treatment and carbonization in a methane stream.

The bimetallic NiMo/MgO samples produced carbon nanotubes with 50-320% yield, while monometallic Ni/MgO or Mo/MgO deactivated fast. The superiority of the MoNi1.2 catalyst in terms of activity, stability and carbon yield was explained by the presence of the equimolar alloyed NiMo particles (Fig. 3.12). The novel microcombinatorial TEM method (TEM grid shown in Fig. 3.13.a) resulted NiMo alloy particles with different compositions (Fig 3.13.b). It was ascertained that the Ni/Mo~1 alloy composition (framed with yellow in Fig. 3.13.b) did not seem to segregate during the carbonization process. The existence, the reasons and structural background of the synergetic interaction between nickel and molybdenum were revealed.

The microcombinatorial TEM method was first applied for catalytic purposes. The most prominent novelty of our work was the disclosure of the nanoscale segregation of bimetallic MoNi particles during carbon deposition process depending on the Mo/Ni atomic ratio and affecting the catalyst lifetime.

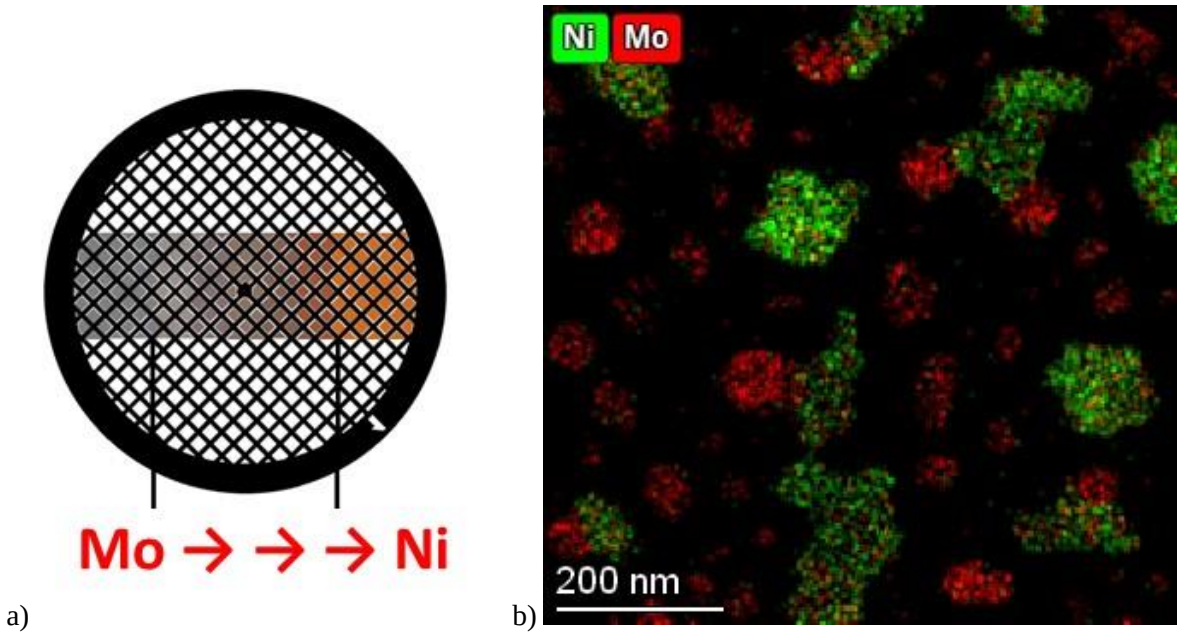

a) b)

Figure 3.13. *a) Scheme of TEM grid with Ni and Mo deposited in linearly changing atomic ratio. b) STEM-EDS elemental maps of a representative area of the grid after reduction at 800 °C with some equimolar alloys framed*

Reductive Treatment of Ti0.8Sn0.2O2-C Composite Supported Pt

OTKA K 143216

E. Dódony, C. Silva[1,2], K. Salmanzade[1], I. Borbáth[2], D. Olasz, Gy. Sáfrán, A. Kuncser[3], E. Pászti-Gere[4], A. Tompos[1], Z. Pászti[1]

[1]*Institute of Materials and Environmental Chemistry, Research Centre for Natural Sciences, Hungary,*
[2]*Department of Physical Chemistry and Materials Science, Faculty of Chemical Technology and Biotechnology, Budapest University of Technology and Economics, Hungary*
[3]*National Institute of Materials Physics, Magurele, Romania*
[4] *Department of Pharmacology and Toxicology, University of Veterinary Medicine, Hungary*

Transition metal-doped titania and carbon composites have emerged as highly effective supports for platinum (Pt) electrocatalysts in proton exchange membrane (PEM) fuel cells. These advanced supports utilize the oxide component to stabilize Pt particles, while the dopants serve a co-catalytic role. Among various dopants, tin (Sn) stands out as a particularly valuable addition. A notable feature of TiO_2-supported Pt catalysts is the strong metal-support interaction (SMSI), which involves the migration of partially reduced oxide species from the support to the Pt surface during reductive treatment. To assess how SMSI affects the stability and performance of Pt/$Ti_{0.8}Sn_{0.2}O_2$-C catalysts, the structural and catalytic properties of freshly prepared samples were analyzed using X-ray diffraction (XRD), transmission electron microscopy (TEM), X-ray photoelectron spectroscopy (XPS), and electrochemical tests, and compared with those of catalysts reduced in hydrogen at high temperatures.

Results indicated that the uniform oxide coverage on the carbon substrate promoted the formation of high-density Pt–oxide–C triple junctions. The electrocatalytic behavior of the as prepared catalysts was determined by the atomic closeness of Sn to Pt, while even a low temperature reductive treatment resulted in Sn–Pt alloying. The segregation of tin oxide on the surface of the alloy particles, a characteristic material transport process in Sn–Pt alloys after oxygen exposure, contributed to a better stability of the reduced catalysts.

As part of our laboratory collaboration, we conducted investigations on the structure, morphology, and elemental composition of the catalysts using the THEMIS TEM of the Thin Films Department. This involved obtaining and analyzing high-resolution and low-resolution images, as well as element mapping with transmission electron microscopy [Ref. 3.11].

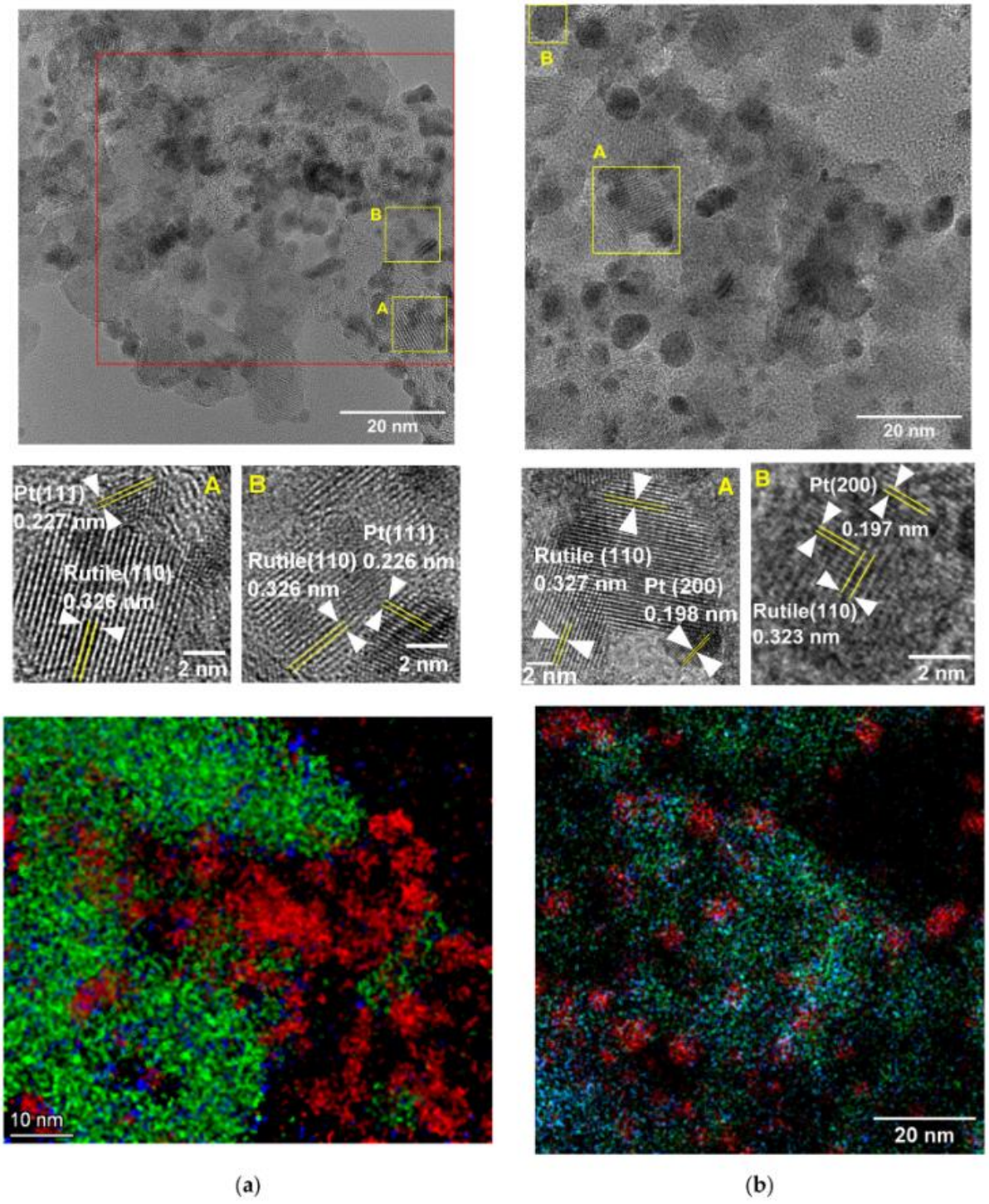

Figure 3.14. *TEM micrographs and elemental maps for (a) the as prepared Pt/Ti0.8Sn0.2O2-C electrocatalyst and (b) the Pt/Ti0.8Sn0.2O2-C electrocatalyst reduced at 200 °C. The locations of the details A and B are indicated by yellow rectangles in the micrographs. The STEM/EDS elemental maps correspond to the area of the red rectangle in (a) and to the entire image area in (b). Color code: red: Pt, green: Ti, blue: Sn.*

Microstructure and growth of α-Mn(Cu) solid solution films

OTKA K 143216

K. Hajagos-Nagy, Zs. Czigány, Gy. Radnóczi

Bulk Mn-Cu alloys are well-known magnetic and shape-memory alloys, which are created from γ-Mn(Cu) solid solution by martensitic (fcc → fct) transformation. The stable form of Mn at room temperature, α-Mn, is considered problematic due to its brittleness; even though the α-Mn structure contains many promising properties, such as para-, antiferro- and weakly ferromagnetic behaviour, anomalous Hall effect and high pressure (220 GPa) stability. The reason behind these properties is the crystal structure of α-Mn, which is considered unique among the elements. It is analogous to the χ phase found in intermetallic systems. The stability of Mn atoms in 3 different electron configurations is almost the same; therefore, Mn is able to create an elementary cell in which atoms of different valence/size are present in different crystallographic positions.

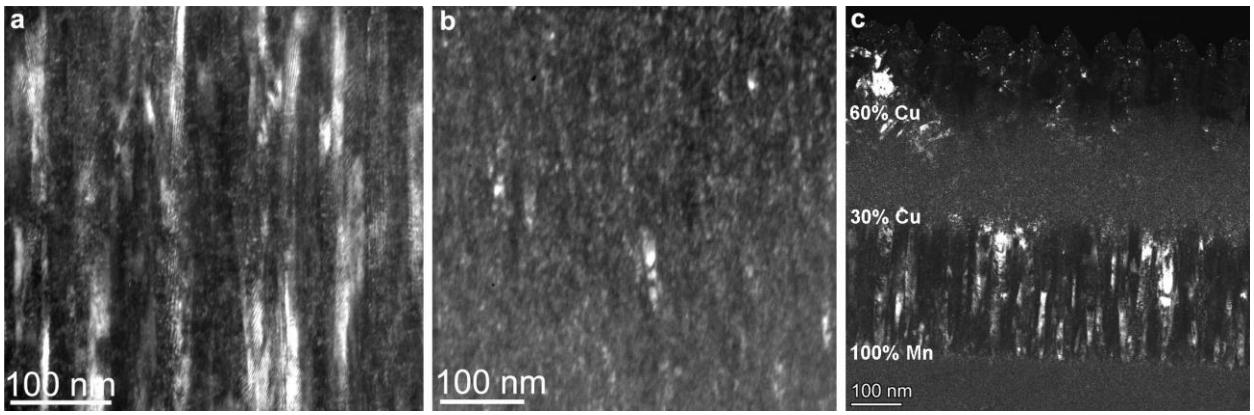

Figure 3.15. *Microstructure of Mn-Cu films with Cu content of 10 at% (a), 20 at% (b) and 0-60 at% (c) on dark field TEM images.*

A possible way of minimizing the brittleness of bulk α-Mn is to use thin film deposition techniques and alloying. In our previous work, we mapped the Cu-Mn thin film system from the point of view of its use in very-large-scale integrated circuits. We discovered that, contrary to our expectations, α-Mn could dissolve at least 10 at% Cu content and the α-Mn(Cu) solid solution was present up to 30 at% Cu. In the current work, we investigated the microstructure and growth of the α-Mn(Cu) layers.

We investigated the non-equilibrium solubility of Cu in α-Mn on a 50 nm thick combinatorial sample grown by DC magnetron sputtering, where the composition varied linearly between pure Mn and 50 at% Cu content. The films contain a crystalline phase up to 30 at% Cu content; the grain size varies between 2-10 nm. Electron diffraction intensity distributions showed that α-Mn can dissolve 30 at% Cu. We examined film growth on 0.5-1 μm thick films, comparing discrete and variable composition (gradient) layers. At 10 at% Cu content a single-phase α-Mn(Cu) solid solution layer grows with a columnar structure (Fig. 3.15.a). As the Cu content increases, an amorphous minority phase appears and hinders the growth of the α-Mn(Cu) grains (Fig. 3.15.b). Examination of gradient films showed that the columnar structure characteristic of single-phase growth can be maintained until the crystalline phase ceases (Fig. 3.15.c). This can be beneficial in many applications where minimization of grain boundaries is required.

Multifunctional biomineralized calcium phosphate-loaded biopolymer composites as biodegradable coatings on implants

OTKA FK 146141

M. Furkó

Bioactive ceramics and scaffolds are extremely important in many biomedical or orthopedic applications owing to their positive interactions with human tissues. There are enormous efforts to develop bioceramic particles that meet the high-quality standard in a cost-effective way. Among the numerous bioceramics, calcium phosphates are the most suitable since the main inorganic compound in human bones is the hydroxyapatite which is a specific phase of the calcium phosphates (CaPs) or apatites. The CaPs can be applied as bone substitutes, types of cement, drug carriers, implants, or coatings. In addition, bioresorbable bioceramics have great potential in tissue engineering since they are usually used as scaffolds that can advance the healing process of bones during the normal tissue repair mechanism. The newest advancement in the CaPs is when they are incorporated with active biomolecules such as Mg, Zn, Sr, and so on. The chemical composition, crystallinity, size, and morphology of the CaP particles and their aggregates play a critical role in determining their properties and potential applications.

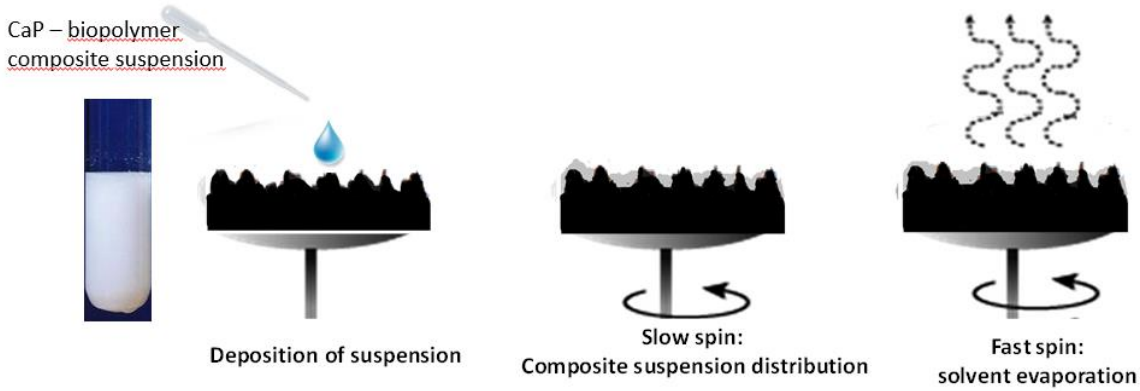

Figure 3.16. *Schematic illustration of spin coating method.*

In our work, amorphous or nanocrystalline calcium phosphates (ACPs) and their combination with biopolymers are prepared as coatings or scaffold matrices. The innovative types of resorbable coatings for load bearing implants that can promote the integration of metallic implants into human bodies. Owing to the bioactive mineral additions (Mg, Zn, Sr) in optimized concentrations, the base CP particles became more similar to the mineral phase in human bones (dCP). The coatings were prepared by spin coating technique (Fig. 3.16).

We investigated and compared the surface roughness of the substrate and the coated substrate and the result showed that the polymer composite decreased the roughness values. The SEM-FIB cross sectional cut revealed a very thin, around 1-5 μm layer. The thickness of the layer was uneven due to the substrate's rough surface. The CP-biopolymer composite can be produced as fibres via electrospinning method (Fig. 3.18). In this case, the resulting composites consist of spider web-like entangled fibres with unevenly incorporated calcium phosphate particles. The CaP particles are embedded between the fibres.

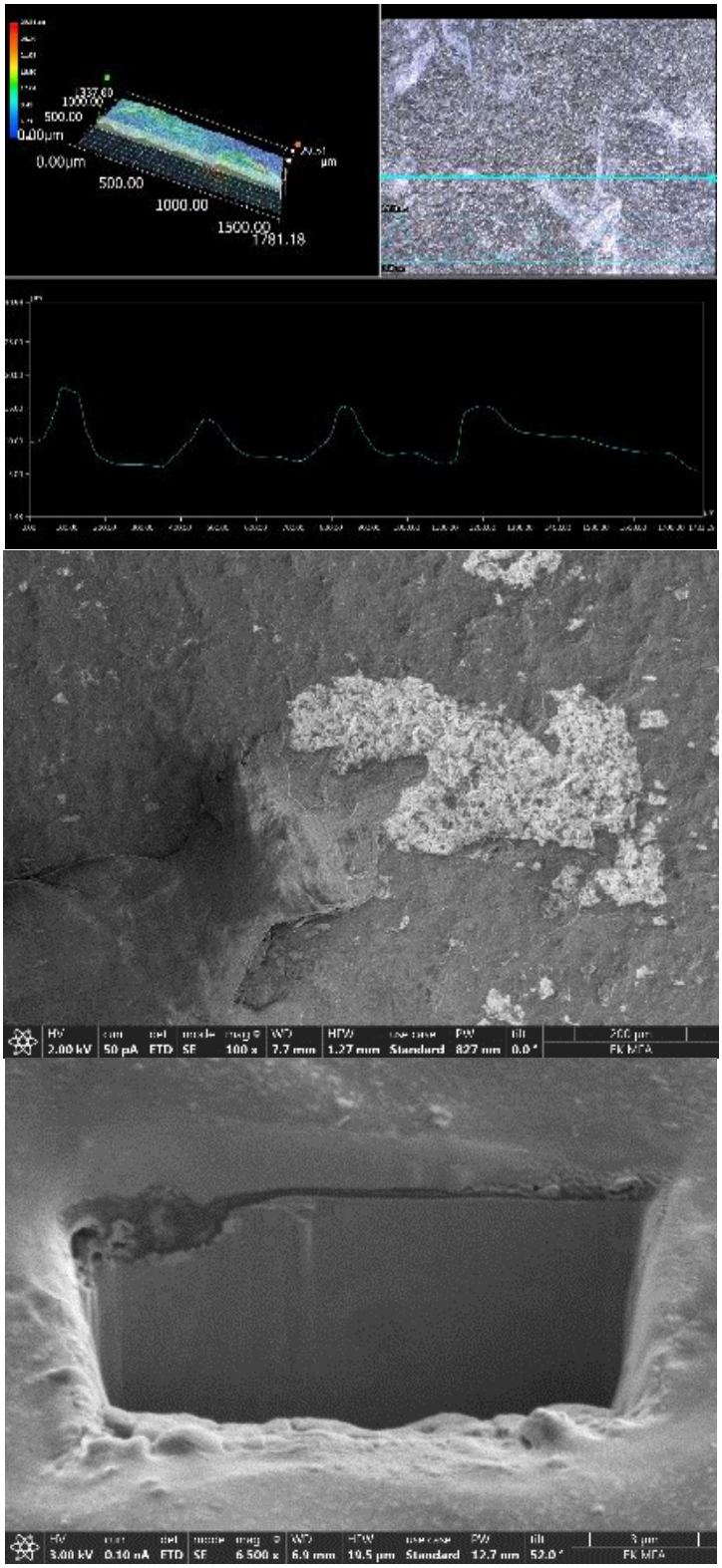

Figure 3.17. *Optical microscope and SEM images of calcium phosphate-PCL thin layer, as well as cross sectional FIB cut for thickness measurement.*

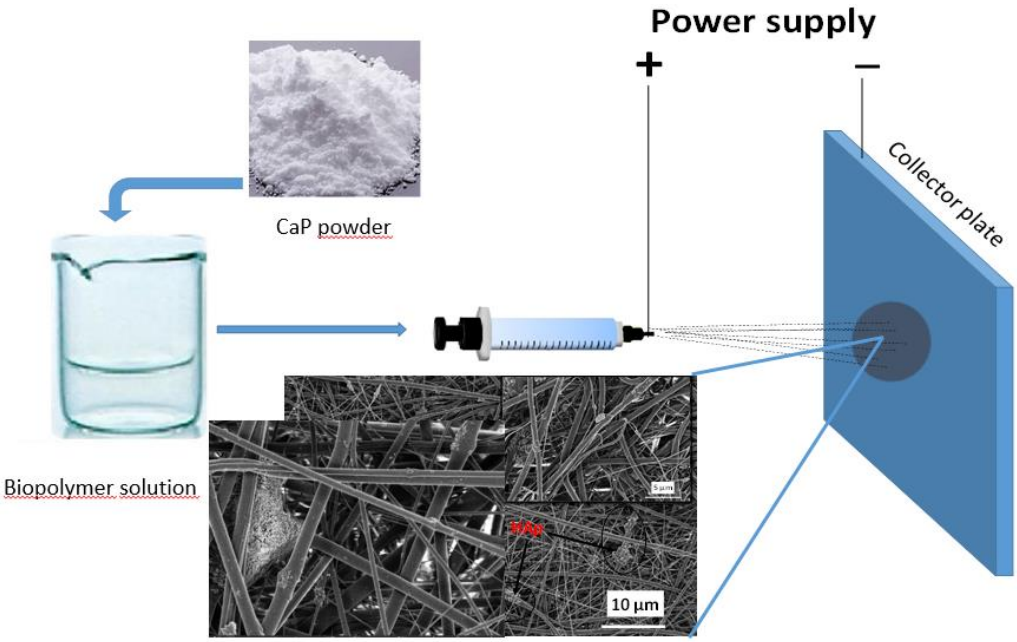

Figure 3.18. *Schematic illustration of electrospinning technique*

R+D+I development and utilization of high-performance electronic chips "CHIPCER" Phase 1

GFM - ÁFF/96/1/2023.

K. Balázsi, Cs. Balázsi, T. Kolonits, K. Hajagos-Nagy, E. Dódony, A. Jakab Fenyvesiné, B. Erki, V. Varga, A. Kovács

The Hungarian government has accepted the Ministry of Economic Development's proposal to launch an R+D+I project for chip-carrying ceramic wafers, so Hungary is also starting to enter the semiconductor manufacturing market. The project, whose partners are the Bay Zoltán Nonprofit Ltd. (PI), Neumann Ltd., Budapest Technical University (BME) and the Thin Film Physics Laboratory of HUN-REN EK MFA, started from 2024 January 1st.

Our task is to develop thin (several hundred micrometers) ceramics as a chip substrate used in the automotive industry and high-performance electronics and to facilitate their production on an industrial scale. In the first year of the project, we determined the ceramic to be tested, silicon nitride, an important parameter of which is that European suppliers provide the raw materials, thereby making the production process independent of various external influences.

All novel results are confidential.

Digitalization of Power Electronic Applications within Key Technology Value Chains

2022-1.2.8-KDT-2022-00001, Horizon Europe KDT 101096387 PowerizeD

K. Balázsi, C. Balázsi, T. Kolonits, M. Furkó, K. Hajagos-Nagy, E. Dódony, A. Fenyvesiné Jakab, V. Osváth, V. Varga, A. Kovács, B. Erki

PowerizeD is an innovative EU funded project aiming to develop breakthrough technologies of digitized and intelligent power electronics to enable sustainable and resilient energy generation, transmission and applications.The project is supported by the Chips Joint Undertaking and its members, including the top-up funding by the national Authorities of Germany, Belgium, Spain, Sweden, Netherlands, Austria, Italy, Greece, Latvia, Finland, Hungary, Romania and Switzerland, under grant agreement number 101096387. The project is co-funded by European Union.

The project focuses on improving the way energy is produced and transmitted through the use of digitized and intelligent electronic energy, which will greatly contribute to the decarbonisation of European society and the protection of our climate. *The research results so far are not yet public, professional publications can only be published after the permission of the project leader, Infineon.*

4 - Nanosensors Laboratory

Head: Dr. János VOLK, Ph.D., senior research fellow

Research Staff:

- Gábor BATTISTIG, D.Sc. (60%)
- Zsófia BAJI, Ph.D.
- Szabolcs CSONKA (20%)
- György MOLNÁR, D.Sc.
- Nguyen Quoc KHÁNH, Ph.D.
- Péter Lajos NEUMANN, PhD (50%)
- László PÓSA, Ph.D.
- Zsolt ZOLNAI, Ph.D.

Ph.D. students / Diploma workers:

- János Márk BOZORÁDI (50%)
- Roland KÖVECS, B.Sc student
- Anett SZELEDI, B.Sc student
- Tímea Nóra TÖRÖK, Ph.D. student (20%)
- Áron VÁNDORFFY, B.Sc student
- Tamás ZEFFER, PhD student (50%)

Technical Staff:

- Ferenc BRAUN, engineer
- János FERENCZ, engineer
- Levente ILLÉS, engineer
- Attila NAGY, technician
- Zoltán KOVÁCS, Ph.D. engineer

Nanosensors Laboratory was established at the beginning of 2019 from the former Department of Microtechnology. The core infrastructure, having two semiconductor clean rooms, is shared and operated together with the Microsystems Laboratory. The mission of the Lab is to utilize the emerging results of nanotechnology and materials science for novel physical sensors, particularly for micro- and nanometer sized electromechanical systems (MEMS/NEMS).

In the following sections 8 selected topics are presented, which relate to

i) characterization of functional thin films (page 72-);
ii) nano- and micrometer sized electronic and sensor devices (page 82-);
iii) novel force sensor systems (page 86-), and
iv) first steps toward Kitaev transmon generation (page 88).

These research topics are conducted mainly in the framework of three domestic projects: TKP2021-NVA-03: Environmental monitoring sensors for emergency and extreme conditions; OTKA: Atomic layer deposition and applications of functional sulfide nanolayers; OTKA: Development of Nanometer Scale Resistive Switching Memory Devices. Besides, the Nanosensors Laboratory provided electronmicroscopy services for several industrial partners (Lighttech Ltd., Technoorg Linda Ltd.), nanofabrication infrastructure for the Quantum Information National Laboratory (QNL), and was engaged in university education as well (Budapest University of Technology and Economic, University of Debrecen, and Óbuda University).

Quantification of Piezoresponse Force Microscopy for Thin Al(1-x)ScxN Film

TKP2021-NVA-03

N. Q. Khánh, L. Pósa, and J. Volk

The most common methods used to study the piezoelectric properties of thin nitride films are those that give the average value of the piezoelectric constant d_{33}, such as the direct piezoelectric Berlincourt piezometer or the inverse piezoelectric vibrometer. As the dimension of the device shrink, there is an increasing need to determine the distribution of d_{33} at the nanometer scale. Piezoresponse Force Microscopy (PFM) in principle can fulfill this demand, however, using sharp tip probe, different non-piezoelectric interfering phenomena, for example electrostatic force, flexoelectricity, substrate clamping effect, unexcited matrix material restraining effect etc., make the quantification of PFM difficult.

To overcome the aforementioned problems we have applied high spring constant (nominally 42 N/m) probe and top electrode for PFM measurement, as well as substrate clamping correction to the d_{33f} measured on $Al_{(1-x)}Sc_xN$ films prepared by pulse DC reactive ion sputtering system (VAKSIS – MiDAS). Fig. 4.1 shows the average effective d_{33f} determined from $1\mu m^2$ scans with and without Pd top electrode on AlN films having different Sc content. The use of a top electrode results in higher d_{33f} for each film, since the restraining effect of the unexcited volume around tip/sample contact is decreasing rapidly with increasing top electrode diameter, i.e. the contact perimeter to its area ratio decreases.

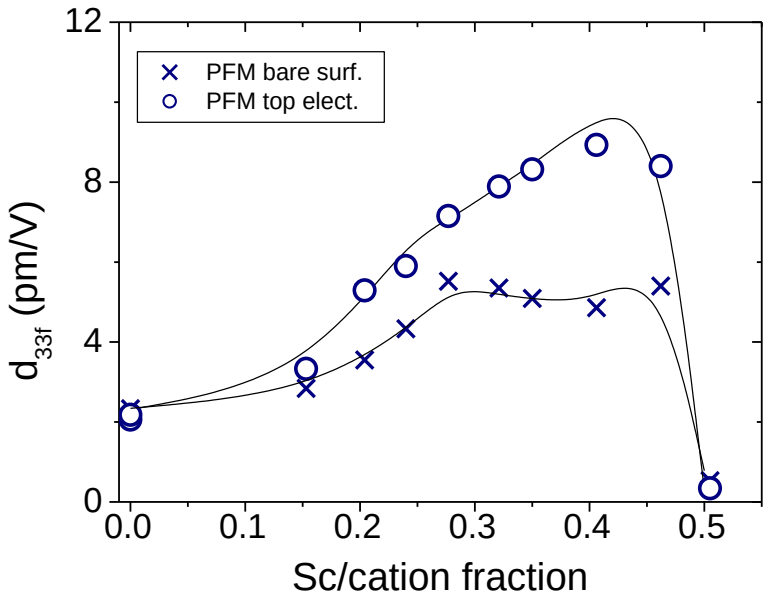

Figure 4.1. *Effective piezoelectric coefficient d_{33f} measured by PFM on bare surface and with top electrode as a function of Sc fractions in $Al_{(1-x)}Sc_xN$ film. Lines are to guide the eyes.*

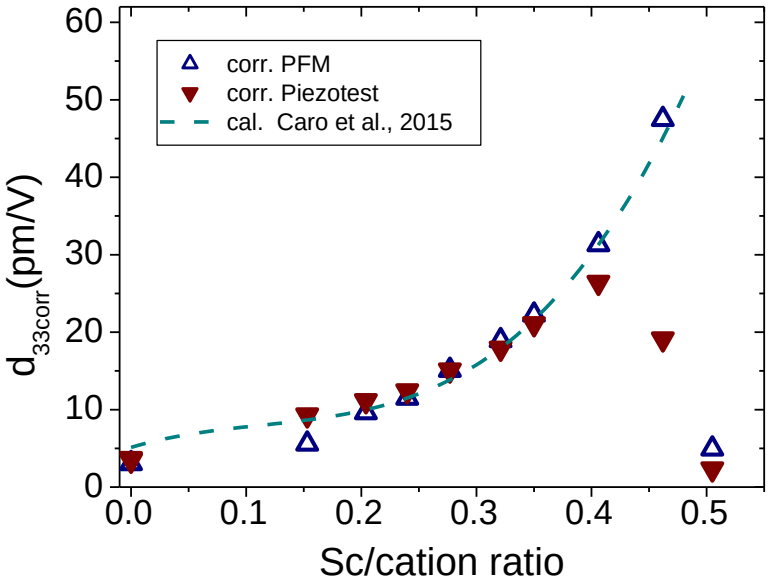

Figure 4.2. *Corrected d_{33corr} values of d_{33f} determined by PFM and Piezotest using top electrode as a function of Sc fraction in nitride film deposited at 1.5 mTorr with 60% N_2 gas ratio. The DFT calculated d_{33} is also shown.*

To obtain a more correct result (d_{33corr}), we have taken into account the effect of substrate for converse piezoelectric (*cp*) measurement,

$$d_{33corr\_cp} = \frac{d_{33f\_cp}(s_{11} + s_{12})}{(s_{11} + s_{12} + s_{13})} \qquad (1)$$

where s_{ij} are the elastic compliance constants of nitride film, and $s_{13} \sim s_{33}/2$.

We used the values of the elastic compliance constants s_{ij} calculated using density functional theory (DFT) reported in literature for substrate effect correction of the d_{33f} measured with top electrode. Fig. 4.2 shows the so corrected piezoelectric coefficients (opened triangle) determined using top electrode for films deposited at 1.5 mTorr with 60% N_2 gas ratio. The corrected d_{33corr} values are in good agreement with those obtained from the Berlincourt piezometer (closed triangle) and from the reported DFT calculation (dashed line) in the range of Sc fraction (*x*) up to ca. 0.35. At higher *x*, they differ significantly from each other. The difference may be due to the fact that pure wurtzite crystal cell was used for DFT calculation, while the piezoelectric and elastic properties of the deposited $Al_{(1-x)}Sc_xN$ films are effected by a number of factors at high *x*, such as crystal softening, formation of multi-phase etc.

For inhomogeneous sample, the corrected d_{33corr} is lower, as being an average, but using top electrode for local calibration, one can obtain d_{33corr} image from d_{33f} measured by PFM on bare film, where the correction factor is

$$d_{33corr} = \frac{d_{33fta}}{d_{33fba}} \times \frac{(s_{11} + s_{12})}{(s_{11} + s_{12} + s_{13})} \times d_{33fb}, \qquad (2)$$

where d_{33fta} is the averaged effective piezoelectric coefficient measured with top electrode, d_{33fba} and d_{33fb} are the average and individual values measured on bare nitride, respectively. The first component is the matrix effect correction, and the second one is the clamp effect correction. Fig. 4.3 shows d_{33corr} image of samples having Sc fraction of about 0.24, but deposited under different conditions, namely 2 mTorr, 30% N_2 and 1.5 mTorr, 60% N_2. One can see that 30% N_2 and 2 mTorr together result in only few areas (~ 20% of whole map) with d_{33corr} values higher than 10.5 pm/V, compared to 50% areal ratio of such high d_{33corr} in

other case. Furthermore, the fluctuation of d_{33corr} is much stronger for higher working pressure, and lower N_2 gas ratio (see the line-cut in Fig. 4.3). [Ref. 4.1]

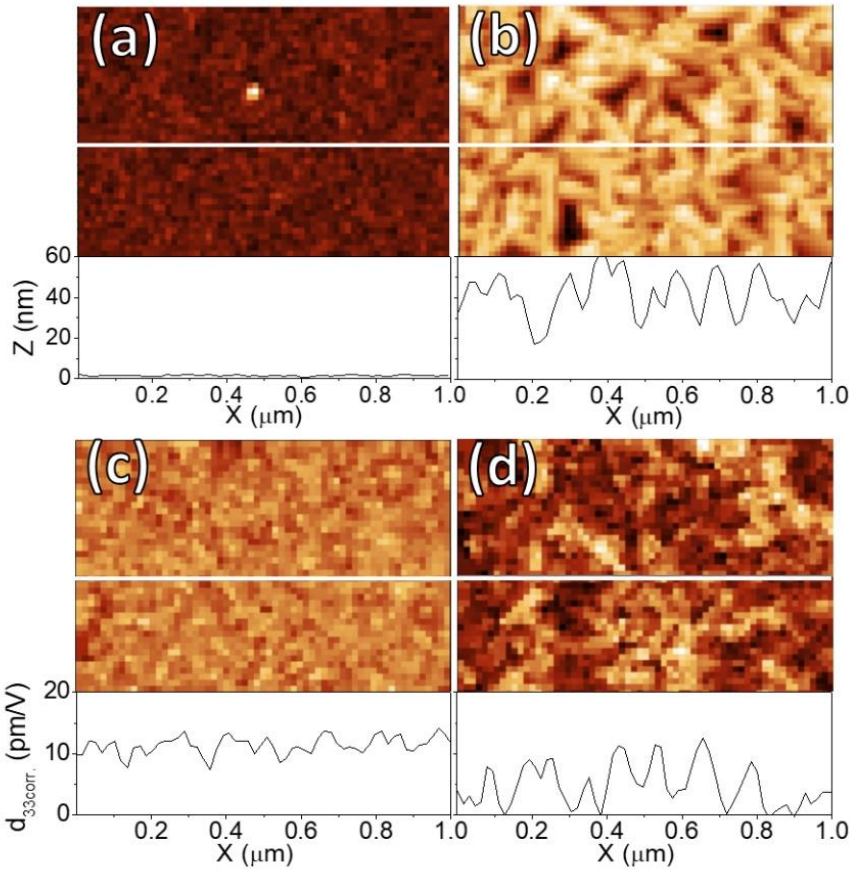

Figure 4.3. *Morphology and d_{33corr} maps of nitride film deposited at 1.5mTorr, 60% N_2 (a,c) and 2 mTorr, 30% N_2 (b, d). White lines indicate the line-cuts*

A Rutherford Backscattering/Channeling and Spectroscopic Ellipsometry study of ε-Ga_2O_3

2019-2.1.11-TÉT-2019-00066

Z. Zolnai, P. Petrik, A. Németh, J. Volk, M. Bosi, L. Seravalli, and R. Fornari

Nowadays, gallium oxide (Ga_2O_3) has become a promising candidate for a number of applications, e.g. power electronics and solar-blind UV-C detectors due to its unique intrinsic properties, such as extra-wide bandgap (E_g > 4.5 eV) and high critical breakdown field, estimated to be higher than that of SiC and GaN [Ref. 4.2]. Most scientific works to date focused on monoclinic β-Ga_2O_3, the thermodynamically stable polymorph. Nevertheless, there is an increasing interest about other polymorphs, the less explored α, γ, δ, κ, and ε phases, as they generally possess a crystallographic structure with higher symmetry and lower anisotropy compared to the β-phase. Therefore, characterization of various polymorphs and transitions between them upon thermal annealing achieved extensive scientific interest.

In this work the structure of thin Ga_2O_3 layers grown by metal–organic vapour phase epitaxy (MOVPE) at temperature of 650 °C on α-Al_2O_3 substrate has been analyzed by Rutherford Backscattering Spectrometry in combination with channeling (RBS/C) and spectroscopic ellipsometry (SE). For the as-grown Ga_2O_3 layer RBS/C angular scan curves were performed (Fig. 4.4) around the major crystallographic axis oriented nearly perpendicular to the sample surface. The measured widths ($\Psi_{1/2}$) and minimum yields (χ_{min}) of the angular scans were determined separately for the Ga and O component and were compared to calculations based on the continuum steering potential model for axial channeling.

The distinct $\Psi_{1/2}$ values of ~0.63° and ~0.38° measured for Ga and O are related to differences in average atomic numbers and average interatomic distances of the atomic rows containing Ga and O atoms along the <0001> axial channel of Ga_2O_3. In addition, the relatively high χ_{min} for oxygen (Fig. 4.4 right) can be explained by a cross-steering effect between different atomic rows with larger and smaller $\Psi_{1/2}$ values. Similar behaviour of χ_{min} has been reported for NbC and SiC crystals. The measured $\Psi_{1/2}$ and χ_{min} of the Ga and O sublattice can be correlated with a crystal structure which contains O atoms arranged in a 4H hexagonal closely packed (HCP) lattice and Ga atoms which preferentially occupy octahedral interstitial sites in the 4H cell (with estimated values of $\Psi_{1/2}$ ~0.59° for Ga and ~0.34° for O). This structure is closely related to the ε-phase of Ga_2O_3 [Ref. 4.3]. Note, significantly different $\Psi_{1/2}$ values than the measured ones can be expected for tetrahedral site occupancy of Ga in a 4H oxygen lattice and also for <-201>-oriented β-Ga_2O_3. The low channeling RBS yield for Ga (Fig. 4.4) reveals good crystalline quality of the Ga_2O_3 epilayer, however, a thin interface region is also detected (the peak in the red line around ch. 450) with somewhat different crystallographic orientation and defect/strain content compared to the epilayer on top. Nevertheless, the Al angular scan curve (Fig. 4.4) reveals good matching between the c-axis of the α-Al_2O_3 substrate and of the ε-Ga_2O_3 layer, verifying high quality epitaxial growth.

After annealing at 1000 °C, remarkable structural transformation occurs perpendicular to the sample surface as it is detected by significant changes in the RBS/C spectra (Fig. 4.5). Such effect primarily can be attributed to transition from the ε- to the β-phase in the Ga_2O_3 film [Ref. 4.4]. As SE measurements show, annealing also leads to noticeable changes in the dielectric function of the Ga_2O_3 layer, especially around the absorption edge (4.5-5 eV photon energy range in Fig. 4.5). In this case, 6h annealing with high cooling rate results in downshift of the optical absorption edge on the photon energy scale as compared to 2h annealing with low cooling rate. The observed SE trends may be related to variation of the preferred crystallographic orientation of the β-phase with respect to the Al_2O_3 substrate after annealing, and differences in residual strain and defect structure determined by the annealing conditions [Ref. 4.4].

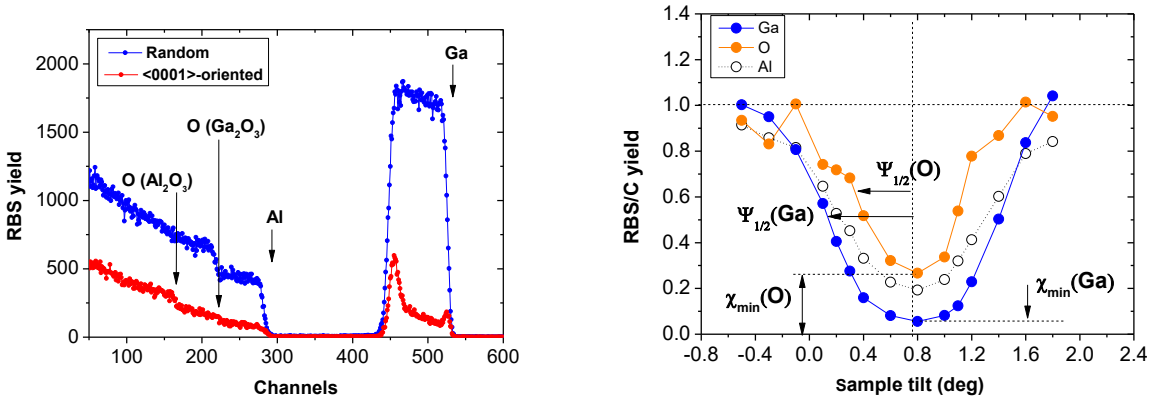

Figure 4.4 *(Left) Random and channeling 2 MeV He^+ RBS/C spectra of a <0001>-oriented ε-Ga_2O_3 layer epitaxially grown on Al_2O_3 substrate. Spectrum edges for different elements in the thin layer and in the underlying substrate are indicated. (Right) 2 MeV He^+ RBS/C angular scan curve for the Ga and O components of <0001>-oriented ε-Ga_2O_3. Critical angles for channeling, $\Psi_{1/2}$, and minimum yields, χ_{min}, are indicated. Angular yield for Al in the α-Al_2O_3 substrate is also shown for comparison.*

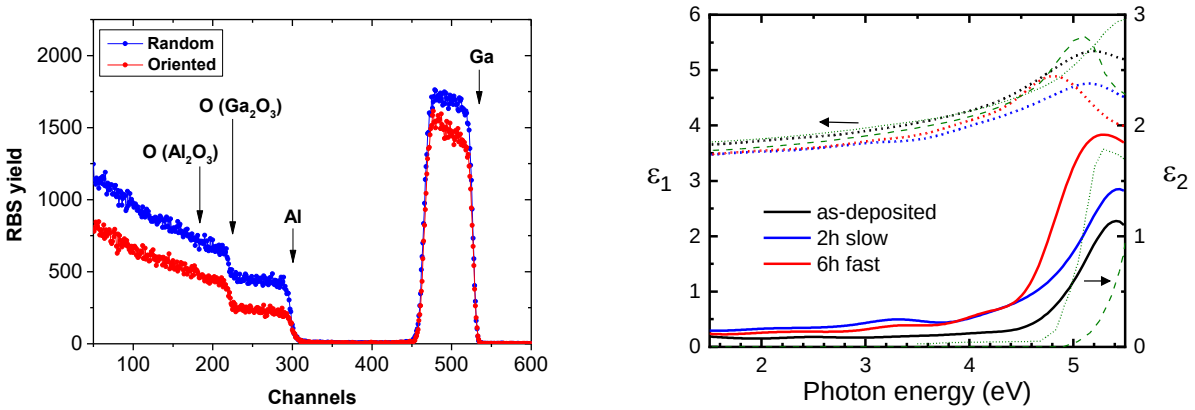

Figure 4.5 *(Left) Random and oriented 2 MeV He^+ RBS/C spectra of a Ga_2O_3 layer epitaxially grown on Al_2O_3 substrate and annealed at 1000 °C for 2h. Spectrum edges for different elements in the thin layer and in the underlying substrate are indicated. (Right) Real (ϵ_1) and imaginary (ϵ_2) parts of the dielectric functions for as-grown and post-annealed Ga_2O_3 layers measured by SE. Annealing was performed for 2h with slow and for 6h with fast cooling. Ordinary and extraordinary (short- and long-dashed green lines) dielectric functions of single-crystalline β-Ga_2O_3 from [Ref. 4.5] are also plotted for comparison.*

Our concept, based on RBS/C and SE analysis, gives the opportunity to ascertain correlations between crystal symmetry (polymorph structure), crystalline quality, interface features, and optical properties of as-grown and annealed Ga_2O_3 layers, as a function of depth on the nanoscale.

He^+ ion beam-induced luminescence from defect centers in α-Al_2O_3

OTKA K 143263, TKP2021-NVA-03

Z. Zolnai, M. K. Pal, E. Kótai*, and E. Szilágyi**
**Institute for Particle and Nuclear Physics, HUN-REN Wigner Research Centre for Physics, Budapest, Hungary*

Al_2O_3 is a promising scintillator material for energetic charged particle detection due to its luminescence in the near UV-visible spectral range emitted by optically active centers related to impurities or structural defects introduced into the wide bandgap material [Ref. 4.6]. To study and optimize scintillator-based particle detector structures, ion beam-induced luminescence (IL) is a sensitive and effective analytical method. In this work, the IL light emission of α-Al_2O_3 was induced by a 1.5-MeV He^+ ion beam and measured as a function of irradiation time (ion fluence) in the wavelength range of 200 nm - 1100 nm. We used He^+ projectiles to simulate the effect of the daughter product in the $^{10}B(n,\alpha)^7Li$ reaction, when thermal neutrons are detected via their conversion to 1.47-MeV α and 0.84-MeV Li^+ projectiles which than generate light emission in a scintillator through electronic stopping. Two prominent IL emission bands were found and recognized as the well-known F and F^+ centers [Ref. 4.7, Ref. 4.8] related to oxygen vacancy defects with two electrons and one electron captured, respectively.

For a scintillator, sufficient sensitivity and proportionality between the number of α-particles (α-flux) and the intensity of the α-induced IL emission can be achieved if the response of the scintillator is fairly intense and stable in time. In order to see the effect of initial concentration of F and F^+ centers on the IL response of Al_2O_3, both unimplanted and pre-implanted sapphire samples were measured by the IL technique. Pre-implantation was performed with 2.8-MeV energy N^+ ions in the fluence range of 5×10^{13} - 5×10^{14} N^+/cm^2, resulting in relatively high defect densities in the top 2 μm region of the α-Al_2O_3 crystal. He^+-IL experiments and N^+ ion irradiation (pre-implantation) were performed by the EG-2R Van de Graaff accelerator at the HUN-REN Wigner Research Centre for Physics in Budapest.

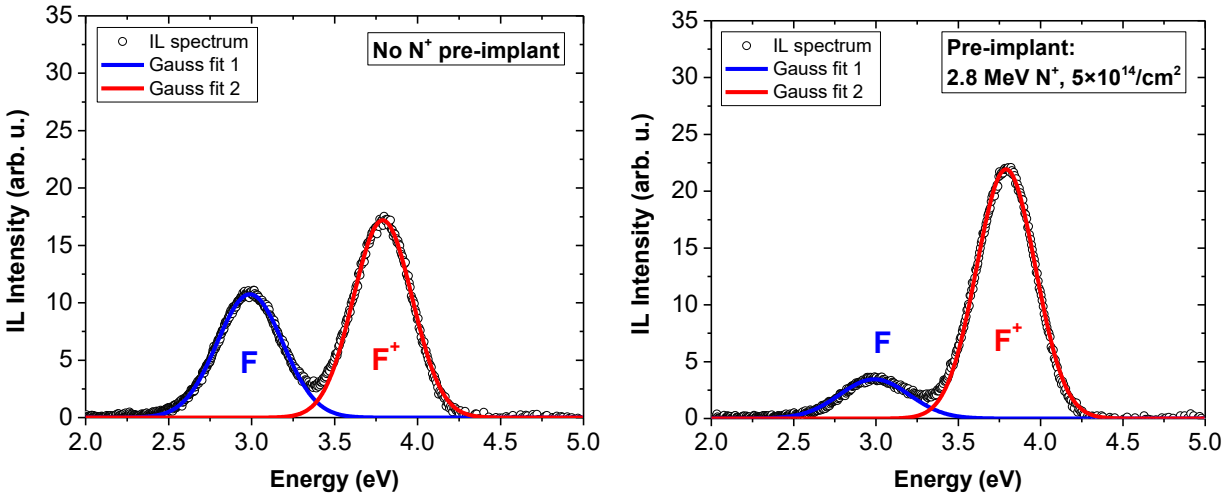

Figure 4.6 *1.5-MeV He^+ ion beam-induced luminescence (IL) spectra of the F and F^+ centers at a fluence of 1.2×10^{16} He^+/cm^2 for (left) unimplanted Al_2O_3, and for (right) Al_2O_3 pre-implanted with 2.8-MeV N^+ ions to a fluence of 5×10^{14} N^+/cm^2 before the IL measurement. Blue and red lines show Gaussian fits for the emission bands related to the F and F^+ centers.*

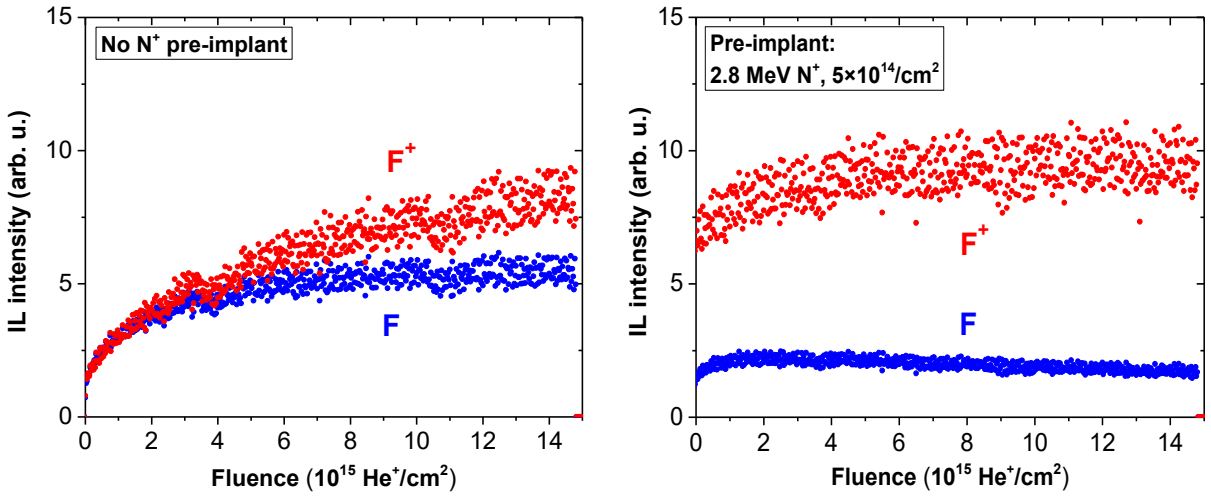

Figure 4.7. *Evolution of 1.5-MeV He^+ ion beam-induced luminescence (IL) intensity of the F and F^+ centers vs. the He^+ irradiation fluence. for (left) unimplanted Al_2O_3 and for (right) Al_2O_3 pre-implanted with 2.8-MeV N^+ ions to a fluence of 5×10^{14} N^+/cm^2 before the IL measurement.*

Fig. 4.6 shows IL spectra of α-Al_2O_3 after 1.2×10^{16} He^+/cm^2 irradiation, both without and with N^+ pre-implantation. Spectra are shown after appropriate background subtraction and intensity normalization, taking into account the instrument function along the optical detection path and the quantum efficiency of the CCD detector. Gaussian fits of the two prominent IL bands give peak positions of 2.99 eV and 3.79 eV, and full widths at half maximums (FWHM) of 0.42 eV and 0.35 eV, for the F and F^+ centers, respectively. These values agree well with previously reported ones [Ref. 4.7, Ref. 4.8]. Strikingly lower F-center related peak appears for the N^+ pre-implanted sample compared to the unimplanted one.

In Fig. 4.7, for α-Al_2O_3 without N^+ pre-implantation, the emergence of the IL peaks starts after the He^+ ion beam was switched on. At higher He^+ fluences, a sublinear increase of the F and F^+ center related IL intensity occurs. Nevertheless, for the F^+ center a monotonous intensity increase can be seen, while for the F center the IL yield saturates at a fluence of about 5×10^{15} He^+/cm^2. The increasing IL yield trends are due to He^+ ion beam-induced defects, i.e., newly generated F and F^+ centers of which concentration increases with the He^+ fluence. On the other hand, for N^+ pre-implanted Al_2O_3, relatively high F^+-center related IL appears right at the beginning of the IL experiment and the IL yield saturates already at a fluence of 4×10^{15} He^+/cm^2. No significant change, yet slight decrease for the F-center related IL can be observed. A striking difference is the more pronounced split between the IL yields of the two centers for the N^+ pre-implanted sample as compared to the unimplanted one.

In conclusion, significantly higher F^+ center related IL can be detected in the low fluence range of He^+ ion irradiation for a sapphire sample with higher defect, i.e. F^+ center concentration introduced by N^+ pre-implantation. Both for the F and F^+ center, the IL intensity vs. He^+ fluence is more stable for higher initial defect concentrations. Differences in the F^+ to F center related IL yield ratios can be due to different defect concentrations and compositions and related changes in the He^+ ion beam-induced excitation and subsequent de-excitation processes. These results can be utilized to optimize the structural properties of Al_2O_3 for charged particle detection via IL emission.

Enhancing the nucleation in atomic layer deposition: a study on vanadium sulphide and oxide layers

OTKA FK 139075

Zs. Baji, Cs. Dücső, A. Sulyok, Zs. Fogarassy, O. Hakkel

Atomic layer deposition (ALD) consists of the consecutive chemisorption and reaction of different precursor materials on a substrate surface. According to theory, in ALD, when one precursor material is introduced into the reaction chamber, it chemisorbs on the heated substrate surface and connects to the reactive surface species on it. When all the available connection sites are taken, the surface is saturated, and the remaining unreacted precursor material is cleared out of the reaction space with an inert gas, and the next precursor is lead into the chamber. Once again, this precursor only reacts with the species of the first one, which are chemically bonded to the surface, after which, another purging follows with an inert gas. Thus, the result of each ALD cycle is exactly one monolayer of the composite material, in theory. However, there are limiting factors in the ALD growth as well. Supposing, that the basic conditions are satisfied, that is, the precursor is stable at the given temperature, the surface temperature is sufficiently high to activate the required chemical reactions, and the dosing of the precursor material is enough to saturate the surface, there are still limiting factors. The saturation density of a given surface depends on the number of reactive sites for the precursor adhesion, as well as the steric hindrance of the precursor molecules. As the ALD precursors are rather large molecules, therefore, when one binds to the surface, it covers more than one connection sites, although it only connects to one. This results in a lower than one monolayer per cycle growth in a usual practical ALD deposition process.

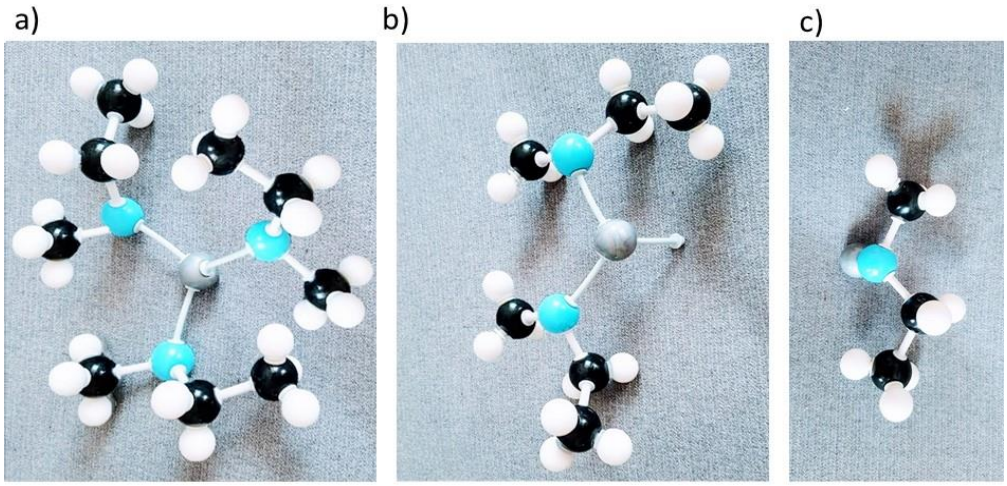

Figure 4.8. *The different connection types of the TEMAV precursor to the Si surface: single bond with 3 remaining ligands (a), double bond with two remaining ligands (b), and one remaining ligands (c) covering more than one available sites*

The other crucial hindering factor is the number of connecting sites on the surface. In a well-established layer growth, this barrier is not present, however, in the initial stages of nucleation it may cause difficulties. In most ALD processes, especially in the case of Si or sapphire substrates, the growth starts by the connection of the precursor molecule to the surface OH species. These can then act as nucleation centres for the following growth cycles.

One way to enhance the nucleation of ALD layers is to use longer precursor exposures in the first growth cycle to help the adsorption of precursor molecules to all available connection sites in the initial phase (first ALD cycle) of the growth. The other possible approach is to specially pre-treat the substrate surface in order to increase the density of the chemically active groups. In the case of oxide ALD, this means the hydroxylation of the surface. This may involve plasma or acidic pretreatment followed by dipping the sample in water to fill the broken bonds with hydroxyl groups. In the case of sulphide layers, however, the situation is more complex.

The growth of sulphide films with atomic layer deposition also starts by the chemisorption of the metallic precursor to the hydroxyl groups on the surface followed by the sulphur containing precursor pulse, which is most commonly H_2S. This means that the first monolayer of the sulphide material consists of a metallic monolayer connected on one side to oxygen, and on the other side to sulphur, and in the further growth steps, more metal-sulphide monolayers follow.

The control of the nucleation of ALD growth is crucial, on the one hand, for the purpose of research aiming at the deposition of few atomic layer thick continuous layers. In the present research the initial growth of vanadium-oxide and vanadium-sulphide was studied on different surfaces. It was found that the growth of vanadium-sulphide always starts with an island-like growth, while vanadium-oxide exhibits a layer-by layer growth on sapphire, which is a lattice matched substrate, while an island-like growth is typical on silicon. The merging of the islands can be enhanced in both cases with an extra long initial ALD cycle to leave enough time for the precursors to fill all the connection sites on the surface.

The other approach is to increase the number of available and active surface sites with chemical pre-treatments of the surface. The number of surface OH groups can be increased with oxygen plasma treatment or a piranha etching prior to ALD growth. This improved the nucleation of both materials. However, the ligand exchange processes in the case of the vanadium-sulphide growth further hinders the nucleation process. This means that the as the V-S bonds are energetically more favourable than the connection of the metal to the OH groups on the surface, the chemisorbed V atoms agglomerate into islands where they share the already connected S atoms and form V-S bonds converted from the V-O bonds. While the surface OH groups resurface, the deposition must continue in a next cycle. Therefore, it proved to be a more favourable approach to increase the OH coverage of the silicon surface, and then exchange these to surface thiol groups to initiate the growth of vanadium- sulphide. With the thiolisation of the surface and 10 long pulses the continuous coverage shown in Fig. 4.9.c and 4.9.d could be achieved, as compared to the scattered islands shown in Fig. 4.9.a and 4.9.b.

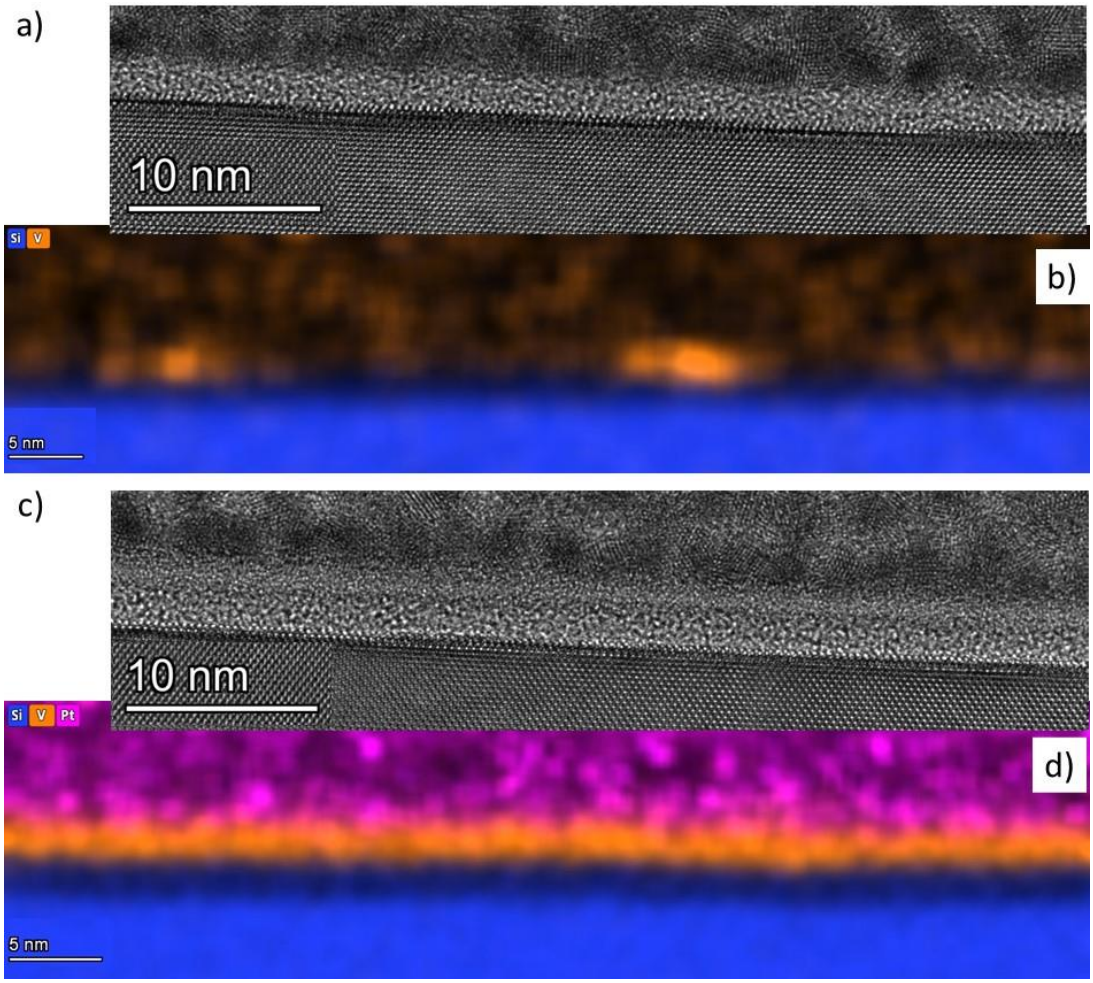

Figure 4.9. *Island like vanadium-sulphide after 5 ALD cycles (a and b), and a continuous vanadium-sulphide layer on a thiolised Si surface after 10 long cycles (c and d)*

Resistor network simulation of VO_2 nanogaps

OTKA K143282, János Bolyai Research Scholarship, ÚNKP Postdoctoral Scholarship

L. Pósa, Sebastian Werner Schmid[1], Tímea Török, Miklós Csontos[2]
[1]Department of Physics, BME, Budapest, Hungary
[2]EMPA, Dübendorf, Svájc

We employed two-dimensional resistor network model to simulate the dynamic behavior of our nanosized VO_2 device. In this concept, the active region is modelled as an array of cells arranged in a square lattice (Fig. 4.10.a). Each cell corresponds to a small, nanosized part of the VO_2 layer, in such a way that its electronic state is still well defined, which can be either insulating (I-VO_2, blue) or metallic (M-VO_2, red). To obtain more accurate results, we applied realistic contact geometry by using gold cells (Gold, yellow) in the simulation area arranged in rectangular and triangular shapes. The 20 nm large electrode separation in the real device is converted into 2 cells in the simulation, accordingly, the cell size in our model is 10x10 nm, whereas the thickness of the layer is 40 nm. Each cell consists of four identical resistors, and initially all VO_2 cells are in the insulating OFF state. In analogy to the experimental setup, a load resistor (R_L) is connected in series with the resistor network and the waveform generator.

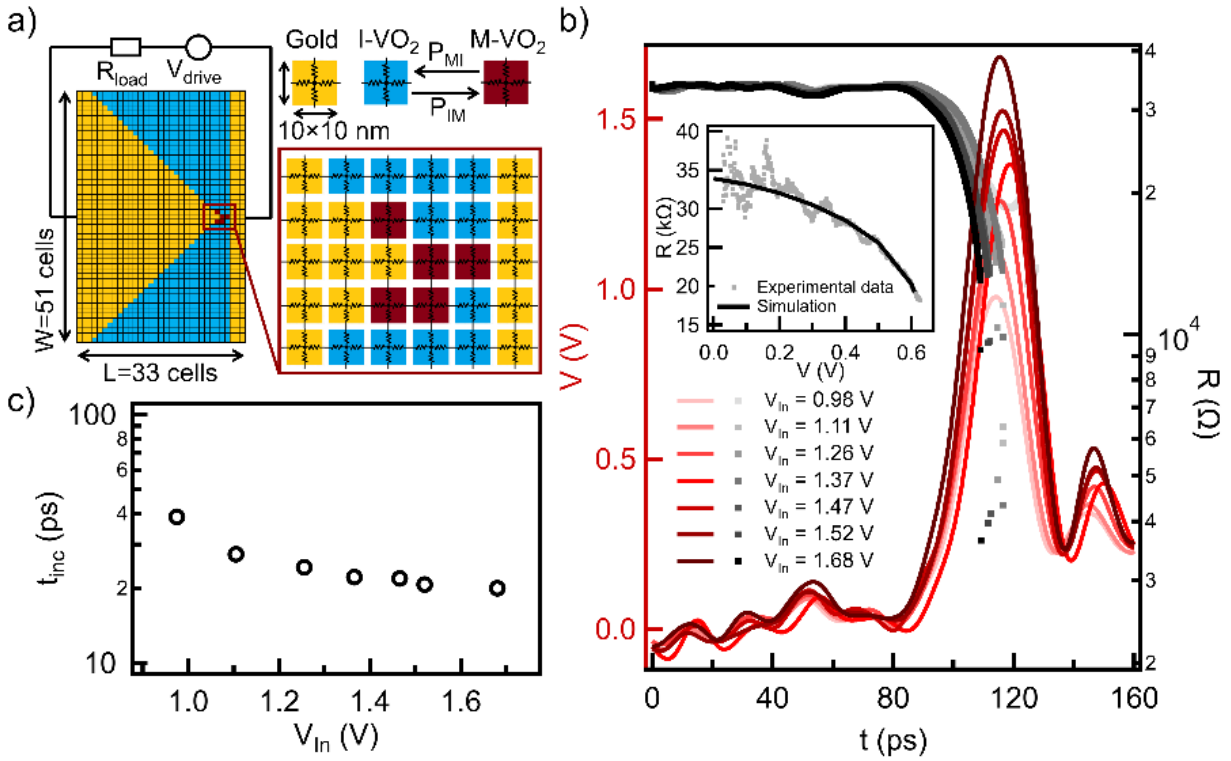

Figure 4.10. *(a) Schematic diagram of the resistor network model and the electrical circuit. The cells in yellow correspond to the gold electrodes with very low resistivity. Cells in blue and red represent the 40 nm thick VO_2 layer, which is in thermal contact with an electrically perfectly insulating substrate. These cells can be either in the insulating (blue) or metallic (red) phases, the dynamics of the transformation between the two states is determined by the transition probability of P_{IM} and P_{MI}. (b) The experimentally applied waveforms (red curves) and the resistance answer of the resistor network (grey dots). At the moment of the set transition the resistance suddenly jumps several orders of magnitude. The different shades of red and grey corresponds to the different voltage amplitudes. The inset shows the experimentally captured R(V) curve of the device in the high resistance state (grey dots) and its fit by the simulation (black curve). c) The simulated incubation time versus driving voltage amplitude, showing good agreement with the experimental data.*

The electrothermal model of the resistor network simulation is based on our previous finite element simulation in COMSOL Multiphysics [Ref. 4.9], applied to the high resistance state of a similar VO_2 phase change memory device. The resistance of a single resistor of an I-VO_2 cell depends on both the local temperature and the local electric field, whereas in the ON state, we assumed temperature and electric field independent resistance. However, the device operation was only modelled until the moment of the set transition, therefore the electrical and thermal parameters of the ON state do not affect the outcome of the simulation.

In our model, the phase transition is a thermally activated process, in which the transition probabilities of the cells (P_{IM} and P_{MI}) depend exponentially on the temperature. The local temperature is determined from the heat equation considering the positive contribution of Joule-heating and the negative contribution of the heat conduction to the neighboring cell and to the substrate. Furthermore, a boundary thermal resistance was considered between the VO_2 and the gold cells.

The electrical and thermal material properties of the VO_2 layer were determined by fitting the experimental R(V) trace of the device by the simulation, see inset of Fig. 4.10.b. After setting the device-specific parameters, the experimentally realized voltage signals (red curves in Fig. 4.10.b) could be applied to the resistor network. The model was solved by using 0.1 ps long time steps. The grey curves in Fig. 4.10.b show the evolution of device resistance in time. In all cases, the phase transition can be captured by the sudden jump of the device resistance, and, in agreement with the experiment, it occurs earlier as the voltage amplitude is increased. To study this trend quantitatively, we determined the incubation time using the same method as for the experimental data, calculated from the moment when the incoming pulse reaches 10% of its maximum until the resistance jump. The simulated incubation times (Fig. 4.10.c) fall to the same 10-50 ps regime as our experimental observation with a similar decreasing tendency with the pulse amplitude [Ref. 4.10].

AlGaN/GaN heterostructure based frequency selective vibration sensor

TKP2021-NVA-03

P.L. Neumann, Á.J. Vándorffy, J. Ferencz, J. Volk

GaN, as a piezoelectric, piezoresistive, and pyroelectric wide-bandgap semiconductor, can be a key material for the new generation of power electronics and micro- and nanoelectromechanical systems (MEMS, NEMS). While commercial Si-based sensors show limited applicability in the field of human bioimplants due to their low interaction rate with the body, GaN shows excellent biocompatibility [Ref. 4.11]. Beyond its outstanding behaviour, epitaxial thin compound-alloy layers are already commercially available on Si carrier wafers, which are technologically compatible with standard Si MEMS processes. However, in contrast to conventional Si piezoresistive devices here, the mechanical strain influences the density of the 2-dimensional electron-gas (2DEG) at the AlGaN/GaN interface by changing the magnitude of polarisation vector discontinuity [Ref. 4.12]. Here, we present a novel AlGaN/GaN heterostructure-based resonant cantilevers for frequency-selective vibration analysis, which can offer a new solution for fully implantable cochlear implants. The external mechanical vibrations generated, e.g., by the middle ear's eardrum, can be converted into electrical signals. Hence, the magnitude and the frequency of the vibration can be determined.

The 2DEG sensor elements were fabricated on a commercial high-electron-mobility transistor (HEMT) epilayer stack (GaN/AlGaN/GaN) grown onto a 4" Si wafer (NTT-AT). Meander-shaped MESA structures were formed at the eigenfrequency-related locations (antinodes) and at the anchoring position of the beam, where the strain in the thin beam layer is the highest. The desired locations were determined by finite element analysis using Comsol Multiphysics (Fig. 4.11.a). The carrier Si layer was etched back by a deep reactive etching step, while the final cantilever tailoring was done by focused ion beam (Fig. 4.11.b). The metal electrodes were prepared by e-beam evaporation and a subsequent rapid thermal annealing (RTA) step for Ohmic contacts. The significant built-in stress causes the cantilever to bend after release.

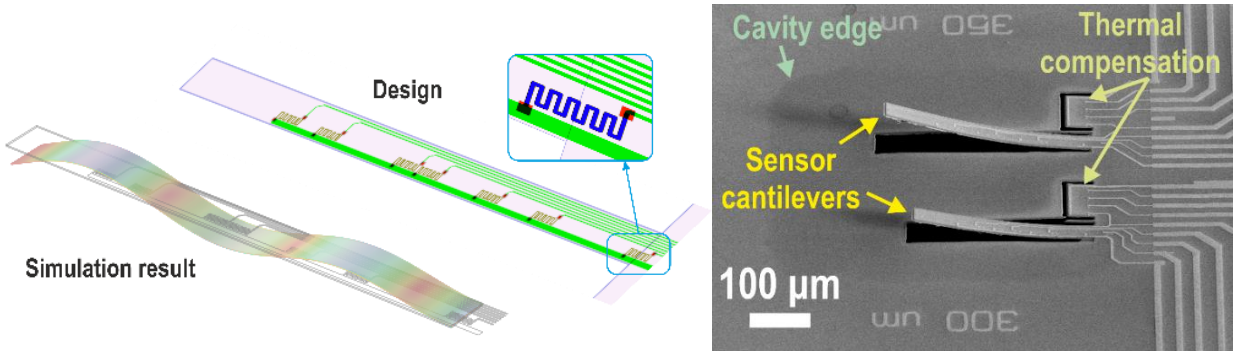

Figure 4.11. *Schematic (top) and dynamic simulation (below) of the AlGaN/GaN beam (450 µm long) with the MESA meander sensor elements in the antinode positions (a-left). SEM image of the 350 µm and 300 µm long compound semiconductor beams with the resistive meanders (b-right) Thermal compensation beams were fabricated using the same meander elements.*

During the previous study as a force sensor experiment, a continuous base signal moving was observed on sensor elements. Analysis of the problem at IV curves of sensor elements on membrane and on bulk show different behaviour because the membrane sensor meander increased the resistance instead of above bulk, which was linear. It can be ascribed to thermal effect: though the thermal resistivity is almost the same for Si and for GaN, heat channel is significantly shallower for the cantilever (1.2 vs. 400 um). To eliminate the self-heating problem, thermal compensation was applied using a subsidiary beam. All sensor elements and

the equivalent value reference resistors set the exact temperature dependence behaviour for the sensor device.

The vibration modes of the cantilevers were analysed using a scanning vibrometer (SmarAct PicoScale) confirming the frequency selectivity of the fabricated cantilevers. The obtained resonances agreed well with the FEA results (Fig. 4.12.a). As expected, the resistance changes due to externally induced static stress in the layer showed linear dependence. This was followed by electrical tests using a source-measure-unit (SMU) to study the self-heating effect and the effect of thermal compensation. Finally, dynamic electromechanical tests were performed on the wire-bonded dies (Fig. 4.12.b) to study the sensitivity and frequency-tunability of the sensor. Besides the results of dynamic electromechanical tests, the role of the composition of the AlxGa1-xN barrier layer, the length and position of the sensitive channel, as well as the thermal stability of the heterostructure sensor will also be addressed.

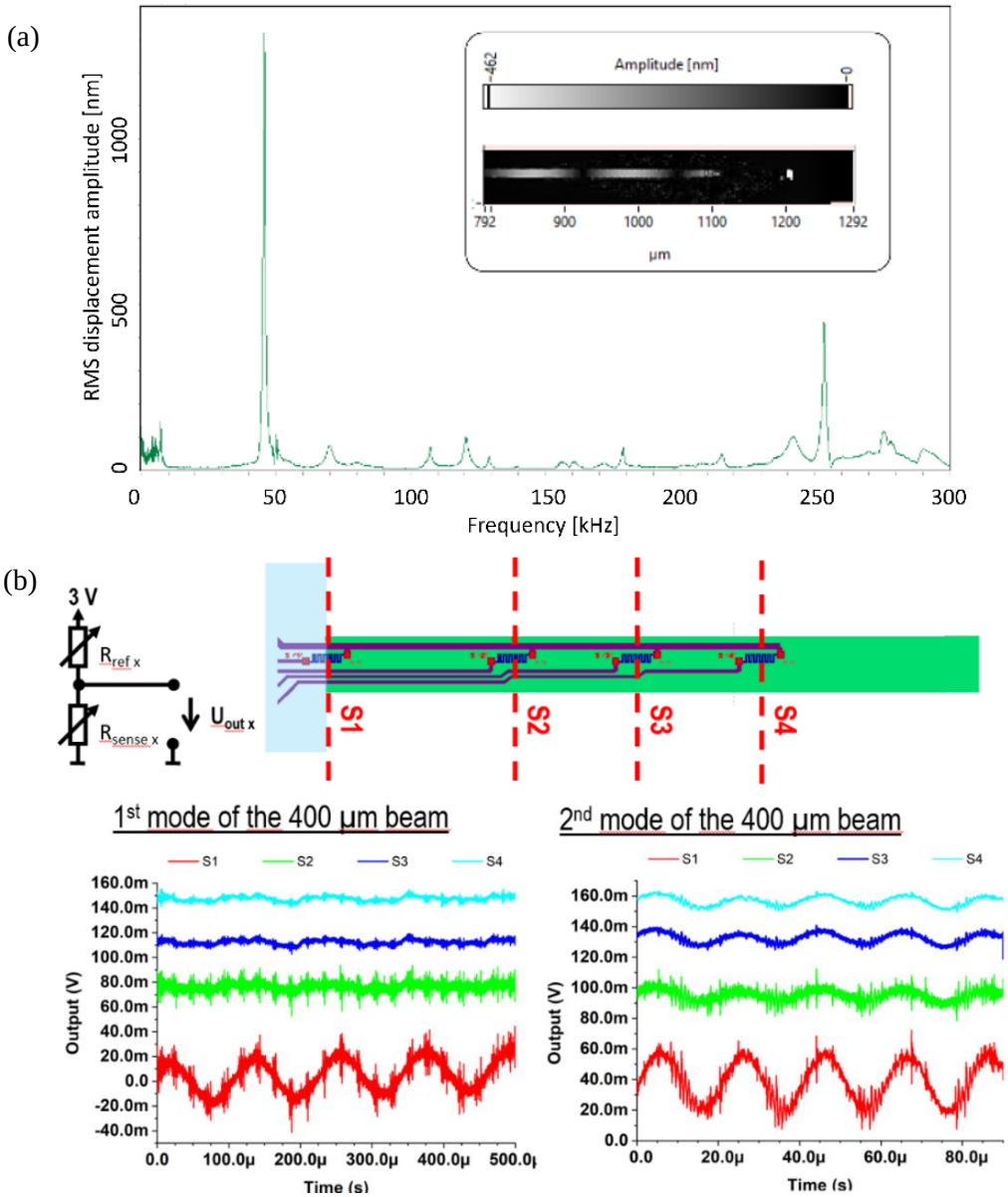

Figure 4.12. *Frequency analysis of a 450 μm beam by scanning vibrometer (a-top). The inset shows the amplitude response for external excitation at one resonance frequency. The output voltages are of the voltage dividers during shaking at the resonance frequencies (b-bottoms). The output voltage characteristics reflects well the position of the meanders on the cantilever.*

Smart scalpel – a novel force-sensor-based surgery hand tool

TKP2021-NVA-03

J.M. Bozorádi, A. Nagy, F. Braun, L. Illés, P. Révész, J. Volk*
**Department of Otorhinolaryngology-Head and Neck Surgery, University of Pécs, Hungary*

In 2022 we carried out experiments on various ex-vivo samples at the Clinic of the University of Pécs. Our goal was to determine the rupture force necessary to cut the chorda tympani, also known as the taste sensing nerve. This small part of the human ear is very easily damaged during surgeries related to otosclerosis and other illnesses. Development of equipment used in this area could greatly benefit from the results. During the earlier tests we suspected that neither micro manipulation, nor traditional tissue testing methods (such as axial and indentation testing) will be suitable for this particular tissue. In early 2023 we carried out an in-situ measurement technique utilizing handheld electronics developed according to the needs of medical professionals. A new UV hardened polymer covering was also developed for the 3 dimensionally sensitive force sensor placed in the scalpels' tip. Last year we reported that the estimated force necessary to cut the chorda tympani could be as high as 1.77 N. Our recent findings from in situ measurements on human cadavers elaborate on this. (Tissue tests were conducted under ethical authorization 8733 – PTE 2023.)

Figure 4.13. *"Smart scalpel" surgical force measurement tool: head and electronics with covering*

The electronics and its coverings were specified with the ergonomics for the surgeon and its application during actual surgical procedures in mind. The tip itself was also designed for easy handling during surgical conditions. The Bluetooth Low Energy circuit ran from a fast chargeable super capacitor which provided about an hour of continuous use. Calibration of the sensor heads were done via reference force gauge both during sensor development and on-site by the surgeon's movements. Readout and data acquisition still run on a laptop using a LabView VI, however we have started the development of an Android based version. Sample preparation consisted of the normal surgical procedure done by the surgeon. After lifting the eardrum to make the inner ear and the chorda tympani accessible, a total number of 10 measurements were performed with varying results. In five cases we measured similar tear characteristics to the in vitro samples. The surgeon concluded that these cuts were not characteristic of the rupture phenomena that occurs during surgery. However, he confirmed that even this – with a load of 300-500mN – is sufficient to damage the structure of the chorda tympani. On the other hand, cuts were deemed appropriate by the surgeon are uncertain as to the value of the tensile force. The measured values are magnitudes higher than what the

sensor could theoretically withstand. The two possible explanations are either measurement error, or that the needle tip was hit to the wall of the inner ear. However, if we look at the force characteristics right before the spikes, we see a similar magnitude as with previous measurements, which further proves that a force as low as a few hundred millinewtons are enough to rupture such sensitive tissue of the human body.

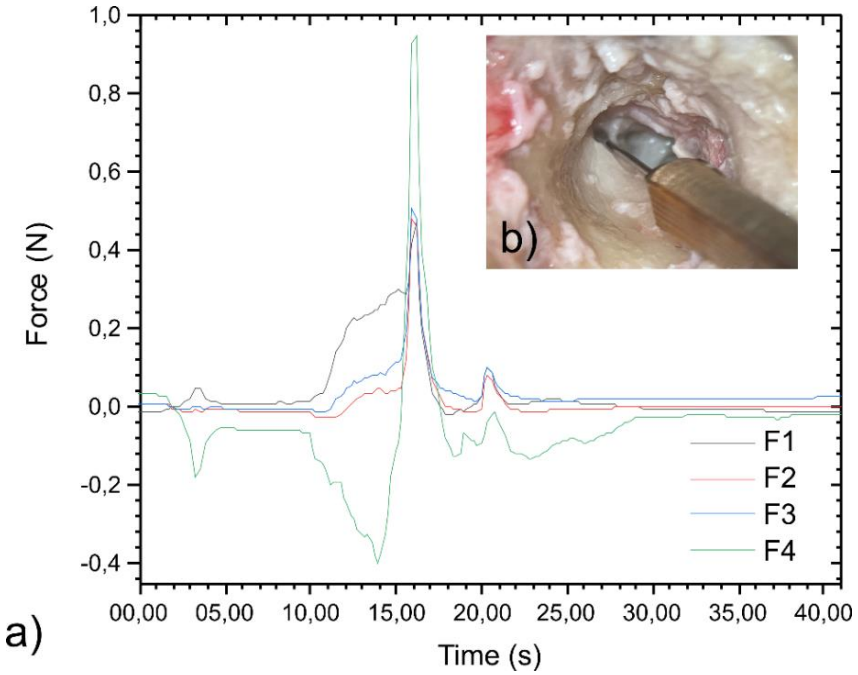

Figure 4.14. *Force sensor signals recorded during a chorda tympani rupture test (a). Photo of the smart scalpel in operation (b).*

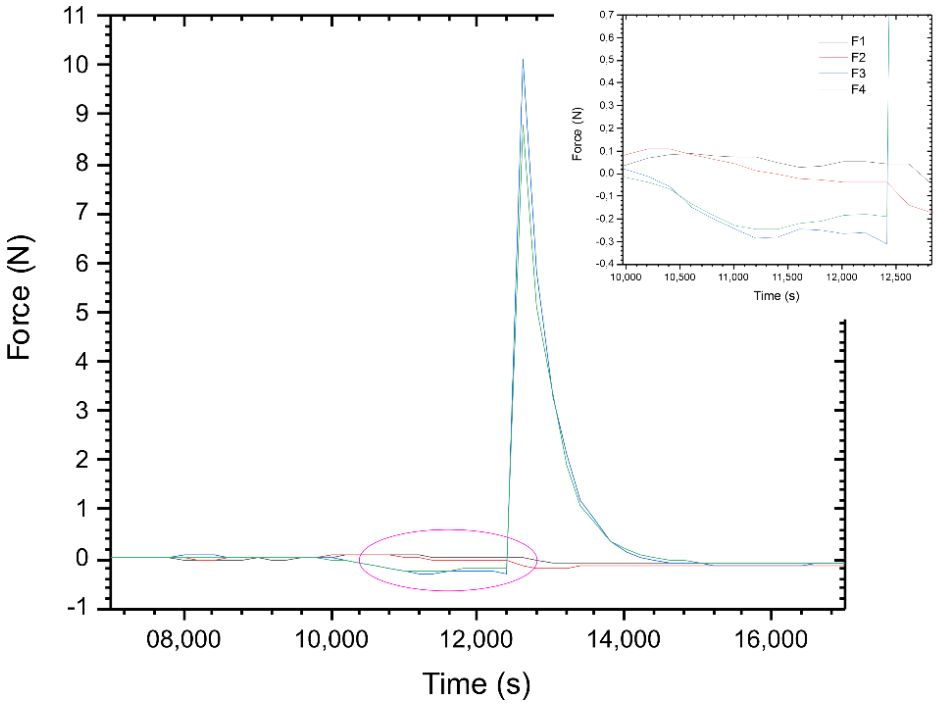

Figure 4.15. *Pulsed rupture characteristics of the so called "perfect cut"*

First steps toward Kitaev transmon generation

Quantum bits with Kitaev Transmons (QuKIT)
HORIZON-EIC-2022-PATHFINDERCHALLENGES-01-06-101115315

M. Sütő, Z. Kovács. P. Makk*, Sz. Csonka**
**in collaboration with the Department of Physics, BME, Budapest, Hungary*

While quantum computing promises algorithms that are orders of magnitude faster than what is achievable by normal computers, the physical realization of such systems is highly challenging. One of the most dominant obstacles is their sensitivity to noise, which strongly limits their current viability. Joining the QuKIT international collaboration, we aim to create a system capable of accommodating a fault tolerant quantum bits by combining the well-established and controllable transmon qubit with a Kitaev chain. It introduces topological protection (Fig. 4.16.a) to significantly enhance their tolerance to external noise. While creating a transmon qubit is a well-established process requiring a high quality superconducting thin film, the challenge of the proposal coming from the other two parts: the realization of the Kitaev chain, and the coupling of the two systems. Our part in the collaboration is related to both challenges.

To realize topological superconductivity required for the Kitaev chain, we use an InAs based near surface (7 nm below surface) two-dimensional electron gas (2DEG), which is contacted by an epitaxially grown aluminum layer. This introduces proximity superconductivity into the semiconductor through their high-quality interfaces. The heterostructure is shown in Fig 4.16.b. Our primary goal is to realize a minimal Kitaev chain, for which the first step would be a simple quantum dot, that later can be expanded to create Andreev molecules (two dots coupled by a superconducting lead), then the Kitaev chain itself. The fabrication of the devices has already started (Fig. 4.16.c). Here the Al layer is removed from the surface, which is then covered by AlO_x thin film. Afterwards we created two sets of gate electrodes, to form the qdot, which electrodes are shown in the SEM image. While in its current form it is only capable of hosting a single quantum dot, the design is highly scalable, and the fabrication steps are basically unchanged. Our aim is to measure a quantum dot this spring, and in the meantime optimize the aluminum's chemical etching, to create a qdot-SC-qdot device, achieving half of a minimal Kitaev chain.

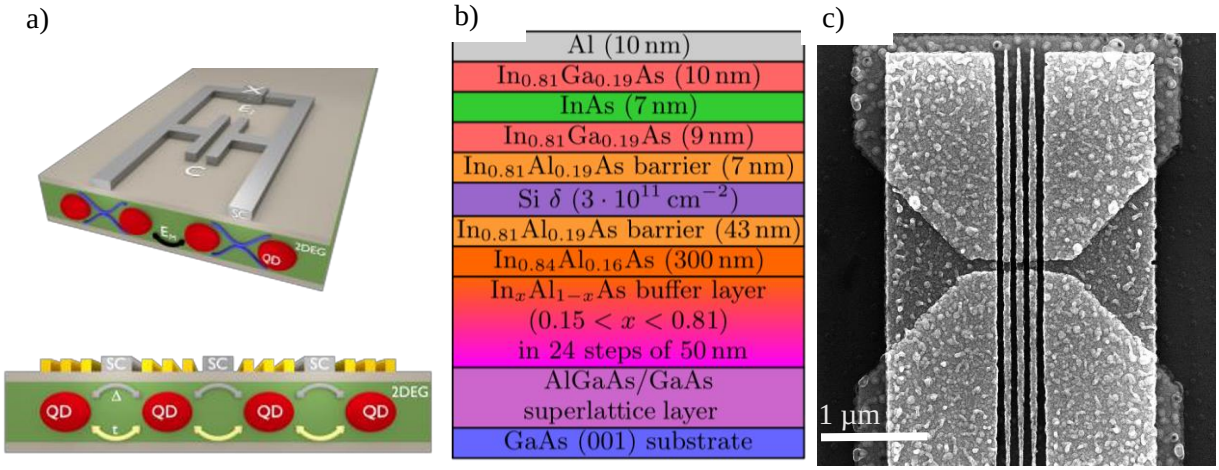

Figure 4.16. *Schematics of the novel Andreev qubit formed by coupling a traditional transmon to a minimal Kitaev chain (a) (source: QUKIT Proposal Part B). A great candidate for the realization of the Kitaev qubit: near surface InAs 2DEG contacted by an epitaxial Al layer (b). One of our early attempts to fabricate gate electrodes necessary for a simple quantum dot, that is scalable to create Andreev molecules and eventually a minimal Kitaev chain (c).*

5 - Microsystems Laboratory

Head: Dr. Péter FÜRJES, Ph.D., senior research fellow

Researchers:

- István BÁRSONY, member of HAS
- Orsolya BÁLINT-HAKKEL, Ph.D.
- Barbara BEILER, Ph.D.
- Ferenc BÍRÓ, Ph.D.
- Csaba DÜCSŐ, Ph.D.
- Péter FÖLDESY, Ph.D.
- András FÜREDI, PhD., MSCA fellow
- Péter FÜRJES, Ph.D.
- Eszter Leelőssyné TÓTH Ph.D.
- Zoltán SZABÓ, PhD.
- Zsófia Sztyéhlikné BÉRCES, Ph.D.

Engineers / technicians:

- Gabriella BÍRÓ, technician
- Tibor CSARNAI, electrical engineer
- Magda ERŐS, technician
- Róbert HODOVÁN, mechatronic engineer
- István LACZKOVICS, technician
- Csaba LÁZÁR, electrical engineer
- Margit PAJER, technician
- Zsuzsanna Brigitta SIK, bioengineer

PhD Students:

- Anita BÁNYAI (ÓE Univ. Óbuda)
- Lilia BATÓ (ÓE Univ. Óbuda)
- Dóra BERECZKI (ÓE Univ. Óbuda)
- János Márk BOZORÁDI (ÓE Univ. Óbuda)
- Zsombor SZOMOR (ÓE Univ. Óbuda)

The main goal of the Microsystems Laboratory is to research and develop integrated sensors and sensor systems, MEMS and BioMEMS devices fabricated by silicon or polymer micro- and nanomachining technology. The activity covers the characterisation of materials, microsystems, development of technology solutions and sensing principles. The application of micromachining technology enables the miniaturisation of sensing and analytical systems and integration of various functions of sample preparation, sensing, readout, actuation or communication. The laboratory is focusing on the development of mechanical, physical, chemical (and biochemical) sensors, functional micro- and nanofluidic devices, implantable microsystems and infrared LED.

Our medium-term goal is to broaden the spectra of perspective research topics of MEMS systems and to develop a systematic organisation by forming a dynamic and growing research group in the Microsystems Laboratory. Considering the financial environment our research directions fit to the European and Hungarian strategic roadmaps and directives (S3 - National Smart Specialisation Strategy) by the following research topics:

Health	*BioMEMS, microfluidic, Lab-on-a-Chip (LoC), Organ-on-a-Chip (OoC) systems, Point-of-Care (POC) diagnostics, therapeutic drug monitoring (TDM), personal medicine, implantable, wearable devices, continuous monitoring,*
Cutting-edge technologies	*driving safety sensors, human-machine interaction and cooperation – sensors for robotics, sensors for space technologies – microfluidic systems and biosensors, novel materials and manufacturing technologies: advanced materials, nanotechnologies, 3D manufacturing, AI based signal and data processing,*
Energy, climate	*sensors for energy industry, characterisation photovoltaic systems, gas sensors (smart home, smart clothes), low consumption electronics,*
Agrifood	*environment safety sensors (water monitoring), food safety sensors, spectroscopy*

Research group structure in the Microsystems Laboratory

The development of MEMS devices requires solid design capacity and advanced cooperation among the research and technical staffs for precise operation of the full micromachining fabrication line. Actually, 11 researchers, 5 PhD students, 4 engineers and 4 technicians work for the Laboratory with close and flexible cooperation with the colleagues of the Nanosensors Laboratory.

- **MEMS / smart sensors (Csaba Dücső, Ferenc Bíró):** The team's primary expertise is traditional MEMS sensor development, such as gas, environmental and mechanical sensors with an emphasis on the technology of 3D microstructure implementation.
- **BioMEMS, integrated systems for medical applications (Péter Fürjes, János Márk Bozorádi, Zsófia Sztyéhlikné Bérces, Csaba Dücső):** Silicon based sensor development and their electro-mechanical integration, specifically for medical applications, are the long-term goals in this topic. The medical field demands the development of tools in low numbers that have extensive added value, which also aligns with the European strategic directives. The topic includes research and development Si and flexible integrated microstructures for Minimal Invasive Surgery or brain research also.
- **Lab-on-a-Chip / Organ-on-Chip systems (Péter Fürjes, Anita Bányai, Lilia Bató, Dóra Bereczki, András Füredi, Orsolya Hakkel, Zsuzsanna Brigitta Sik, Zsombor Szomor):** The Lab-on-a-Chip and Organ-on-Chip systems are essential building blocks of Point-of-Care diagnostic and drug analytical tools in the medical field. We have vast experience in this topic, especially in microfluidics. Accordingly, we actively collaborate with companies, research institutes and universities in this field (77 Elektronika Ltd., Aedus Space Ltd., Budapest University of Technology and Economics, Micronit B.V., Microfluidic ChipShop GmbH, University of Pécs) as well.
- **IRLED (Zoltán Szabó, Barbara Beiler, Ferenc Bíró):** The team develops and manufactures special infrared LEDs (partners: Anton Paar GmbH, Senop OY). Additionally, we envisaged a larger scope spectroscopic development and application in the frame of actual KDT/CHIPS JU grant. Environmental analytics and food safety applications are also important goals for IR spectroscopy and other optical developments.
- **Technology and FEM Modelling (Eszter Leelőssyné Tóth, Zsombor Szomor):** Modelling, such as digital twin, is a widely applied method in engineering practice. It speeds up development and manufacturing of prototypes while also lowering costs. The application of these methods regarding the development of microstructures is challenging due to the physical effects of microenvironments. However, the use of these simulations is indispensable. The group is effectively corroborating the research and development tasks.

Infrastructure and technological competencies

The Laboratory operates a unique infrastructure in Hungary, therefore its sustainable operation and development is a strategic goal. The infrastructure is open for academic and industrial partners to fabricate (and to characterise) complex, purpose-designed microsystems, nanocircuits, as well as Lab-on-a-Chip devices and to develop their technology solutions.

The high-tech microtechnology related fabrication and characterisation systems work in a class 10 cleanroom facility. The laboratory is dedicated for 3D processing of 4" Si / glass / polymer substrates with maximal resolution of 1µm, together with lithographic mask manufacturing. Electron beam lithography and focused ion beam (FIB) milling are also available with resolution of 20nm. Multi-domain Finite-Element Modelling (FEM), and process simulation also support the structural design and development. Wide spectra of characterisation techniques are also available: optical (fluorescent) and electron microscopy (SEM and EDS), atomic force microscopy (AFM), profilometry, optical and electrical measurements, electrochemical impedance spectroscopy, microfluidic characterisation, mechanical vibration and climate test chambers, UV-Vis / IR / FTIR / FLUORESCENT / RAMAN spectroscopy, etc.

Available micromachining techniques:

- Patterning – mask design, laser pattern generator, photolithography, (double side) alignment, electron beam lithography (E-Beam), Focused Ion Beam processing – FIB milling, nanoimprinting
- Structured polymer layers – PMMA, PI, SU8 patterning, micromoulding, soft lithography – PDMS, hot embossing technique for polymers
- Wet chemistry – chemical wafer cleaning, isotropic and anisotropic etching techniques
- Dry chemistry – deep reactive ion etching, plasma etching techniques (DRIE, RIE)
- High temperature processes – thermal oxidation, diffusion, annealing, rapid thermal annealing (RTA)
- Physical thin film depositions – Thermal and electron beam evaporation, DC and RF Sputtering
- Chemical thin film depositions – Atmospheric and Low Pressure Chemical Vapour Deposition (CVD, LPCVD, LTO), thermal and plasma enhanced Atomic Layer Deposition (ALD)
- Liquid Phase Epitaxy of III-V compound semiconductors (LED manufacturing)
- Wafer bonding – Si-glass, glass-glass, polymer-glass anodic and thermal bonding
- Chip dicing, wire bonding especially for sensor applications
- Special packaging techniques and methods
- 3D printing and CNC milling for application-specific polymer packages or microfluidic structures

Cooperations

Apart from the European and bilateral international R&D projects wide cooperative and knowledge network was established by the large number of joint research projects with Hungarian universities and research centres (BME, DE, ÓE, PPKE, PTE, SE, HUN-REN ATOMKI, HUN-REN SZBK, HUN-REN WIGNER, HUN-REN TTK, HUN-REN SZTAKI) or research groups to perform interdisciplinary research. We were and are supporting the National Quantum Technology Programme (HunQuTech), the National Brain Programme and National Laboratory on Human Reproduction Programme by our infrastructural background. Besides the scientific projects, the Lab offers technology development services for several industrial partners (77 Elektronika Ltd., Aedus Space Ltd., Anton Paar GmbH (Austria), Bay Zoltán Ltd. for Appl. Res., Mirrotron Ltd., Semilab Inc., Senop O.Y. (Finland), Z-Microsystems GmbH (Austria)) to support their developments or achieve higher technology readiness levels in our projects (TRL 2 → 6).

The technological and scientific results are directly transferred into the higher education, by means of several lectures, laboratory practices, TDK, diploma and PhD works. Our researchers give lectures at various departments of BME, DE, ELTE, PPKE, ÓE, SZE and TalTech (Estonia).

Major research projects

The researchers of the Microsystems and Nanosensors Laboratories are involved in development, fabrication and integration micro- and nanosystems, sensor structures to open new perspectives in the field of medical diagnostics, Minimal Invasive Surgery techniques, energy-efficient autonomous systems (sensor networks, autonomous driving). Our interest covers the topics of optical analytics (spectroscopy), environmental and safety (gas detectors) sensors.

- Accelerating Innovation in Microfabricated Medical Devices – Moore4Medical, ECSEL Innovation Actions (IA), Call ECSEL-2019-1-IA
- Advanced Aerosol Metrology for Atmospheric Science and Air Quality - AEROMET II, European Metrology Programme for Innovation and Research (EMPIR 9ENV08)
- Monitoring sensors deployed in emergency situations and in harsh environment, Thematic Excellence Programme - TKP2021 National Defence and Security, TKP2021-NVA-03
- Innovative biosensing technologies for medical applications – INBIOM, Thematic Excellence Programme - TKP2021 Health, TKP2021-EGA-04
- Development of a point-of-care microfluidic device for Therapeutic Drug Monitoring in cancer treatment (POC-TDM), Marie Skłodowska-Curie Actions - Postdoctoral Fellowships (HE MSCA PF) – András Füredi, Péter Fürjes
- Low-dimensional nanomaterials for the optical sensing of organic molecules on liquid and gas interfaces - OTKA K 131515 (participant)
- IR spectroscopy of extracellular vesicles: from exploratory study towards IR-based diagnostics – OTKA K 131594 (participant)
- Thin film integrity check by capillary bridge test – OTKA FK 128901 (participant)

Scientific cooperation:

- Providing optrode devices and their characterisation background for Implantable Microsystems Research Group of Pámány Péter Catholic University
- Development Lab-on-a-Chip technology for detection nucleic acid content in extracellular vesicles for University of Pécs (cooperative partner: BME SZAKT)
- Manufacturing SERS substrates for Bay Zoltán Nonprofit Ltd. for Applied Research

Industrial cooperation:

- Development and optimisation polymer based autonomous microfluidic cartridge, its production technology and measurement methodology for high sensitive Point-of-Care detection of bacteria and blood biomarkers for 77 ELEKTRONIKA Ltd.
- Development, manufacturing and characterisation microfluidic systems for AEDUS SPACE Ltd.
- Development CVD technology and equipment for deposition low roughness polycrystalline Silicon layers for MIRROTRON Ltd.
- Development and manufacturing specific calibration test samples for characterisation methods of semiconductor industry for the SEMILAB Inc.
- Development and manufacturing Near InfraRed LED devices for spectroscopic applications for SENOP Ltd. (Finland)

Wearable gas sensors for emergency and extreme conditions

Thematic Excellence Programme TKP2021-NVA-03

F. Bíró, I. Bársony, Z. Szabó, Cs. Dücső

Gas sensor applications for wearable devices

In the „ Chemical gas sensors" workpackage of the Thematic Excellence Programme TKP2021-NVA-03 „Environmental monitoring sensors for emergency and extreme conditions" project we plan to develop wearable and mobile gas sensors (on drones and controlled robots) for detection dangerous gases carry high risk during natural or industrial disaster management (time frame: April 1. 2022 – March 31. 2026). The primary goal is the recognition of methane leakage; however, detection of other risky gases will also be investigated. Our goal is to reach the TRL4 (in demo devices) and TRL6 for prototypes with dedicated readout and communication electronics, or commercial demo kit.
Two families of gas sensors are considered:

1) **low cost solid-state catalytic and chemoresistive sensors** for demo applications
   target gases: H_2S, HCN, NH_3, N_2O, Cl_2 or HCl (1-10-100ppm - TLV level or above) – upon the interest of the corresponding Partner of supervising authority
2) **moderate cost optical sensor for more accurate concentration measurements**
   target gases: CH_4, LPG, PB 1—5 %v/v (possibly CH_4 ~ 100 ppm)

Test platform for chemoresistive gas detectors

Regardless the operation principle, the calorimetric or chemoresistive sensors operate at elevated temperatures between 100 – 500°C. The basis of our calorimetric sensors is a newly developed small diameter (150µm) microhotplate exhibiting ±1% temperature uniformity on the heated area below 550°C. The stability of the heater is 5000 hours at least at the operation temperature of 530°C, thereby in pulsed mode operation ca. 5 years operation can be achieved. The power dissipation at 500°C is 27mW/1.5V, so the chip can be utilized in portable or wearable devices for personal safety. A utility model protection was given for the microhotplate design in 2021 (*Microheater with uniform surface temperature*, U 20 001150, registration number 5279). Accordingly, we exploit our previously developed microhotplate structure as the carrier of the gas sensitive material.

In a parallel device development, we have started to elaborate a dedicated tool for functional testing the chemoresistive materials. Our goal to provide easy-to-use platform for the laboratories intended to develop gas sensing materials for testing the performance of their locally deposited sensing layers. Our kit will contain an easy-handle hotplate chip with read-out electrodes and a masking element to enable the selective deposition of the sensitive layer. With this kit many research group can easily enter in the device development as they do not need the complex technology to fabricate the carrier chip.

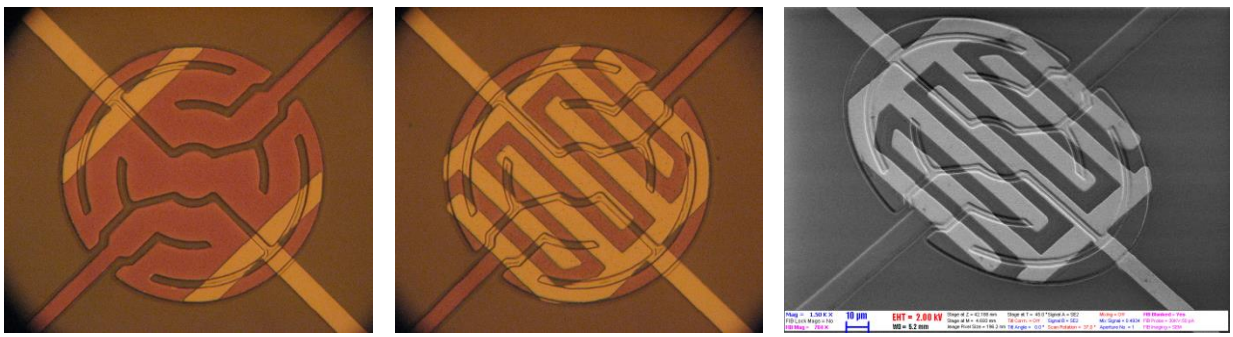

Figure 5.1. *Microheaters with different electrodes for performance testing the sensitive materials.*

Optical gas sensing

We have been investigating the construction and capability of methane detection by non-dispersive operation principle in the mid infrared region. The goal is to develop a complete setup consists of MEMS elements, such as microheaters and reflectors for IR source, optical channels and detectors. Test setup was built from commercial components, whereas the electronics was constructed in modular form for **driving the IR source** and the **appropriate read-out**. The preliminary results show that the construction is capable to detect methane in the 500 – 50000 ppm concentration range with the accuracy of 1-10%. We continued the work with the construction of a **dedicated and optimized electronics** to minimize the device size and investigate its long term performance. In frame of the TKP 2021-NVA-03 Grant 2nd workpackage design and fabrication of novel prototypes of non-dispersive infrared (NDIR) optical gas detector had been carried out. Based on preliminary experimental results the compact analogue and also the digital version of the NDIR methane detector have been designed and fabricated. Calibration procedure, sensitivity and stability tests were performed indoor. According to test results we may say **digital NDIR sensors are capable to response in 7-8 seconds to 1 or 2 %v/v methane exposure as it is recommended by the industrial standard**. Meanwhile, the detector consumes 120-150mA current which is still below the maximum permissible 200mA current consumption. Fig. 5.2. illustrates the constructed devices and some experimental results.

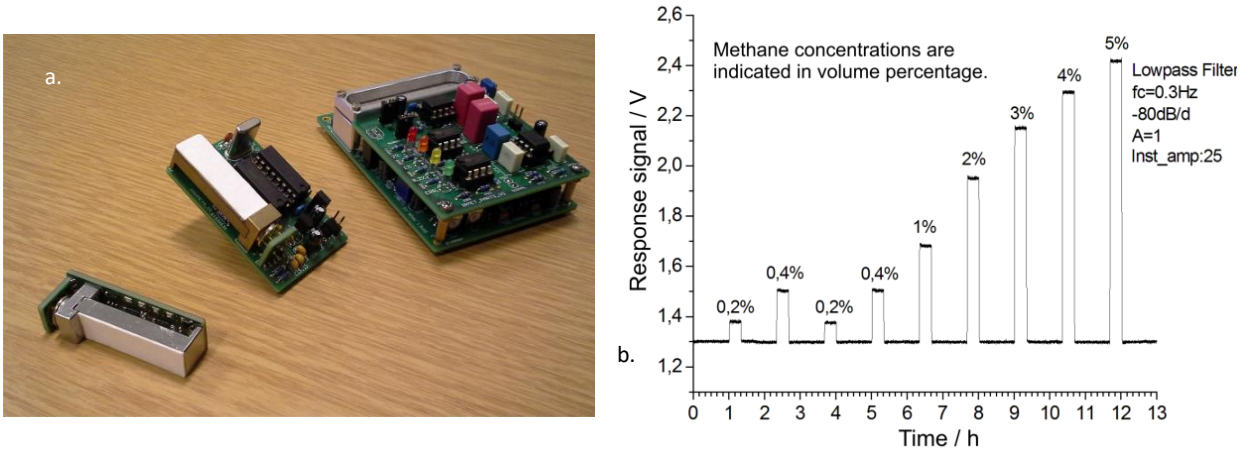

Figure 5.2. *Illustration of the NDIR detector prototypes and their response signals. a) The analogue (right) and the two versions of the digital NDIR methane detectors equipped with dust filters. Device at left was designed for the portable gas sensing systems. b) Typical response signal of the analogue detector.*

Microcalorimeters

Having in hand the **stable heaters** we now focus on other applications also. In cooperation with the University Debrecen we develop a **micro-calorimetric measuring method** to investigate thermally indicated physical-chemical phenomena in thin films. [Ref. 5.1, Ref. 5.2]

3D MEMS force sensor for tissue recognition

H2020-ECSEL-2017-2-783132 POSITION-II, 2018-2.1.6-NEMZ-ECSEL-2018-00001

J. M. Bozorádi, Zs. Bérces, P. Földesy, G. Pap (Uzsoki Hospital), Cs. Dücső, P. Fürjes

Laparoscopic devices have been widely used in the past decades during surgical procedures. Currently they are the golden standard in minimal invasive surgery. Furthermore combining these devices with robotic platforms is more and more common. Minimally invasive (robotic) surgery (MIS) offers several advantages for the patients, although the lack of sensory feedback for the surgeon is also a barrier in its progress. Gathering immediate multi-parametric information about the physical and anatomic conditions of tissues is crucial for the operator to precisely control the robotic actions or support the tissue recognition and pathologic characterization. Smart devices with integrated MEMS force sensors can provide such feedback and improve the safety of these interventions or help in on-site pathologic decisions. *A growing interest was recognised in these compact systems to be able to provide information regarding tissue thickness, stiffness, composition and the effect of the surgeon's current action.*

Accordingly our goal was to develop a novel device with integrated micromachined 3D force sensors to provide tactile information about the different organs and tissues touched. Piezoresistive force sensory units were integrated with dedicated readout electronics and precisely controlled linear motors solving the accurate tissue deformation to provide more information about the mechanical (elastic) parameters of the analysed materials. We demonstrated the complex, automatized measurement system – as well as hardware and software solutions – which is capable of implementing in vitro mechanical tissue characterization and thus provides elastomeric and pathological data. On the basis of the preliminary results both a compact measurement setup and a prototype electronics were adapted in a more compact test stage applicable for on-site in vitro human tissue measurements (see Fig. 5.3.). This version was outfitted with a more robust precision stepper motor which had a DC servo controller integrated for component reduction. Without any reference force gauge, it relies only on the sensor and electronics developed at Microsystems Laboratory. Disposable sensor PCB-s were used for sterility reasons, each calibrated before distributing them in a 3D printed carrybox to the hospital. The whole measurement can be controlled through a LabView based Windows application.

The setup and the LabView based software package were optimized for the easy use of medical professionals. The human tissue measurements were initialized in the Uzsoki Hospital, after receiving ethical permissions – as presented in Fig. 5.3. More than 40 samples were tested with various results which involved a section of the large intestine in most cases. Numerical analysis of the force-displacement curves shows that an integrated version of the system can be used to determine tissue thickness and the modulus of elasticity. However, to provide relevant feedback to medical personnel we need a more complex and statistically larger dataset with more information. [Ref. 5.3]

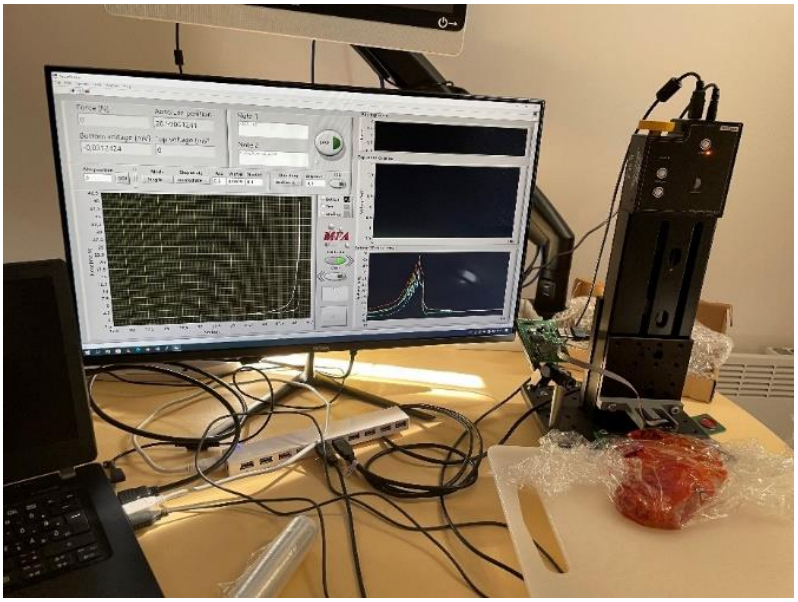

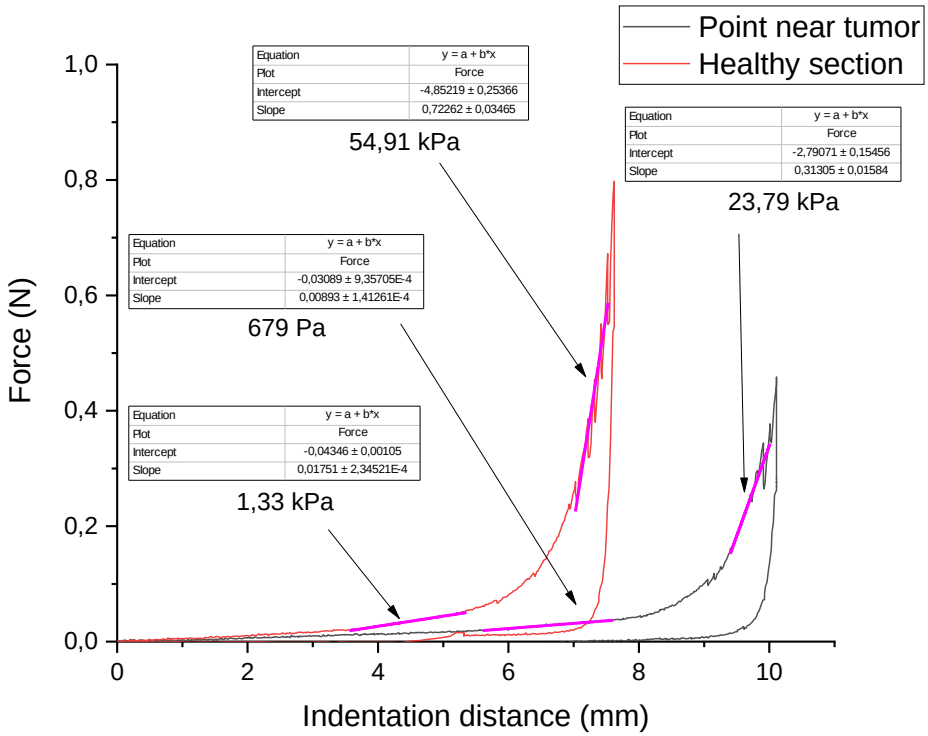

Figure 5.3. *Compact automated tissue elasticity measurement setup in the Uzsoki Hospital (top), and the comparision of the mechanical characteristics (force vs. deformation function) of the healthy and cancerous gastric tissues (bottom).*

Microfluidic methods for particle and cell manipulation and analysis

Thematic Excellence Programme TKP2021-EGA-04

A. Bányai, L. Bató, Zs. Szomor, E. Leelőssyné Tóth, M. Varga (77Elektronika Ltd.), P. Fürjes

In the field of microfluidics, the development of medical Point-of-Care (POC) diagnostic platforms, which can be used at the patient's bedside, ambulances or medical offices, has received great emphasis in recent decades. The applied integrated Lab-on-a-Chip cartridges must include transport and filtration of the liquid sample, positioning of cells and bacteria in the detection chamber over the sensing layer, and high sensitive detectors also.

Lateral focusing model particles and real cell samples

Related to the development of the Rapid Urine Bacteria Analyser (RUBA) by 77 Elektronika Kft., the need arose for a consumable, which is suitable for appropriate sample transport, sample preparation, target separation, enrichment, and lateral positioning in the sensor zone. In urine elements with various size can be found from the squamous cells with a typical diameter of 60 µm, through various shapes and sizes (crystals, fungi, hematopoiesis), even bacteria with a size of 1- 4 µm. The advantage of the label-free cell separation methods is that these can be performed by utilising the variety of the physical parameters of the cells - size, shape, density, flexibility, polarizability. Hydrodynamic principle based **microfluidic filters and lateral concentrating structures** were developed and evaluated by their filtration efficiency for different particle sizes. The particle size, the channel geometry, its cross-section and the flow Reynolds number also influence the focal points of the particles' position in the cross-section of a microfluidic channel. Counter-rotating Dean vortices in the channel cross-section also can help the degree of focusing. Particles of different sizes occupy different equilibrium positions in the flow. The method can be used to filter cancer cells, to separate haematopoiesis or bacteria, also in the case of samples that behave as non-Newtonian fluids (milk, undiluted blood).

The possibilities of lateral concentration and positioning of cells and particles were investigated in a microfluidic channel with a periodically changing cross-section and geometry with asymmetrical bends. In this case the focusing positions of the particles in the channel are affected by the appropriate ratio of the occurring hydrodynamic forces: the radial migration is more dominant as the ratio of the particle size to the channel size and the Reynolds number of the flow increase, in addition, the secondary Dean flow occurring in the tortuous channel. The position of focused beads were tested at different flow rates. As expected, the larger beads were focused in the middle of the channel with a shorter path, but the concentration of the smaller beads could only be achieved by significantly narrowing the critical cross-section of the fluidics or by significantly increasing the period number. The experimental measurements were compared to the results of the numerical simulation of finite element models, examining the effect of the channel cross-section and the flow velocity on the behavior of the emerging Dean vortices. The simulation results were in good agreement and supported the experimental data (Fig. 5.4.). Accordingly, the applicability of the applied model was convincing in case of predicting the behavior of the microfluidic systems.

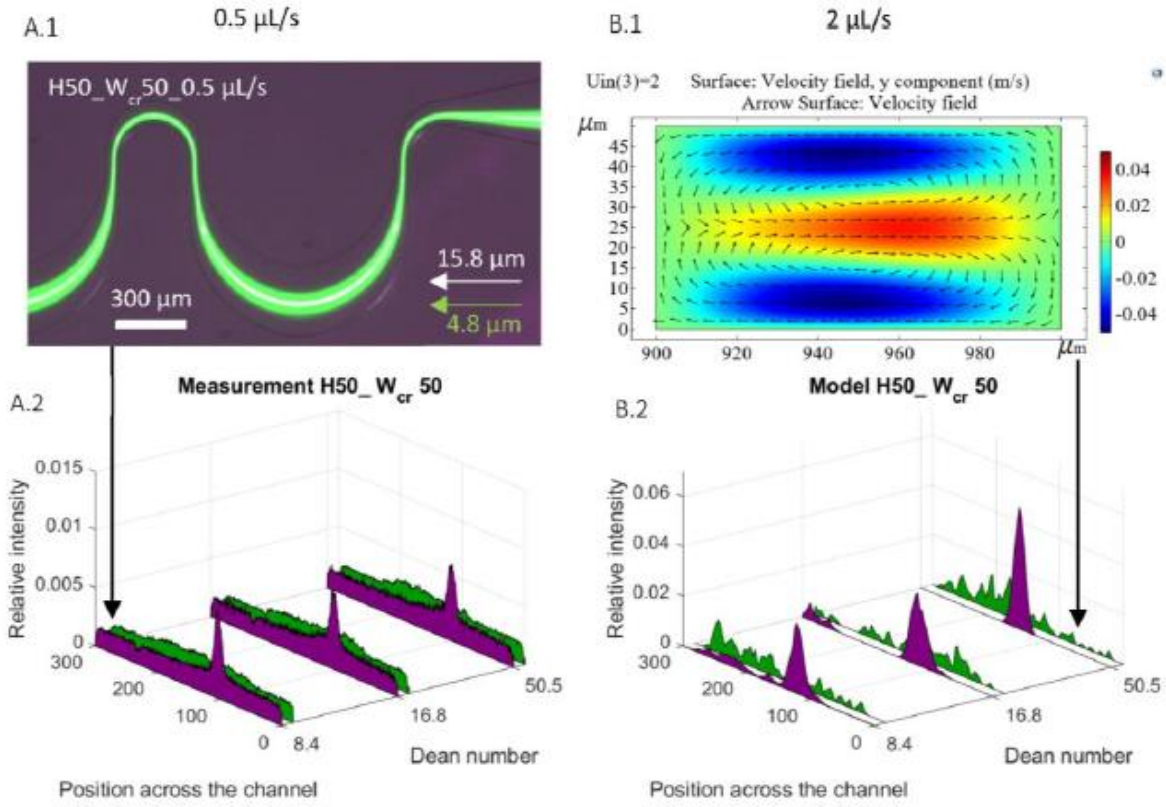

Figure 5.4. *Illustration of the behavior of rigid polystyrene beads (Ø 4.8 and 15.8 µm) in H50_W_{cr}50 fluidic channels with different critical cross-sections at flow rates of 0.5 – 1 – 2 µl/s (Dean numbers calculated from it). Experimental results: detection of the bead positions taken at the output based on fluorescence intensity (A.1 – A.2). The results of the numerical simulations illustrate the distribution of the velocity field in the x-y plane in the smaller bend of the channel (W_{cr} + 50 µm) at a flow rate of 2 µl/s (B.1), as well as the lateral distribution of the beads (on the y axis) after 23 bends (B.2).*

Spherical polystyrene particles are well suited for modeling the behavior of cells in microfluidic systems, where the degree of deformation of the cells or their form of movement in the flow does not affect their equilibrium positions. Model bead position map was recorded for reproducing the behavior of the chosen biological cells in our microfluidic system: E. coli [0.5-2µm; stick], red blood cell [2.5; 6-8 µm; disc-shaped biconcave], yeast Saccharomyces cerevisiae [5-10 µm; round or oval] and HeLa cell line [16-29 µm; diverse, inhomogeneous, spherical in suspension], which differ not only in size but also in shape. To set up a position map (Fig. 5.5.), the following bead sizes were used: Ø = 0.5 – 1.1 – 1.97 – 2.9 – 4.8 – 5.4 – 6.08 – 10.2 – 15.8 – 16.5 µm. The experiments took place in the chosen H=25_W_{cr}=50 structure. The equivalent bead size used for modeling the biological sample was determined by overlapping the lateral focusing positions.

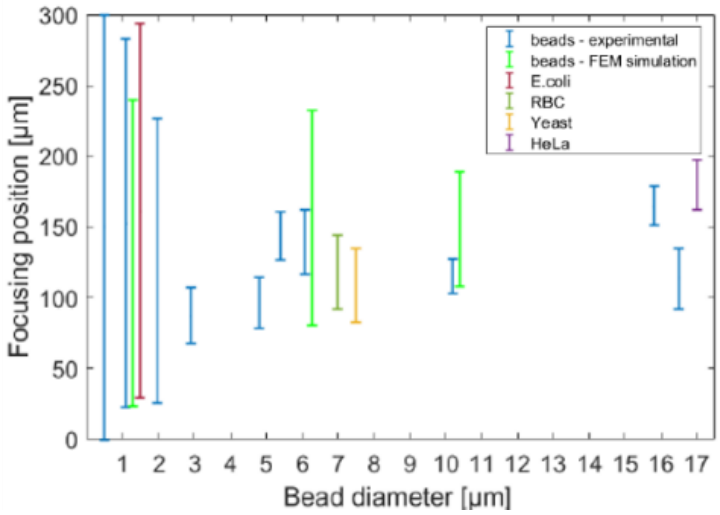

Figure 5.5. *Lateral focusing of biological cells and polystyrene beads in the H25_W_{cr}50 channel (at 1µL/s). The lateral focusing was examined by fluorescent or dark field microscope at the last bend of the microfluidic channel. The represented focusing position map is valid for rigid polystyrene beads of different sizes and biological target cells; the FEM calculated lateral position of some particle dimensions is also demonstrated.*

Microfluidic environment for analysis single cells and cell populations

In vitro testing of cell populations or individual cells in artificial systems that model their real environment is highly prospective from a biomedical and environmental point of view. Specially designed microfluidic systems allow the development of such a controllable chemical environment that is comparable to the size of cells. The application of such Organ-on-Chip devices, which integrate sensing functions, can be a significant step in the research of pharmaceutical agents, but also in facilitating the spread of personalized medicine. Cell trapping and in-vitro analysis are powerful tools that enable the investigation of cell viability and proliferation in microfluidic structures.

Diffusion coefficients of dedicated molecules were measured in the free-diffusion based obstacle free microfluidic device using fluorescent microscopy. The simple design of the device and ease of application enables fast measurements and easy fabrication. Diffusion coefficient of fluorescently labelled bovine serum albumin (BSA), immunoglobulin G and rhodamine B were determined using fluorescent microscopy. To acquire the intensity profiles along the channels time-lapse images were taken. A developed Python evaluation code was applied to fit complementary error functions to the measured profiles and calculate the diffusion coefficient. The measured diffusion coefficients were in nice accordance with the values found in literature and estimated by the Stokes-Einstein-equation.

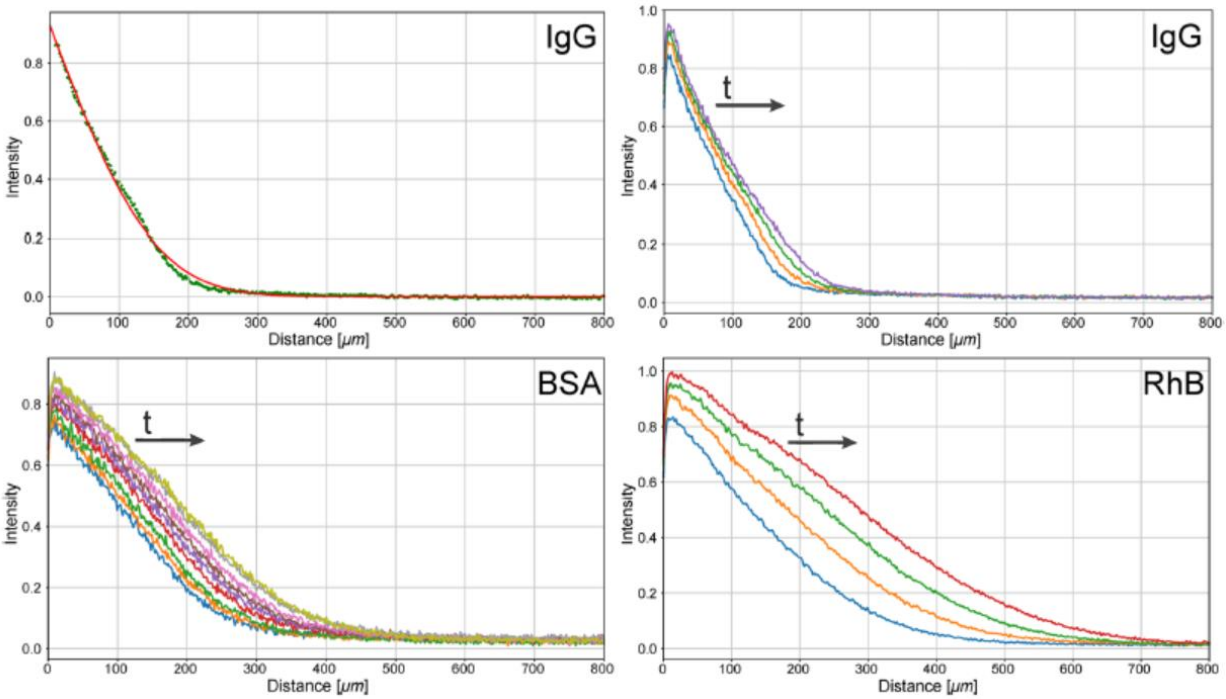

Figure 5.6. *The first image is raw data of an IgG profile (green) and the fitted error function (red) serving as an example of the fitting with error below 1%. Time evolution of the diffusion profiles of the measured proteins IgG, BSA and rhodamine B along the 800 m wide main channel. The time difference between the profiles is 30 s.*

Two-phase microfluidic systems for cell analytical applications

In the last two decades, the utilization of microengineered systems has revolutionized the manner in the fields of chemical and biological sciences in which high-throughput experimentation is conducted. The capacity to construct intricate microfluidic architectures has empowered researchers to devise novel experimental formats for processing extremely small analytical volumes within short timeframes and with remarkable efficiency. By reducing the reaction volumes, heat transfer is enhanced, leading to significant reductions in overall reaction times when conducted on a chip. These artificial microscopic containers enable accelerated mixing of chemical agents, prevent contamination and non-specific molecular binding on channel walls, and support highly parallelized processes with the opportunity of single cell or molecule analysis. In this work high performance finite element modelling (FEM) were applied for comprehensive analysis and description of fluid and heat transfer phenomena in two-phase microfluidic system to be able to predict reliably the thermal environment of proposed chemical reactions in the droplet size containers.

A novel Computational Fluid Dynamics-based multi-modal optimization approach is introduced and employed to investigate the impact of geometry, materials, and flow parameters of the two-phase microfluidic system on the evolving temperature distribution in a multi-zone thermal flow model. Finite element modelling code – COMSOL Multiphysics – was applied to analyse the droplet formation process in 3D two-phase models to achieve more accurate comprehension of the flow characteristics and heat transfer by comparison the single and two-phase fluid flow systems. The analysis is based on the numerical solution of the governing Navier-Stokes, continuity equations and coupled heat transfer model. For handling multiphase fluids in 3D models a robust Level Set calculation method was applied. During the study, the temperature distribution alongside the channel has been investigated at different volume flows, considering the inhomogeneous thermal capacity, heat conductivity and convection within and between the fluidic environment and the generated droplets as the system reaching the equilibrium state. Fig. 5.7. represents the evolving flow characteristics and temperature distribution in the time dependent single and two-phase model at the initial time period when the heater surface has reached the 90°C temperature and

droplet formation has been starting. The temperature distribution was analysed at different heights in the fluidic channel by comparison single phase to two-phase flows in order to reveal the effects of material inhomogeneity using similar flow rates. Higher although localised fluid temperatures were estimated in the two-phase flow according to the higher thermal conductivity of the oil phase. The periodic character of the temperature distribution in the two-phase flow demonstrates the inhomogeneous local heat capacity and the significantly decreased convective heat transfer through the boundary surface of a droplet. [Ref. 5.4-5.9]

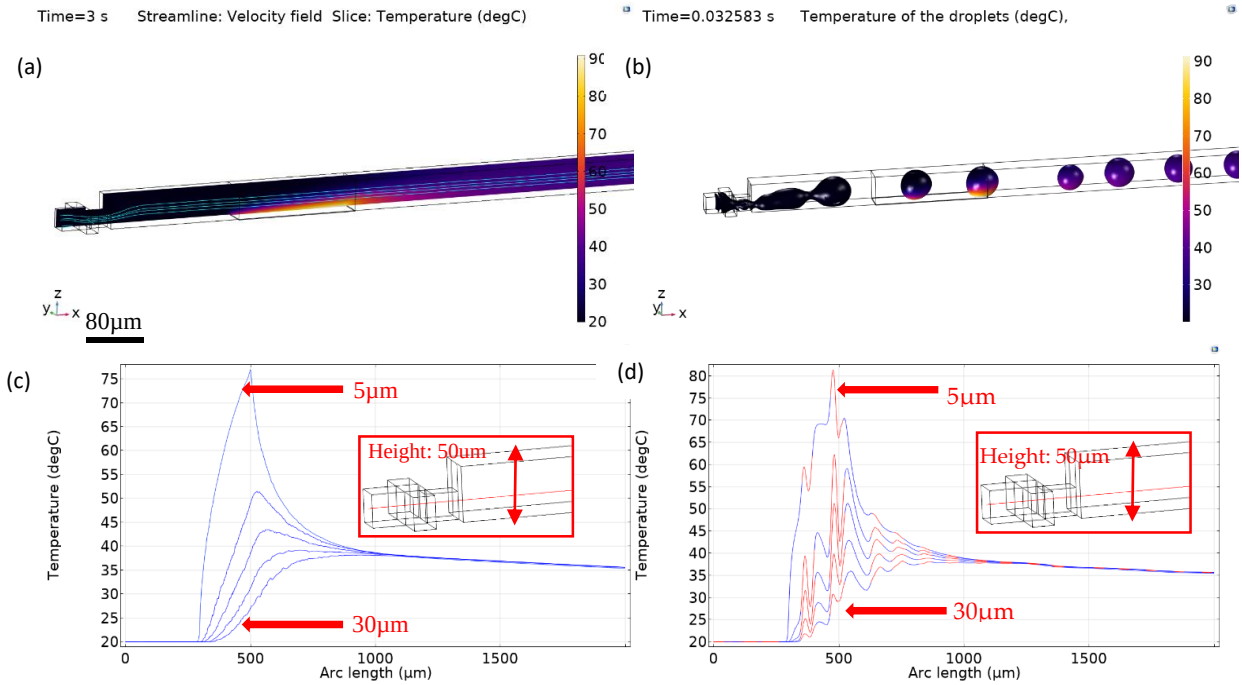

Figure 5.7. *Simulated temperature distribution longwise the channel in case single phase flow (a) and within the generated droplets (b). Cut lines (c, d) also represent the temperature distribution longwise the channel, while the red segments indicate the location of the droplets. The flow rate was 0.295 µl/s.*

Small scale production and development of near infrared LEDs for spectroscopic applications

ECSEL-2019-1-IA -876190Moore4Medical, 2019-2.1.3-NEMZ_ECSEL-2020-00005

B. Beiler, J. M. Bozorádi, Cs. Dücső, F. Bíró, P. Fürjes, Z. Szabó

Infrared spectroscopy is a very popular measurement technique especially in food industry, pharmaceutical industry and agriculture for the detection and measurement of organic materials. The 1^{st}-3^{rd} harmonic absorption bands of valence-bond vibrations in the -OH, -NH and -CH functional groups are located in the range of the near infrared (NIR), where smaller signals can be measured effectively in practice. NIR LEDs have narrow wavelength; therefore, they are suitable for measurements at given wavelength. Further advantages of LEDs compared to incandescent lamps are their small dimensions, high efficiency, and low power consumption, which is critical in small handheld devices.

GaInAsP/InP is an ideal material system for the fabrication of double heterostructure devices as the emission wavelength is easily tuneable between 950-1650 nm. As InP has higher bandgap than the lattice-matched GaInAsP active layer the absorption losses inside the device structure can be minimized. In order to tune the emission wavelength of the LED, the composition of the semiconductor light-emitting layer has to be properly set. Our high quality single peak LED chips (1220nm) have a stable market.

Wide emission-spectrum NIR LEDs

Specific InGaAsP/InP layer structures were grown by liquid phase epitaxy (LPE) to fabricate wide emission-spectrum near-infrared LEDs. The final multilayer structure could be achieved in two consecutive LPE growth steps: by growing 2 InGaAsP photoluminescent layers with the emission peaks of about 1300 nm and 1450 nm first, and by growing other photo-luminescent (1650 nm) and active (1200 nm) layers in the second step. Samples were fabricated and characterized by optical transmittance measurements, by photo-luminescent measurements using various excitation sources in the NIR range, and by scanning electron microscopy to measure layer thicknesses and verify epitaxial crystal formation. The results were continuously fed back to refine the growth parameters.

LED chips were characterized electrically and optically (Fig. 5.8.) after dicing. The 500x500 μm^2 LED chips were driven with continuous I_{FW}. A NIR spectrophotometer was used to examine the emission spectrum at a 30° angle to the normal of the chip. The emitted optical power was estimated using a small area InGaP photodiode at a 45° to the normal of the chip in a well-defined geometry. The shape of the spectra is quite stable, only slightly distorts with the increasing current due to the saturation in the thinner layers. The angle distribution of the radiation shows the expected Lambertian (cosine) pattern and the spectrum is independent of the angle.

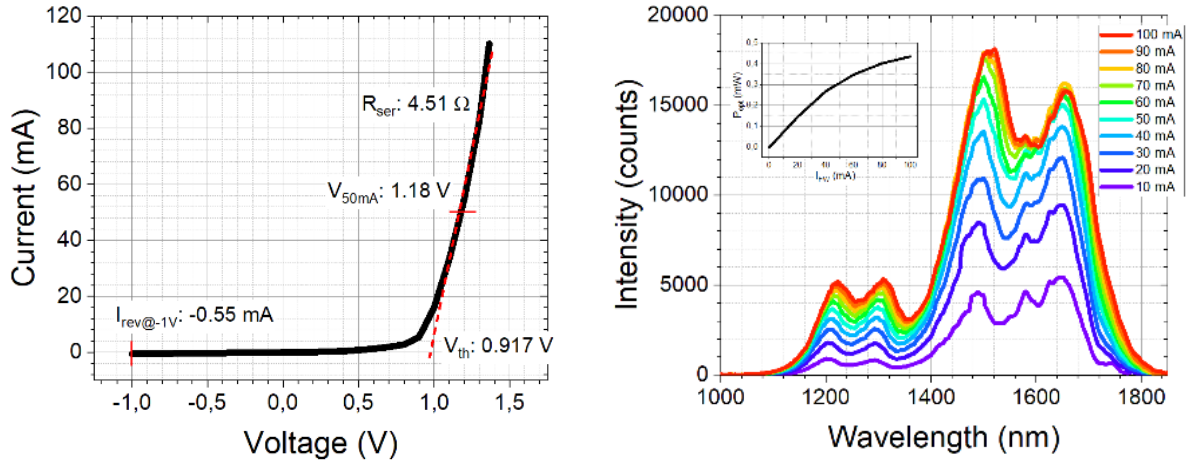

Figure 5.8. *I-V characteristic of the LED chip (left) and the emission spectra of the 4-wavelength LED chip at I_{fw} 10-100 mA and the total optical power vs. I_{fw} in the inset (right).*

The total emitted optical power of the wide spectrum LED was compared to the emission of a standard LED with a similar wavelength as the active layer. The power of the primarily emitted wavelength distributes on a wide wavelength range, which is the reason for the lower intensities. The emitted optical power, however, shows only 3x lower power compared to the reference LED, which is mainly originates from the natural conversion loss of the photon energy.

Cell culture media analysis in Organ-on-Chip applications

ECSEL-2019-1-IA -876190Moore4Medical, 2019-2.1.3-NEMZ_ECSEL-2020-00005

B. Beiler, Zs. Baji, L. Bató, K. Pankász, Zs. Szomor, J. M. Bozorádi, Z. Szabó, P. Fürjes

Optical Spectroscopy in microfluidic environment

The concentration of molecular markers – such as relevant amino-acids, carbohydrates and drugs – is an important signal of the metabolic or chemical processes unfolding in Organ-on-Chip applications. In recent years the advanced and miniaturized sources, detectors and spectrometers has proven the applicability of optical spectroscopy to be an excellent tool for the analysis of different sample compositions or chemical reactions. UV-Vis or infrared spectroscopy combined with microfluidic sample transport and preparation can be a powerful, in-situ analysis method for continuous monitoring of complex cell culture media and revealing the molecular fingerprints of the relevant molecular contents.

Polymeric microfluidic cuvettes were fabricated by CNC milling and also by hot embossing techniques using microstructured molds. The optical measurements were carried out in the wavelength range of 950 - 1690 nm using Avantes spectrophotometer combined with optical fiber waveguide for excitation and detection. The **sample volume effect** was characterized by comparison the spectral transmittances of benchmark aqueous solutions (ethanol-water, lactate-water) measured in a standard macroscopic cuvette and in microfluidics. In case of the microfluidic cuvettes transmittance and transreflectance mode spectral analysis were also elaborated. The IR absorbance of water over 1400 nm wavelength causes significant deterioration of the signal-to-noise ratio and this effect could be eliminated by using radically shorter pathways of the microfluidic cuvettes as highlighted in Fig. 5.9.

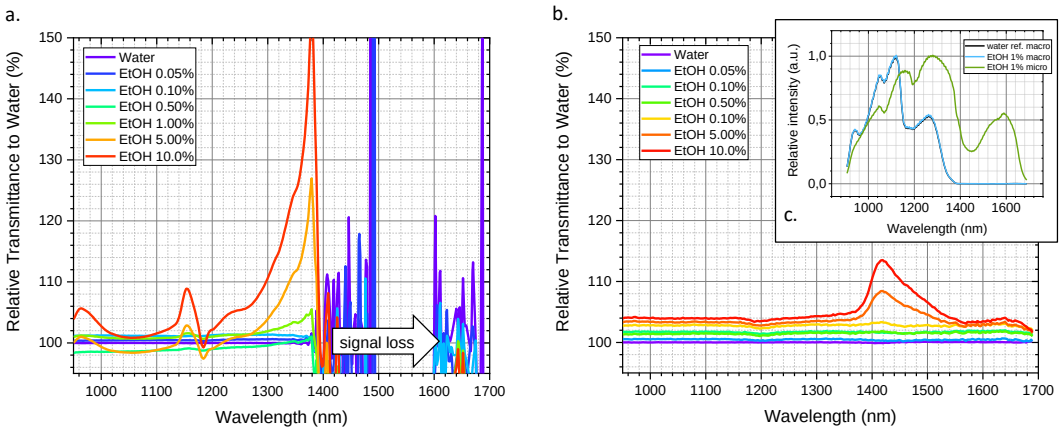

Figure 5.9. *Concentration-dependent near-IR transmittance spectra for ethanol solutions (0.05, 0.1, 0.5, 1.0, 5.0, 10 % v/v) compared to water as reference in macroscopic (a.) and microfluidic (b. HE, 100 µm, transmittance) cuvettes. Relative intensities (c.) demonstrates the signal loss over 1400 nm wavelength.*

OoC-compatible microfluidic cuvettes were designed and manufactured for transreflectance mode optical measurements with adequate material properties, excellent surface quality and suitable architecture. By decreasing the optical path, the aspecific absorbance of water could be decreased, resulting in an increase of the signal-to-noise ratio. The optical measurement setup was characterised in case of fluorescent analysis also.

The first electronic board for optical transmittance and photoluminescence measurement was tested with cuvette and transistor outline-packaged LEDs and photodiodes. The board features an LED driver, a 4-channel photodiode input, and lock-in detection. Based on our comprehensive tests, the compact LED and detector driver electronics were designed and manufactured to be tested and integrated with the optical measurement head.

Electrochemical analysis of cell culture media

Besides different marker molecules – such as relevant amino-acids, carbohydrates, etc. and drugs as antibiotics – pH is another important parameter to characterize the metabolic parameters of cell cultures and tissues in Organ-on-Chip applications. Miniaturized and robust pH detectors based on potentiometric, conductometric methods or ion-selective field effect transistors (ISFET) and extended gate field effect transistors (EGFET) have been demonstrated utilysing various ion sensitive metal-oxide (MO_x) materials such as RuO_2, IrO_2, TiO_2, SnO_2, Ta_2O_5, WO_3, ZnO, etc. In case of the ISFET and EGFET pH sensors the source-drain current of the transistor is controlled by the electrostatic field generated by the gate covered by ion-sensitive material. The pH sensitivity of the gate materials can be explained by the surface charging of the metal-oxides mainly due to specific adsorption of H^+/OH^- ions, protonation and deprotonation reactions at surface sites. The MO_x sensing layer can be fabricated by screen printing, vacuum sputtering, sol-gel or electrodeposition methods and characterized mainly by potentiometry, cyclic voltammetry (CV) and electrochemical impedance spectroscopy (EIS) to define their sensing performance. The electrochemical method implemented in integrable architecture was proved to be applicable for pH measurement in various culture media. [Ref. 5.10-5.12]

Electrochemical electrodes including integrated Pt reference / counter electrodes and metal-oxide working electrodes with comb-like Pt or Au contacts were manufactured on Borofloat™ glass substrate (Fig. 5.10.c.). Titanium-oxide layers were deposited by vacuum sputtering and atomic layer deposition (ALD) at 300°C and 100° as sensitive materials. The MO_x functionalized electrochemical electrodes were connected as extended gate in the proposed EGFET based circuit represented in Fig. 5.10.a-b and the performance of the system was tested. The pH sensitivity of the EGFET based circuit containing different MO_x materials were characterized using pH calibration solutions. The TiO_2 layers deposited by sputtering and ALD prepared at 300°C showed moderated pH sensitivity according to their perfectly stoichiometric, inert structure. The TiO_x layer deposited by ALD at 100°C proved to be perfectly applicable for pH sensing applications having close to Nernstian 59.12 mV/pH response (Fig. 5.10.d). The difference of the pH sensitivities of various titanium-oxides can be explained by the material structures and compositions.

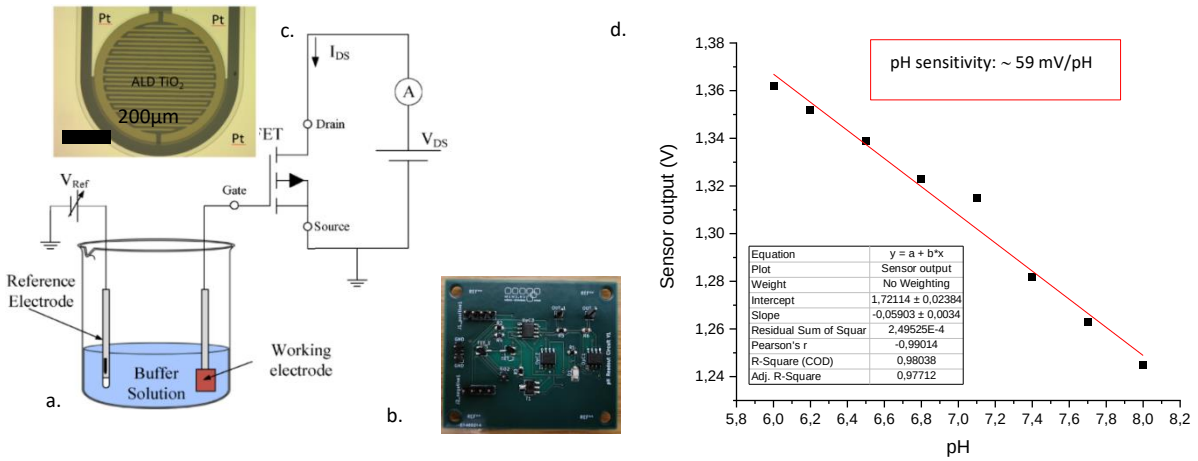

Figure 5.10. *Schematic measurement setup (a.) representing the electronic architecture of EGFET based pH sensor, the manufactured read-out electronics (b.) and the MO_x functionalized working electrode (c.). The pH sensitivity of the non-stoichiometric TiO_x layer was close to the Nernstian response.*

6 - Nanobiosensorics Department

Head: Robert HORVATH, Ph.D., Senior Scientist

Research Staff

- Robert HORVATH, Ph.D.
- Sándor KURUNCZI, Ph.D.
- Inna SZÉKÁCS, Ph.D.
- Beatrix PÉTER, Ph.D.
- Boglárka KOVÁCS, Ph.D.
- Zoltán SZITTNER, Ph.D.
- Enikő FARKAS, Ph.D
- Nicolett KANYÓ, MSc

Ph.D. students / Diploma workers

- Beatrix MAGYARÓDI, PhD student
- Igor SALLAI, PhD student
- Bálint BÉRES, PhD student
- Kinga Dóra KOVÁCS, PhD student
- Imola RAJMON, BSc student
- Anna BALOGH, BSc student
- Szabolcs NOVÁK, MSc student
- Viktor Sándor KOVÁCS, BSc student
- Lili FARKAS, MSc student
- Róbert TARR, BSc student
- Kinga TÓTH, MSc student
- Barbara MAJOROS, MSc student
- Péter JOÓ, MSc student
- Krisztina BORBÉLY, MSc student
- Dorina SZIN, BSc student

The research profile of the Nanobiosensorics Department is the development and application of label-free optical biosensors, the mathematical modeling of the relevant biological and biophysical processes. Building on their broad national and international collaborative network the group conducts research in the fields of instrument development, monitoring of cell-secreted extracellular vesicles, development of protein-based functional coatings, adhesion studies on human cancer and immune cells, and theoretical modeling. In 2014, the application for an ERC Consolidator Grant by the head of the research group received qualification category “A (fully meets the ERC excellence criteria and should be funded if sufficient funds are available)” after the interview in Brussels, but the funding line did not reach this proposal due to budgetary constraints. However, using this achievement the Group could successfully apply for funding from NKFIH in the framework of the ERC_HU call. In the framework of this project, they aim for single cell manipulation and label-free sensing. Building on this expertise, in 2018 they won an Élvonal (NKFIH) research project for single-cell biosensing. In 2022, the research group won the Thematic Research Excellence grant (Tématerületi Kiválósági Program, TKP) as well in collaboration with other groups of the MFA.

Dean-flow affected lateral focusing and separation of particles and cells in periodically inhomogeneous microfluidic channels

LP2012-26/2012 Lendület, OTKA ERC_HU 117755, TKP2021-EGA-04, OTKA KKP 129936

A. Bányai, E. Farkas, H. Jankovics, I. Székács, E. Leelőssyné Tóth, F. Vonderviszt, R. Horváth, M. Varga (77E), P. Fürjes

The purpose of the recent work is to give a better explanation of how Dean vortices affect lateral focusing and to understand how cell morphology can alter the focusing position compared to spherical particles. The position and extent of the focused region were investigated using polystyrene fluorescent beads with different bead diameters (Ø = 0.5, 1.1, 1.97, 2.9, 4.8, 5.4, 6.08, 10.2, 15.8, 16.5 µm) at different flow rates (0.5, 1, 2 µL/s). Size-dependent focusing generated a precise map of the equilibrium positions of the spherical beads at the end of the periodically altering channels, which gave a good benchmark for focusing multi-dimensional particles and cells. The biological samples used for experiments were rod-shaped *Escherichia coli* (*E. coli*), discoid biconcave-shaped red blood cells (RBC), round or ovoid-shaped yeast, *Saccharomyces cerevisiae*, and soft-irregular-shaped HeLa cancer-cell-line cells to understand how the shape of the cells affects the focusing position at the end of the channel (Fig.6.1) [Ref. 6.1].

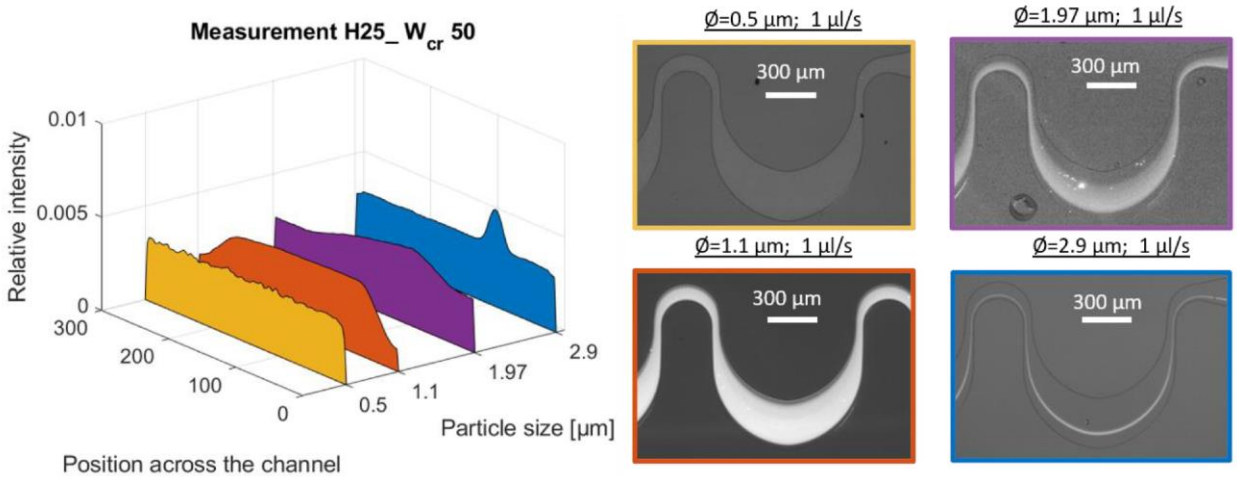

Figure 6.1. *The size limit of lateral focusing in channel H25_Wcr50 at 1µL/s. The applied bead sizes are Ø = 0.5, 1.1, 1.97 and 2.9 µm.*

Label-free biosensing of lignans for therapeutics using engineered model surfaces

LP2012-26/2012 Lendület, OTKA ERC_HU 117755, TKP2021-EGA-04, OTKA KKP 129936, OTKA PD 131543, OTKA PD 134195

B. Péter, B. Majoros, S. Kurunczi, A. V. Ács, I. Székács, Sz. Bősze (ELTE), G. M. Kovács (ELTE), I. Boldizsár (ELTE), R. Horváth

The label-free interaction analysis of macromolecules and small molecules has increasing importance nowadays, both in diagnostics and therapeutics. In the blood vascular system, human serum albumin (HSA) is a vital globular transport protein with potential multiple ligand binding sites. Characterizing the binding affinity of compounds to HSA is essential in pharmaceutics and in developing new compounds for clinical application. Aryltetralin lignans from the roots of *Anthriscus sylvestris* are potential antitumor therapeutic candidates, but their molecular scale interactions with specific biomolecules are unrevealed. Here, we applied the label-free grating-coupled interferometry (GCI) biosensing method with a polycarboxylate-based hydrogel layer with immobilized HSA on top of it. With this engineered model surface, we could determine the binding parameters of two novel aryltetralin lignans, deoxypodophyllotoxin (DPT), and angeloyl podophyllotoxin (APT) to HSA (Fig. 6.2).

Exploiting the multi-channel referencing ability, the unique surface sensitivity, and the throughput of GCI, we first revealed the specific biomolecular interactions. Traditional label-free kinetic measurements were also compared with a novel, fast way of measuring affinity kinetics using less sample material (repeated analyte pulses of increasing duration (RAPID)). Experiments with well-characterized molecular interactions (furosemide to carbonic-anhydrase (CAII) and warfarin, norfloxacin to HSA) were performed to prove the reliability of the RAPID method. In all investigated cases, the RAPID and traditional measurement gave similar affinity values. These results could be also adapted to other biomolecules and applications where sample consumption and the rapidity of the measurements are critical [Ref. 6.2].

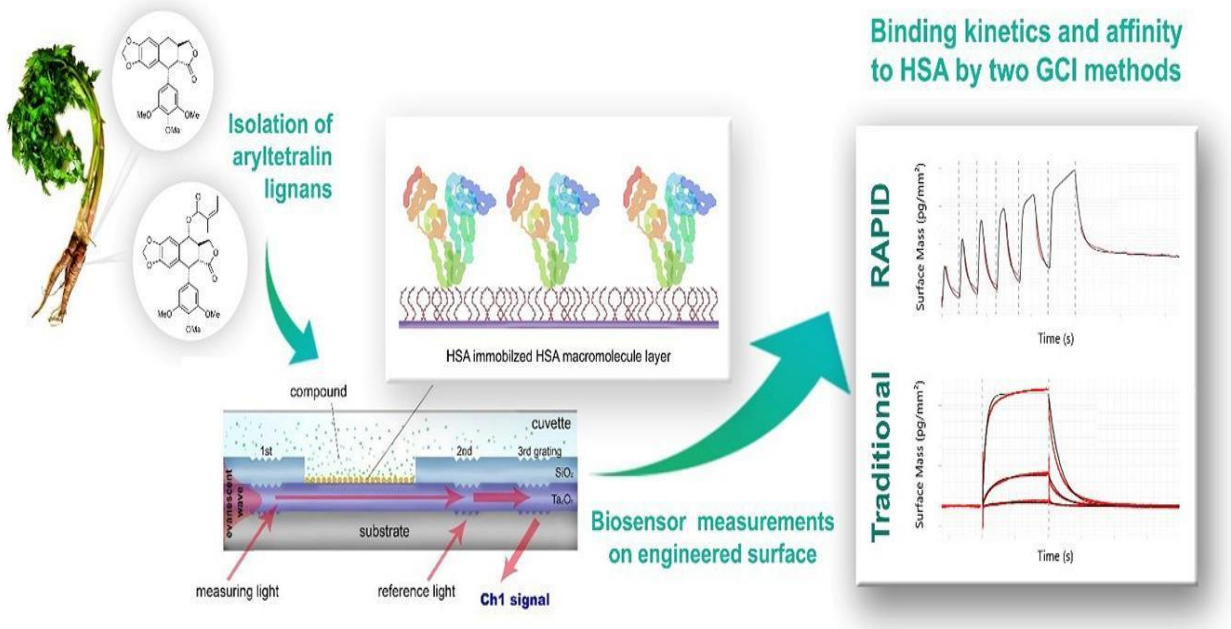

Figure 6.2 *Schematic illustration of the applied methodology*.

Design, fabrication, and characterization of picowell arrays on cyclic olefin copolymer surfaces generated with a 10.5 MeV N4+ ion microbeam

LP2012-26/2012 Lendület, OTKA ERC_HU 117755, TKP2021-EGA-04, OTKA KKP 129936

I. Bányász (Wigner), I. Rajta (ATOMKI), V. Havránek (NPI, Prague), A. Mackova (NPI, Prague), A. J. Laki (Pázmány University), M. S. Z. Kellermayer (SE), Z. Szittner, S. Kurunczi, Sz. Novák, I. Székács, R. Horváth, M. Fried, G. U. L. Nagy (Óbuda University)

Handling of picoliter-to-nanoliter-scale volumes and objects has increasing importance in life sciences. This is the volume scale of cell extractions and individual living cells. Here, we introduce a method of generating a picoliter-scale device by direct writing of picowell arrays on a ZEONOR™ copolymer surface with high-energy medium-mass ion microbeam. Arrays of various microstructures were written in the sample using a microbeam of 10.5 MeV N4+ ions at various implanted ion fluences. The best array was obtained by implantation of annuli of 10 and 11 μm of inner and outer diameters with a fluence of 7.8×10^{12} ions/cm^2 (Fig.6.3) [Ref. 6.3].

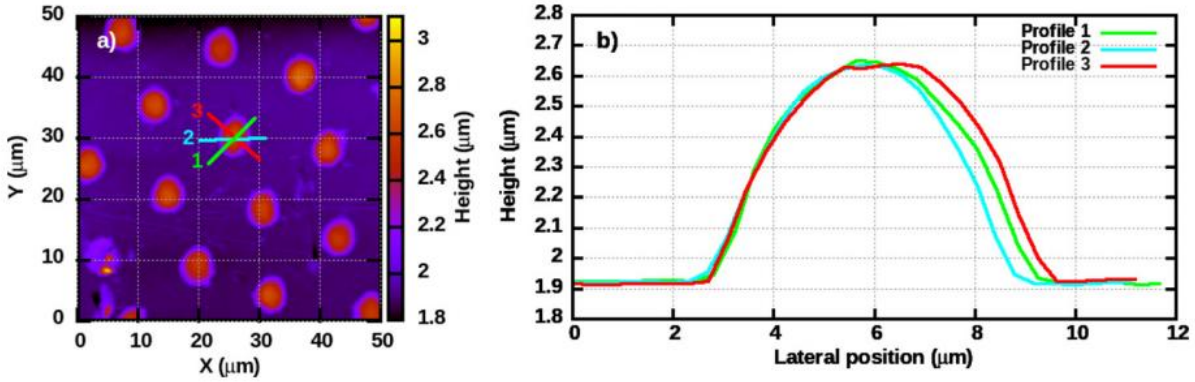

Figure 6.3. *Height-contrast AFM image (a) of part of array D, and topographical height profiles along the indicated sections of a user-defined single element (b) in it.*

Nanoinjection of extracellular vesicles to single live cells by robotic fluidic force microscopy

LP2012-26/2012 Lendület, OTKA ERC_HU 117755, TKP2021-EGA-04, OTKA KKP 129936, Bolyai Scholarship, OTKA PD 131543, OTKA PD 134195

K. D. Kovács, T. Visnovitz (SE), T. Gerecsei, B. Peter, S. Kurunczi, A. Koncz (SE), K. Németh (SE), D. Lenzinger (SE), K. V. Vukman (SE), A. Balogh, I. Rajmon, P. Lőrincz (SE), I. Székács, E. I. Buzás, R. Horváth

In the past decade, extracellular vesicles (EVs) have attracted substantial interest in biomedicine. With progress in the field, we have an increasing understanding of cellular responses to EVs. In this Technical Report, we describe the direct nanoinjection of EVs into the cytoplasm of single cells of different cell lines. By using robotic fluidic force microscopy (robotic FluidFM), nanoinjection of GFP positive EVs and EV-like particles into single live HeLa, H9c2, MDA-MB-231 and LCLC-103H cells proved to be feasible. This injection platform offered the advantage of high cell selectivity and efficiency. The nanoinjected EVs were initially localized in concentrated spot-like regions within the cytoplasm (Fig.6.4). Later, they were transported towards the periphery of the cells. Based on our proof-of-principle data, robotic FluidFM is suitable for targeting single living cells by EVs and may lead to information about intracellular EV cargo delivery at a single-cell level [Ref. 6.4].

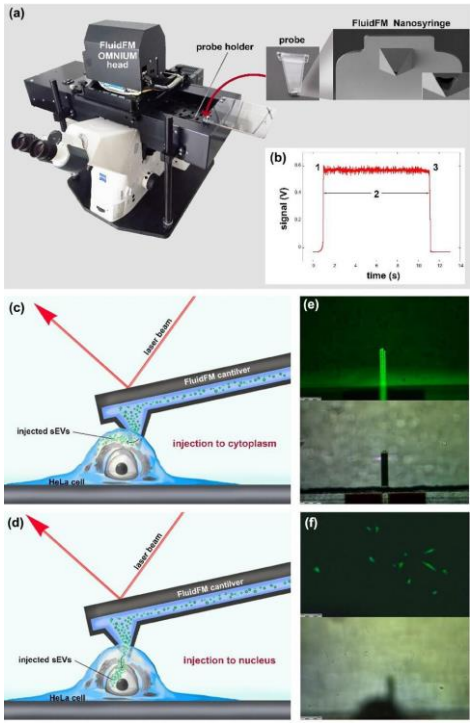

Figure 6.4. *Summary of the FluidFM measurements. (a) Photo of the FluidFM appliance, probe and the FluidFM Nanosyringe. (b) Change of the voltage signal during injection of a live cell. (c) Schematic illustration of the injection of sEVs to the cytoplasm by FluidFM. (d) Schematic illustration of the injection of sEVs to the nucleus by FluidFM. (e) Microscopic image of the FluidFM cantilever in fluorescent mode (upper part) and bright field mode (bottom part). (f) Microscopic image of the cells in fluorescent mode (upper part) and bright field mode (bottom part).*

Polysaccharide-based nano-engineered multilayers for controlled cellular adhesion in label-free biosensors

LP2012-26/2012 Lendület, OTKA ERC_HU 117755, TKP2021-EGA-04, OTKA KKP 129936, OTKA PD 131543, OTKA PD 134195

M. Wasilewska (Poland), A. Michna (Poland), A. Pomorska (Poland), K. Wolski (Poland), S. Zapotoczny (Poland), E. Farkas, Z. Szittner, I. Szekacs, R. Horvath

Controlling cellular adhesion is a critical step in the development of biomaterials, and in cell- based biosensing assays. Usually, the adhesivity of cells is tuned by an appropriate biocompatible layer. Here, synthetic poly(diallyldimethylammonium chloride) (PDADMAC), natural chitosan, and heparin (existing in an extracellular matrix) were selected to assembly PDADMAC/heparin and chitosan/heparin films. The physicochemical properties of macroion multilayers were determined by streaming potential measurements (SPM), quartz crystal microbalance (QCM-D), and optical waveguide lightmode spectroscopy (OWLS). The topography of the wet films was imaged using atomic force microscopy (AFM). Polysaccharide-based multilayers can be considered versatile systems for medical applications. One can postulate that the presented results are relevant not only for modeling studies but also for applied research (Fig.6.5) [Ref. 6.5].

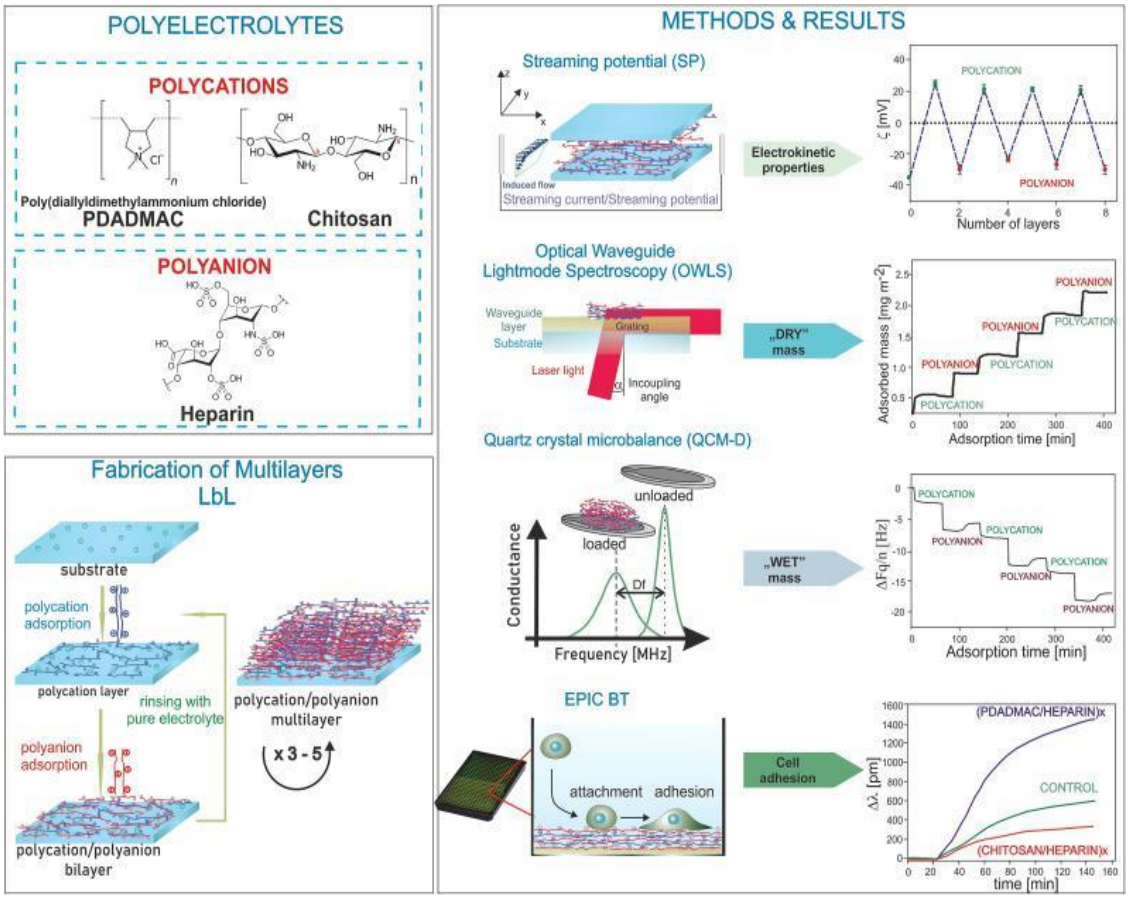

Figure 6.5. *Scheme representing the procedures used to prepare/investigate PDADMAC (or chitosan)/ heparin films.*

7 - Complex Systems Department

Head: Dr. Géza Ódor D.Sc., Scientific advisor

Research Staff

- Balázs KIRÁLY PhD
- István BORSOS
- Zoltán JUHÁSZ PhD
- György SZABÓ D.Sc., Professor emeritus

Ph.D. students / Diploma workers

- Katalin KOVÁCS LFZE diploma
- Krisztián KISS LFZE diploma
- Kristóf BENEDEK BME MSc student

The research field of the group is the investigation of complex systems by the methods of statistical physics in equilibrium as well as non-equilibrium states.

Project OTKA K128989 aimed to study critical dynamics in heterogeneous systems. We have demonstrated this for energy outages using the Manna universality class self-organized criticality, as well as in Kuramoto type of models. ELKH project SA-44/2021 targeted to better understand cascade failures in power-grids. Failure dynamics has also been studied in fiber boundle type models on complex networks.

Project OTKA PD 138571 studies statistical physical models of relevance for game theory using the tensor renormalization group method proposed by Levin and Nave, including the Blume-Capel model in an external magnetic field, which can be shown to be equivalent to the combination of an elementary coordination-type game and some elementary self-dependent games under the right conditions, making it a prime candidate for investigating the basic mechanics of the interplay between elementary game theoretic interactions.

Theoretical investigation of multi-agent evolutionary game models studies processes supporting fair behavior of individuals by numerically analysing mathematical models when a player's own interest opposes that of the community. Mathematical models have been used to investigate the effect of one kind of penalties, the combinations of the rules of strategy updates, and systems in which the income of the players is obtained from two or three interconnection systems (communities). The effects of special players, whose only duty is to watch the population and punish defectors was investigated and cyclic dominance like structures have been found. Self-organizing impact of averaged payoffs on the evolution of cooperation has also been studied.

The increase of data in folk music and genetic data sets implies the continuous improvement of algorithms to analyze them. The newly developed algorithms are able both to identify clusters and to follow the evolutionary inheritance of clusters, both in genetic (haplogroup) features and in popular characteristics of folk music tunes. Genetic studies have proven that the total weights of common haplogroups in the Hungarian population can be found at the level of 30% in Hungarian and 70% in bronze age population.

The competition of alliances with inner blocking mechanism

OTKA K 128989

A. Szolnoki and X. Chen

Competitors in an intransitive loop of dominance can form a defensive alliance against an external species. The vitality of this superstructure, however, is jeopardized if we modify the original rock-scissors-paper-like rule and allow that the vicinity of a predator blocks stochastically the invasion success of its neighboring prey towards a third actor. To explore the potential consequences of this multipoint interaction we introduce a minimal model where two three-member alliances are fighting but one of them suffers from this inner blocking mechanism. We demonstrate that this weakness can be compensated by a faster inner rotation which is in agreement with previous findings. This broadly valid principle, however, is not always true here because the increase of rotation speed could be harmful and results in a series of reentrant phase transitions on the parameter plane.

In our model two three-member loops compete. One of them still represents the traditional rock-scissors-paper-like interaction where during a potential invasion only the state of involved pair counts. In the alternative triplet, however, we introduce a blocking mechanism. More precisely, staying at the rock-scissors-paper example, a rock will only beat scissors with a limited probability if there is a paper in the nearest neighborhood of the actor representing rock state. Further details are explained in Fig. 7.1.

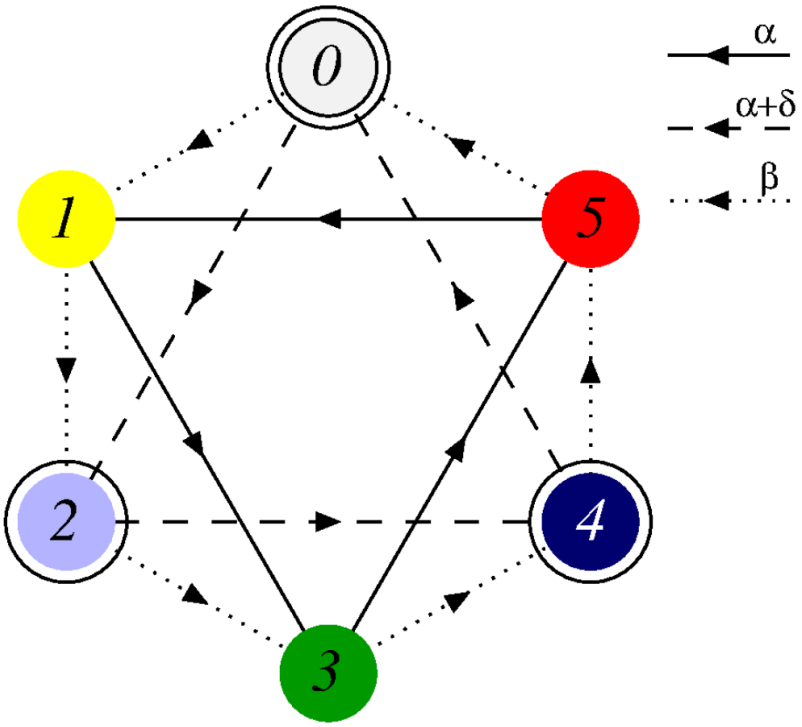

Figure 7.1. *Food-web characterizing the microscopic dynamics in our six-member ecological system. Arrows indicate the direction of invasion between species. Two triplets form defending alliances, whose members are in a rock-scissors-paper-like relation. While the inner invasion probability in the 1→3→5→1 loop is α, the same probability in the 0→2→4→0 circle is α + δ. Importantly, the members of the latter triplet can block each other with probability γ. If, for instance, there is a species 4 in the neighborhood of species 0 then the 0→2 or the 0→1 invasion is blocked with probability γ. The invasion probability between the members of competing triplets is β.*

Fig. 7.2 shows some representative phase diagrams, when the inner invasion of odd-labeled triplet is fast, moderate, or very weak. When the inner rotation is fast, displayed in panel (a), the system behavior is similar to those we observed for large β. Namely, (1+3+5) species can form a solid winning alliance almost everywhere, the only exception is the low γ - large δ corner where the faster rotation in the even-labeled triplet can compensate the shortage of blocking. When the invasion strength in the sound triplet is weaker, shown in panel (b), we can observe that there is a parameter region where neither (0+2+4) nor (1+3+5) alliance is strong enough to beat the rival group hence all six species survive. If we fix γ, for instance, and only increase the value of δ then we can detect some non-monotonous behavior: starting from (1+3+5) phase we can enter to "all," after (0+2+4), followed by "all" again, and finally arriving back to (1+3+5) phase again.

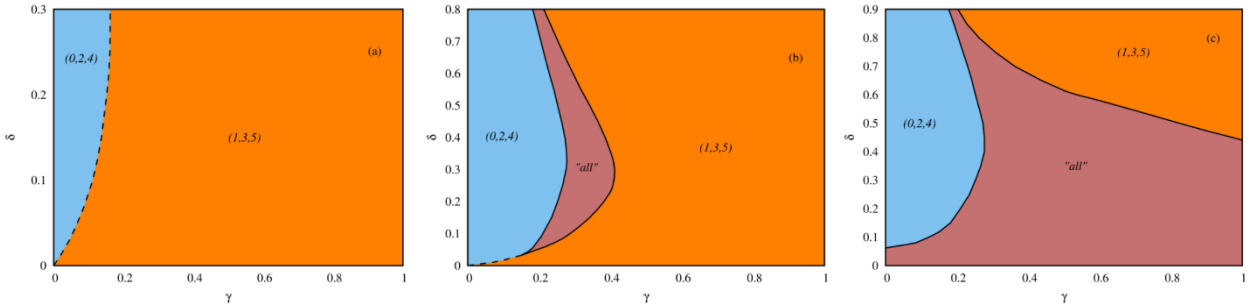

Figure 7.2. *Phase diagrams when interaction between rival triplets is intermediate (β = 0.5). Horizontal axis shows the γ blocking strength while vertical axis denotes the δ extra value of inner invasion in the even group. (a) to (c) respectively show cases when the inner invasion strength in the odd-labeled group is strong (α = 0.7), moderate (α = 0.2), or very weak (α = 0.1). Light blue (orange) marks the parameter area where even (odd) species prevail, while pink shows the area where all six species coexist. Dashed (solid) lines denote the position of discontinuous (continuous) phase transition points.*

The top-left panel of Fig. 7.3 illustrates quantitatively the above mentioned curious re-entering phenomenon. In all three cases the evolution starts from a prepared initial state where triplets are separated by domains containing neutral species. The common starting state is shown in panel (a) where we indicate those species who are present in a specific stripe. In Case *I* the sound (1+3+5) triplet beat both (0+3) and (1+4) duplets. In Case *II* both triplets can grow on the expense of domains formed by duplets. When triplets meet and the superiority of even-labeled triplet over odd-labeled triplet becomes evident. In Case *III* the inner rotation in the blocked triplet is almost maximal and duplet of neutral pairs becomes stronger again. While too fast rotation could be harmful for blocked triplet, the sound triplet still dominates the two-member domains, hence odd-labeled group will be the final victor, no matter they would be weaker against the even-labeled group in a direct interaction.

Our system provides a nice example that the consequences of dynamical rules determining the vitality of a solution are more subtle than we might expect based purely on the microscopic dynamical rules. As we show, when two triplets compete their frontier serves as a birthplace of alternative solutions. Namely, there is always a chance that a two-member solution of neutral species emerges. If the rotation speed is too high in the blocked triplet then such two-member solution, formed by a triplet member and an external species, can be more effective: while the invasion of external party is not blocked, it can meet more easily with its internal predator who cannot beat it due to blocking. As a consequence, the two-member formations invade the blocked triplet, leaving only the alternative triplet alive. Importantly, the defensive mechanism still working in the sound triplets, hence they eventually prevail. No matter they would be weaker in a direct comparison against the blocked triplet. [Ref. 7.1]

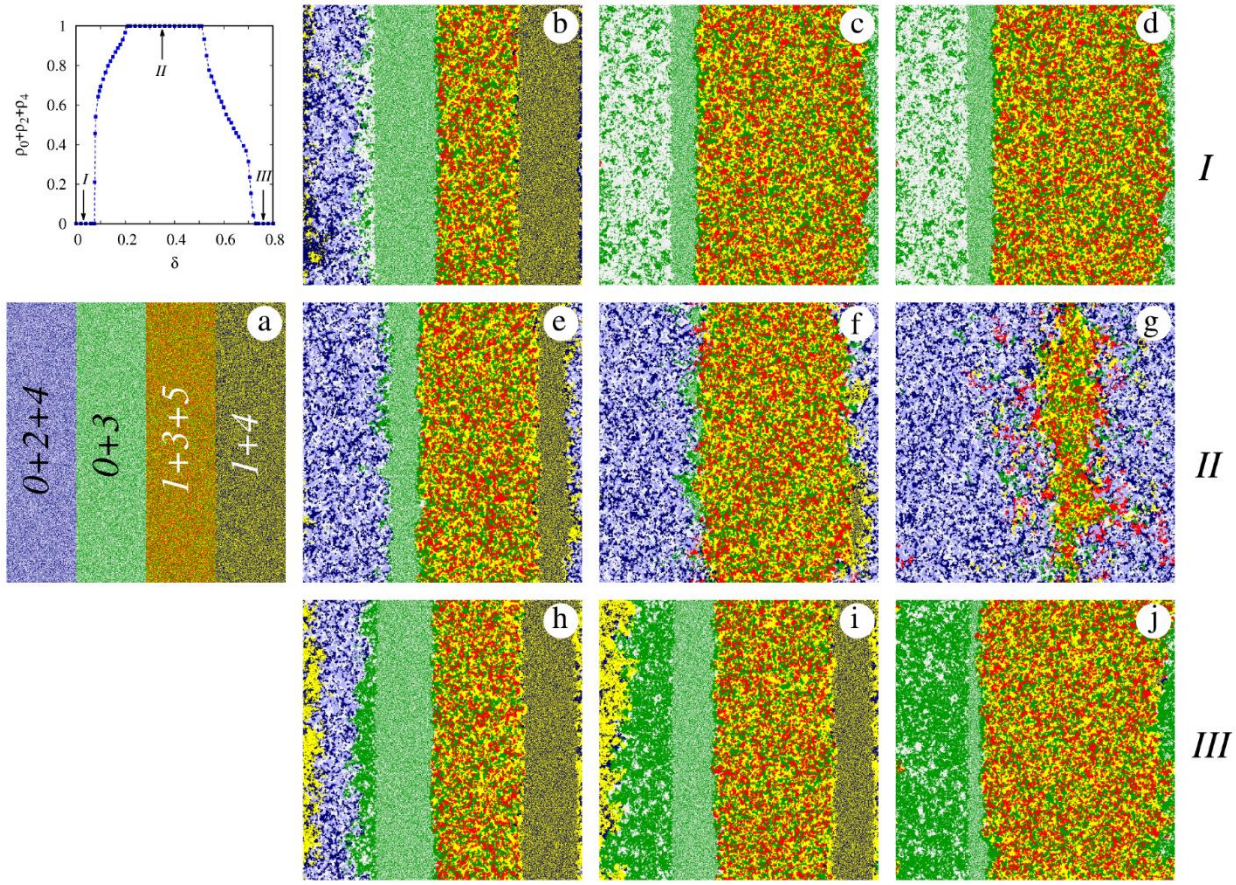

Figure 7.3. *Reentrant phase transitions when rotation intensity is changed in the blocked triplet. Panel in the top-left corner shows the order parameter in dependence of δ at β = 0.5, α = 0.2, and γ = 0.25. Arrows show the positions of the δ values where we launched the evolution from a specific initial state shown in (a). The diverse evolution of patterns in cases I, II, and III are shown in the rows. Final destinations, which are (1+3+5), (0+2+4), and (1+3+5) phase again, are not shown. The color code of species is identical those used in Fig 7.1. The applied linear system size is L = 800.*

Revisiting and Modeling Power-Law Distributions in Empirical Outage Data of Power Systems

*B. Hartmann, S. Deng, G. Ódor, and J. Kelling**
**HZDR Dresden-Rossendorf*

The size distributions of planned and forced outages and their restoration times in power systems have been studied for almost two decades and have drawn great interest as they display heavy tails. Understanding heavy tails has been provided by various threshold models, which are self-tuned at their critical points, but as many papers pointed out, explanations are intuitive, and more empirical data are needed to support hypotheses. In this paper, we analyze outage data collected from various public sources to calculate the outage energy (Fig.7.4) and outage duration exponents of possible power-law fits. Temporal thresholds are applied to identify crossovers from initial short-time behavior to power-law tails. We revisit and add to the possible explanations of the uniformness of these exponents. By performing power spectral analyses on the outage event time series and the outage duration time series (Fig.7.5), we find that, on the one hand, while being overwhelmed by white noise, outage events show traits of self-organized criticality, which may be modeled by a crossover from random percolation to a directed percolation branching process with dissipation, coupled to a conserved density. On the other hand, in response to outages, the heavy tails in outage duration distributions could be a consequence of the highly optimized tolerance mechanism, based on the optimized allocation of maintenance resources. [Ref. 7.2]

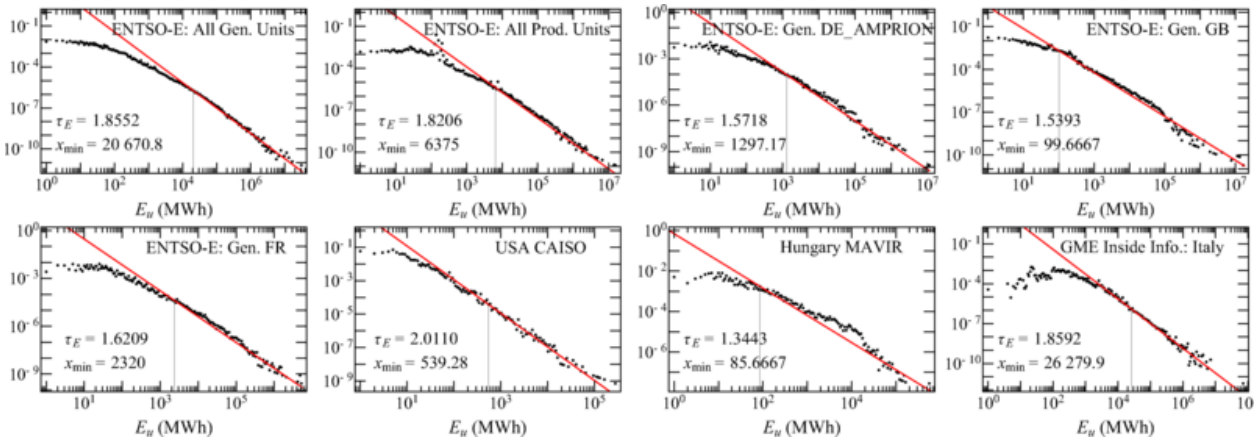

Figure 7.4. *Probability distributions (black dots) of generation outages measured in terms of the unavailable energy. For the ENTSO-E data, we show the generation outage data for the control areas "DE_AMPRION," "GB," and "FR," as well as the generation and production outage data from all control areas. The fitted power laws and their corresponding Emin values are marked by solid red lines and vertical black lines, respectively.*

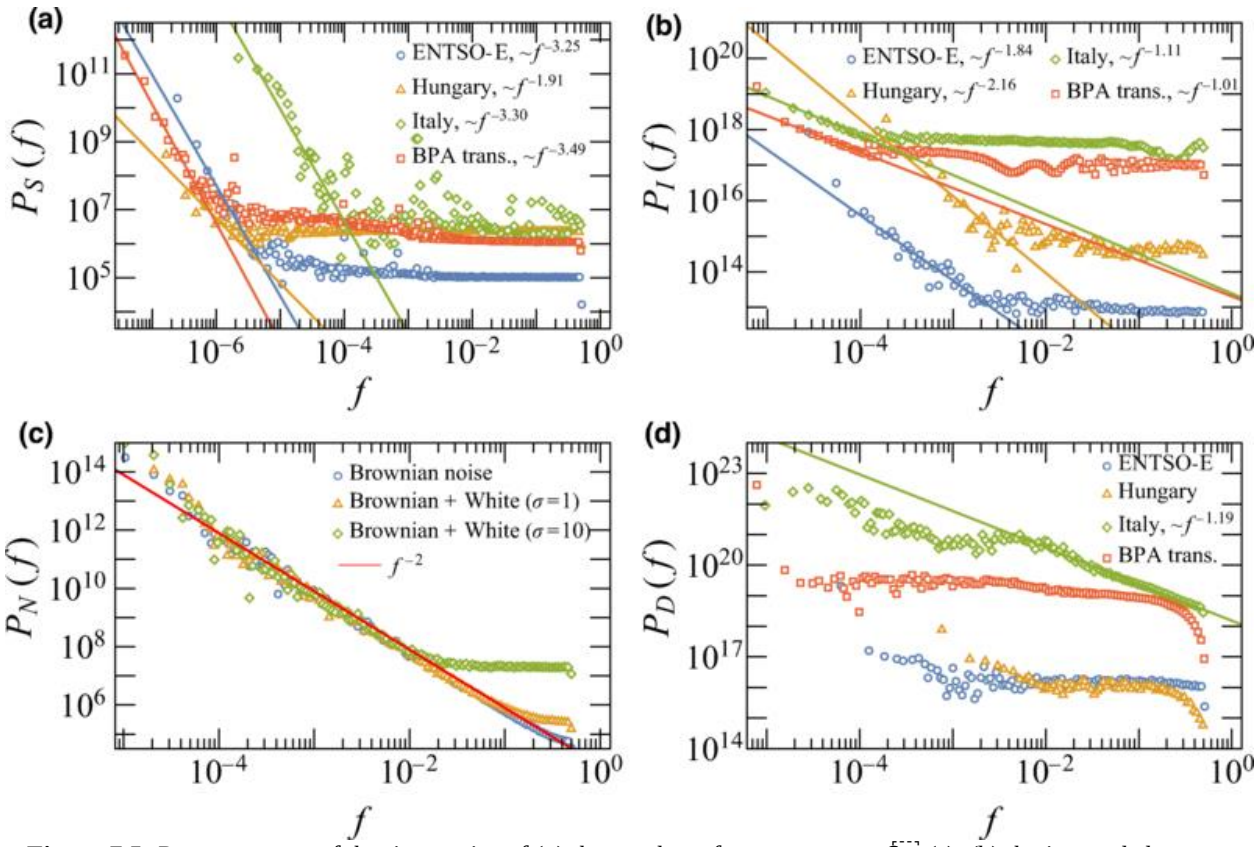

Figure 7.5. *Power spectra of the time series of (a) the number of outage events $S_{f_0}(t)$, (b) the intervals between successive outage events $I_{f_0}(t)$, (c) the Brownian noise $N_{f_0}(t)$, with and without the presence of a white noise background, and (d) the outage duration $D_{f_0}(t)$. In panels (a), (b), and (d), we show the respective power spectra for the ENTSO-E generation outage data from all control areas, the Hungarian MAVIR generation outage data, the GME Italian generation outage data, and the BPA transmission outage data.*

Scaling laws of failure dynamics on complex networks

G. Pál[1], Zs. Danku[1], A. Batool[1], V. Kádár[1], N. Yoshioka[2], N. Ito[2], G. Ódor, F. Kun [3]

1-Department of Theoretical Physics, Faculty of Science and Technology, University of Debrecen, Hungary. 2 RIKEN Center for Computational Science, Kobe, Japan, 3-Institute for Nuclear Research (Atomki), Hungary.

The topology of the network of load transmitting connections plays an essential role in the cascading failure dynamics of complex systems driven by the redistribution of load after local breakdown events. In particular, as the network structure is gradually tuned from regular to completely random a transition occurs from the localized to mean feld behavior of failure spreading. Based on finite size scaling in the fiber bundle model of failure phenomena, here we demonstrate that outside the localized regime, the load bearing capacity and damage tolerance on the macro-scale, and the statistics of clusters of failed nodes on the micro-scale obey scaling laws with exponents which depend on the topology of the load transmission network and on the degree of disorder of the strength of nodes.

Most notably, we show that the spatial structure of damage governs the emergence of the localized to mean feld transition: as the network gets gradually randomized failed clusters formed on locally regular patches merge through long range links generating a percolation like transition which reduces the load concentration on the network. The results may help to design network structures with an improved robustness against cascading failure. [Ref. 7.3]

Spontaneous symmetry-breaking in spatial evolutionary games

C. Hauert and G. Szabó*
**Department of Mathematics, University of British Columbia, Vancouver, BC, Canada*

Spontaneous symmetry-breaking occurs in a wide scale of models describing order-disorder phase transitions when the temperature is increased. The best-known examples are the ferromagnetic-paramagnetic phase transitions or similar ordering in the atomic arrangements (e.g., solid electrolytes, metal-hydrogen systems, electro-chromatic materials, atomic depositions on a single crystal, etc.) described by lattice gas models. In these systems one of the two or more equivalent states is stabilized at low temperatures.

In spatial evolutionary games players with different strategies are located on the sites of a lattice or graph. These players can represent species in biological systems or human individuals with some possible strategies in economic models. The pair interactions between the neighbouring players are described by simple matrix games and the evolution of strategy distribution is controlled by consecutive random strategy updates. Spontaneous symmetry-breaking was previously reported in social and biological systems where game theoretical interactions enforced the appearance of critical (continuous) phase transitions with spontaneous symmetry-breaking belonging to the Ising- or Potts-type universality class.

Christoph Hauert suggested a model where similar symmetry-breaking phase transitions are caused by the separation of interaction and imitation neighbourhoods. In this model the players are located on the sites of a two-layer square lattice. The players get incomes from games with five nearest neighbours located on the opposite layer while they can adopt strategy form one of their four nearest neighbours in the same layer. The interaction is described by a two-strategy donation game when the cooperative player provides a benefit b to their partner at a cost c ($b>c>0$). The defective player declines to pay the cost that yields zero income for the partner. In this social dilemma the selfishness dictates to choose defection for both players who receive nothing. On the contrary, the players receive higher income (b-c) for mutual cooperation. The macroscopic behaviour is quantified by the average frequency of cooperation and their fluctuations on both layers with using Monte Carlo simulations for different cost-to-benefit (c/b) ratio at a fixed noise level in the imitation process as illustrated in Fig. 7.6.

The results show several curiosities. On both layers the cooperation becomes extinct simultaneously if b/c goes to a threshold value (r_1~0.0228) (from below) dependent on the noise level. This extinction process belongs to the directed percolation universality class and accompanied with a power law divergence in the fluctuation. There exists a range of b/c where cooperation occurs with the same frequency on both layers. Spontaneous symmetry-breaking can be observed in the cooperation frequencies if $r_2<c/b<r_1$ (r_2~0.002166). For this state the players in one of the layers exploit the others. The corresponding critical phase transition possesses the general features observed for the two-dimensional Ising model. Notice that this type of exploitation occurs when the average frequency of cooperation is sufficiently large (>0.5) and it reaches a maximum when c/b is decreased. For further decrease in c/b results in rarer and larger avalanches (bursts) in the time-dependence of cooperation frequencies as it is indicated by the huge increase of fluctuations.

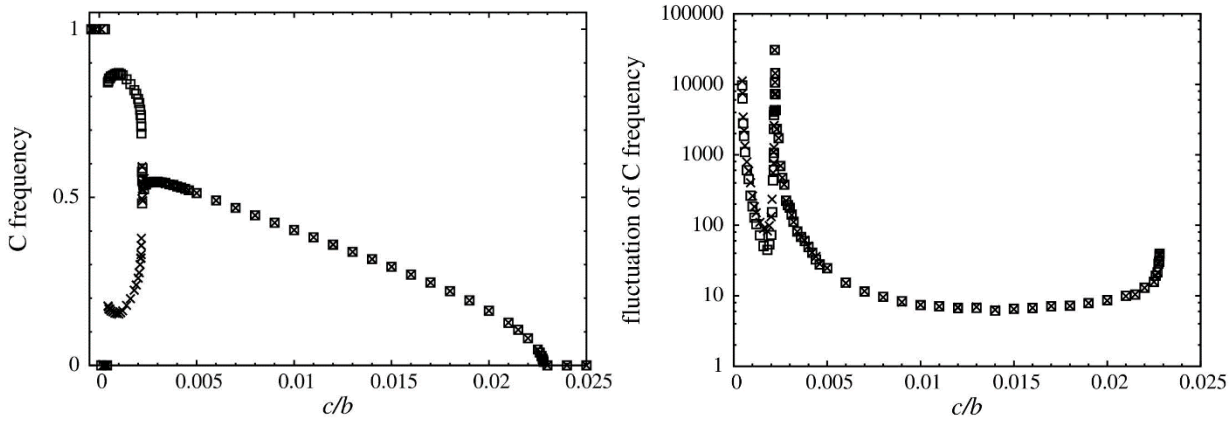

Figure 7.6. *Strategy frequencies in the upper and lower square lattice (left) and their fluctuations (right) vs. c/b at low noises in the imitations. Boxes and crosses denote Monte Carlo data in the upper and lower layers.*

Due to this phenomenon the finite system can evolve into one of the states where strategy distributions are homogeneous in both layers. The final state depends on the initial state, size, and stochastic events. Finally, we emphasize the absence of spiteful behaviour for negative cost ($c<0$) when the solitary defector benefits from the high loss she caused for her co-players in several spatial evolutionary games. The present model can explain some phenomena reported in biological systems.

Preliminary results indicate similar phenomena in other models and raise the clarification of other mechanisms yielding spontaneous symmetry breaking or polarizations in many biological or social systems. [Ref. 7.4]

An investigation of evolutionary potential games using the tensor renormalization group method

OTKA PD 138571

B. Király

Some of the structurally simplest many-player models of game theory become equivalent to classical spin models when the strategy choices of the players follow the so-called logit strategy update rule, a close relative of Glauber dynamics. Consequently, the properties of these game-theoretic models can be directly studied using concepts and methods developed in the field of statistical physics. This project fits into this interdisciplinary approach.

The emergence of coordination has always interested game theorists. Recent research has shown that general coordination-type symmetric pair interaction games consist of linear combinations of voluntary games that describe coordination between strategy pairs: In such an elementary coordination game, the two interacting players receive equal rewards when they choose the same coordinated strategy; similarly, they are both punished when they choose opposing coordinated strategies; and neither of them receives any payoff when either one of them chooses any other strategy. As basic building blocks, these elementary coordination games have a key role in determining outcomes in general games. In an effort to learn more about their interplay with each other and the remaining (self-dependent, cross-dependent, and cyclic dominance) elementary game types, the tensor renormalization group (TRG) method introduced by Michael Levin and Cody P. Nave was applied to a couple of games defined by simple combinations involving elementary coordination components. The players were located at the sites of square lattice and followed the logit strategy update rule.

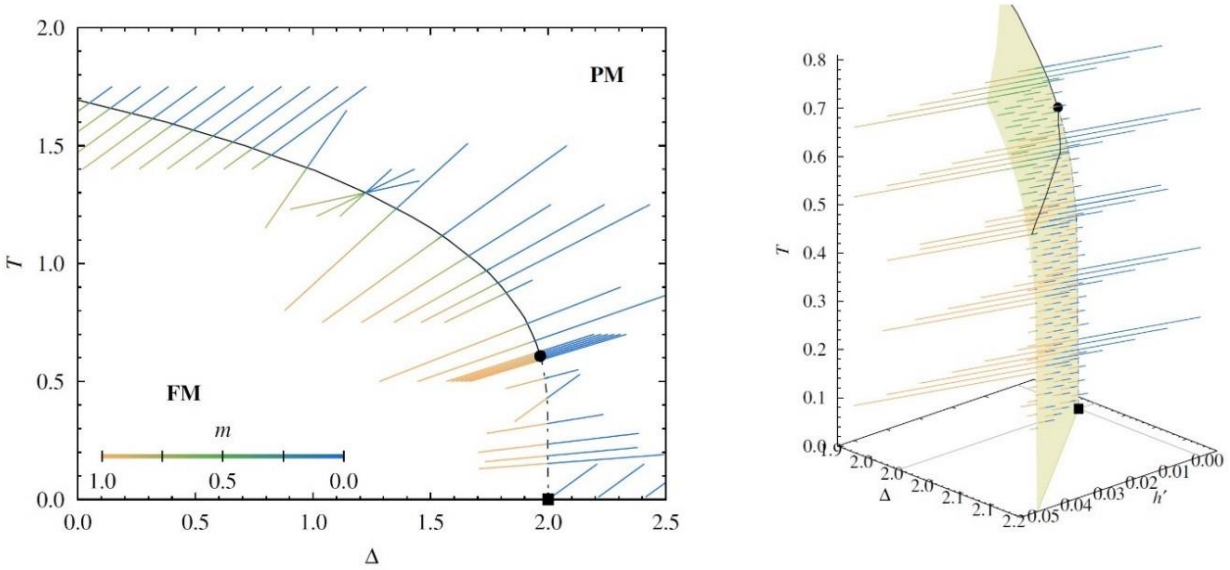

Figure 7.7. *Heat maps of the TRG magnetization along elementary coordination game cross sections of the Blume–Capel model in the absence and presence of an external magnetic field. The data used to draw the zero-field phase boundary were taken from Zierenberg et al.: Eur. Phys. J. Special Topics 226 (2017) 789.*

The first game combines an elementary coordination with self-dependent games (games, in which a player's payoffs are independent of their opponent's strategy choice) that respect and break the symmetry of its two coordinated strategies. This game model is equivalent to an unusual parametrization of the Blume–Capel model of statistical physics: The presence of the neutral, non-coordinated strategies acts as an effective temperature-dependent crystal field and thus defines oblique cross sections of the phase diagram of the Blume–Capel model. (see Fig. 7.7.)

The second, five-strategy game models the interplay between different elementary coordination components. It consists of two competing coordination-type subgames, one involving the first two strategies that has the symmetry of the Ising model and one that involves the last three strategies and has the symmetry of the Potts model.

The results obtained using the TRG method are consistent with the expected properties (order, location, critical exponents, etc.) of the various order–disorder phase transitions of the two games, they corroborate and extend the existing literature of both models. [Ref. 7.5, Ref. 7.6]

Evolutionarily stable payoff matrix in hawk–dove games

OTKA PD 138571

B. Király, T. Varga, Gy. Szabó, J. Garay***
** Bolyai Institute, University of Szeged,*
*** Institute of Evolution, HUN-REN Centre for Ecological Research*

The classical evolutionary models of game theory typically assume that the interactions are fixed and the players can only alter their payoffs by adapting their behaviour. Most real decision situations are not like this, as their outcomes clearly depend on not only the behaviour but also the abilities of the players involved, which may also change over time. To study the effects of this broader decision space, we introduced a modified version of the hawk–dove game in which each player phenotype is defined through two independent attributes, one that describes behaviour and one that quantifies a trait that determines interaction outcomes. In the original hawk–dove game, two players contest a resource using one of two strategies: A player who chooses the "dove" strategy will avoid conflict at all cost, while a player who chooses the "hawk" strategy will always escalate conflict, to the point of causing or receiving grievous injury, if necessary. When both players choose the same pure strategy, the winner is chosen randomly. In our modified version, the players have an additional evolving phenotypic trait called fighting ability, which determines the probability of winning and the cost of losing escalated hawk–hawk conflicts. (Fig. 7.8 shows a hawk–hawk payoff function constructed in this manner.)

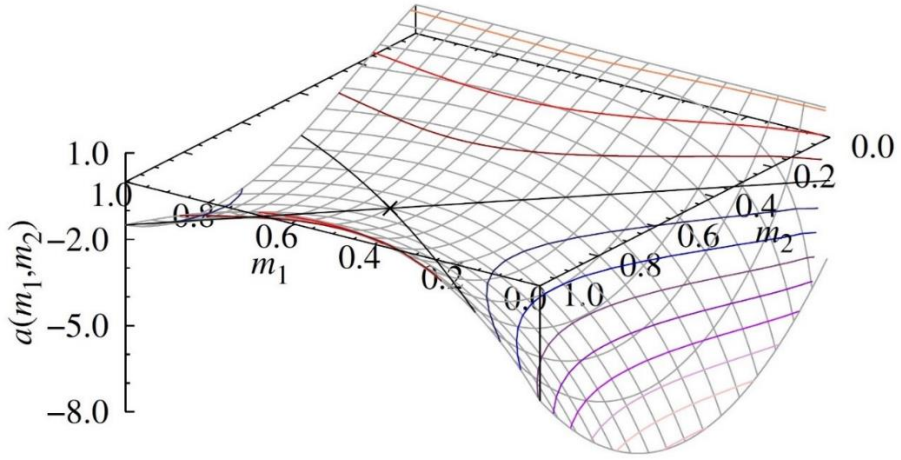

Figure 7.8. *An example of a trait-dependent hawk–hawk interaction payoff function whose corresponding game has a non-trivial evolutionarily stable phenotype. × evaluates the payoff function at the evolutionarily stable phenotype.*

We studied the modified game in a framework consistent with the monomorphic model setup of Maynard Smith and Price. Applying the classical verbal definition of evolutionary stability ("a strategy such that, if most of the members of a population adopt it, there is no 'mutant' strategy that would give higher reproductive fitness", J. Maynard Smith, G. R. Price, Nature 248 (1973) 15), we defined evolutionary stable phenotypes as consisting of an evolutionarily stable strategy and an evolutionarily stable trait (and a corresponding evolutionarily stable payoff matrix), and determined the sufficient conditions for their existence in our modified hawk–dove game. We found that the maximal possible cost of escalating conflicts remains constant in the limit of fast behavioural and slow trait evolution. [Ref. 7.7]

REFERENCES

[Ref. 1.1] Aitor García-Ruiz, Sergey Slizovskiy, Marcin Mucha-Kruczyński*, and Vladimir I. Fal'ko : Spectroscopic Signatures of Electronic Excitations in Raman Scattering in Thin Films of Rhombohedral Graphite Nano Lett. 19, 6152–6156 (2019)
[Ref. 1.2] Andrew McEllistrim, Aitor Garcia-Ruiz, Zachary A. H. Goodwin, and Vladimir I. Fal'ko: Spectroscopic signatures of tetralayer graphene polytypes Phys. Rev. B 107, 155147 (2023)
[Ref. 2.1] N. Nagy, "Contact Angle Determination on Hydrophilic and Superhydrophilic Surfaces by Using *r–θ*-Type Capillary Bridges" LANGMUIR, vol. 35, iss. 15, 5202-5212, 2019.
[Ref. 2.2] N. Nagy, " Capillary Bridges on Hydrophobic Surfaces: Analytical ContactAngle Determination" LANGMUIR, vol. 38, iss. 19, 6201-6208, 2022.
[Ref. 2.3] Zámbó, D.; Kovács, D.; Südi, G.; Zolnai, Z.; Deák, A. Composite Ligand Shells on Gold Nanoprisms – an Ensemble and Single Particle Study. RSC Adv. 2023, 13 (44), 30696–30703. https://doi.org/10.1039/D3RA05548E.
[Ref. 2.4] Kovács, D.; Deák, A.; Radnóczi, G. Z.; Horváth, Z. E.; Sulyok, A.; Schiller, R.; Czömpöly, O.; Zámbó, D. Position of Gold Dictates the Photophysical and Photocatalytic Properties of Cu2O in Cu2O/Au Multicomponent Nanoparticles. J. Mater. Chem. C 2023, 11 (26), 8796–8807. https://doi.org/10.1039/D3TC01213A.
[Ref. 2.5] Back Cover. J. Mater. Chem. C 2023, 11 (26), 9038–9038. https://doi.org/10.1039/D3TC90154H.
[Ref. 2.6] C. Major, G. Juhasz, Z. Labadi, M. Fried, "High speed spectroscopic ellipsometry technique for on-line monitoring in large area thin layer production," 2015 IEEE 42nd Photovoltaic Specialist Conference (PVSC), 2015, pp. 1-6, doi: 10.1109/PVSC.2015.7355640
[Ref. 2.7] G. Juhász, Z. Horváth, C. Major, P. Petrik, O. Polgár, M. Fried, Non-collimated beam ellipsometry, Physica Status Solidi C Volume 5, Issue 5 p. 1081-1084, https://doi.org/10.1002/pssc.200777862
[Ref. 2.8] Horváth Z Gy, Juhász G, Fried M, Major C, Petrik P: Imaging optical inspection device with a pinhole camera; EP2160591B1, Submission Number: PCT/HU2008/000058, NSZO: G01N21/8422, Country of patent: Europe
[Ref. 2.9] J. W. P. Bakker, H. Arwin, I. Lundström, and D. Filippini: Computer screen photoassisted off-null ellipsometry, Applied Optics Vol. 45, Issue 30, pp. 7795-7799 (2006), https://doi.org/10.1364/AO.45.007795
[Ref. 2.10] Nugusse, Berhane ; Juhász, György ; Major, Csaba ; Petrik, Péter ; Kálvin, Sándor ; Horváth, Zoltán György ; Fried, Miklós, Multi-color ellipsometric mapping tool from cheap parts, SPIE Proceedings Volume 12428, Photonic Instrumentation Engineering X; 124280H (2023), https://doi.org/10.1117/12.2649926
[Ref. 2.11] Granqvist, C.G. Handbook of Inorganic Electrochromic Materials, Elsevier: Amsterdam, The Netherlands, (1995)
[Ref. 2.12] Noor, Taha Ismaeel ; Lábadi, Zoltán ; Petrik, Peter ; Fried, Miklós, Investigation of Electrochromic, Combinatorial TiO2-SnO2 Mixed Layers by Spectroscopic Ellipsometry Using Different Optical ModelsMaterials 2023, 16(12), 4204.
[Ref. 2.13] Berg, S., Särhammar, E., Nyberg, T. Upgrading the "Berg-Model" for Reactive Sputtering Processes. Thin Solid Films. 2014, 565, 186–192.
[Ref. 2.14] Wijaya, E., Lenaerts, C., Maricot, S., Hastanin, J., Habraken, S., Vilcot, J.-P., Boukherroub, R., and Szunerits, S., "Surface plasmon resonance-based biosensors: From the development of different spr structures to novel surface functionalization strategies," Current Opinion in Solid State and Materials Science 15(5), 208–224 (2011).
[Ref. 2.15] Gong, C. and Leite, M. S., "Noble metal alloys for plasmonics," ACS Photonics 3(4), 507–513 (2016).
[Ref. 2.16] West, P., Ishii, S., Naik, G., Emani, N., Shalaev, V., and Boltasseva, A., "Searching for better plasmonic materials," Laser & Photonics Reviews 4(6), 795–808 (2010).
[Ref. 2.17] Kretschmann, E. and Raether, H., "Notizen: Zur plasmaresonanzemission im festen körper," Zeitschrift fűr Naturforschung A 23(4), 615–617 (1968).
[Ref. 2.18] F. Riesz, "Visual Approach to the Imaging of Magic Mirrors (Makyohs)," RESULTS IN OPTICS, vol. 12, art. 100477, 2023.
[Ref. 3.1] Yao Yao, Daniel F. Fernandes, Tereza Košutová, Tomas Kubart, Zhen Zhang, François Lefloch, Frédéric Gustavo, Axel Leblanc, János L. Lábár, Béla Pécz, Shi-Li Zhang; Self-aligned formation of superconducting sub-5 nm PtSi films. APL Quantum 1 June 2024; 1 (2): 026112. https://doi.org/10.1063/5.0205444
[Ref 3.2] Berg, S., Särhammar, E., Nyberg, T. Upgrading the "Berg-Model" for Reactive Sputtering Processes. Thin Solid Films. 2014, 565, 186–192.
[Ref. 3.3] M. Kroker, P. Souček, L. Zábranský, V. Buršíková, Zs. Czigány, V. Sochora, K. Balázsi, M. Jílek, P. Vašina Industrially deposited hard and damage resistant W-B-C coatings, Surface & Coatings Technology 454 (2023) 129150
[Ref. 3.4] J. Ženíšek, P. Souček, P. Ondračka, Zs. Czigány, V. Buršiková, D. Holec, K. Balázsi, P. Vašina - Effect of Nb incorporation in Mo_2BC coatings on structural and mechanical properties — ab initio modelling and experiment, Acta Materialia 268 (2024) 119741
[Ref. 3.5] Sáfrán G, Petrik P, Szász N, Olasz D, Chinh NQ, Serényi M. Review on High-Throughput Micro-Combinatorial Characterization of Binary and Ternary Layers towards Databases. Materials. 2023; 16(8):3005. https://doi.org/10.3390/ma16083005
[Ref. 3.6] L. J Murray, The aluminium-copper system. International Metals Reviews 30 (1985): 211 - 234.
[Ref. 3.7] W. Bedjaoui; Z. Boumerzoug, F. Delaunois: Solid-State Diffusion Welding of Commercial Aluminum Alloy with Pure Copper Int. J. Automot. Mech. Eng. 2022, 19, 9734.

[Ref. 3.8] Olasz, D.; Kis, V.; Cora, I.; Németh, M.; Sáfrán, G. High-Throughput Micro-Combinatorial TEM Phase Mapping of the DC Magnetron Sputtered YxTi1−xOy Thin Layer System. *Nanomaterials* 2024, *14*, 925. https://doi.org/10.3390/nano14110925
[Ref. 3.9] Korányi, T.I.; Németh, M.; Beck, A.; Horváth, A. Recent Advances in Methane Pyrolysis: Turquoise Hydrogen with Solid Carbon Production. Energies 2022, 15, 6342. https://doi.org/10.3390/en15176342
[Ref. 3.10] Horváth, A., Németh, M., Beck, A., Sáfrán, G., Horváth, Z.E., Rigó, I., May, Z., Korányi, T.I. Applied Catalysis A: General, 2024, 676, 119651.
[Ref. 3.11] Silva C., Salmanzade K., Borbáth I., Dódony E., Olasz D., Sáfrán Gy., Kuncser A., Pászti-Gere E., Tompos A., Pászti Z.; Reductive Treatment of Pt Supported on Ti0.8Sn0.2O2-C Composite: A Route for Modulating the Sn–Pt Interactions; NANOMATERIALS 13 : 15 Paper: 2245 , 23 p. (2023)
[Ref. 4.1] N. Q. Khánh, Z. E. Horváth, Z. Zolnai, P. Petrik, L. Pósa, és J. Volk, Materials Science in Semiconductor Processing, 169, (2024) 107902
[Ref. 4.2] Gallium Oxide: Technology, Devices and Application, ed. S. Pearton, F. Ren and M. Mastro, Elsevier, 2018, ISBN: 9780128145210 (e-book), ISBN: 9780128145227 (Imprint)
[Ref. 4.3] I. Cora, F. Mezzadri, F. Boschi, M. Bosi, M. Čaplovičová, B. Pécz: The real structure of ε-Ga2O3 and its relation to κ-phase. Cryst. Eng. Comm. 19 (2017) 1509
[Ref. 4.4] R. Fornari, M. Pavesi, V. Montedoro, D. Klimm, F. Mezzadri, I. Cora, B. Pécz, B., F. Boschi, A. Parisini, A. Baraldi, C. Ferrari, E. Gombia, M. Bosi (2017). Thermal stability of ε-Ga 2 O 3 polymorph. Acta Materialia. 140. 10.1016/j.actamat.2017.08.062.
[Ref. 4.5] C. Sturm; J. Furthmüller; F. Bechstedt; R. Schmidt-Grund; M. Grundmann APL Materials. 3 (2015) 106106
[Ref. 4.6] G. Akselrod, M. S. Akselrod E. R. Benton, and N. Yasuda, Nucl. Intr. Meth. B: 247 (2006) 295.
[Ref. 4.7] J. D. Brewer, B. T. Jeffries, and G. P. Summers, Phys. Rev. B: 22 (1980) 4900.
[Ref. 4.8] B. D. Evans and M. Stapelbroek, Phys. Rev. B: 18 (1978) 7089.
[Ref. 4.9] L. Pósa et al., Interplay of thermal and electronic effects in the mott transition of nanosized VO2 phase change memory devices, ACS Applied Nano Materials 6 (2023) 9137–9147.
[Ref. 4.10] S. W. Schmid et al. „Picosecond Femtojoule Resistive Switching in Nanoscale VO 2 Memristors", ACS Nano, 18 (2024) 21966–21974
[Ref. 4.11] S.A. Jewett, M.S. Makowski, et al., Gallium nitride is biocompatible and non-toxic before and after functionalisation with peptides, Acta Biomaterialia 8, 2 (2012) 728-7333.
[Ref. 4.12] J. Jiang, Q. Wang, B. Wang: Direct lift-off and the piezo-phototronic study of InGaN/GaN heterostructure membrane, Nano Energy 59 (2019) 545–552.
[Ref. 5.1] Ferenc Bíró, András Deák, Csaba Dücső, Zoltán Hajnal, "Microheater with uniform surface temperature", Utility model: U 20 001150, registration number 5279
[Ref. 5.2] L. Harasztosi, I. A. Szabó, F. Bíró, R. Gy. Kiss, G. Battistig, Temperature Calibration of Twin Micro-heater Based Microcalorimeter, Sensors&Transducers 260 : 1 2023
[Ref. 5.3] Bozorádi János Márk: 3D MEMS erőmérő szenzorok alkalmazása biomechanikai vizsgálatokra, 36. OTDK Műszaki Tudományi Szekció, Egészségtudomány 1 Tagozat, II. HELYEZÉS – témavezető: Fürjes Péter
[Ref. 5.4] A. Bányai, E. Farkas, H. Jankovics, I. Székács, E. L. Tóth, F. Vonderviszt, R. Horváth, M. Varga, P. Fürjes, Dean-Flow Affected Lateral Focusing and Separation of Particles and Cells in Periodically Inhomogeneous Microfluidic Channels, SENSORS 23 (2) 800, 2023 (IF: 3.576)
[Ref. 5.5] Bányai A., Bató L., Leelőssyné Tóth E., Varga M., Fürjes P., Áramlástani jelenségek mikroszkopikus mérettartományban – mikrofluidikai rendszerek és alkalmazásaik, Fizikai Szemle LXXIII 383-389, 2023
[Ref. 5.6] Lilia Bató, Péter Fürjes, An obstacle-free microfluidic system for monitoring protein diffusion, XXIX. Congress of the Hungarian Association of Biophysics, Budapest, Hungary, 2023
[Ref. 5.7] Lilia Bató, Péter Fürjes, Microfluidic System With Integrated Electrode Array for High-Throughput EIS Analysis of Localised Cells, Proceedings of Eurosensors 2023 Conference, Lecce, Italy, 2023 (MDPI Proceedings, oralpresentation)
[Ref. 5.8] Zsombor Szomor, Eszter L. Tóth, Péter Fürjes, Finite element modelling and analysis of fluid dynamic phenomena in two-phase droplet based microfluidic systems, XXIX. Congress of the Hungarian Association of Biophysics, Budapest, Hungary, 2023
[Ref. 5.9] Zsombor Szomor, Eszter L. Tóth, Péter Fürjes, 3D Finite Element Modelling of Heat Transfer in Continuous Flow Two-phase Droplet Microfluidic Systems Using On-chip Thermal Control, Therminic 2023 – 29th International Workshop for Thermal Investigations of ICs and Systems, Budapest, Hungary, 2023, https://doi.org/10.1109/THERMINIC60375.2023.10325685
[Ref. 5.10] Fürjes P., Szabó. Z., Új hazai fejlesztés is hozzájárulhat a gyógyszerhatóanyag-vizsgálatok felgyorsításához, Innotéka 2023/09
[Ref. 5.11] Zoltán Szabó, Kitti Pankász, János Márk Bozorádi, Orsolya Hakkel, Szabolcs Bella, Bianka Fabinyi, Sandro Meucci, Péter Fürjes, Microfluidic Cuvette for Near Infrared Spectroscopy, Proceedings of Eurosensors 2023 Conference, Lecce, Italy, 2023 (MDPI Proceedings, oralpresentation)
[Ref. 5.12] Zsombor Szomor, Lilia Bató, Csaba Dücső, Zsófia Baji, Péter Fürjes, Non-Stoichiometric Titanium-Oxide Gate Electrodes for EGFET Based pH Sensors, Proceedings of Eurosensors 2023 Conference, Lecce, Italy, 2023 (MDPI Proceedings, oralpresentation)
[Ref. 6.1.] A. Bányai, E. Farkas, H. Jankovics, I. Székács, E. Leelőssyné Tóth, F. Vonderviszt, R. Horváth, M. Varga (77E), P. Fürjes, "Dean-flow affected lateral focusing and separation of particles and cells in periodically inhomogeneous microfluidic channels", SENSORS, vol. 23, 2023

[Ref. 6.2] B. Péter, B. Majoros, S. Kurunczi, A. V. Ács, I. Szekacs, Sz. Bősze, G. M. Kovács, I. Boldizsár, R. Horvath, „Label-free biosensing of lignans for therapeutics using engineered model surfaces", INTERNATIONAL JOURNAL OF BIOLOGICAL MACROMOLECULES, vol. 233., 2023.
[Ref. 6.3] I. Bányász, I. Rajta, V. Havránek, A. Mackova, A. J. Laki, M. S. Z. Kellermayer, Z. Szittner, S. Kurunczi, Sz. Novák, I. Székács, R. Horváth, M. Fried, G. U. L. Nagy, „Design, fabrication, and characterization of picowell arrays on cyclic olefin copolymer surfaces generated with a 10.5 MeV N4+ ion microbeam", APPLIED PHYSICS LETTERS, vol. 123, 2023
[Ref. 6.4] K. D. Kovács, T. Visnovitz, T. Gerecsei, B. Peter, S. Kurunczi, A. Koncz, K. Németh, D. Lenzinger, K. V. Vukman, A. Balogh, I. Rajmon, P. Lőrincz, I. Székács, E. I. Buzás, R. Horvath, „Nanoinjection of extracellular vesicles to single live cells by robotic fluidic force microscopy", JOURNAL OF EXTRACELLULAR VESICLES, vol. 12, 2023.
[Ref. 6.5] M. Wasilewska, A. Michna, A. Pomorska, K. Wolski, S. Zapotoczny, E. Farkas, Z. Szittner, I. Szekacs, R. Horvath, „Polysaccharide-based nano-engineered multilayers for controlled cellular adhesion in label-free biosensors", INTERNATIONAL JOURNAL OF BIOLOGICAL MACROMOLECULES, vol. 247, 2023.
[Ref. 7.1] A. Szolnoki, X, Chen, "When faster rotation is harmful: The competition of alliances with inner blocking mechanism" Physical Review Research **6** (2024) 02387.
[Ref. 7.2] B. Hartmann, S. Deng, G. Ódor, and J. Kelling: Revisiting and Modeling Power-Law Distributions in Empirical Outage Data of Power Systems, PRX Energy 2, (2023) 033007.
[Ref. 7.3] G. Pál, Zs. Danku, A. Batool, V. Kádár, N. Yoshioka, N. Ito, G. Ódor, F. Kun: Scaling laws of failure dynamics on complex networks Scientific Reports, 13 (2023) 19733.
[Ref. 7.4] C. Hauert and G. Szabó, Spontaneous symmetry breaking of cooperation between species, PNAS Nexus 3 (2024) 326.
[Ref. 7.5] B. Király: A tensor renormalization group analysis of the Blume–Capel model inspired by game theory, Physica A 630 (2023) 129296
[Ref. 7.6] B. Király: A tensor renormalization group analysis of an evolutionary game of competing Ising and Potts subgames, Phys. Lett. A 502 (2024) 129392
[Ref. 7.7] B. Király, T. Varga, Gy. Szabó, J. Garay: Evolutionarily stable payoff matrix in hawk–dove games, BMC Ecol. Evol. 24 (2024) 65

FULL LIST OF MFA PUBLICATIONS IN 2023

1. A. Q. Ahmed, D. Olasz, E. V. Bobruk, R. Z. Valiev, and N. Q. Chinh, “Effect of the Equal Channel Angular Pressing on the Microstructure and Phase Composition of a 7xxx Series Al-Zn-Mg-Zr Alloy.,” *MATERIALS*, vol. 16, no. 19, 2023.
2. G. Alkhalil, J. A. Burunkova, A. Csik, B. Döncző, M. Szarka, P. Petrik, S. Kökényesi, and N. Saadaldin, “Photoinduced structural transformations of Au-As2S3 nanocomposite impregnated in silica porous glass matrix,” *JOURNAL OF NON-CRYSTALLINE SOLIDS*, vol. 610, 2023.
3. Z. Baji, L. Pósa, G. Molnár, Z. Szabó, M. Volom, A. K. Surca, G. Drazic, and J. Volk, “VO2 layers with high resistive switching ratio by atomic layer deposition,” *MATERIALS SCIENCE IN SEMICONDUCTOR PROCESSING*, vol. 162, 2023.
4. K. Bajnok, Z. Kovács, B. Döncző, M. Rigo, L. Maritan, and G. Szakmány, “Understanding technological choices in the production of early medieval marble tempered coarse wares in Pannonia,” *PLINIUS: SUPPLEMENTO ITALIANO ALL EUROPEAN JOURNAL OF MINERALOGY*, vol. 48, no. Special Issue, pp. 72–72, 2023.
5. L. Balázs, F. Braun, and J. Lengyel, “Energy Saving Potential of Traffic-Regulated Street Lighting,” *SUSTAINABILITY*, vol. 15, no. 8, 2023.
6. Z. Bálint, G. Katona, S. Sáfián, S. Collins, G. Piszter, K. Kertész, and L. P. Biró, “Measuring and Modelling Structural Colours of Euphaedra neophron (Lepidoptera: Nymphalidae) Finely Tuned by Wing Scale Lower Lamina in Various Subspecies,” *INSECTS*, vol. 14, no. 3, 2023.
7. A. Balogh, K. D. Kovács, I. Rajmon, I. Székács, B. Peter, and R. Horvath, “Label-free tracking of cell adhesion kinetics as a function of various parameters,” in *Magyar Biofizikai Társaság XXIX. Kongresszusa*, 2023, pp. 102–102.
8. A. Bányai, L. Bató, T. E. Leelőssyné, M. Varga, and P. Fürjes, “Áramlástani jelenségek mikroszkopikus mérettartományban – mikrofluidikai rendszerek és alkalmazásaik,” *FIZIKAI SZEMLE*, vol. 73, no. 11, pp. 383–389, 2023.
9. A. Bányai, E. Farkas, H. Jankovics, I. Székács, E. L. Tóth, F. Vonderviszt, R. Horváth, M. Varga, and P. Fürjes, “Dean-Flow Affected Lateral Focusing and Separation of Particles and Cells in Periodically Inhomogeneous Microfluidic Channels,” *SENSORS*, vol. 23, no. 2, 2023.
10. I. Bányász, I. Rajta, V. Havránek, A. Mackova, A. J. Laki, M. S. Z. Kellermayer, Z. Szittner, S. Kurunczi, S. Novák, I. Székács, R. Horváth, M. Fried, and G. U. L. Nagy, “Design, fabrication, and characterization of picowell arrays on cyclic olefin copolymer surfaces generated with a 10.5 MeV N4+ ion microbeam,” *APPLIED PHYSICS LETTERS*, vol. 123, no. 5, 2023.
11. B. P. Barna, “Elmaradt beszélgetés Keszthelyi Lajossal,” *FIZIKAI SZEMLE*, vol. 73, no. 3, pp. 77–84, 2023.
12. I. Bársony, T. Dózsa, J. Radó, A. Nagy, F. Braun, E. Simonyi, G. Battistig, A. Soumelidis, P. Kovács, and J. Volk, “Tire Deformation Monitoring Sensor for Advanced Driver-Assistance Systems.” 2023.
13. L. Bató and P. Fürjes, “An obstacle-free microfluidic system for monitoring protein diffusion,” in *Magyar Biofizikai Társaság XXIX. Kongresszusa*, 2023, pp. 48–48.
14. L. Bató and P. Fürjes, “Microfluidic system with integrated electrode array for EIS analysis of localised cells.” 2023.
15. T. Bebesi, M. Pálmai, A. Gaál, I. Csilla Szigyarto, O. Bálint-Hakkel, Z. Varga, and J. Mihály, “Spectroscopic study of extracellular vesicles using plasmonic nanoobjects,” in *12th International Conference on Advanced Vibrational Spectroscopy (ICAVS12)*, 2023, pp. 89–89.
16. T. Benkó, S. Shen, M. Németh, J. Su, Á. Szamosvölgyi, Z. Kovács, G. Sáfrán, S. M. Al-Zuraiji, Z. E. Horváth, A. Sápi, Z. Kónya, and J. S. Pap, “BiVO4 charge transfer control by a water-insoluble iron complex for solar water oxidation,” *APPLIED CATALYSIS A-GENERAL*, vol. 652, 2023.
17. H. R. Ben Zine, Z. E. Horváth, K. Balázsi, and C. Balázsi, “Novel Alumina Dispersion-Strengthened 316L Steel Produced by Attrition Milling and Spark Plasma Sintering,” *COATINGS*, vol. 13, no. 2, 2023.
18. D. Bereczki, I. Lidia Haffaressas, P. Fürjes, and A. Füredi, “Optical parameters of leukemia-related chemotherapeutic drugs.” 2023.
19. S. Bilicz, S. Gyimóthy, and G. Vértesy, “Electromagnetic Non-Destructive Evaluation (XXIV).” 2023.
20. I. Borsos, “Generating small random grids with a given number of occupied sites.” 2023.
21. J. M. Bozorádi, A. Nagy, J. Radó, P. Földesy, I. Bársony, G. Papp, C. Dücső, and P. Fürjes, “Characterisation tissue elasticity by MEMS force sensors.” 2023.
22. J. Budai, Z. Pápa, P. Petrik, and P. Dombi, “Ellipsometric probing of hot electrons in plasmonic media,” in *Proceedings of the 13th International Conference on Metamaterials, Photonic Crystals and Plasmonics, META 2023*, 2023, pp. 287–288.
23. J. Budai, Z. Pápa, P. Petrik, and P. Dombi, “Ultrasensitive Optical Probing of Plasmonic Hot Electron Occupancies,” in *2023 Conference on Lasers and Electro-Optics Europe & European Quantum Electronics Conference (CLEO/Europe-EQEC)*, 2023.

24. A. Cadena, Á. Pekker, B. Botka, E. Dodony, Z. Fogarassy, B. Pécz, and K. Kamarás, “Encapsulation of the Graphene Nanoribbon Precursor 1, 2, 4-trichlorobenzene in Boron Nitride Nanotubes at Room Temperature,” *PHYSICA STATUS SOLIDI - RAPID RESEARCH LETTERS*, vol. 17, no. 1, 2023.
25. P. Castenetto, P. Lambin, and P. Vancsó, “Edge Magnetism in MoS2 Nanoribbons: Insights from a Simple One-Dimensional Model,” *NANOMATERIALS*, vol. 13, no. 24, 2023.
26. N. Q. Chinh, D. Olasz, A. Q. Ahmed, E. V. Bobruk, and R. Z. Valiev, “Review on Grain Size- and Grain Boundary Phenomenon in Unusual Mechanical Behavior of Ultrafine-Grained Al Alloys,” *MATERIALS TRANSACTIONS (2001-)*, vol. 64, no. 8, pp. 1844–1855, 2023.
27. N. Q. Chinh, D. Olasz, A. Q. Ahmed, G. Sáfrán, J. Lendvai, and T. G. Langdon, “Modification of the Hall-Petch relationship for submicron-grained fcc metals,” *MATERIALS SCIENCE AND ENGINEERING A-STRUCTURAL MATERIALS PROPERTIES MICROSTRUCTURE AND PROCESSING*, vol. 862, 2023.
28. C. Cretu, R. Nicola, S.-A. Marinescu, E.-M. Picioruș, M. Suba, C. Duda-Seiman, A. Len, L. Illés, Z. E. Horváth, and A.-M. Putz, “Performance of Zr-Based Metal–Organic Framework Materials as In Vitro Systems for the Oral Delivery of Captopril and Ibuprofen,” *INTERNATIONAL JOURNAL OF MOLECULAR SCIENCES*, vol. 24, no. 18, 2023.
29. S. Czene, N. Jegenyes, O. Krafcsik, S. Lenk, Z. Czigány, G. Bortel, K. Kamarás, J. Rohonczy, D. Beke, and A. Gali, “Amino-Termination of Silicon Carbide Nanoparticles,” *NANOMATERIALS*, vol. 13, no. 13, 2023.
30. Z. Czigány, *Structure and Phase Transformations in Thin Films*. Basel: MDPI, 2023.
31. Z. Czigány, “Structure and Phase Transformations in Thin Films,” *COATINGS*, vol. 13, no. 7, 2023.
32. Z. Czigány and V. Kovács Kis, “Acquisition and evaluation procedure to improve the accuracy of SAED,” *MICROSCOPY RESEARCH AND TECHNIQUE*, vol. 86, no. 2, pp. 144–156, 2023.
33. O. Czömpöly, M. Fábián, T. I. Korányi, G. Nagy, Z. E. Horváth, I. Zizak, S. Pollastri, M. Aertsens, and J. Osán, “Adsorption and diffusion of selenite on Boda Claystone Formation,” *APPLIED CLAY SCIENCE*, vol. 241, 2023.
34. B. Cserép, M. Szemerédi, S. Harangi, S. Erdmann, O. Bachmann, I. Dunkl, I. Seghedi, K. Mészáros, Z. Kovács, A. Virág, T. Ntaflos, D. Schiller, K. Molnár, and R. Lukács, “Constraints on the pre-eruptive magma storage conditions and magma evolution of the 56–30 ka explosive volcanism of Ciomadul (East Carpathians, Romania),” *CONTRIBUTIONS TO MINERALOGY AND PETROLOGY*, vol. 178, no. 12, 2023.
35. S. Deng and G. Ódor, “Critical behavior of the diffusive susceptible-infected-recovered model,” *PHYSICAL REVIEW E: COVERING STATISTICAL NONLINEAR BIOLOGICAL AND SOFT MATTER PHYSICS (2016-)*, vol. 107, no. 1, 2023.
36. E. Dodony, I. Dódony, and G. Sáfrán, “In-situ study of nickel silicide formation in thin films,” in *Symposium on Materials Science 2022*, 2023, pp. 32–33.
37. E. Dódony, I. Dódony, Z. Fogarassy, P. Pekker, and G. Sáfrán, “DIFFRAKCIÓS INTENZITÁS MÉRÉSEK TEM-BEN II.: AZ EWALD KORREKCIÓ KITERJESZTÉSE,” in *A Magyar Mikroszkópos Társaság éves konferenciájának kivonatkönyve 2023 : Book of the Abstracts of the Annual Conference of HSM 2023*, 2023, pp. 28–31.
38. E. Dódony, I. Dódony, Z. Fogarassy, P. Pekker, and G. Sáfrán, “A γ -NIKKEL-SZILICID SZERKEZETI VÁLTOZATOSSÁGA,” in *A Magyar Mikroszkópos Társaság éves konferenciájának kivonatkönyve 2023 : Book of the Abstracts of the Annual Conference of HSM 2023*, 2023, pp. 26–28.
39. T. Dózsa, A. Ámon, F. Braun, E. Simonyi, A. Soumelidis, J. Volk, and P. Kovács, “Towards intelligent tire development,” in *XIII. International Conference on Transport Sciences / XIII. Nemzetközi Közlekedéstudományi Konferencia, Győr*, 2023, pp. 145–155.
40. G. Dravecz, T. Kolonits, and L. Péter, “Formation of LiNbO3 Nanocrystals Using the Solvothermal Method,” *CRYSTALS*, vol. 13, no. 1, 2023.
41. R. Drevet, P. Souček, P. Mareš, M. Dubau, Z. Czigány, K. Balázsi, and P. Vašina, “Multilayer thin films of aluminum oxide and tantalum oxide deposited by pulsed direct current magnetron sputtering for dielectric applications,” *VACUUM*, vol. 210, 2023.
42. P. Dumas, M. Opprecht, S. Kerdilès, J. Lábár, B. Pécz, F. Lefloch, and F. Nemouchi, “Superconductivity in laser-annealed monocrystalline silicon films: The role of boron implant,” *APPLIED PHYSICS LETTERS*, vol. 123, no. 13, 2023.
43. M. El-Tahawy, L. Peter, J. Gubicza, G. Molnár, C. Li, L. Vitos, and I. Bakonyi, “Metastable Phase Formation in Electrodeposited Co-Rich Co-Cu and Co-Ni Alloys,” *JOURNAL OF THE ELECTROCHEMICAL SOCIETY*, vol. 170, 2023.
44. E. Farkas, K. D. Kovács, B. Peter, A. Bonyár, S. Kurunczi, I. Szekacs, and R. Horvath, “Controlling Live Cell Adhesion through Characterization of Biofunctionalized Surfaces using Label-Free Biosensors,” in *Magyar Biofizikai Társaság XXIX. Kongresszusa*, 2023, pp. 108–108.
45. E. Farkas, “Development of functionalized and tunable cell adhesive layers using label-free optical biosensor.” 2023.
46. Z. Fogarassy, U. Kentsch, P. Panjan, and A. S. Racz, “Experimental and theoretical study on the production of carbide-rich composite nano-coatings,” *SURFACES AND INTERFACES*, vol. 38, 2023.
47. M. Furko, R. Detsch, I. Tolnai, K. Balázsi, A. R. Boccaccini, and C. Balázsi, “Biomimetic mineralized amorphous carbonated calcium phosphate-polycaprolactone bioadhesive composites as potential coatings on implant materials,” *CERAMICS INTERNATIONAL*, vol. 49, no. 11, pp. 18565–18576, 2023.
48. M. Furko, K. Balázsi, and C. Balázsi, “Calcium Phosphate Loaded Biopolymer Composites—A Comprehensive Review on the Most Recent Progress and Promising Trends,” *COATINGS*, vol. 13, no. 2, 2023.
49. A. Füredi and D. Bereczki, “Point-of-Care Therapeutic Drug Monitoring of chemotherapy from microvolume blood samples with a specifically designed microfluidic system.” 2023.

50. M. Gajdics, M. Serényi, T. Kolonits, A. Sulyok, Z. E. Horváth, and B. Pécz, "Reactive Sputter Deposition of Ga2O3 Thin Films Using Liquid Ga Target," *COATINGS*, vol. 13, no. 9, 2023.
51. N. G. Galkin, K. N. Galkin, D. L. Goroshko, S. A. Dotsenko, O. V. Kropachev, I. M. Chernev, E. Y. Subbotin, A. Y. Alekseev, D. B. Migas, Z. Fogarassy, B. Pecz, and A. K. Gutakovskii, "Ca silicide films-promising materials for silicon optoelectronics," *JAPANESE JOURNAL OF APPLIED PHYSICS (2008)*, vol. 62, no. SD, 2023.
52. A. Gasparics and A. Gilányi, "Mágneses képalkotás alkalmazási lehetősége összetett geometriájú alkatrészek roncsolásmentes vizsgálatára," *EINNOVÁCIÓ*, vol. 1, no. 1, pp. 94–107, 2023.
53. B. Gémes, E. Takács, I. Székács, R. Horváth, and A. Székács, "A glyphosate és szerkezeti analógjai gátló hatásának vizsgálata RGD-specifikus integrineken ELISA módszer alkalmazásával," *ÖKOTOXIKOLÓGIA*, vol. 5, no. 3–4, pp. 60–61, 2023.
54. B. Gergics, F. Vajda, M. Puskás, A. Füredi, and D. András Drexler, "Mathematical modeling of phototoxicity during fluorescent imaging of tumor spheroids," in *IEEE 27th International Conference on Intelligent Engineering Systems 2023 (INES 2023)*, 2023, pp. 291–296.
55. F. Giannazzo, S. E. Panasci, E. Schilirò, G. Greco, F. Roccaforte, G. Sfuncia, G. Nicotra, M. Cannas, S. Agnello, E. Frayssinet, Y. Cordier, A. Michon, A. Koos, and B. Pécz, "Atomic resolution interface structure and vertical current injection in highly uniform MoS2 heterojunctions with bulk GaN," *APPLIED SURFACE SCIENCE*, vol. 631, 2023.
56. F. Giannazzo, S. E. Panasci, E. Schiliro, P. Fiorenza, G. Greco, F. Roccaforte, M. Cannas, S. Agnello, A. Koos, B. Pecz, M. Spankova, and S. Chromik, "Highly Homogeneous 2D/3D Heterojunction Diodes by Pulsed Laser Deposition of MoS2 on Ion Implantation Doped 4H-SiC," *ADVANCED MATERIALS INTERFACES*, vol. 10, no. 1, 2023.
57. M. Gracheva, Z. Klencsár, V. Kovács Kis, K. A. Béres, Z. May, V. Halasy, A. Singh, F. Fodor, Á. Solti, L. F. Kiss, G. Tolnai, Z. Homonnay, and K. Kovács, "Iron nanoparticles for plant nutrition: Synthesis, transformation, and utilization by the roots of Cucumis sativus," *JOURNAL OF MATERIALS RESEARCH*, vol. 38, no. 4, pp. 1035–1047, 2023.
58. K. Hajagos-Nagy, F. Misják, P. Lobotka, and G. Radnóczi, "CU-MN RÉTEGEK MIKROSZERKEZETE ÉS ELEKTROMOS TULAJDONSÁGAI," in *A Magyar Mikroszkópos Társaság éves konferenciájának kivonatkönyve 2023 : Book of the Abstracts of the Annual Conference of HSM 2023*, 2023, pp. 36–38.
59. L. Harasztosi, A. I. Szabó, F. Biró, G. R. Kiss, and G. Battistig, "Temperature Calibration of Twin Micro-heater Based Microcalorimeter," *SENSORS AND TRANSDUCERS*, vol. 260, no. 1, pp. 7–13, 2023.
60. L. HARASZTOSI, I. A. SZABÓ, G. KISS Rebeka, and G. BATTISTIG, "Differenciális mikrokaloriméter hőmérséklettartományának kiterjesztése alacsony hőmérsékletű felhasználásokhoz," *ENELKO - SZÁMOKT*, pp. 1–6, 2023.
61. B. Hartmann, S. Deng, G. Ódor, and J. Kelling, "Revisiting and Modeling Power-Law Distributions in Empirical Outage Data of Power Systems," *PRX ENERGY*, vol. 2, no. 3, 2023.
62. M. Hegedűs, V. Kis, Á. Szabó, I. Kovács, N. Rózsa, and Z. Kovács, "Gradient structural anisotropy of dental enamel is optimized for enhanced mechanical behaviour," *MATERIALS AND DESIGN*, vol. 234, 2023.
63. N. Hegedüs, "Rádiófrekvenciás porlasztással előállított szilícium és szilíciumnitrid vékonyrétegek vizsgálata," Óbudai Egyetem, 2023.
64. P. Herman, D. Pércsi, T. Fodor, L. Juhász, Z. Dudás, Z. E. Horváth, V. Ryukhtin, A.-M. Putz, J. Kalmár, and L. Almásy, "Selective and high capacity recovery of aqueous Ag(I) by thiol functionalized mesoporous silica sorbent," *JOURNAL OF MOLECULAR LIQUIDS*, vol. 387, 2023.
65. L. Himics, D. Gál, P. Csíkvári, R. Holomb, M. Koós, A. Sulyok, B. Pécz, and M. Veres, "A modified plasma immersed solid-phase impurity assisted doping geometry for the creation of highly fluorescent CVD nanodiamond," *VACUUM*, vol. 216, 2023.
66. A. Horváth, A. Sulyok, C. Dücső, and R. Schiller, "Work function of titanium thin layers," *JOURNAL OF APPLIED PHYSICS*, vol. 134, no. 14, 2023.
67. R. Horvath, A. Bonyár, I. Szekacs, S. Kurunczi, B. Peter, K. Dóra Kovács, and E. Farkas, "Biomaterial surfaces for regulating live cell adhesion characterized by label-free biosensors." 2023.
68. N. T. Ismaeel, Z. Lábadi, P. Petrik, and M. Fried, "Investigation of Combinatorial TiO2-MoO3 Mixed Layers to Optimize the Electrochromic Properties." pp. 31–31, 2023.
69. M. Itatani, G. Holló, D. Zámbó, H. Nakanishi, A. Deák, and I. Lagzi, "Oppositely Charged Nanoparticles Precipitate Not Only at the Point of Overall Electroneutrality," *JOURNAL OF PHYSICAL CHEMISTRY LETTERS*, vol. 14, no. 40, pp. 9003–9010, 2023.
70. B. Jákri, M. Szemerédi, I. Dunkl, Z. Kovács, and E. Pál-Molnár, "Variszkuszi, S-típusú granitoidok a Codru-takarórendszerben (Erdélyi-khg.): a Galsai pluton kőzettani-geokémiai vizsgálata és korrelációja a Tiszai-főegységben," in *13. Kőzettani és Geokémiai Vándorgyűlés*, 2023, pp. 17–17.
71. B. Járki, M. Szemerédi, Z. Kovács, and E. Pál-Molnár, "Variscan S type granitoids in the Codru Nappe System (Apuseni Mts.): petrography, whole rock geochemistry and correlations in the Tisza Mega unit," in *53. Meeting of Young Geoscientists - Ifjú Szakemberek Ankétja*, 2023, pp. 73–75.
72. B. Kakasi, E. Gácsi, H. Jankovics, and F. Vonderviszt, "Extreme thermal stability of the antiGFP nanobody – GFP complex," *BMC RESEARCH NOTES*, vol. 16, no. 1, 2023.
73. M. H. Kaou, M. Furkó, K. Balázsi, and C. Balázsi, "Advanced Bioactive Glasses: The Newest Achievements and Breakthroughs in the Area," *NANOMATERIALS*, vol. 13, no. 16, 2023.
74. M. H. Kaou, Z. E. Horváth, K. Balázsi, and C. Balázsi, "Eco-friendly preparation and structural characterization of calcium silicates derived from eggshell and silica gel," *INTERNATIONAL JOURNAL OF APPLIED CERAMIC TECHNOLOGY*, vol. 20, no. 2, pp. 689–699, 2023.

75. K. Kertész, G. Piszter, A. Beck, A. Horváth, G. Nagy, G. Molnár, G. Z. Radnóczi, Z. E. Horváth, L. Illés, and L. P. Biró, "Hybrid Bio-Nanocomposites by Integrating Nanoscale Au in Butterfly Scales Colored by Photonic Nanoarchitectures," *PHOTONICS*, vol. 10, no. 11, 2023.
76. B. Király, "A tensor renormalization group analysis of the Blume–Capel model inspired by game theory," *PHYSICA A - STATISTICAL MECHANICS AND ITS APPLICATIONS*, vol. 630, 2023.
77. B. Király, I. Borsos, and G. Szabó, "Quantification and statistical analysis of topological features of recursive trees," *PHYSICA A - STATISTICAL MECHANICS AND ITS APPLICATIONS*, vol. 617, 2023.
78. T. Kolonits and M. Serényi, "Detailing the problem of the analytical solution for the reflectivity of a double-layer coating deposited from different refractive indexes films," in *Symposium on Materials Science 2022*, 2023, pp. 22–31.
79. G. Koplányi, E. Bell, Z. Molnár, G. Katona, P. L. Neumann, F. Ender, G. T. Balogh, P. Žnidaršič-Plazl, L. Poppe, and D. Balogh-Weiser, "Novel Approach for the Isolation and Immobilization of a Recombinant Transaminase," *CHEMBIOCHEM*, vol. 24, no. 7, 2023.
80. B. Kovács, A. Saftics, I. Székács, H. Jankovics, S. Kurunczi, F. Vonderviszt, and R. Horvath, "Flagellin: a convenient protein in biosensorics," in *Magyar Biofizikai Társaság XXIX. Kongresszusa*, 2023, pp. 49–49.
81. D. Kovács, A. Deák, G. Z. Radnóczi, Z. E. Horváth, A. Sulyok, R. Schiller, O. Czömpöly, and D. Zámbó, "Position of gold dictates the photophysical and photocatalytic properties of Cu2O in Cu2O/Au multicomponent nanoparticles," *JOURNAL OF MATERIALS CHEMISTRY C*, vol. 11, no. 26, pp. 8796–8807, 2023.
82. K. D. Kovács, T. Visnovitz, N. Kanyo, T. Gerecsei, B. Peter, I. Lagzi, S. Kurunczi, A. Koncz, K. Németh, D. Lenzinger, K. V. Vukman, K. Molnár, M. Truszka, H. Nakanishi, P. Lőrincz, I. Székács, E. I. Buzás, and R. Horvath, "Nanoinjection of fluorescent and gold nanoparticles to single live cells by robotic fluidic force microscopy." 2023.
83. K. D. Kovács, T. Visnovitz, T. Gerecsei, B. Peter, S. Kurunczi, A. Koncz, K. Németh, D. Lenzinger, K. V. Vukman, P. Lőrincz, I. Székács, E. I. Buzás, and R. Horvath, "Nanoinjection of fluorescent nanoparticles to single live cells by robotic fluidic force microscopy," in *Magyar Biofizikai Társaság XXIX. Kongresszusa*, 2023, pp. 35–35.
84. K. D. Kovács, T. Visnovitz, T. Gerecsei, B. Peter, S. Kurunczi, A. Koncz, K. Németh, D. Lenzinger, K. V. Vukman, A. Balogh, I. Rajmon, P. Lőrincz, I. Székács, E. I. Buzás, and R. Horvath, "Nanoinjection of extracellular vesicles to single live cells by robotic fluidic force microscopy," *JOURNAL OF EXTRACELLULAR VESICLES*, vol. 12, no. 12, 2023.
85. Z. Kovács-Krausz, D. Nagy, A. Márffy, B. Karpiak, Z. Tajkov, L. Oroszlány, J. Koltai, P. Nemes-Incze, S. P. Dash, P. Makk, S. Csonka, and E. Tóvári, "Signature of pressure-induced topological phase transition in ZrTe5." 2023.
86. Z. Kovács-Krausz, E. Tóvári, D. Nagy, A. Márffy, B. Karpiak, Z. Tajkov, L. Oroszlány, J. Koltai, P. Nemes-Incze, S. P. Dash, P. Makk, and S. Csonka, "Revealing the band structure of ZrTe5 using multicarrier transport," *PHYSICAL REVIEW B*, vol. 107, no. 7, 2023.
87. L. Kovács, T. Ferenci, B. Gombos, A. Füredi, I. Rudas, G. Szakács, and D. A. Drexler, "Positive Impulsive Control of Tumor Therapy—A Cyber-Medical Approach," *IEEE TRANSACTIONS ON SYSTEMS MAN AND CYBERNETICS: SYSTEMS*, vol. 54, no. 1, pp. 597–608, 2023.
88. M. Kroker, P. Souček, L. Zábranský, V. Buršíková, Z. Czigány, V. Sochora, K. Balázsi, M. Jílek, and P. Vašina, "Industrially deposited hard and damage resistant W-B-C coatings," *SURFACE AND COATINGS TECHNOLOGY*, vol. 454, 2023.
89. P. Kun, "Grafén nanométeres léptékű megmunkálásának hatásai a töltéshordozók szórási és vezetési folyamataira," Budapesti Műszaki és Gazdaságtudományi Egyetem, 2023.
90. Z. Labadi, C. Bakos, M. Szucs, A. Bonyar, D. Mukherjee, H. Jankovics, F. Vonderviszt, and P. Petrik, "Ellipsometry monitoring of sensor processes based on gold nanoparticle bonded proteins," *PROGRESS IN BIOMEDICAL OPTICS AND IMAGING (PROCEEDINGS OF SPIE)*, vol. 12395, 2023.
91. Z. Lábadi, "Fotonika villamosmérnököknek," in *KVK Habilitációs Workshop Minikonferencia*, 2023, pp. 49–54.
92. J. Lábár, B. Pécz, A. Sulyok, and F. Chiod, "SZUPRAVEZETŐ SZILÍCIUM," in *A Magyar Mikroszkópos Társaság éves konferenciájának kivonatkönyve 2023 : Book of the Abstracts of the Annual Conference of HSM 2023*, 2023, pp. 54–56.
93. J. L. Lábár, K. Hajagos-Nagy, P. P. Das, A. Gomez-Perez, and G. Radnóczi, "Simple ePDF: A Pair Distribution Function Method Based on Electron Diffraction Patterns to Reveal the Local Structure of Amorphous and Nanocrystalline Materials," *NANOMATERIALS*, vol. 13, no. 24, 2023.
94. J. L. Lábár, B. Pécz, W. A. van, G. Hallais, L. Desvignes, and F. Chiodi, "Strain Measurement in Single Crystals by 4D-ED," *NANOMATERIALS*, vol. 13, no. 6, 2023.
95. K. Lázár, L. K. Varga, V. Kovács-Kis, S. Stichleutner, A. Tegze, and Z. Klencsár, "Electric explosion of amorphous iron alloy ribbons in water and in ethylene glycol," *JOURNAL OF MATERIALS RESEARCH*, vol. 38, pp. 1090–1101, 2023.
96. H.-W. Lee, C. Cleveland, and A. Szolnoki, "Restoring spatial cooperation with myopic agents in a three-strategy social dilemma," *APPLIED MATHEMATICS AND COMPUTATION*, vol. 458, 2023.
97. H.-W. Lee, C. Cleveland, and A. Szolnoki, "Group-size dependent synergy in heterogeneous populations," *CHAOS SOLITONS & FRACTALS*, vol. 167, 2023.
98. S. Lipcsei, S. Kalácska, P. D. Ispánovity, J. L. Lábár, Z. Dankházi, and I. Groma, "Statistical properties of fractal type dislocation cell structures," *PHYSICAL REVIEW MATERIALS*, vol. 7, no. 3, 2023.
99. C. Liu, K. Lu, X. Chen, and A. Szolnoki, "Game-theoretical approach for task allocation problems with constraints," *APPLIED MATHEMATICS AND COMPUTATION*, vol. 458, 2023.
100. L. Liu, X. Chen, and A. Szolnoki, "Coevolutionary dynamics via adaptive feedback in collective-risk social dilemma game," *ELIFE*, vol. 12, no. 1, 2023.

101. B. Magyaródi, B. Kovács, I. Székács, and R. Horvath, “Role of glycocalyx in cancer cell adhesion: kinetics of interactions from label-free optical biosensor measurement,” in *Magyar Biofizikai Társaság XXIX. Kongresszusa*, 2023, pp. 113–113.
102. Ł. Maj, Z. Fogarassy, D. Wojtas, A. Jarzębska, F. Muhaffel, A. Sulyok, A. Góral, M. Kulczyk, H. Çimenoğlu, and M. Bieda, “In-situ formation of Ag nanoparticles in the MAO coating during the processing of cp-Ti,” *SCIENTIFIC REPORTS*, vol. 13, no. 1, 2023.
103. G. I. Márk, P. Vancsó, and A. Mayer, “New local pseudopotential for multilayer carbon materials and its application in wave packet dynamics,” *CARBON TRENDS*, vol. 13, 2023.
104. J. Markhulia, S. Kekutia, V. Mikelashvili, L. Saneblidze, T. Tsertsvadze, N. Maisuradze, N. Leladze, Z. Czigány, and L. Almásy, “Synthesis, Characterization, and In Vitro Cytotoxicity Evaluation of Doxorubicin-Loaded Magnetite Nanoparticles on Triple-Negative Breast Cancer Cell Lines,” *PHARMACEUTICS*, vol. 15, no. 6, 2023.
105. P. Márton, Ö. T. Nagy, D. Kovács, B. Szolnoki, J. Madarász, N. Nagy, G. S. Szabó, and Z. Hórvölgyi, “Barrier behaviour of partially N-acetylated chitosan layers in aqueous media,” *INTERNATIONAL JOURNAL OF BIOLOGICAL MACROMOLECULES*, vol. 232, 2023.
106. P. Mazzolini, Z. Fogarassy, A. Parisini, F. Mezzadri, D. Diercks, M. Bosi, L. Seravalli, A. Sacchi, G. Spaggiari, D. Bersani, O. Bierwagen, B. M. Janzen, M. N. Marggraf, M. R. Wagner, I. Cora, B. Pécz, A. Tahraoui, A. Bosio, C. Borelli, S. Leone, and R. Fornari, “Silane-Mediated Expansion of Domains in Si-Doped κ-Ga 2 O 3 Epitaxy and its Impact on the In-Plane Electronic Conduction,” *ADVANCED FUNCTIONAL MATERIALS*, vol. 33, no. 2, 2023.
107. B. Medgyes, A. Gharaibeh, G. Harsányi, B. Pécz, and I. Felhősi, “Electrochemical corrosion and electrochemical migration characteristics of SAC-1Bi-xMn solder alloys in NaCl solution,” *CORROSION SCIENCE*, vol. 213, 2023.
108. D. G. Merkel, K. Sájerman, T. Váczi, S. Lenk, G. Hegedűs, S. Sajti, A. Németh, M. A. Gracheva, P. Petrik, D. Mukherjee, Z. E. Horváth, D. L. Nagy, and A. Lengyel, “Laser irradiation effects in FeRh thin film,” *MATERIALS RESEARCH EXPRESS*, vol. 10, no. 7, 2023.
109. D. G. Merkel, S. Sajti, L. Deák, G. Hegedűs, Z. E. Horváth, and A. Lengyel, “Iron self-diffusion in B2-FeRh thin film,” *VACUUM*, vol. 218, 2023.
110. D. G. Merkel, G. Hegedűs, M. Gracheva, A. Deák, L. Illés, A. Németh, F. Maccari, I. Radulov, M. Major, A. I. Chumakov, D. Bessas, D. L. Nagy, Z. Zolnai, S. Graning, K. Sájerman, E. Szilágyi, and A. Lengyel, “Ion-induced nanopattern formation in FeRh thin films,” *ESRF HIGHLIGHTS*, vol. 2022, pp. 28–29, 2023.
111. D. G. Miklós, S. Józsa, Z. Kasztovszky, I. Harsányi, K. Gméling, Z. Kovács, F. Horváth, E. Starnini, and G. Szakmány, “Complex petrographic, micromineralogical and geochemical analysis of ground stone tools made of different types of sandstone from the Late Neolithic tell settlement of Hódmezővásárhely-Gorzsa (SE Hungary),” in *Anthropological insights into Ground Stone technologies (AGSTR 2023 - Paris)*, 2023, pp. 11–11.
112. D. G. Miklós, S. Józsa, Z. Kasztovszky, I. Harsányi, K. Gméling, Z. Kovács, and G. Szakmány, “Permian-Triassic red sandstones from the Balaton Highlands and the Mecsek Mountains. Comparative micromineralogical and geochemical study,” in *53. Meeting of Young Geoscientists - Ifjú Szakemberek Ankétja*, 2023, pp. 39–41.
113. D. Mukherjee, B. Kalas, S. Burger, G. Safran, M. Serenyi, M. Fried, and P. Petrik, “Nanostructures for in-situ surface-enhanced Kretschmann-Raether ellipsometry,” *PROCEEDINGS OF SPIE - THE INTERNATIONAL SOCIETY FOR OPTICAL ENGINEERING*, vol. 12428, pp. 206–214, 2023.
114. D. Mukherjee and P. Petrik, “Real-Time Ellipsometry at High and Low Temperatures,” *ACS OMEGA*, vol. 8, no. 4, pp. 3684–3697, 2023.
115. N. Nagy, “Contact angle determination by the Capillary Bridge Probe method: from perfect wetting to hydrophobic surfaces,” in *Symposium on Materials Science 2022*, 2023, pp. 18–19.
116. N. Nagy, “Capillary Bridge Probe method on hydrophobic surfaces: liquid bridges without neck or haunch,” in *Symposium on Materials Science 2022*, 2023, pp. 10–11.
117. P. Nagy, L. Péter, Z. Czigány, N. Q. Chinh, and J. Gubicza, “Processing and characterization of an electrodeposited nanocrystalline Co–Fe–Ni–Zn multi-principal element alloy film,” *SURFACE AND COATINGS TECHNOLOGY*, vol. 467, 2023.
118. P. L. Neumann, J. Radó, J. M. Bozorádi, and J. Volk, “AlGaN/GaN heterostructure based 3-dimensional force sensors,” *MICRO AND NANO ENGINEERING*, vol. 19, 2023.
119. T. I. Noor, Z. Lábadi, P. Petrik, and M. Fried, “Investigation of Electrochromic, Combinatorial TiO2-SnO2 Mixed Layers by Spectroscopic Ellipsometry Using Different Optical Models,” *MATERIALS*, vol. 16, no. 12, 2023.
120. S. Novák, Z. Szittner, I. Sallai, I. Székács, and R. Horvath, “Investigation of antibody-mediated adhesion force of individual immune cells using computer-controlled micropipette and fluidic force microscopy,” in *Magyar Biofizikai Társaság XXIX. Kongresszusa*, 2023, pp. 86–86.
121. B. Nugusse, G. Juhász, C. Major, P. Petrik, S. Kálvin, Z. György Horváth, and M. Fried, “Multi-color ellipsometric mapping tool from cheap parts,” in *Symposium on Materials Science 2022*, 2023, pp. 12–17.
122. B. Nugusse, G. Juhász, C. Major, P. Petrik, S. Kálvin, Z. G. Horváth, and M. Fried, “Multi-color ellipsometric mapping tool from cheap parts,” *PROCEEDINGS OF SPIE - THE INTERNATIONAL SOCIETY FOR OPTICAL ENGINEERING*, vol. 12428, pp. 134–141, 2023.
123. G. Ódor, I. Papp, S. Deng, and J. Kelling, “Synchronization transitions on connectome graphs with external force,” *FRONTIERS IN PHYSICS*, vol. 11, 2023.
124. G. Ódor and S. Deng, “Synchronization Transition of the Second-Order Kuramoto Model on Lattices,” *ENTROPY*, vol. 25, no. 1, 2023.

125. D. Olasz, K. V. Kovácsné, I. Cora, and G. Sáfrán, “Y-TI-O VÉKONYRÉTEGRENDSZER ÖSSZETÉTELFÜGGŐ SZERKEZETE: A PIROKLÓR SZERKEZETŰ Y2TI2O7 HATÉKONY ELŐÁLLÍTÁSA,” in *A Magyar Mikroszkópos Társaság éves konferenciájának kivonatkönyve 2023 : Book of the Abstracts of the Annual Conference of HSM 2023*, 2023, pp. 68–70.
126. D. Olasz, G. Sáfrán, N. Szász, G. Huhn, and N. Quang Chinh, “Indentation size effect in exceptionally hard AlCu thin films,” in *Symposium on Materials Science 2022*, 2023, pp. 20–21.
127. D. Olasz, G. Sáfrán, N. Szász, G. Huhn, and N. Q. Chinh, “Indentation size effect in exceptionally hard AlCu thin films,” *MATERIALS LETTERS*, vol. 330, 2023.
128. G. Pál, Z. Danku, A. Batool, V. Kádár, N. Yoshioka, N. Ito, G. Ódor, and F. Kun, “Scaling laws of failure dynamics on complex networks,” *SCIENTIFIC REPORTS*, vol. 13, no. 1, 2023.
129. S. E. Panasci, I. Deretzis, E. Schilirò, M. A. La, F. Roccaforte, A. Koos, B. Pécz, S. Agnello, M. Cannas, and F. Giannazzo, “Interface Structure and Doping of Chemical Vapor Deposition-Grown MoS2 on 4H–SiC by Microscopic Analyses and Ab Initio Calculations,” *PHYSICA STATUS SOLIDI - RAPID RESEARCH LETTERS*, vol. 17, no. 10, 2023.
130. S. E. Panasci, E. Schilirò, A. Koos, M. Nemeth, M. Cannas, S. Agnello, F. Roccaforte, B. Pécz, and F. Giannazzo, “Micrometer-size crystalline monolayer MoS2 domains obtained by sulfurization of molybdenum oxide ultrathin films,” *MICROELECTRONIC ENGINEERING*, vol. 274, 2023.
131. J. Park, X. Chen, and A. Szolnoki, “Competition of alliances in a cyclically dominant eight-species population,” *CHAOS SOLITONS & FRACTALS*, vol. 166, 2023.
132. C. Pauline, P. Lambin, L. Henrard, and P. Vancsó, “Effects of disorder in the electronic properties of monolayers and nanoribbons MoS2,” in *Graphene2023*, 2023, p. n.a.
133. B. Pécz, M. Nemeth, F. Giannazzo, and A. Kakanakova-Georgieva, “On the possibility of realizing a 2D structure of Si-N bonds by MOCVD,” *PHYSICA STATUS SOLIDI B-BASIC RESEARCH*, vol. 260, no. 10, 2023.
134. B. Peter, N. Kanyo, K. D. Kovacs, V. Kovács, I. Szekacs, B. Pécz, K. Molnár, H. Nakanishi, I. Lagzi, and R. Horvath, “In-situ nanoparticle uptake measurement of live cells with tuned glycocalyx.” 2023.
135. B. Peter, N. Kanyo, K. D. Kovacs, V. Kovács, I. Szekacs, B. Pécz, K. Molnár, H. Nakanishi, I. Lagzi, and R. Horvath, “Nanoparticle uptake of living cells with digested glycocalyx,” in *Magyar Biofizikai Társaság XXIX. Kongresszusa*, 2023, pp. 88–88.
136. B. Peter, N. Kanyo, K. D. Kovacs, V. Kovács, I. Szekacs, B. Pécz, K. Molnár, H. Nakanishi, I. Lagzi, and R. Horvath, “Glycocalyx Components Detune the Cellular Uptake of Gold Nanoparticles in a Size- and Charge-Dependent Manner,” *ACS APPLIED BIO MATERIALS*, vol. 6, no. 1, pp. 64–73, 2023.
137. B. Péter, “Measurements with gold nanoparticles and cells by optical biosensors.” 2023.
138. B. Péter, B. Majoros, S. Kurunczi, A. Violetta Ács, I. Szekacs, S. Bősze, G. M. Kovács, I. Boldizsár, and R. Horvath, “Label-free biosensing of lignans for therapeutics using engineered model surfaces.” 2023.
139. B. Péter, B. Majoros, S. Kurunczi, A. V. Ács, I. Szekacs, S. Bősze, G. M. Kovács, I. Boldizsár, and R. Horvath, “Label-free biosensing of lignans for therapeutics using engineered model surfaces,” *INTERNATIONAL JOURNAL OF BIOLOGICAL MACROMOLECULES*, vol. 233, 2023.
140. A. Pintérné Csordás-Tóth, L. Illés, E. Perez-Feró, T. Novotny, Z. Hózer, J. Stuckert, and M. Sevecek, “Magas hőmérsékleteken oxidált krómbevonatos Zr burkolatminták elektronsugaras vizsgálatai,” *ANYAGVIZSGÁLÓK LAPJA*, no. 3, pp. 11–26, 2023.
141. G. Piszter, Z. Bálint, K. Kertész, L. Szatmári, G. Sramkó, and L. P. Biró, “Breeding Polyommatus icarus Serves as a Large-Scale and Environmentally Friendly Source of Precisely Tuned Photonic Nanoarchitectures,” *INSECTS*, vol. 14, no. 8, 2023.
142. G. Piszter, G. Nagy, K. Kertész, Z. Baji, K. Kovács, Z. Bálint, Z. E. Horváth, J. S. Pap, and L. P. Biró, “Investigating the Effect of Reflectance Tuning on Photocatalytic Dye Degradation with Biotemplated ZnO Photonic Nanoarchitectures Based on Morpho Butterfly Wings,” *MATERIALS*, vol. 16, no. 9, 2023.
143. G. Piszter, K. Kertész, Z. Bálint, and L. P. Biró, “Wide-gamut structural colours on oakblue butterflies by naturally tuned photonic nanoarchitectures,” *ROYAL SOCIETY OPEN SCIENCE*, vol. 10, no. 4, 2023.
144. L. Pósa, P. Hornung, T. N. Török, S. W. Schmid, S. Arjmandabasi, G. Molnár, Z. Baji, G. Dražić, A. Halbritter, and J. Volk, “Interplay of Thermal and Electronic Effects in the Mott Transition of Nanosized VO2 Phase Change Memory Devices,” *ACS APPLIED NANO MATERIALS*, vol. 6, no. 11, pp. 9137–9147, 2023.
145. A. S. Racz, P. Kun, Z. Kerner, Z. Fogarassy, and M. Menyhard, “Tungsten Carbide Nanolayer Formation by Ion Beam Mixing with Argon and Xenon Ions for Applications as Protective Coatings,” *ACS APPLIED NANO MATERIALS*, vol. 6, no. 5, pp. 3816–3824, 2023.
146. Á. Révész and M. Gajdics, “The Effect of Severe Plastic Deformation on the Hydrogen Storage Properties of Metal Hydrides,” *MATERIALS TRANSACTIONS (2001-)*, vol. 64, no. 7, pp. 1387–1400, 2023.
147. Á. Révész, R. Paramonov, T. Spassov, and M. Gajdics, “Microstructure and Hydrogen Storage Performance of Ball-Milled MgH2 Catalyzed by FeTi,” *ENERGIES*, vol. 16, no. 3, 2023.
148. F. Riesz, “Visual approach to the imaging of magic mirrors (Makyohs),” *RESULTS IN OPTICS*, vol. 12, 2023.
149. F. Riesz, “Modelling of the backside pattern transfer in magic mirror (Makyoh) imaging,” *JOURNAL OF OPTICS*, vol. 25, no. 2, 2023.
150. M. Rosebrock, R. Graf, D. Kranz, H. Christmann, H. Bronner, A. Hannebauer, D. Zámbó, D. Dorfs, and N. Bigall, “Controlled Morphological Arrangement of Anisotropic Nanoparticles via Oxidation or Ionic Cross-Linking,” *SMALL STRUCTURES*, vol. 4, no. 12, 2023.

151. M. Rosebrock, J. Schlenkrich, H. Christmann, R. Graf, P. Bessel, D. Dorfs, D. Zámbó, and N. C. Bigall, “Interpenetrating Self-Supporting Networks from Anisotropic Semiconductor Nanoparticles and Noble Metal Nanowires,” *SMALL STRUCTURES*, vol. 4, no. 12, 2023.
152. M. Rosebrock, D. Zámbó, P. Rusch, R. T. Graf, D. Pluta, H. Borg, D. Dorfs, and N. C. Bigall, “Morphological Control Over Gel Structures of Mixed Semiconductor-Metal Nanoparticle Gel Networks with Multivalent Cations,” *SMALL*, vol. 19, no. 10, 2023.
153. M. Roškarič, J. Zavašnik, D. Zámbó, T. Kotnik, S. Kovačič, G. Žerjav, and A. Pintar, “Optimization Method Based on Simplex for Surface Area Improved Photocatalytic Performance of g-C3N4,” *ACS CATALYSIS*, vol. 13, no. 20, pp. 13282–13300, 2023.
154. G. Sáfrán, P. Petrik, N. Szász, D. Olasz, N. Q. Chinh, and M. Serényi, “Review on High-Throughput Micro-Combinatorial Characterization of Binary and Ternary Layers towards Databases,” *MATERIALS*, vol. 16, no. 8, 2023.
155. I. Sallai, Z. Szittner, S. Novák, B. Béres, I. Székács, and R. Horvath, “Analysis of immune cell activation by label-free optical biosensors.” 2023.
156. I. Sallai, Z. Szittner, S. Novák, B. Béres, I. Székács, and R. Horvath, “Label-free immune cell analysis using optical biosensor.” 2023.
157. I. Sallai, Z. Szittner, S. Novák, I. Székács, and R. Horvath, “Label-free immune cell analysis using optical biosensor,” in *Magyar Biofizikai Társaság XXIX. Kongresszusa*, 2023, pp. 119–119.
158. E. Schilirò, S. E. Panasci, A. M. Mio, G. Nicotra, S. Agnello, B. Pecz, G. Z. Radnoczi, I. Deretzis, M. A. La, F. Roccaforte, N. R. Lo, and F. Giannazzo, “Direct atomic layer deposition of ultra-thin Al2O3 and HfO2 films on gold-supported monolayer MoS2,” *APPLIED SURFACE SCIENCE*, vol. 630, 2023.
159. M. Serényi and G. Safran, “Biased reactive high power impulse sputtering of silica,” in *PLATHINIUM 2023*, 2023, pp. 166–166.
160. G. Sfuncia, G. Nicotra, F. Giannazzo, B. Pécz, and G. K. Gueorguiev, “2D graphitic-like gallium nitride and other structural selectivity in confinement at the graphene/SiC interface,” *CRYSTENGCOMM*, vol. 25, no. 41, pp. 5810–5817, 2023.
161. C. Silva, K. Salmanzade, I. Borbáth, E. Dódony, D. Olasz, G. Sáfrán, A. Kuncser, E. Pászti-Gere, A. Tompos, and Z. Pászti, “Reductive Treatment of Pt Supported on Ti0.8Sn0.2O2-C Composite: A Route for Modulating the Sn–Pt Interactions,” *NANOMATERIALS*, vol. 13, no. 15, 2023.
162. A. Singh, M. Gracheva, V. Kovács Kis, Á. Keresztes, M. Sági-Kazár, B. Müller, F. Pankaczi, W. Ahmad, K. Kovács, Z. May, G. Tolnai, Z. Homonnay, F. Fodor, Z. Klencsár, and Á. Solti, “Apoplast utilisation of nanohaematite initiates parallel suppression of RIBA1 and FRO1&3 in Cucumis sativus,” *NANOIMPACT*, vol. 29, 2023.
163. M. Španková, Š. Chromik, E. Dobročka, S. L. Pribusová, M. Talacko, M. Gregor, B. Pécz, A. Koos, G. Greco, S. E. Panasci, P. Fiorenza, F. Roccaforte, Y. Cordier, E. Frayssinet, and F. Giannazzo, “Large-Area MoS2 Films Grown on Sapphire and GaN Substrates by Pulsed Laser Deposition,” *NANOMATERIALS*, vol. 13, no. 21, 2023.
164. Z. Sun, X. Chen, and A. Szolnoki, “State-dependent optimal incentive allocation protocols for cooperation in public goods games on regular networks,” *IEEE TRANSACTIONS ON NETWORK SCIENCE AND ENGINEERING*, vol. 10, no. 6, pp. 3975–3988, 2023.
165. B. Szabó, V. Hutkai, G. Novodárszki, F. Lónyi, Z. Pászti, Z. Fogarassy, J. Valyon, and R. Barthos, “A study of the conversion of ethanol to 1,3-butadiene: effects of chemical and structural heterogeneity on the activity of MgO-SiO2 mixed oxide catalysts,” *REACTION CHEMISTRY & ENGINEERING*, vol. 8, no. 3, pp. 718–731, 2023.
166. B. Szabó, R. Ungai-Salánki, B. Francz, T. Gerecsei, and R. Horváth, “Egyedi sejtek manipulációi robotizált mikropipettával,” *FIZIKAI SZEMLE*, vol. 73, no. 9, pp. 303–305, 2023.
167. Z. Szabó, K. Pankász, J. Márk Bozorádi, O. Hakkel, S. Bella, B. Fabinyi, S. Meucci, and P. Fürjes, “Microfluidic Cuvette for Near Infrared Spectroscopy.” 2023.
168. K. Szakolczai, *EK MFA Yearbook 2022*. Budapest: Energiatudományi Kutatóközpont, 2023.
169. K. Szebényi, A. Füredi, E. Bajtai, S. N. Sama, A. Csiszar, B. Gombos, P. Szabó, M. Grusch, and G. Szakács, “Effective targeting of breast cancer by the inhibition of P-glycoprotein mediated removal of toxic lipid peroxidation byproducts from drug tolerant persister cells,” *DRUG RESISTANCE UPDATES*, vol. 71, 2023.
170. M. Szemerédi, A. Varga, R. Lukács, I. Dunkl, I. Seghedi, Z. Kovács, B. Raucsik, S. Harangi, É. Kosztolányi, and E. Pál-Molnár, “Trace elements and zircon ages to unravel Late Palaeozoic igneous episodes and Variscan geodynamic processes in the Tisza Mega-unit (Carpathian–Pannonian region),” in *Goldschmidt 2023 Conference: abstracts*, 2023.
171. M. Szemerédi, A. Varga, R. Lukács, I. Dunkl, I. Seghedi, M. Tatu, Z. Kovács, B. Raucsik, Z. Benkó, S. Harangi, and E. Pál-Molnár, “Large-volume Permian felsic volcanism in the Tisza Mega-unit (East-Central Europe): Evidence from mineralogy, petrology, geochemistry, and geochronology,” *LITHOS*, vol. 456–457, 2023.
172. M. Szemerédi, A. Varga, R. Lukács, I. Dunkl, I. Seghedi, M. Tatu, Z. Kovács, J. Szepesi, B. Raucsik, M. Horvat, S. Harangi, B. Jákri, Á. Máthé, and E. Pál-Molnár, “Permo–Carboniferous magmatism in the Tisza Mega-unit (Pannonian Basin and Apuseni Mts.): Petrology, zircon U–Pb dating and regional correlations,” in *5th Bohemian Massif Symposium*, 2023, pp. 28–29.
173. M. Szemerédi, Z. Kovács, I. Dunkl, R. Lukács, M. Horvat, B. Jákri, and E. Pál-Molnár, “Variscan S-type granitoids in the Tisza Mega-unit (Carpathian–Pannonian region): petrology, geochronology, geotectonic implications, and correlation,” in *EGU General Assembly 2023: Abstracts*, 2023.
174. M. Szendrő, “Moiré-mintázatok modellezése kétdimenziós heteroszerkezetekben,” Eötvös Loránd Tudományegyetem (ELTE), 2023.

175. Z. Szittner, S. Novák, I. Sallai, B. Béres, I. Székács, and R. Horvath, “Label-free single-cell compatible biophysical methods in immune cell activation,” in *Magyar Biofizikai Társaság XXIX. Kongresszusa*, 2023, pp. 52–52.
176. A. Szolnoki and X. Chen, “Emerging solutions from the battle of defensive alliances,” *SCIENTIFIC REPORTS*, vol. 13, no. 1, 2023.
177. A. Szolnoki and M. Perc, “Oppressed species can form a winning pair in a multi-species ecosystem,” *APPLIED MATHEMATICS AND COMPUTATION*, vol. 438, 2023.
178. Z. Szomor, E. L. Tóth, and P. Fürjes, “Finite element modelling and analysis of fluid dynamic phenomena in two-phase droplet based microfluidic systems,” in *Magyar Biofizikai Társaság XXIX. Kongresszusa*, 2023, pp. 96–96.
179. Z. Szomor, L. Bató, S. Stagl, O. Hakkel, A. Sulyok, C. Dücső, Z. Baji, and P. Fürjes, “Non-stoichiometric titanium-oxide gate electrodes for EGFET based pH sensors.” 2023.
180. Z. Szomor, E. L. Tóth, and P. Fürjes, “3D Finite Element Modelling of heat transfer in continuous flow two-phase droplet microfluidic systems using on-chip thermal control,” in *Proceedings of the 29th International Workshop on THERMal INvestigation of ICs and Systems (THERMINIC’23)*, 2023.
181. N. Taha Ismaeel, Z. Lábadi, and M. Fried, “Combinatorial Preparation and Characterization Methods for High Throughput Study of WO3-MoO3 Mixtures,” in *Symposium on Materials Science 2022*, 2023, pp. 7–9.
182. B. Tegze, G. Tolnai, D. Hessz, M. Kubinyi, J. Madarász, G. Sáfrán, and Z. Hórvölgyi, “Effect of heat treatment temperature on the morphology and upconversion properties of LaF3:Yb,Er nanoparticles,” *JOURNAL OF THERMAL ANALYSIS AND CALORIMETRY*, vol. 148, no. 20, pp. 10795–10802, 2023.
183. I. Tolnai, J. Osan, O. Czompoly, A. Sulyok, and M. Fabian, “Glass/steel/clay interactions in a simulated radioactive waste geological disposal system,” *SCIENTIFIC REPORTS*, vol. 13, no. 1, 2023.
184. T. N. Török, P. Makk, Z. Balogh, M. Csontos, and A. Halbritter, “Quantum Transport Properties of Nanosized Ta2O5 Resistive Switches: Variable Transmission Atomic Synapses for Neuromorphic Electronics,” *ACS APPLIED NANO MATERIALS*, vol. 6, no. 22, pp. 21340–21349, 2023.
185. D. Ugi, G. Péterffy, S. Lipcsei, Z. Fogarassy, E. Szilágyi, I. Groma, and P. D. Ispánovity, “Irradiation-induced strain localization and strain burst suppression investigated by microcompression and concurrent acoustic emission experiments,” *MATERIALS CHARACTERIZATION*, vol. 199, 2023.
186. P. Vancsó, “A 2022. évi Gyulai Zoltán-díj: kétdimenziós anyagok modellezése,” *FIZIKAI SZEMLE*, vol. 73, no. 5, pp. 173–177, 2023.
187. G. Varga, I. Szenti, J. Kiss, K. Baán, G. Halasi, L. Óvári, Á. Szamosvölgyi, R. Mucsi, E. Dodony, Z. Fogarassy, B. Pécz, L. Olivi, A. Sápi, Á. Kukovecz, and Z. Kónya, “Decisive role of Cu/Co interfaces in copper cobaltite derivatives for high performance CO2 methanation catalyst,” *JOURNAL OF CO2 UTILIZATION*, vol. 75, 2023.
188. G. Vertesy, A. Gasparics, and I. Szenthe, “Non-destructive Magnetic Method for the Inspection of Neutron Irradiation Generated Embrittlement of Cladded Nuclear Reactor Pressure Vessel Steel Blocks,” in *Advances and Challenges in Science and Technology Vol. 3*, 2023, pp. 139–166.
189. G. Vértesy, “Coercive Properties of Magnetic Garnet Films,” *CRYSTALS*, vol. 13, no. 6, 2023.
190. G. Vértesy, I. Mészáros, and B. Bögre, “Application of Magnetic Adaptive Testing for Nondestructive Investigation of 2507 Duplex Stainless Steel,” *SENSORS*, vol. 23, no. 7, 2023.
191. C. Wang, W. Zhu, and A. Szolnoki, “When greediness and self-confidence meet in a social dilemma,” *PHYSICA A - STATISTICAL MECHANICS AND ITS APPLICATIONS*, vol. 625, 2023.
192. C. Wang, W. Zhu, and A. Szolnoki, “The conflict between self-interaction and updating passivity in the evolution of cooperation,” *CHAOS SOLITONS & FRACTALS*, vol. 173, 2023.
193. C. Wang and A. Szolnoki, “Inertia in spatial public goods games under weak selection,” *APPLIED MATHEMATICS AND COMPUTATION*, vol. 449, 2023.
194. C. Wang and A. Szolnoki, “Evolution of cooperation under a generalized death-birth process,” *PHYSICAL REVIEW E: COVERING STATISTICAL NONLINEAR BIOLOGICAL AND SOFT MATTER PHYSICS (2016-)*, vol. 107, no. 2, 2023.
195. S. Wang, X. Chen, Z. Xiao, A. Szolnoki, and V. V. Vasconcelos, “Optimization of institutional incentives for cooperation in structured populations,” *JOURNAL OF THE ROYAL SOCIETY INTERFACE*, vol. 20, no. 199, 2023.
196. M. Wasilewska, A. Michna, A. Pomorska, K. Wolski, S. Zapotoczny, E. Farkas, Z. Szittner, I. Szekacs, and R. Horvath, “Polysaccharide-based nano-engineered multilayers for controlled cellular adhesion in label-free biosensors,” *INTERNATIONAL JOURNAL OF BIOLOGICAL MACROMOLECULES*, vol. 247, 2023.
197. J. Xiao, L. Liu, X. Chen, and A. Szolnoki, “Evolution of cooperation driven by sampling reward,” *JOURNAL OF PHYSICS - COMPLEXITY*, vol. 4, no. 4, 2023.
198. J. Xiao, L. Liu, X. Chen, and A. Szolnoki, “Evolution of cooperation driven by sampling punishment,” *PHYSICS LETTERS A*, vol. 475, 2023.
199. T. F. Yang, R. G. Zeng, L. H. Yang, A. Sulyok, M. Menyhárd, K. Tőkési, and Z. J. Ding, “Energy loss function of samarium,” *SCIENTIFIC REPORTS*, vol. 13, no. 1, 2023.
200. D. Zambo, D. Kovacs, G. Sudi, Z. Zolnai, and A. Deak, “Composite ligand shells on gold nanoprisms - an ensemble and single particle study,” *RSC ADVANCES*, vol. 13, no. 44, pp. 30696–30703, 2023.
201. D. Zámbó, D. Kovács, G. Südi, and A. Deák, “Surface modification of gold nanoprisms and Their self-assembly with nanospheres,” *PARTICLE & PARTICLE SYSTEMS CHARACTERIZATION*, vol. 40, no. 3, 2023.
202. Z. Zolnai, P. Petrik, A. Németh, J. Volk, M. Bosi, L. Seravalli, and R. Fornari, “Atomic structure and annealing-induced reordering of ε-Ga2O3: a Rutherford Backscattering/Channeling and Spectroscopic Ellipsometry study,” *APPLIED SURFACE SCIENCE*, vol. 636, 2023.